**General Disclaimer**

**One or more of the Following Statements may affect this Document**

- This document has been reproduced from the best copy furnished by the organizational source. It is being released in the interest of making available as much information as possible.

- This document may contain data, which exceeds the sheet parameters. It was furnished in this condition by the organizational source and is the best copy available.

- This document may contain tone-on-tone or color graphs, charts and/or pictures, which have been reproduced in black and white.

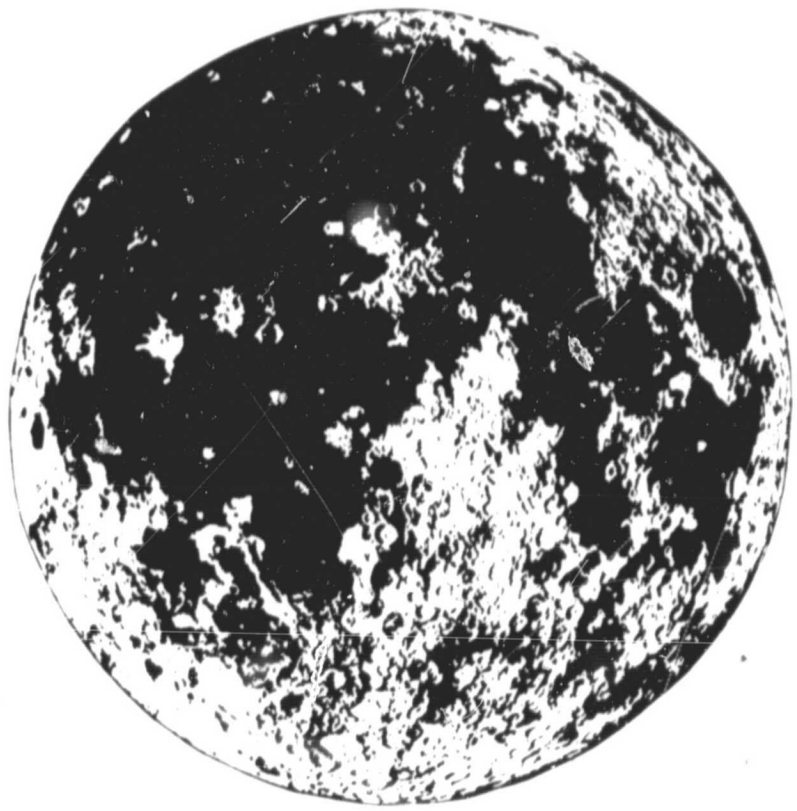
- This document is paginated as submitted by the original source.

- Portions of this document are not fully legible due to the historical nature of some of the material. However, it is the best reproduction available from the original submission.

Produced by the NASA Center for Aerospace Information (CASI)

# MINERALOGY AND PETROLOGY OF THE APOLLO 11 LUNAR SAMPLE

J. A. WOOD, U. B. MARVIN, B. N. POWELL, and J. S. DICKEY, JR.



FACILITY FORM 602
(ACCESSION NUMBER) 1135
(PAGES)
(NASA CR OR TMX OR AD NUMBER)
(THRU)
(CODE) 13
(CATEGORY)



FEB 1970
RECEIVED

Smithsonian Astrophysical Observatory
SPECIAL REPORT 307

Research in Space Science
SAO Special Report No. 307

# MINERALOGY AND PETROLOGY OF THE APOLLO 11 LUNAR SAMPLE

J. A. Wood, U. B. Marvin, B. N. Powell, and J. S. Dickey, Jr.

January 9, 1970

Smithsonian Institution
Astrophysical Observatory
Cambridge, Massachusetts 02138

912-111

Key to Plates 1 and 2. Plate 1 is a macroscopic view of a collection of lunar lithic fragments, chosen to represent most of the rock types encountered in our study (though not in the proportions that occur in the Apollo 11 bulk sample). Plate 2 is a thin section of the same fragments, arranged as nearly as possible in the same configuration as Plate 1 (and this Key); illuminated by unpolarized transmitted light. Spherule E is missing from Plate 2. Colors noted in the Key are as they appear in thin section, not macroscopically. Circular structures in the fragments are genuine vesicles in the lunar material; circles between fragments are air bubbles in the mounting medium.

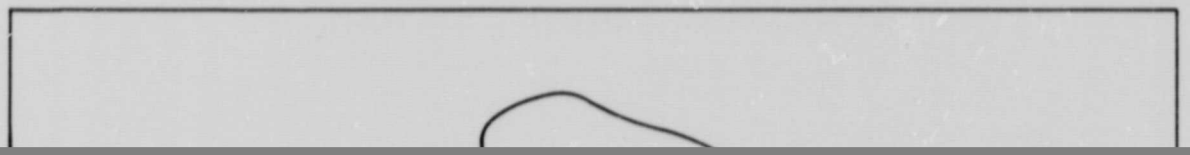




Plate 1.

PRECEDING PAGE BLANK NOT FILMED.

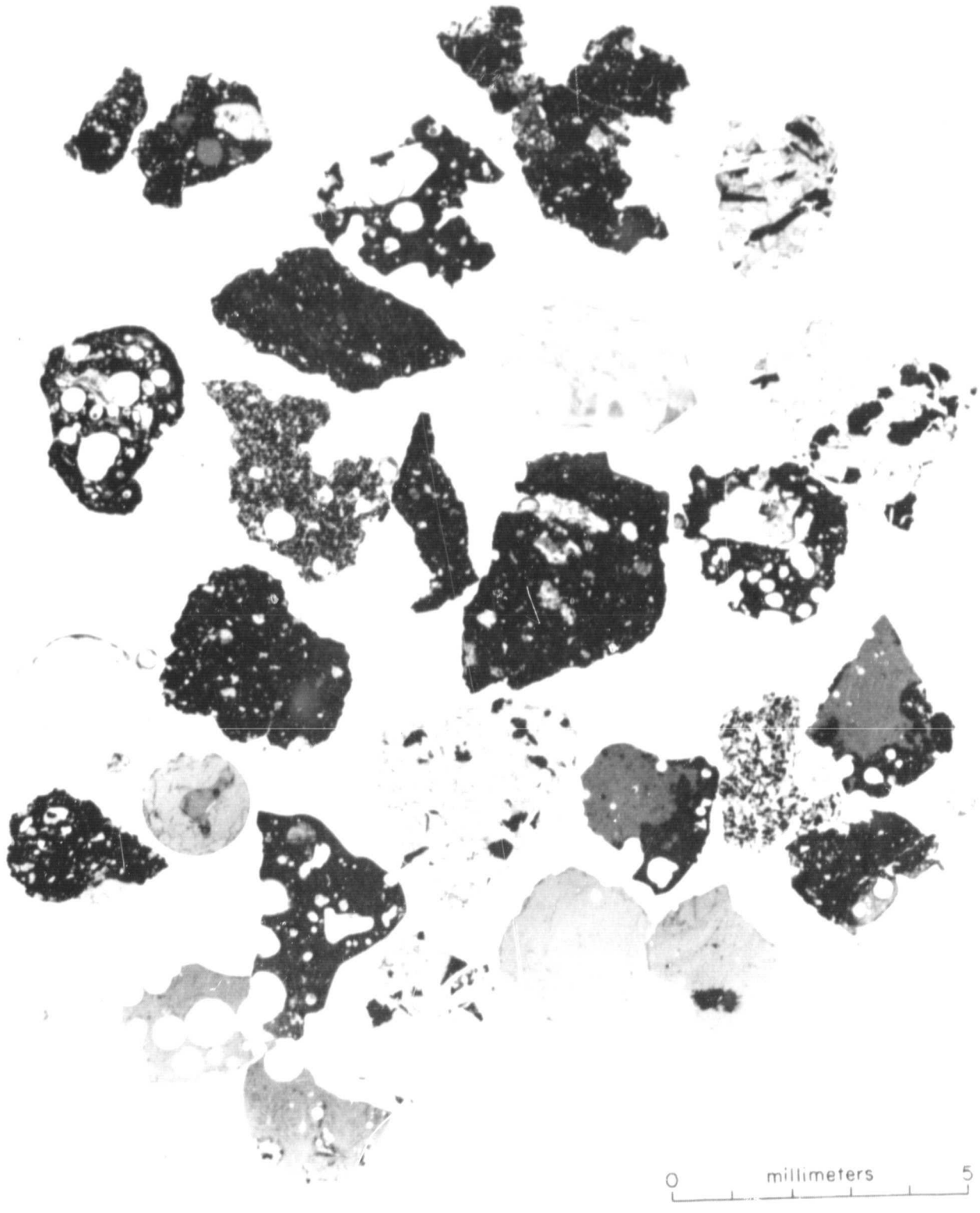



Plate 2.

PRECEDING PAGE BLANK NOT FILMED.

TABLE OF CONTENTS


| Section | | Page |
|---|---|---|
| | ABSTRACT | ix |
| I | INTRODUCTION | 1 |
| | Geologic Setting | 1 |
| | Preparation and General Procedures | 3 |
| II | DESCRIPTIONS OF LUNAR ROCK TYPES | 5 |
| | A. Lunar Soils and Soil Breccias | 5 |
| | B. Basalts | 13 |
| | C. Anorthositic Rocks | 37 |
| | D. Glasses | 43 |
| | E. "Meteorites" | 51 |
| III | SHOCK METAMORPHISM | 59 |
| IV | DISCUSSION AND INTERPRETATION | 61 |
| | Anorthosites as Highlands Material | 61 |
| | A Model of Lunar Structure and Evolution | 63 |
| | Melting of the Moon | 67 |
| | Lunar Mascons | 70 |
| | Origin of the Moon | 74 |
| V | ANALYTICAL PROCEDURES | 75 |
| | A. Preliminary Sample Treatment | 75 |
| | B. Thin-Section Preparation | 77 |
| | C. Microprobe Analysis | 79 |
| | D. Grain Mounting for Optical and X-Ray Measurements | 85 |
| | E. Refractive Index and Optic Axial Angle Measurements | 87 |
| | F. Density Determinations | 89 |
| | G. X-Ray Diffraction Procedures | 91 |
| VI | ACKNOWLEDGMENTS | 93 |
| VII | REFERENCES | 95 |

PRECEDING PAGE BLANK NOT FILMED.

## RÉSUMÉ

Les auteurs ont préparé et étudié des minces lames de 1676 fragments rocheux (de 1-5 mm. de diamètre) provenant de la prise massive d'Apollo XI. La plupart des roches ont un grain si fin que des fragments de cette taille donnent des échantillons typiques. On a trouve les proportions suivantes de types rocheux, évidemment d'origines diverses: sols breccias 52,4%; basaltes 37,4%; verres 5,1%; roches anorthosiques 3,6%; autres 1,5% (y compris moins de 0,1% de débris météorique reconnaissables).

Les basaltes varient en taille de grain de moins d'un micron à plus de trois cent et consistent surtour de pyroxène (environ 50% en poids; augite titanifère ou augite sous-calcique accompagnée de pigeonite; environ 30% des molécules avec terminaison ferrosilicique), de feldspath plagioclase (environ 25% en poids, nombre d'anorthite presque toujours de 90 à 100) et d'ilménite (environ 20% en poids). Quelque spécimens de basalte sont étonnament riches en $K_2O$ (0,7%). Leur poids spécifique est environ 3,3 $gm/cm^3$.

Les verres ont été fondus par impact. Leur teinte varie de foncée (brune, jaune-orange) à incolore, leur structure de claire et uniforme à tourbillonaire, globulaire et hétérogene.

Le sol breccia forme un mélange de fragments minéraux, rocheux et vitreux fixé dans une gangue sombre, au grain fin (plutôt vitreux, mais contenant aussi des particules minérales). La cimentation résulte sans doute de vitrification partielle à l'impact d'un sol meuble superficiel. Globalement, les breccias ont essentiellement la même composition que les basaltes.

Seules les 61 fragments d'anorthose étaient complétement inattendus. Ils sont de couleur claire, de basse densité (environ 2,9 $gm/cm^3$) et couvrent la gamma des pures anorthoses jusqu'aux gabbros anorthosiques. Ils ont un

grain bien plus fin (10-100μ) que les anorthoses terrestres, mais sont apparemment vraiment d'origine accumulative. Leur feldspath est un peu plus clacique que le feldspath basaltique et l'olivine ($Fa_{50}$) est le principal minéral mafique. Le contenu de Titane est faible. La composition génèrale d'un tel fragment, sans doute typique, reproduit les résultâts de Surveyer VII pour les éjecta du cratère montagneux Tycho. Les auteurs croient que les anorthoses proviennent du terrain montagneux.

On propose un modèle de structure lunaire: une écorce de 25 km d'anorthose fut produite par fractionnement d'un magma et flotte sur un gabbro plus dense; jadis, on a vu de forts impacts percer l'écorce les laves de basalte jaillir par ces fissures jusqu'au niveau d'équilibre et se solidifier, formant ainsi les maria. On explique aussi les mascons.

Les débris météoriques et les effets de choc sur la surface lunaire sont aussi discutés. Le contenu de zirconium dans la matiére lunaire est de ~ 400 ppm.

## ZUSAMMENFASSUNG

Wir präparierten und untersuchten die Dünnschliffe von 1676 Gesteinbruchteilen (im Durchmesser von 1 bis 5 mm) des Apollo 11 Gesamt-Exemplares. In beinahe jedem Falle sind die Gesteine von einer entschiedenen feinen Korngrösse, so dass Bruchteile dieser Grösse ein vorbildendes Muster abgeben. Wir fanden die folgenden Proportionen von Gesteintypen, anscheinend eine Ansammlung von vielen Quellen; Mondstaub Breccia, 52.4%; Basalte, 37.4%; Glasarten, 5.1%; Anorthositisches Gestein, 3.6%; und andere Typen (einschliesslich weniger als 0.1% erkennbarer meteoritischer Abfall), 1.5%.

Die Basalte sind von einer Korngrösse von $< 1\mu$ bis $> 300\mu$ vorzufinden und bestehen meist aus Pyroxen ($\sim$ 50% pro Gewicht; Ti-enthaltend Augit oder kalkarmer Augit, plus Pigeonit; $\sim$ 30 Molen Prozent von Ferrosilit Molekül), Plagioklas ($\sim$ 25%, $An_{90-100}$ in den meisten Fällen), und Ilmenit ($\sim$ 20%). Einige Basaltexemplare sind überraschend reich an $K_2O$ (0.7%). Deren specifisches Gewicht ist ungefähr 3.3 $gm/cm^3$.

Die Glastypen waren im Anstoss geschmolzen, und reichen von farbreich (braun, orange-gelb) bis farblos, von klar und einheitlich bis zu wirbelig, blasenhaltig und heterogen.

Die Mondstaub Breccia ist eine gefestigte Sammlung von Mineralien, Gesteinen und Glasbruchteilen in einer feinkörnigen, dunkelen Grundmasse (meist glasige, aber auch Mineral-Anteile). Das Zusammenfügen ist wahrscheinlich ein Resultat von teilweisem Anstoss-Schmelzen eines ursprünglich losem Mondstaub. Die allgemeine Zusammensetzung der Breccia ist wesentlich die gleiche wie von Basalt.

Nur die 61 angefundenen Anorthosit Bruchteile waren gänzlich unerwartet. Sie sind hell in Erscheinung, niedrig im spezifischen Gewicht ($\sim$ 2.9 $gm/cm^3$), und reichen von genauen Anorthositen bis anorthositischen Gabbros. Diese

Bruchteile sind von kleinerer Korngrösse (10 bis 100μ) ais die irdischen Anorthositien, aber anscheinend wahre Kristallanhäufung. Der Plagioklas ist etwas kalkhaltiger als der basaltische Plagioklas, und Olivin ($Fa_{50}$) ist gewöhnlich anwesend. Der Ti Inhalt ist niedrig. Die chemische Zusammensetzung eines solchen Teiles, wahrscheinlich typisch der meisten, gleicht der Surveyor VII Analyse von vertriebenem Material des Krater Tycho, gelegen im Mond-Kontinent. Wir glauben, dass diese Anorthositen vom Mond-Kontinent stammen.

Ein Mond Struktur Model ist vorgesehen, in welchem eine 25 km anorthosite Schicht, hervorgerufen von magmatischer Differenzierung, auf einer dichten Gabbro schwebt. Wo einst grössere Anstösse durch die Kruste brachen, schwoll basaltische Lava zur Gleichgewicht-Oberfläche und hartete sich, und somit entstand die Maria. Eine Erklärung für Mascons ist angegeben.

Meteoritische Abfälle und Stossefekte auf der Mond-Oberfläche sind auch diskutiert. Der Zr Inhalt des Mond Exemplares beträgt ~400 ppm.

## КОНСПЕКТ

Мы приготовили и исследовали тонкое рассечение фрагментов камня 1676 (зона диаметра 1 до 5 мм) из массы образцов Аполло 11. Почти во всех случаях камни достаточно мелкозернисты и могут составить типичные образцы. Мы обнаружили следующие пропорции типов камней, -- очевидно смешание многих источников: почва брекчия, 52.4%; базальты, 37.4%; стёкла, 5.1%; анортозитичные камни, 3.6%; другие (включая меньше чем 0.1% знакомых метеорических обломков), 1.5%.

Зёрна базальтов различаются в размерах от $< 1\mu$ до $>300\mu$ и в значительной степени состоят из пироксенов ($\sim$ 50 wt.%; титанический авгит или суб-кальций авгит и пиджаонит; $\sim$ 30 моль % ферросилит последний член), плагиоклаз-фельдшпат ($\sim$ 25%, $An_{90-100}$ в большинстве случаев), и ильменит ($\sim$ 20%). Некоторые образцы базальтов очень богаты элементом $K_2O$ (0.7%). Их специфическая тяжесть приблизительно 3.3 $gm/cm^3$.

Стёкла расплавленны ударом, и различаются в цветах от тёмных (коричневых, оранжевых-желтых) до безцветных; некоторые из них прозрачные и однообразные, некоторые круженные, некоторые с полостью в минерале, и еще дрчгие — гетерогенные.

Почва брекчия является смешанием фрагментов минерала, камней и стёкла, в мелкозернистой, тёмной форме (главным образом она стеклянная, смешанная с миннральными частицами). Цементация

вероятно произошла частичным сотрясением стекловидного вещества и начальной пыхлой, поверхностной почвы. По существу, общий состав брекчий и базальтов кажется одинаковым.

Только 61 из этих фрагментов были сове рщенно неожиданны. Они светлые, со слабой плотностью ( $\sim 2.9$ gm/cm$^3$), некоторые из них действительные анортозиты, другие анортозтические базальты. Они очень мелкозернисты (10 до 100$\mu$), гораздо мелче зернистые чем земные анортозиты, но по видимому предстовляются действительными накоплениями. Их фельдшпат слегка больше кальций чем фельдшпат базальтов, и оливин ($Fa_{50}$) оказывается главным мафическим минералом. Содержание Ti чниженно. Состав основной массы одного такого фрагмента, вероятно типичного почти всех, соглашается с анализом эжестов Surveyor VII с нагорья кратера Tycho. Мы пологаем что анортозиты происходят с нагорьев.

Предложенна есть структурная модель луны, в которой 25-км анортозит-кора, созданная магма-тической фракцией, держится над поверхностью плотного габбро. В местах, где прежние главные удары проделали отверстия сквозь кору, базальтная лава хлынула к поверхности, затвердела, и таким образом образовала марию. Предложено и обьяснение масконцев.

Было тоже обсуждение метеорических обломков и результатов сотрясения на поверхности луны. Содержание Zr в лунном материале $\sim$ 400 ppm.

# MINERALOGY AND PETROLOGY OF THE APOLLO 11 LUNAR SAMPLE

J. A. Wood, U. B. Marvin, B. N. Powell, and J. S. Dickey, Jr.

## I. INTRODUCTION

The Apollo 11 mission, which was mounted for the purpose of landing men on the lunar surface and returning them safely to Earth, was eminently successful in its primary and also in most of its secondary goals, including the return of rock and soil samples for exhaustive study by some 140 groups of scientific investigators around the world.

The landing site (Figure I-1), just north of the lunar equator near the southwestern edge of Mare Tranquillitatis, was selected as a level, unobstructed surface relatively safe for manipulation of the module and for the first lunar walk by men. As the module approached touch-down, the crew piloted it across a small crater to a position of their own choosing (Figure I-2) at Latitude 0°41'15" N, Longitude 23°25'45" E. The landing took place on July 20, 1969, at 3:17:40 PM EST; and 6 hr and 40 min later, Neil Armstrong stepped upon the surface of the Moon. He was soon joined by Edwin Aldrin, and for the next 2 hr and 14 min the two astronauts collected samples, took photographs, and deployed various scientific experiments.

### Geologic Setting

Mare Tranquillitatis is part of the complex of dark, lowland plains that lends a striking appearance to the Earth-facing side of the Moon. The petrology, age, and origin of the maria, and their asymmetrical distribution on the lunar surface constitute fundamental problems in lunar geology. Mare Tranquillitatis is irregular in form and, in contrast to several of the ringed maria, is not marked by a positive gravity anomaly. Topographic relations suggest that Mare Tranquillitatis is an older feature than are the ringed maria.

This work was supported in part by Contract NAS 9-8106 from the National Aeronautics and Space Administration.

The landing site, Tranquillity Base, proved to be heavily strewn with blocky debris and pockmarked with small pits and craters ranging from a few centimeters to nearly 200 m in diameter. West Crater, the largest sharply-defined crater in the vicinity, lies 400 m east of the landing site of the module. It is about 180 m in diameter and 30 m deep, and has a raised rim surrounded by a symmetrical apron of throwout about 250 m wide and by rays, one of which appears to extend past the landing site. Four broad, subdued craters also occur nearby. All craters examined by the astronauts appeared to be excavated in the lunar regolith. None showed visible outcrops or evidence of stratification in their walls or floors. However, most of the loose blocks in the rim of West Crater and piled on the floor of a small crater, 33 m wide and 4 m deep and lying 60 m east of the module, probably come from mare bedrock. At least three craters larger than 1 km in diameter (Moltke, Sabine D, and Sabine E) lie within 50 km (Figure I-1) and are deep enough to be excavated in mare rock.

Although the lunar rocks and soils at the landing site should consist predominantly of mare material, some admixture of highlands material and meteoritic debris is to be expected. A promontory of the highland Kant Plateau stands only 41.5 km south southwest of Tranquillity Base (Figure I-3). Two ray systems cross the southern part of Mare Tranquillitatis. One comes from the crater Theophilus, 420 km to the southeast, while the other is from an unknown source to the southwest, possibly the crater Alfraganus or even Tycho. Although neither ray system visibly intersects the landing site, fine particles of material associated with the rays may be present.

Unlike the residual soils overlying terrestrial bedrock, the lunar soils must certainly derive from multiple sources, some close by and others at great distances. A continual mixing of rock types is likely as a result of primary and secondary impacts. Thus, the particles in any given soil sample will record a long history of crystallization in igneous rocks under diverse conditions of temperature and pressure, followed by impact with possible shock metamorphism or melting.

## Preparation and General Procedures

In planning our laboratory investigations, we recognized the likelihood that lunar soils would constitute an important fraction if not the entire sample that would be returned by the Apollo 11 astronauts. The predicted complexity of the lunar soils made them seem very promising material for beginning to unravel the history of the Moon. Our formal request to NASA, therefore, specified unsorted soil as our sample of first choice. We expected it to consist of very fine, probably monomineralic grains, and planned to study it grain by grain by means of optical microscopes, x-ray diffraction, and the electron microprobe. By this approach we hoped to establish the relative abundances of minerals present and the probable rock types from which they were derived, and to trace some of the processes that are active on the lunar surface.

In the expectation that lunar soils might occur mainly in fine-grain sizes, we acquired an x-ray microfocus generator for making diffraction films of small particles in short exposure times and designed a two-axis rotating crystal mount for approximating Debye-Scherrer patterns from small single crystals. Much of the summer of 1969 was spent devising a technique for mounting single grains on fibers in order to carry out optical measurements on a spindle stage, followed by x-ray diffraction of the crystal on the same fiber. We also experimented with techniques of embedding, sectioning, and polishing fine grains for microprobe analyses.

Our sample was picked up at the Manned Spacecraft Center in Houston on September 17 and was brought to the laboratory the following morning. It consisted of about 16 gm of the bulk sample collected on the lunar surface by Neil Armstrong. A cursory examination indicated that the material was much coarser, easier to manipulate, and even more interesting than we had hoped. We received 11.0944 gm of material ranging in grain size from 1 mm

to 1 cm (Sample No. 10085,24); and 5.057 gm of soil finer than 1 mm (Sample No. 10084,108). The majority of grains 1 mm and larger proved to be lithic fragments and therefore of infinitely greater value than single minerals for interpreting lunar petrology.

To gain the maximum amount of information from such materials, we immediately embarked on a two-part program of study: Some 1700 of the coarser rock fragments were embedded in epoxy and cut into polished thin sections for a petrographic survey of rock textures, to be followed by analyses of selected fragments on the electron microprobe. Minerals of special interest were to be extracted from the probe sections for x-ray diffraction determinations. Meanwhile, the finer materials were sieved, then separated magnetically and in heavy liquids for a study of the minerals and glasses present by the optical immersion method and x-ray diffraction. A selection of these grains would later be analyzed on the microprobe. Several hundred grains from an aliquot of the fines were mounted on fibers for the general survey previously planned. We placed major emphasis on the study of thin sections, to which the mineralogical studies added useful confirmatory data.

As a result of our studies, we identified four main types of rock from the lunar surface. These types, which will be described in detail in the following sections, were observed in thin sections in the following proportions:

| | | |
|---|---|---|
| Soil breccias (including 9.9% partially vitrified breccias) . . | | 52.4 vol.% |
| Basalts . . . . . | | 37.4 |
| Coarse . . . . . | 13.6 | |
| Medium . . . . . | 11.5 | |
| Fine . . . . . | 12.6 | |
| Anorthosites . . . . . | | 3.6 |
| Glasses . . . . . | | 5.1 |
| Homogeneous, colorless . . | 0.3 | |
| Homogeneous, colored . . . | 0.5 | |
| Inhomogeneous . . . . . | 3.3 | |
| Displaying devitrification or quench structures . . . . | 1.0 | |
| Others (meteorite fragments, shocked debris, etc.) . . . . . | | 1.5 |
| | | 100.0% |




Figure I-1. Landing site of Apollo 11 (arrow) on Mare Tranquillitatis (black plain), looking west approximately along the lunar equator. Highlands areas to south and west are lighter in color. Craters visible are Sabine (S), Ritter (R), Moltke (M), Sabine D (D), Sabine E (E). Lunar Orbiter V-64M.

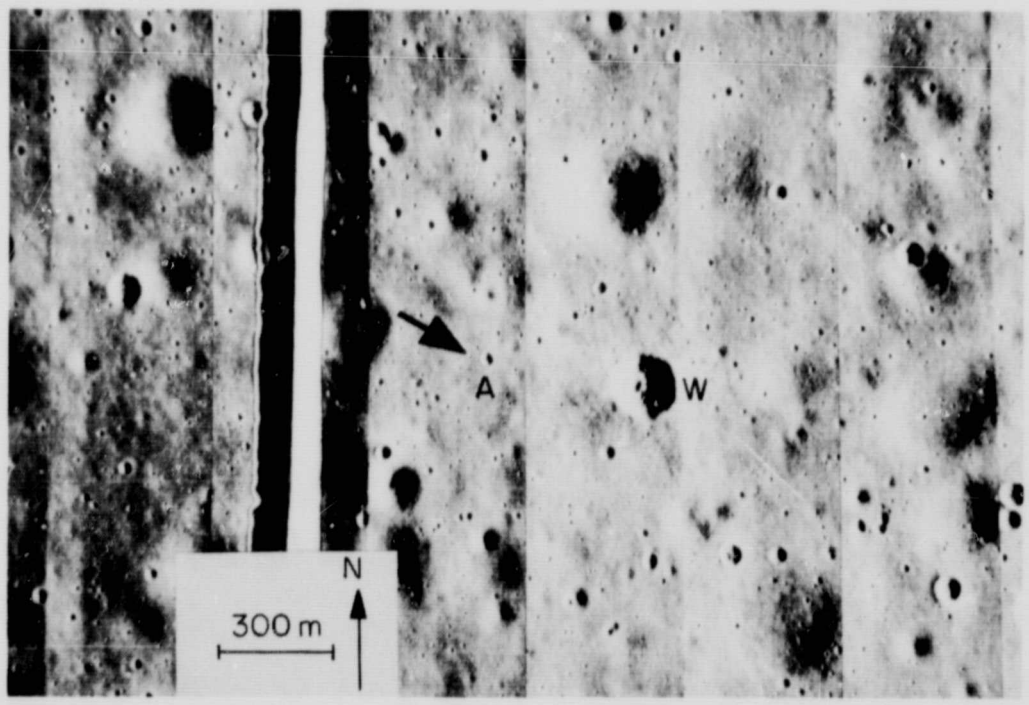



Figure I-2. Landing site of Apollo 11 (arrow), large scale photograph. W, West crater; A, crater visited by Armstrong. Lunar Orbiter V-76$H_3$.

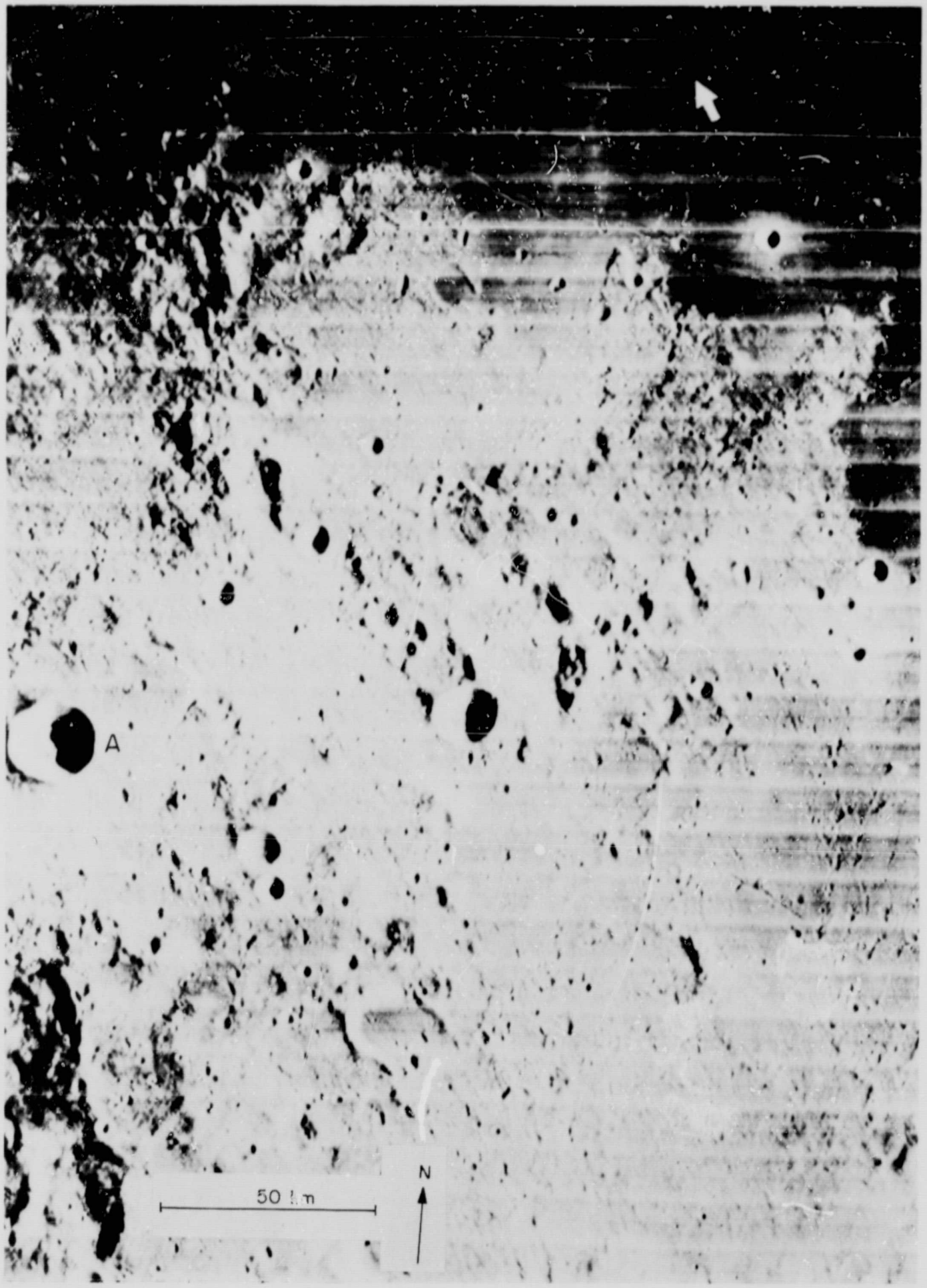



Figure I-3. Highlands area immediately south of Apollo 11 landing site (arrow). Crater Alfraganus is shown (A); Theophilus is off the photograph to lower right, but ejecta pattern of this crater can be seen extending toward Mare Tranquillitatis. Lunar Orbiter IV-84$H_3$.

# II. DESCRIPTIONS OF LUNAR ROCK TYPES

## IIA. Lunar Soils and Soil Breccias

In the bulk and core samples from the lunar surface, all materials in the size range below 1 cm are classified as fines. The fines fall into two sub-groups. Those ranging from about 1 mm to 1 cm are largely poly-mineralic fragments of lunar bedrock and of glass-welded soil breccias, along with a relatively few large glass spherules, glass shards, and scraps of meteoritic metal. The materials in the <1-mm range make up over 90% of the fines (LSPET, 1969b). This fraction also contains an abundance of grains consisting of two or more minerals, and of breccia fragments. Below about 120μ, however, the soils consist mainly of angular particles of single mineral grains and glass with a generous admixture of melted forms: spherules, dumbells, rods, and ellipsoids. The very finest fraction, below about 25μ, appears to be mainly glass.

### Breccia Fragments

About 52% of the fragments in the 1-mm to 1-cm size range are micro-breccias. The remainder are pieces of basalt, anorthosite, and shock-melted glasses. To the unaided eye the breccias appear dense and dark gray to black with a few lighter colored inclusions (Plate 1, Fragments A, B, K, L, M, O, T, U; Figures IIA-1 and -2). They vary in cohesiveness from easily friable to firmly cemented.

Thin sections reveal that most of the breccias are aggregates of angular rock, mineral, and glass detritus embedded in a very fine-grained matrix of the same material (Figure IIA-3). Glass spherules, some whole, some broken, are a common constituent. The embedded particles range in size from a few microns to over 5 mm, but the majority lie between 40 and 300μ. Most of these grains show evidence of shock in the form of micro-fractures, lamellar structures, randomization of crystal lattices, and various degrees of melting.

The breccia matrix consists of rock flour in the sub-micron to ~35μ size range. It appears dark brown and opaque excepting in ultra-thin sections where it is pale brown, transparent, and essentially isotropic, which indicates the presence of a large proportion of glass. Electron microprobe analyses show that the matrix is variable in composition but, on the average, similar to the maria basalts (Table IIA-I). This basaltic composition is borne out by x-ray powder patterns that show an admixture of augite and ilmenite with a minor amount of plagioclase feldspar.

In about 10% of our breccia thin sections, one can see that the matrix has been partly melted to a tawny glass. The proportions of melted material vary from a few thin wisps to virtually the entire matrix, as shown in Figures IIA-4 through IIA-8. We conclude that glass is the welding agent in all of the soil breccias though it cannot actually be seen in most breccia thin sections of normal thickness (30μ). That this glass is simply melted soil is shown by its textural relations to embedded detritus, and also by its amber color, which is identical to that of a sample of very fine soil that was artificially melted in our laboratory (Figures IIA-8 and -9).

The soil breccias record a complex history beginning with the production of detritus by primary and secondary impacts on lunar bedrocks, followed by reduction to ever finer grain sizes coupled with continuous mixing. Most of the primary impacts are energetic enough to cause shock damage and melting and to largely destroy the impacting projectiles. Less than 0.1% of the fines are identifiable meteoritic debris.

The lunar soils are firmly packed but largely unconsolidated, as described by the astronauts and shown by the character of the core sample (LSPET, 1969a, b). The breccias were produced by heating events that welded the soils into second-generation rocks that were then broken again into fragments, some of which were aggregated into later breccias. Figure IIA-10 shows a shocked and nearly glassy breccia fragment, retaining a few unmelted pyroxene grains, embedded in a younger breccia.

Other details of breccia history are illustrated in Figures IIA-11 through IIA-21. Several varieties of glassy detritus are shown in the first five of these figures. A broken piece of glass with flow banding, near a small yellow glass spherule, is surrounded by angular glass and mineral detritus in Figure IIA-11. Figures IIA-12 and -13 show a large angular piece of colorless glass and a large yellow glass spherule, respectively. This spherule, like the majority of others, is clear and isotropic. Unlike many others it is neither cracked nor broken, which suggests that it is the most recently formed of the detritus in this field. A glass ellipsoid, in Figure IIA-14, exhibits a reaction rim with the matrix and a feathery internal structure. As the glass was hot enough to react with the matrix, it may have grown internal crystallites prior to cooling. Possibly, however, the structure results from later shock or devitrification. Figure IIA-15 shows a colorless, glassy mass that has lost its outlines in reaction with the matrix, itself largely glass. We attribute this structure to intense shock of a rock consisting largely of plagioclase feldspar.

Rock and mineral fragments embedded in the matrix are shown in Figures IIA-16 through IIA-20. A large, angular piece of coarse basalt with one shattered edge that seems forcibly packed into the matrix is seen in Figure IIA-16. A rounded particle of similarly coarse basalt that has been abraded earlier in its history is in Figure IIA-17. Figures IIA-18 and -19 show embedded feldspathic fragments, partly shocked to finely granular glass. We believe these are small particles of anorthositic highlands material. A virtually undamaged pyroxene crystal from a coarse basalt lies close to the anorthosite fragment in Figure IIA-19. Another fresh and distinctly zoned pyroxene grain, embedded in dense matrix material, is seen in Figure IIA-20.

A rock breccia formed <u>in situ</u> by impact on maria basalt is shown in Figure IIA-21. Unlike the soil breccias, this rock retains vestiges of its original fabric, although clear grain boundaries have been largely obliterated. No glass spherules occur and no evidence of melting and flow, yet the minerals in these rocks have been shocked to a predominantly glassy state.

Lunar soils (-1 mm fraction)

Over 90% of the fines are less than 1 mm in grain size. Rock fragments consisting of two or more minerals, and glass-welded breccias make up the majority of particles from 1 mm to about 120μ. Below that range the detritus consists mainly of single mineral fragments and glass, including an abundance of spherules ranging from colorless through pale brown, green and yellow to amber, mahogany and nearly black. These spherules, along with other glasses, are described in detail in Section IID.

The finest (-35μ) fraction of the unconsolidated soils has the same mineralogical composition as the matrix material in the breccias. Optical examination shows a large percentage of very fine detrital glass; x-ray powder patterns show an admixture of augite, ilmenite, and plagioclase.

In order to study the range of minerals present in the soils we have carried out magnetic and heavy liquid separations, mainly on materials in the 100 to 200 mesh (149 to 74μ) size range. Two hundred grains, picked at random from this range, were mounted on glass rods for optical and x-ray determinations. In addition, we have examined numerous samples of finer grain-size by the optical immersion method. From the results of these studies combined with those on the microprobe we estimate the following approximate abundances for the unconsolidated lunar soil:

| | |
|---|---|
| Glass | ~ 50% |
| Pyroxenes | 25 |
| Plagioclase | 15 |
| Ilmenite | 8 |
| Olivine | 1 |
| Others: (Tridymite, Quartz, Cristobalite, Troilite, Iron metal, Ni-Fe metal, Zircon, Unidentified) | 1 |
| | 100% |

The glasses range in index of refraction from 1.490 to 1.750, but fall into two main groups, one of feldspathic, the other of basaltic composition. A very small amount of silica glass is also present. Glasses are discussed in more detail in Section IID.

The pyroxenes include pigeonites and sub-calcic augites with a narrow range of compositions. No orthopyroxenes were detected. The plagioclase feldspars are all Ca-rich, ranging from $An_{76}$ to $An_{98}$. In several cases it was possible to establish the high temperature origin of feldspar grains by the optic angle and sign (for a given index of refraction). The olivines are generally light yellow in color and range from $Fa_{32}$ to $Fa_{51}$. Optical properties and compositions of these rock-forming minerals are combined with the report on basalt minerals in Section IIB, since it is safe to assume that most of the detrital mineral grains were derived from lunar basalts.

Finely ground ilmenite in the lunar soil and soil breccia is responsible for the overall dark color of these materials and of Mare Tranquillitatis in general. Although samples from future mare landings will undoubtedly reveal regional differences in chemistry and petrology, it seems likely from their uniformly dark color that all the lunar maria must contain substantial amounts of ilmenite and therefore abnormal (by terrestrial standards) levels of Ti.

The silica minerals tridymite, cristobalite, and quartz occur in the detritus in sparing amounts. Tridymite is the most common. At least two types of tridymite are present, apparently differing slightly in minor element content. One group of crystals that gave a tridymite x-ray powder pattern included a flake with a minimum index of refraction of 1.472 attached to another with a maximum index of 1.480. Both indices are within the tridymite range, but the birefringence would be too great for any one composition. Cristobalite, intergrown with a plagioclase grain, was identified by its optic sign, uniaxial negative, and an $\omega$ index of refraction of 1.486. Quartz, some grains of which are strained and slightly biaxial, was identified by its optical properties and x-ray pattern. One grain contains minute (1$\mu$) inclusions of an unidentified clear, emerald green phase.

Zircon was found in very sparing amounts in fractions of the fines that sank in Clerici solution of specific gravity 3.95. The grains are colorless, somewhat cloudy with microfractures, uniaxial or slightly biaxial (+); $\omega = 1.869$, $e = 1.901$. X-ray patterns indicate that the zircon is intergrown with an as yet unidentified phase.

Troilite, identified by its x-ray powder pattern, occurs in sparse grains in the heavy mineral separates. Metallic nickel-iron is present as small irregular grains, as melted forms such as spatter droplets, in small dendritic crystal groups, and as coatings on and inclusions in glass spherules. Many of these particles are clearly meteoritic in origin (Section IIE). One micrometeorite, 500μ in length, was found to have a 40μ impact pit on one surface. Some of the metal is low in Ni, however; this is undoubtedly primary igneous iron, such as we know occurs in the lunar basalts (Section IIB).

Several of the phases encountered have not yet been identified. We have not attempted a microprobe analysis of the emerald green phase found included in quartz. One fragment of colorless glass with a refractive index of 1.576 was found to contain inclusions that yield the following x-ray powder pattern:

| d | I |
|---|---|
| 9.51 | medium |
| 4.46 | very strong |
| 3.68 | weak |
| 3.18 | medium |
| 2.92 | weak |
| 2.75 | medium |
| 2.52 | medium |
| 1.79 | weak |
| 1.67 | weak |

We have not been able to match this to the pattern of any known phase or phases.

The impact origin of the lunar soils and soil breccias is indicated by several lines of evidence, most of which would be inconsistent with their formation as welded and unwelded tuffs. A wide range of rock types is present, including older breccia fragments, coarse and fine-grained igneous basalts, and anorthosites. Some of the embedded fragments are rounded, others are partially encrusted with glass, suggesting an earlier history of abrasion or surface melting. Glass is abundant, including some inhomogeneous particles. In composition, the various glasses appear to represent two dominant rock types, basalts and anorthosites (Section IID). Shock effects are ubiquitous and dramatic, and small particles of meteoritic debris occur in the soils and breccias. None of these features are characteristic of volcanic detritus. The lunar breccias are therefore a rock type unknown on Earth, having been formed, fragmented, and reconstituted over a long repetitious history by a process wholly external to the planet on which they occur.

Table IIA-I. Microprobe analyses of fine matrix in lunar soil breccias (defocussed beam, 50μ).

| | Average of four analyses | Range of four analyses |
|---|---|---|
| $SiO_2$ | 44.5 | 43.4 - 45.9 |
| $TiO_2$ | 3.2 | 0.9 - 5.2 |
| $Al_2O_3$ | 20.5 | 14.9 - 28.2 |
| $Cr_2O_3$ | 0.3 | 0.2 - 0.4 |
| FeO | 10.6 | 6.0 - 16.0 |
| MnO | 0.2 | 0.1 - 0.3 |
| MgO | 7.9 | 6.4 - 9.7 |
| CaO | 12.8 | 11.1 - 14.6 |
| $Na_2O$ | 0.5 | 0.4 - 0.7 |
| $K_2O$ | 0.2 | 0.1 - 0.4 |
| NiO | 0.0 | 0.0 - 0.1 |
| $SO_3$ | 0.2 | 0.0 - 0.4 |
| Sum | 100.9 | |



Figure IIA-1. Typical lunar soil breccia fragment (10048, 39) with millimeter scale. Mineral and rock fragments are visible, embedded in a fine, dark gray matrix. Black inclusion is a glass spherule, split in half.

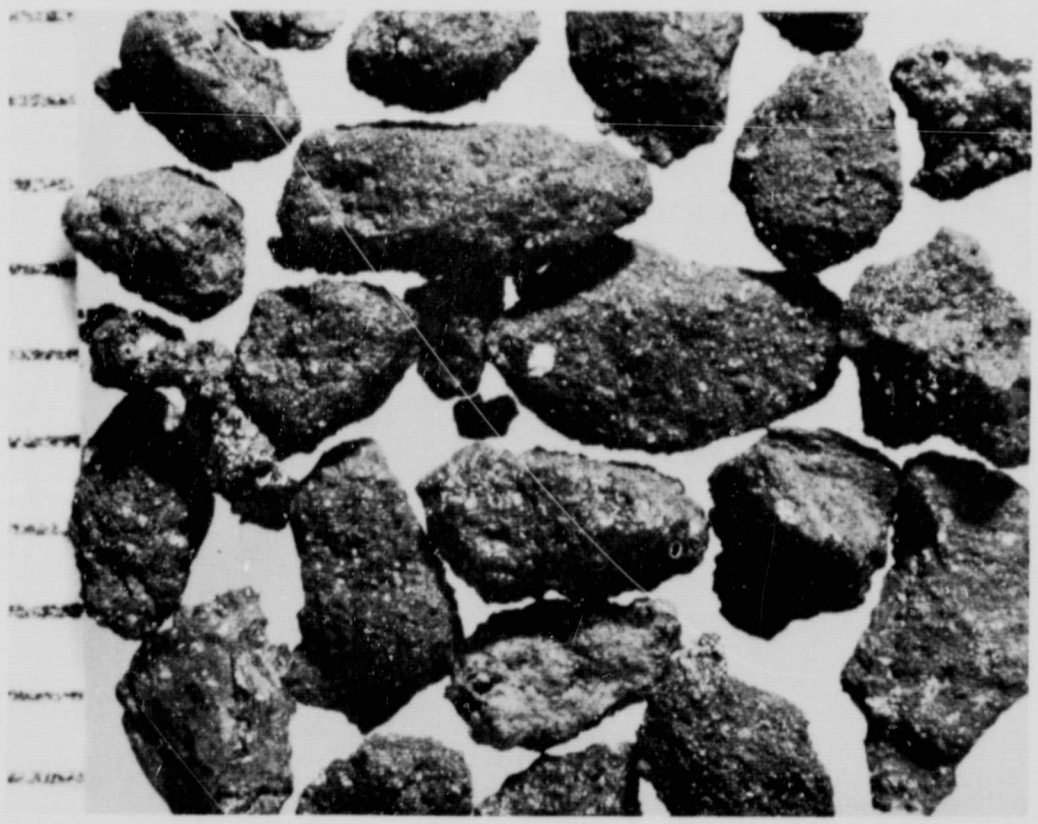


Figure IIA-2. Smaller fragments of soil breccia, typical of those sectioned and studied by us.

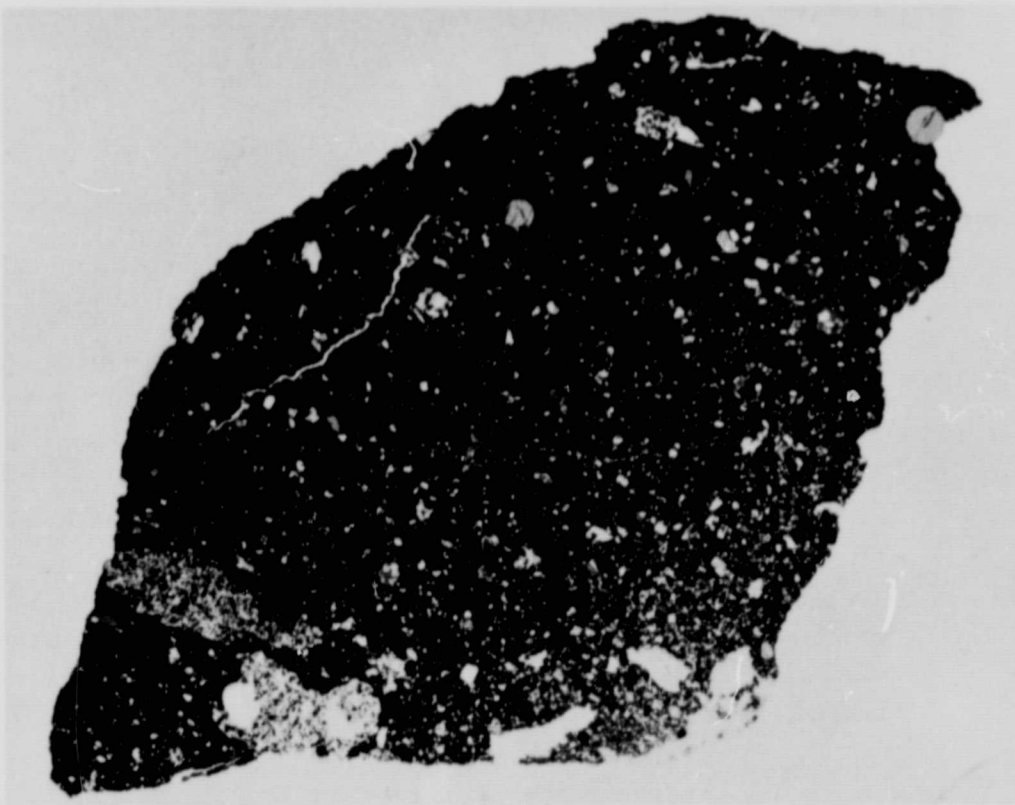



Figure IIA-3. Thin section of a large soil breccia fragment (10067,6). Section is thinner toward bottom of photograph. Included mineral and rock fragments are visible, as well as several yellow-orange glass spherules (round, medium gray in appearance).

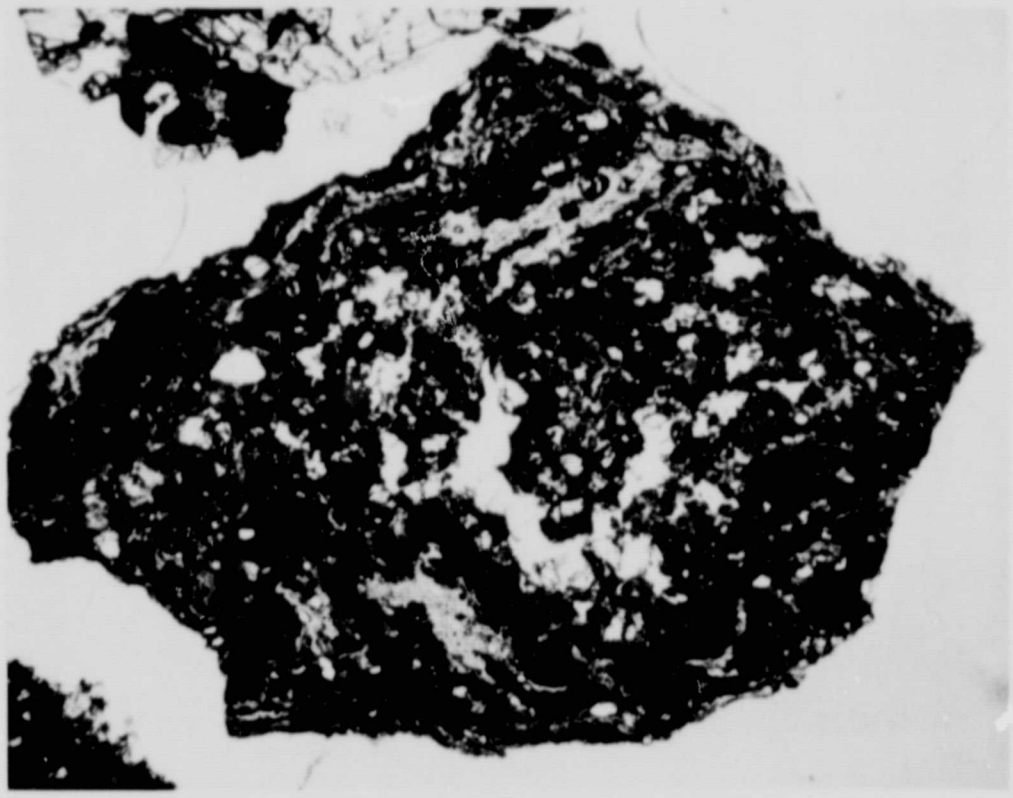



Figure IIA-4. Breccia fragment with matrix partially melted to thin streaks of tawny glass.

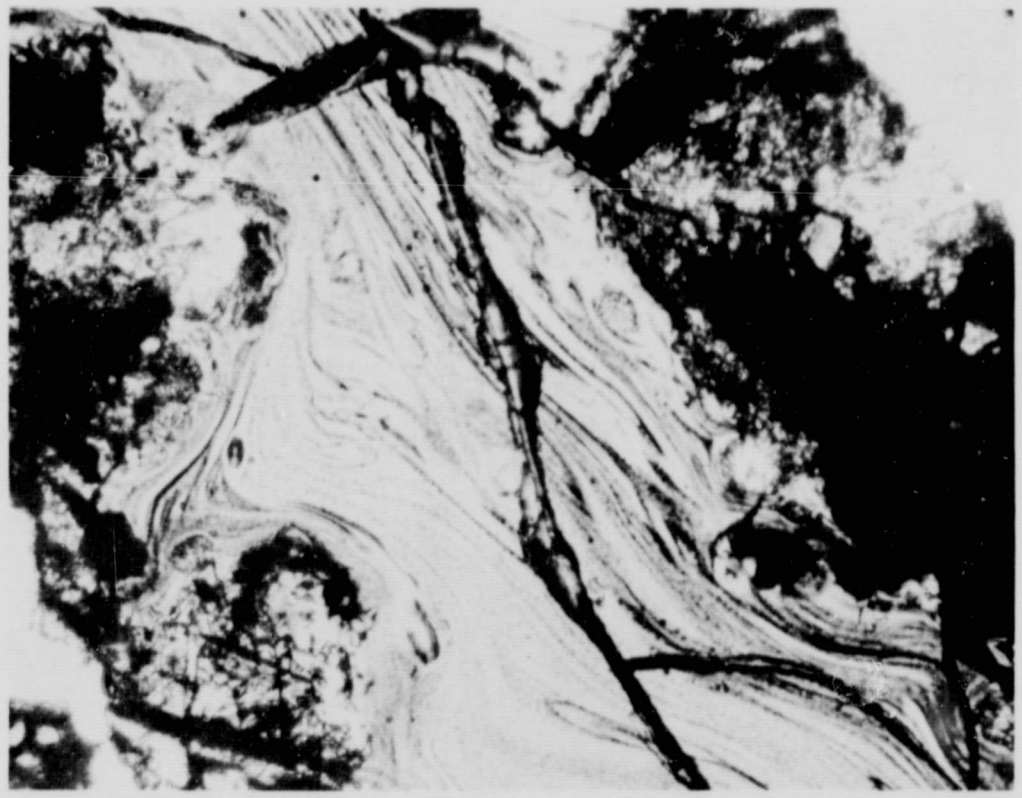



Figure IIA-5. Melted matrix with flow banding and embedded fragments of basalt. About half the matrix is visibly melted in this fragment.

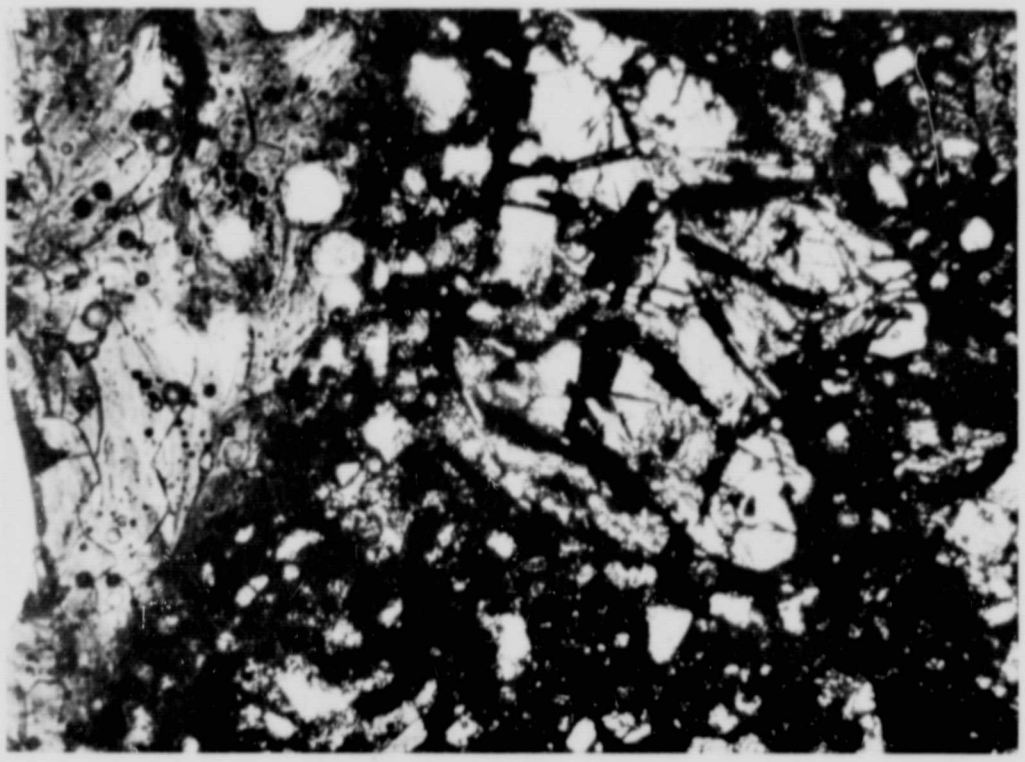



Figure IIA-6. Breccia with basalt fragment, about 700 μ in diameter, surrounded by much finer angular detritus and embedded in a matrix partially melted to brown glass. White circles are gas cavities in the glass.

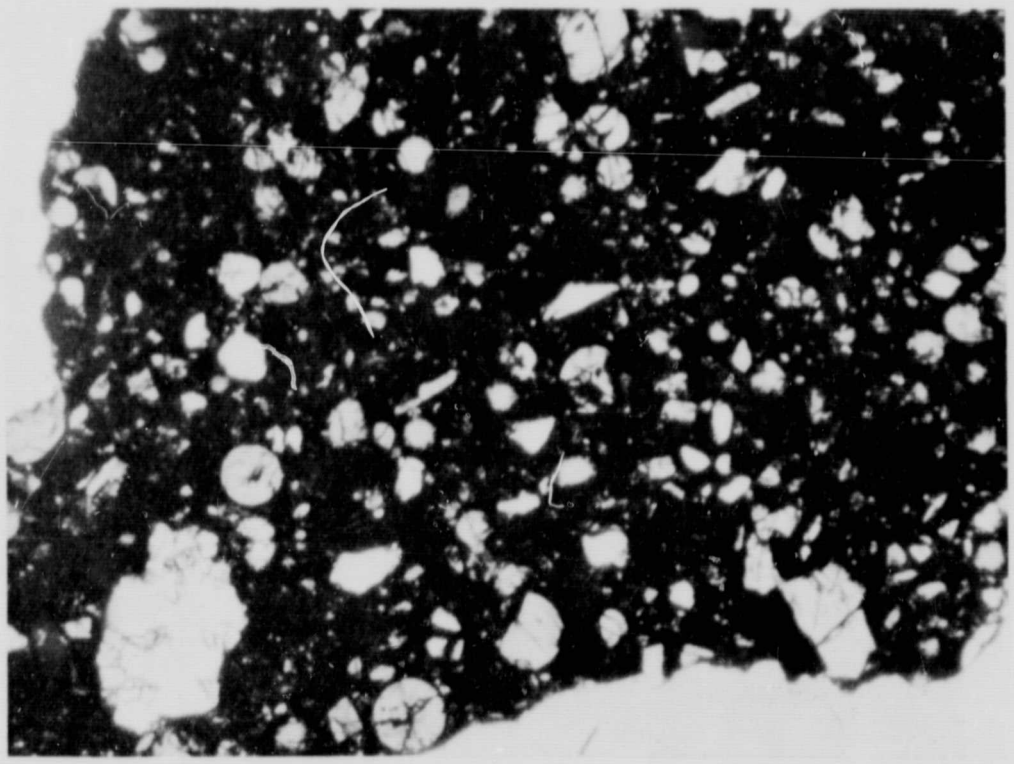



Figure IIA-7. A breccia fragment consisting mainly of bright orange spherules embedded in glass of the same color. The detrital origin of this assemblage is indicated by the presence of some angular fragments and by the condition of the spherules, some of which are undamaged while others are shattered or in broken pieces. A soil, unusually rich in spherules, has here been almost completely melted before final fragmentation.

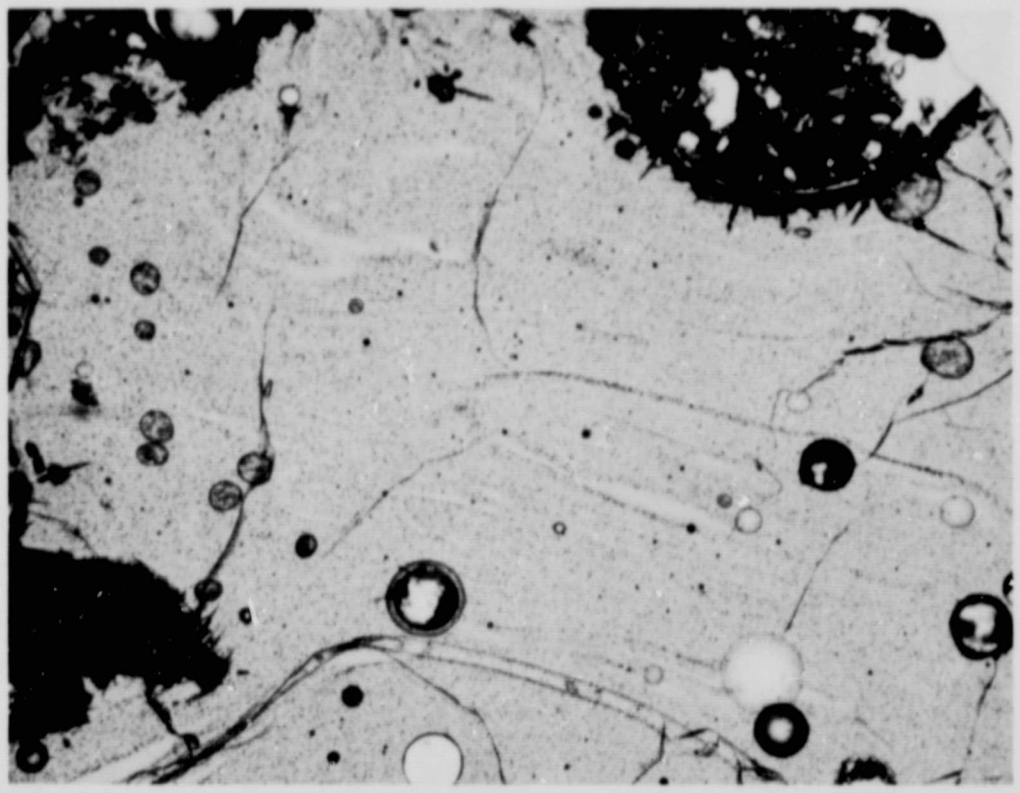



Figure IIA-8. Final stage of melting of a soil breccia in which the matrix and detritus have been transformed to a cindery glass, rich in gas cavities. Vestiges of mineral fragments remain; these typically give x-ray patterns of pyroxene and ilmenite.

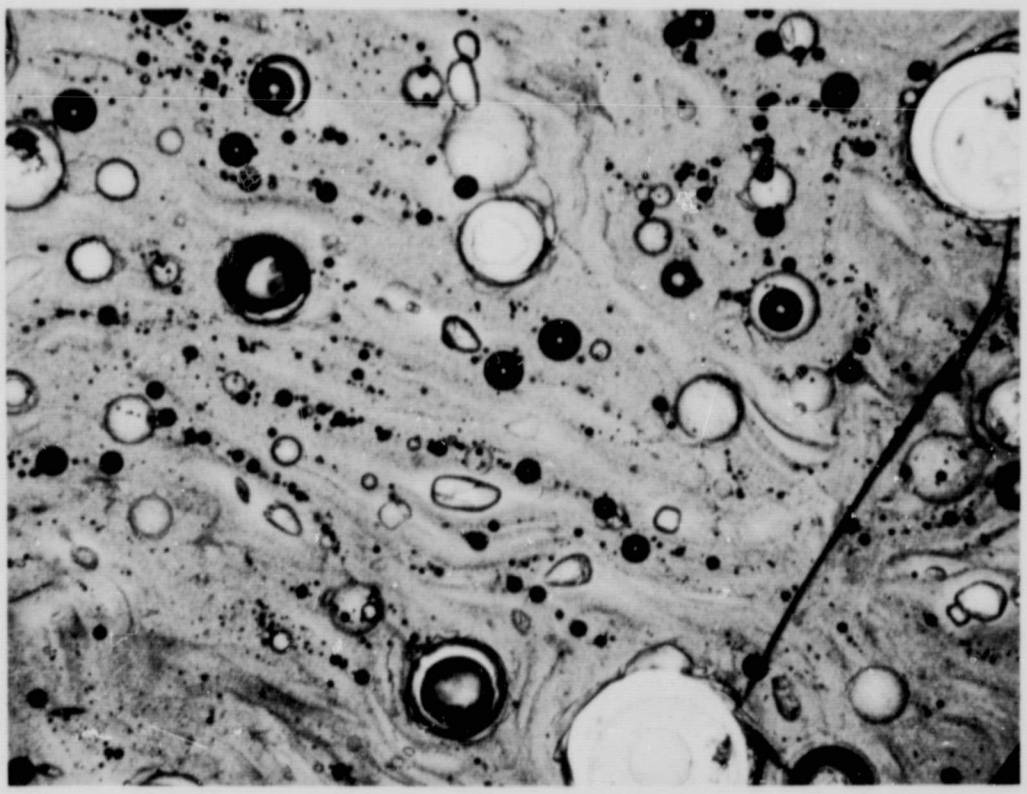



Figure IIA-9. Thin section of a glass produced by laboratory melting of fine lunar soil. This glass matches the amber color of the natural glass in Figure IIA-8.

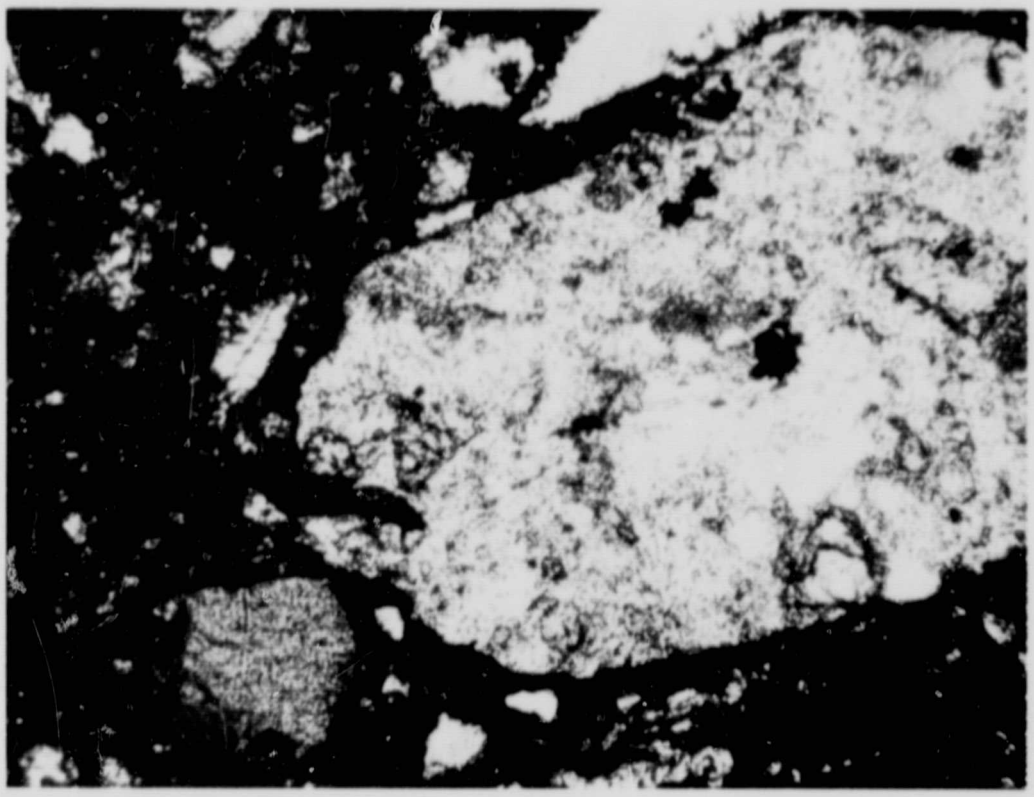



Figure IIA-10. A large, light-colored fragment of a breccia now embedded in a second-generation breccia. The fragment is finely granular glass excepting for a few relicts of pyroxene.

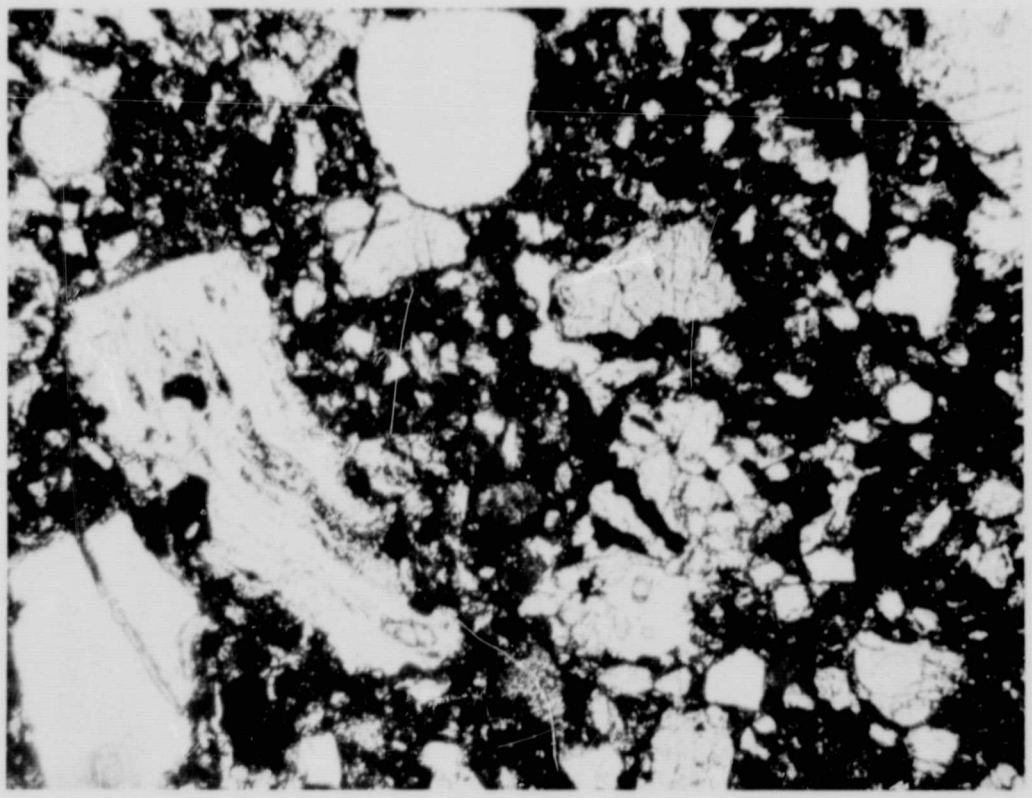



Figure IIA-11. Glassy detritus, including a broken piece of a former melted crust with flow banding, a small yellow spherule, and some angular mineral fragments (now isotropic).

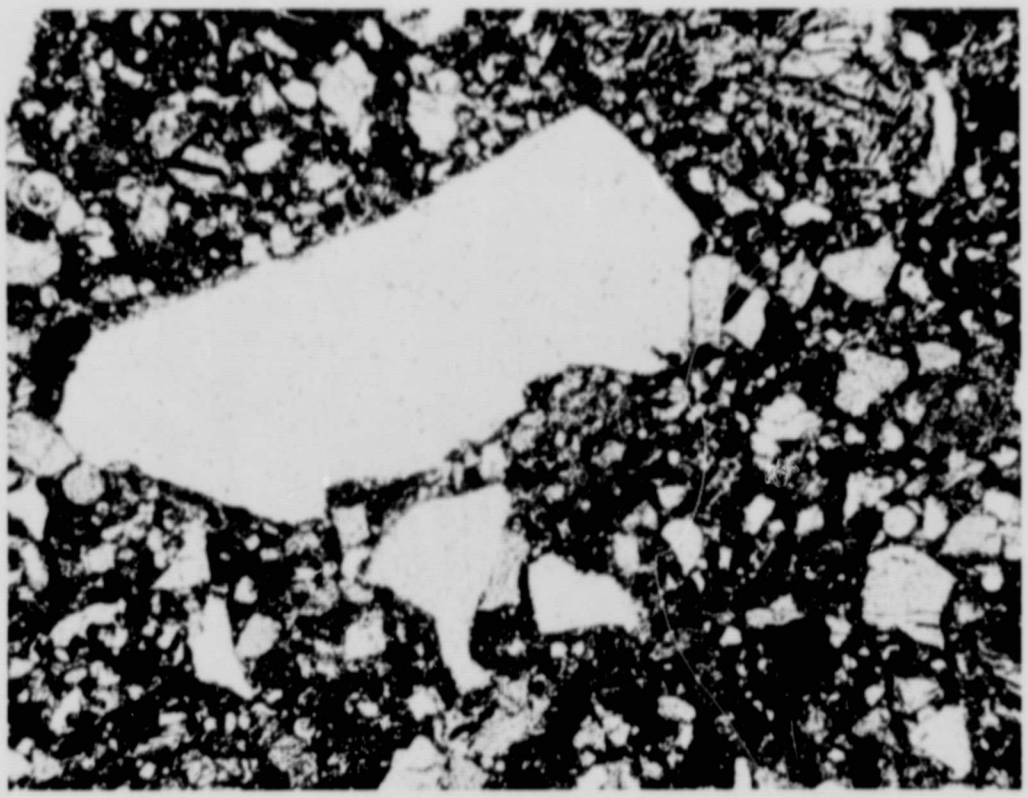



Figure IIA-12. A large, angular glass fragment embedded in finer shocked and largely glassy mineral detritus, including several clear spherules. The matrix is not visibly melted, but all parts of this field are essentially isotropic.

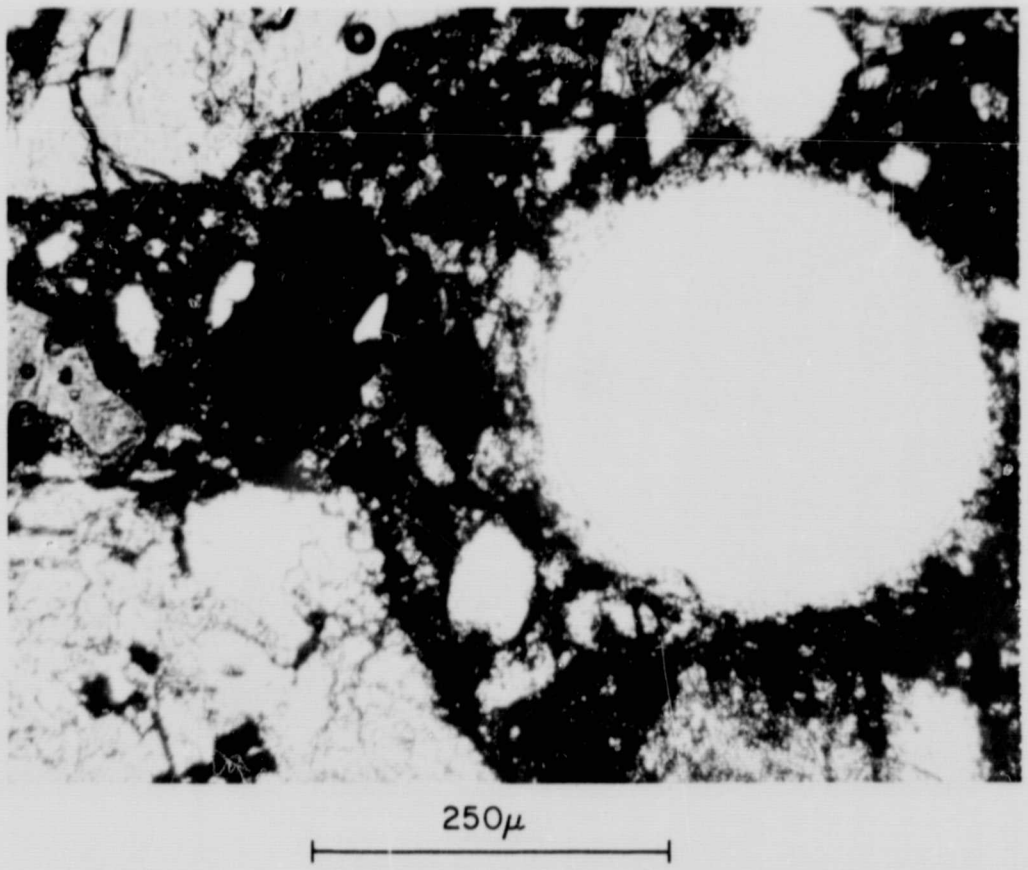



Figure IIA-13. A large, clear, yellow glass spherule bearing no signs of damage is embedded near two severely shocked fragments of an older breccia. At far left is a melted mass of dark brown glass with faintly anisotropic character. At left center is a large grain of detrital ilmenite.

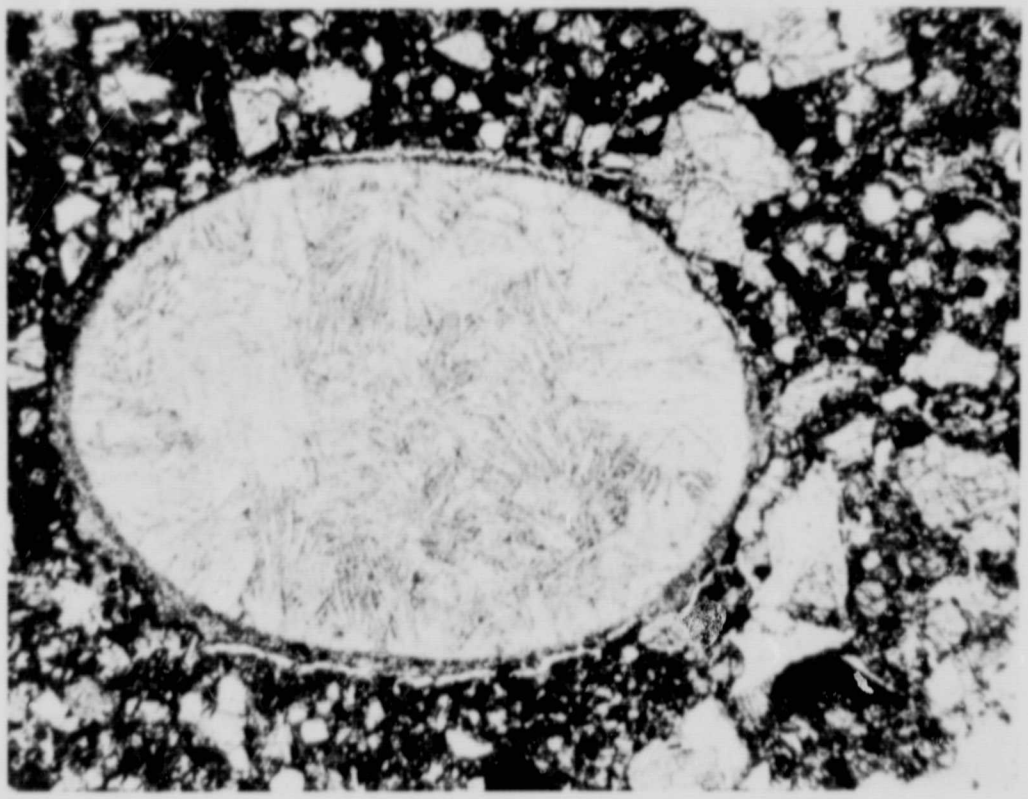



Figure IIA-14. A glass ellipsoid with a feathery internal structure and a reaction rim with the matrix. This body seems to have been hot when it struck the soil. The internal structure may be crystallites formed during quenching; possibly they are shock or devitrification structures.

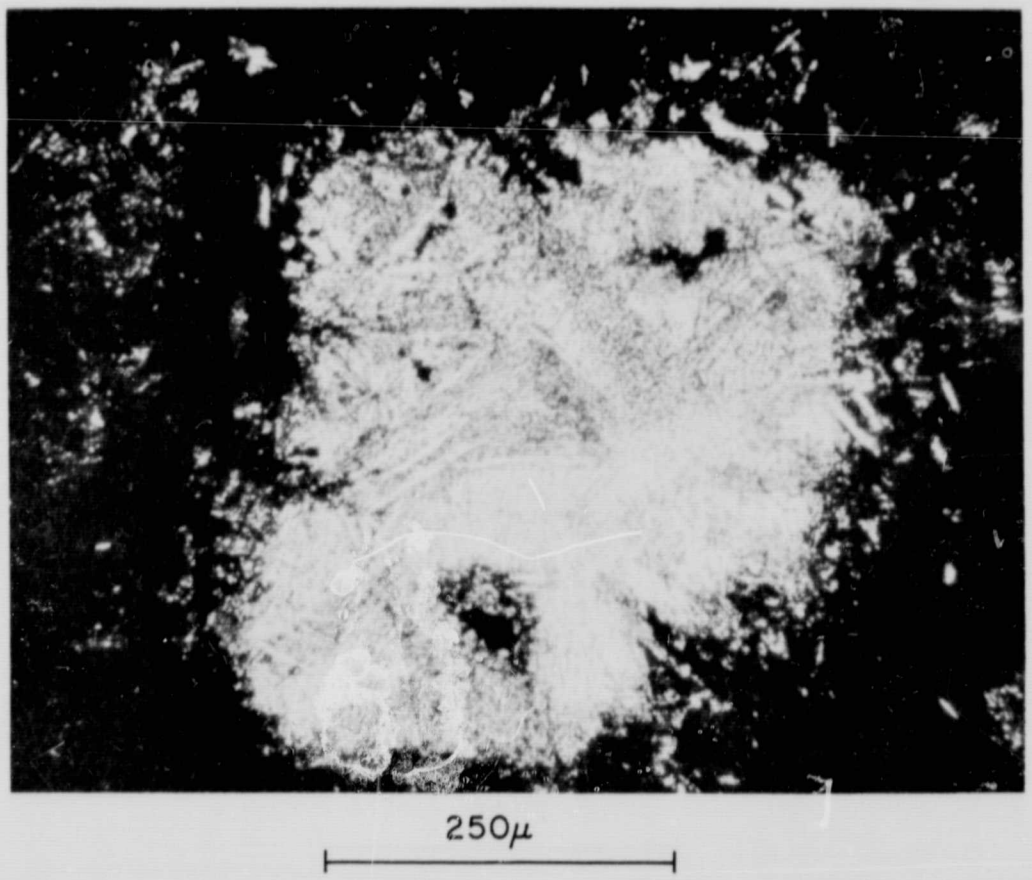



Figure IIA-15. An irregular mass of colorless, finely granular isotropic material grading, with no defined boundaries, into the matrix. This fragment (originally a group of feldspar crystals) appears to have been shocked <u>in situ</u>, along with the matrix.

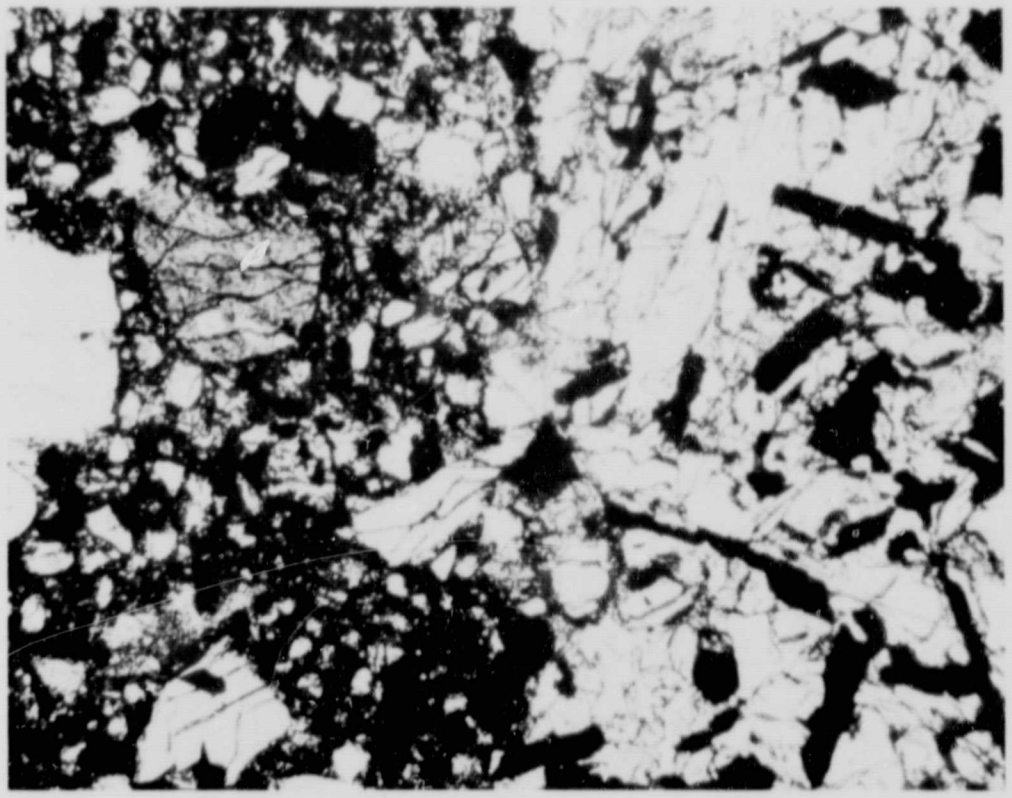



Figure IIA-16. At right is part of a large angular fragment of coarse basalt with pyroxene and ilmenite crystals. The edges of the fragment are shattered and appear forcibly pressed into the matrix. Fresh pyroxene fragments, possibly from the same mass, appear elsewhere in the groundmass.




Figure IIA-17. A rounded fragment of the same type of coarse gabbro as seen in Figure IIA-16. This fragment has had a prior history of breakage and abrasion before aggregation in its present matrix.

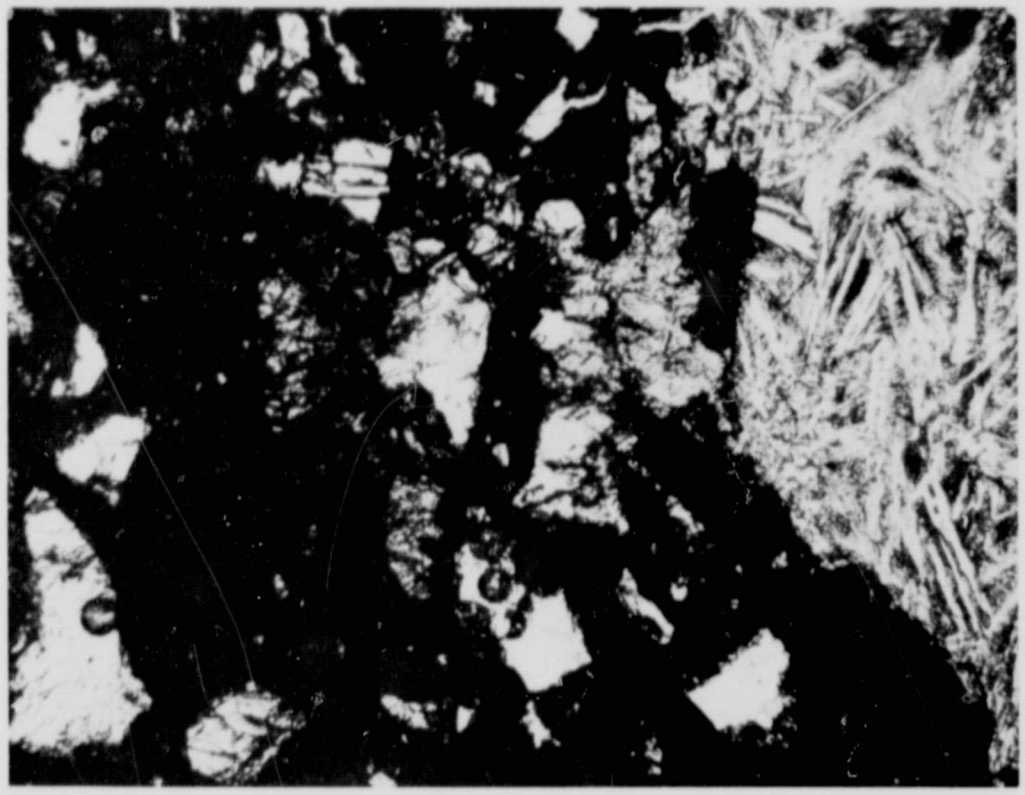



Figure IIA-18. Thin section of soil breccia. At right is a fragment of shocked and partially glassy anorthosite retaining the outlines of feldspar laths. The angular detritus also includes two pyroxene grains (lower left, top center).

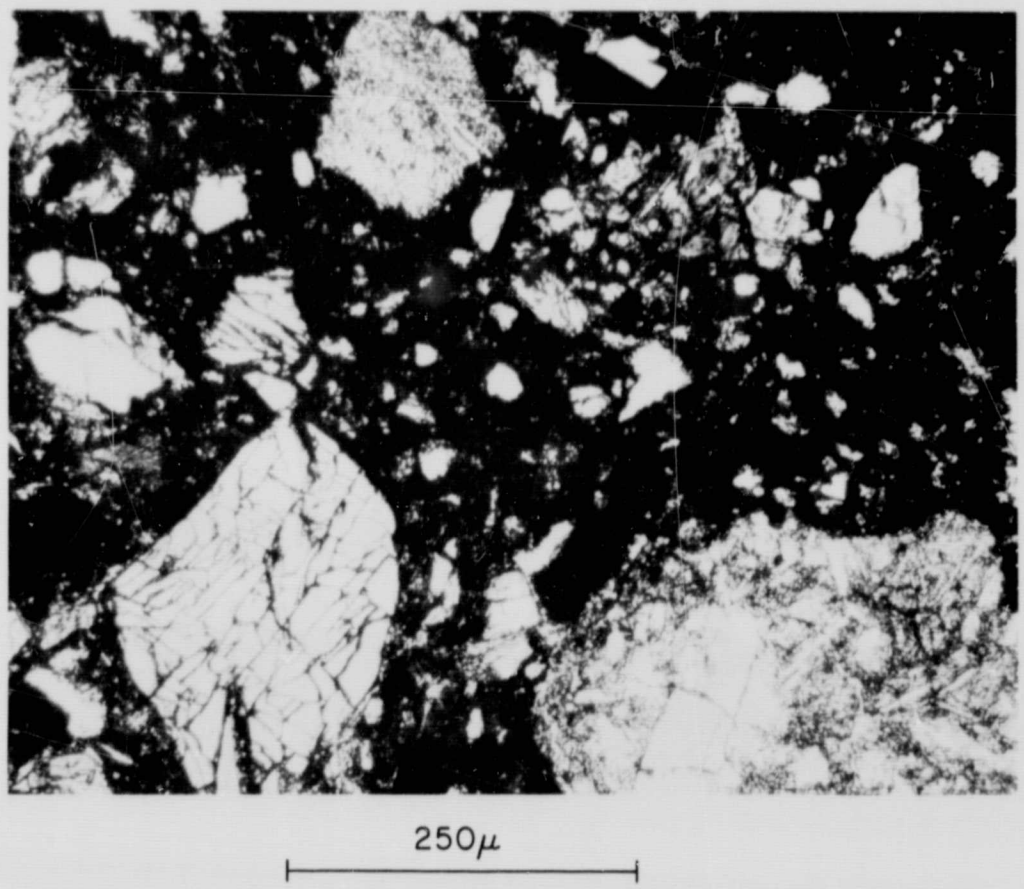



Figure IIA-19. A shocked remnant of anorthosite at lower right lies close to a large, fresh, essentially euhedral pyroxene grain, illustrating at least two sources, conditions, and periods of impact that have contributed to the making of this breccia.



100μ

ure IIA-20. A strongly zoned fragment of a pyroxene crystal, embedded in very fine-grained matrix. This crystal illustrates the extremely fresh condition of some of the unshocked and unmelted detritus.

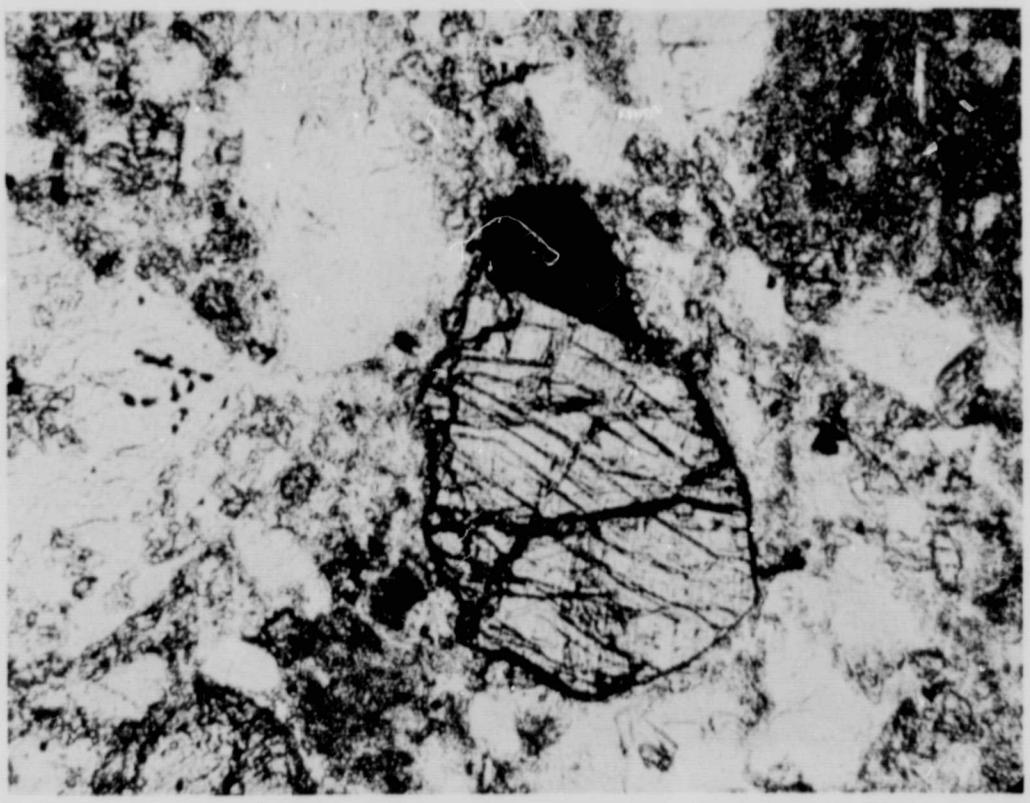



Figure IIA-21. This brecciated rock is not a soil breccia, but rather a piece of gabbro shocked in situ. With the exception of a few pyroxene and ilmenite crystals, minerals have been partly vitrified and have lost their grain boundaries.

## IIB. Basalts

The Apollo 11 lunar sample consists largely of Ti-rich basalt in one form or another. Some 37% of the lithic fragments we surveyed were basalt per se, and the other two most abundant types of lunar rock (soil breccias and glasses) consist largely of crushed and/or melted basalts. The Apollo 11 basalts contain clinopyroxene, Ca-rich plagioclase feldspar, and ilmenite as major constituents. Relative proportions of these 3 phases in 12 representative basalt fragments are shown in Table IIB-I. (Percentages in this table must be regarded as approximate, since they are based on only about 200 points sampled in each fragment; in the case of the coarser-grained fragments, the area sampled (fragment size) was not large enough to be truly representative of the rock.) Minor minerals we detected are olivine, troilite, native iron, quartz and tridymite, pseudobrookite, rutile, and chrome spinel.

We use the term "basalt" in the broad sense, to include all igneous rock fragments of the mineralogy noted above that occur in the Apollo 11 sample, instead of following the precedent set by LSPET (1969a), which terms the coarser rocks of this type "microgabbro" or "gabbro." The distinction between basalt and gabbro is drawn primarily on the basis of occurrence, and secondarily according to texture: gabbro is deep-seated and coarse-grained, basalt is volcanic and fine-grained. We know nothing about the occurrence of the rocks in the Apollo 11 sample, but surmise from the nature of the locality in which they were collected that most or all were of volcanic origin. The coarser fragments in our sample are only marginally out of the category of basalts so far as their texture is concerned, so we prefer for the sake of simplicity to refer to all as basalts.

For our own convenience, we defined three textural categories of basalts: coarsely crystalline fragments (mineral grains > 150μ), medium (between 50 and 150μ), and fine (< 50μ). The Apollo 11 sample is approximately evenly divided among these categories (13.3% coarse basalt, 11.5% medium, 12.6% fine). The macroscopic appearance of coarse, medium, and

fine basalts is shown in Figures IIB-1, -2, and -3. The coarse basalts correspond for the most part to the Type B vuggy microgabbros as defined by LSPET (1969a, b). They are decidedly lighter in color than fine and medium basalts (Type A of LSPET), as can be seen in Plate 1 as well as Figures IIB-1, -2, and -3. The lighter color appears to be due to a lower concentration of ilmenite in the coarse basalts, as well as the coarser grain size of this black, opaque mineral. (We have the impression from visual inspections of sections that ilmenite is less abundant in our coarse basalt fragments than in the medium and fine ones, in agreement with the estimates of ilmenite abundance made by LSPET (1969b) – ~19% and ~11%, respectively, in coarse and medium-plus-fine basalts – but our coarse basalt fragments are too small to permit estimation of modes.) Our lithic fragments are also too small to include the vugs noted by LSPET. We have found no evidence of this feature. We also found no evidence (in the form of coarse monocyrstalline fragments) of lunar rocks substantially coarser than those described in this section.

Specific gravities determined by us for two fragments of coarse basalt were 3.27 and 3.42 $gm/cm^3$.

## Textures

Coarse basalt textures vary somewhat from one grain to another but are usually hypidiomorphic-granular, ophitic (Figure IIB-4), or subophitic (Figure IIB-5), resembling terrestrial diabases. (Textural terms are defined in Table IIB-II.) Mineral orientations are random, so far as we can tell. The medium basalts vary considerably in texture. In some, the feldspar and ilmenite crystals are long and spiky (Figure IIB-7); in others, the grains are more nearly equant (Figure IIB-8). A texture bordering on porphyritic is also common among the medium basalts, in which coarse and obviously early-formed crystals of pyroxene, plagioclase and/or ilmenite are interspersed with later-formed, fine-grained sheafs or swatches of fibers and blades of the same three minerals (Figure IIB-9).

Fine basalts range from finer-grained textural equivalents of the medium basalts (Figure IIB-10), down through texturally uniform hypidiomorphic-granular textures with mineral grains of 1 to 10μ dimension (Figures IIB-11 and -12), to ultrafine grained rocks in which the only mineral microscopically visible is ilmenite, in patterns of tiny feathers and whorls or equant grains. In some fragments these ultrafine basalts can be seen to grade into pure glass. The finer-grained basalt fragments are, the darker they appear in thin section (Figure IIB-11): as the dimension of opaque ilmenite grains becomes progressively smaller than the thickness of the thin section (25μ), the surface/volume (or cross-sectional area/volume) ratio of the grains increases until they are able to effectively block every possible light path through the section. The finest-grained basalts appear completely black in thin section.

Preferred alignment of elongated mineral grains (which would be suggestive of rock crystallization from a vigorously flowing lava) is uncommon and never well developed in any of the lunar basalts.

Pyroxenes

The lunar basalts we examined contain two pyroxenes, titaniferous augite (sometimes sub-calcic) and pigeonite. These frequently coexist in the same basalt fragment. We have found no orthopyroxene in the basalts. The pyroxenes are usually allotriomorphic in the coarser basalts (as is evident in the textural photomicrographs presented above), but sometimes hypidiomorphic in the finer basalts, both as pyroxene phenocrysts when these occur and as field minerals in the fine, uniform hypidiomorphic-granular basalts just noted.

The pyroxene grains in thin section are remarkably clear and clean by terrestrial standards, containing no alteration or weathering products or exsolution lamellae, and very few inclusions. They usually appear a very pale brown or buff color in thin section, while their macroscopic color is a medium cinnamon brown (Plate 1).

Compositions of representative basalt pyroxenes we analyzed are presented in Table IIB-III, and in Figures IIB-13, -14, and -15. Figure IIB-13 shows compositions relative to the three principal pyroxene end-members, enstatite, ferrosilite, and wollastonite. Analyses of coexisting grains are identified, but the variability of compositions within each fragment seems to be great enough to make doubtful the value of these relationships. The lunar basaltic pyroxenes are more similar in Ca content to terrestrial volcanic pyroxenes than plutonic pyroxenes: the dearth of very high- and very low-Ca pyroxenes points to volcaric conditions of rapid cooling and crystallization, and little subsolidus readjustment. The absence of exsolution lamellae suggests the same.

Zoning of Ca, Mg, and Fe contents in the pyroxene grains is relatively feeble (compare analyses C with D and G with H, Table IIB-III); Al, Ti, and minor element zonations are more pronounced. There is a clear positive correlation between Al content and Ca content among the pyroxenes (Figure IIB-14) similar to that displayed by terrestrial rocks, such that the more diopsidic pyroxenes are more aluminous. A positive correlation also exists between Ti and Al concentrations in pyroxenes (Figure IIB-15). The tendency of Al/Ti atomic ratios to approach the value 2 can be understood as a charge balance effect: most or all of the Al in these pyroxenes occurs in tetrahedral sites (Table IIB-III), and the substitution of two Al ions (+3) for two Si ions (+4) in these sites results in a charge deficiency equivalent to 2 protons. The mineral makes this up by accepting one Ti ion (+4) in an octahedral site, substituting for (Mg, Fe, Ca) (+2).

A relationship appears to exist between pyroxene composition and grain size, such that pyroxenes in the medium basalts are richer in Ca, Ti, and Al than those in coarse basalts (Figures IIB-13, -14, and -15). We do not have enough good analyses in fine basalts to be able to tell if the trend continues with further decreasing grain size.

Optical properties of a number of lunar pyroxene grains (refractive indices, 2V) are presented in Figures IIB-16 and -17. These are in essential agreement with measurements previously made on terrestrial minerals (Deer, Howie, and Zussman, 1963).

The most significant feature of the lunar basalt pyroxenes we analyzed is that, as a group, they do not span much of a range in Fe/Mg ratio (Figure IIB-13). This suggests that our samples have come from a thin, undifferentiated lava flow, or from several similar undifferentiated lava flows. They have not come from a differentiated basic pluton, sill, or lava lake.

## Plagioclase Feldspars

The lunar basaltic plagioclase is remarkably calcic, consisting in almost all cases of bytownite ($An_{70}$-$An_{90}$) or anorthite ($An_{90}$-$An_{100}$). A histogram of anorthite contents of the plagioclase crystals we microprobed is shown in Figure IIB-18; the orthoclase content of albite in Figure IIB-19. Representative plagioclase compositions are presented in Table IIB-IV.

Plagioclase appears in idiomorphic to hypidiomorphic crystals, almost always polysynthetically twinned (often in combination with Carlsbad twinning), in the coarse basalts. Crystal proportions range from tabular (Figure IIB-5) to lathlike (Figure IIB-4) to acicular (Figure IIB-22). Crystal faces tend to be less forcefully expressed in the finer basalts, where the plagioclase is frequently allotriomorphic; it is also less often obviously twinned. The plagioclase is colorless and, like the pyroxene, extraordinarily clear and uncluttered by alteration products or inclusions, although the latter are sometimes observed (Figure IIB-23).

The plagioclase crystals are always zoned in the traditional manner (more calcic toward the center), though the compositional variation is not great (compare analysis A with B and D with E, Table IIB-IV). Reverse or oscillatory zoning was not observed.

Refractive indices of a number of lunar feldspar grains that were subsequently microprobed are shown in Figure IIB-20. Lunar and terrestrial feldspars do not seem to differ in this property.

## Ilmenite

The abundance of ilmenite is the most striking feature of the lunar basalts; it is this mineral that makes the lunar maria as dark as they are. Microprobe analyses of several basalt ilmenites appear in Table IIB-V. In coarse basalts it is idiomorphic or hypidiomorphic, tabular to equant in form (Figure IIB-4); in the range of medium grain sizes it tends to be more lathlike or platey. The ilmenite commonly equals or exceeds coexisting feldspar crystals in size. In fine basalts it may occur as idiomorphic phenocrysts, as evenly disseminated hypidiomorphic blebs, or as curling, feathery dendrites (groundmass in Figure IIB-28). It is black and in almost every occurrence completely opaque in appearance; however, the lunar basalts contain occasional ilmenite plates or flakes so thin ($\sim$0.5$\mu$) as to be transparent. These appear dark brown in thin section. The ilmenite flake I surfacing in Figure IIB-34 is transparent in thin section.

From its crystal perfection and dimensions, and occasional appearance as phenocrysts, it appears that ilmenite is one of the first phases to crystallize in the lunar basalts. On the other hand ilmenite crystals frequently have embayed outlines (Figure IIB-26), showing that during later stages of cooling solubility of this mineral in the melt increased, and crystal surfaces began to be resorbed. Ilmenite is also usually present in the fine-grained areas that appear to represent the last phase of (eutectic) crystallization in the basalts (Figure IIB-25), so it seems to have been actively crystallizing or dissolving throughout the solidification history of these rocks.

## Minor Minerals

### Olivine

A minority of lithic fragments in all our grain-size categories contain olivine. When present, the olivine appears in idiomorphic or hypidiomorphic crystals that are usually somewhat larger than the other rock-forming mineral grains (Figures IIB-6, IIB-27). The most perfectly formed olivine crystals are idiomorphic phenocrysts that occur in many ultrafine basalts (Figure IIB-28). In the medium and coarse basalts, olivine crystals usually display uneven, embayed borders; clearly the melt phase around them tended to react with and resorb them during later stages of cooling. Presumably this led to the incongruent crystallization of pyroxene, but we must suppose it occurred via resolution of the olivine and appearance of pyroxene elsewhere in the system, because clearcut pyroxene reaction rims are seldom to be seen around the remaining olivine.

Chemical compositions of several typical lunar basalt olivine grains are shown in Table IIB-VI. We did not observe strong zoning in these basaltic olivines (D vs. E, Table IIB-VI).

### Pseudobrookite

This mineral occurs in some of the lunar basalt fragments, either as phenocrysts separate from and coexisting with ilmenite phenocrysts (Figure IIB-28) or as cores surrounded by ilmenite reaction rims (Figure IIB-31). The grains in which we observed it always contained olivine as well.

Two microprobe analyses of lunar pseudobrookites are shown in Table IIB-V. They are remarkably similar in composition. Their Ti content is much higher than that of classical pseudobrookite ($Fe_2TiO_5$) – 45% vs. 20% –

but Ramdohr (1960, p. 957) points out that mixed crystals between the end members $Fe_2TiO_5$ and $Ti_3O_5$ occur.

Our identification of this mineral rests largely on its microscopic appearance by reflected light, our microprobe analyses, and rumors from other groups studying the lunar sample. Also, the product we obtained by melting a mixture of oxides identical to our microprobe analysis of this mineral was shown unequivocally, by x-ray diffraction, to be pseudobrookite. Our efforts to obtain x-ray diffraction patterns of the lunar mineral itself from tiny chips pried out of our thin sections have been only partially successful to date, yielding two rings appropriate to the strongest diffractions of pseudobrookite.

Potassium mineral

We found areas in a few lunar basalts that are relatively rich in K (Figure IIB-30, Table IIB-VII). The K is not simply dissolved in anorthite; anorthite is present in these basalts (Figure IIB-30) and contains the usual low concentration of K(~0.2 wt. %). Nor are the areas orthoclase, as we first suspected. Analyses indicate a composite material, not a single mineral. Analyses B-D in Table IIB-VII, averaged, yield the following norm: 43% orthoclase; 36% quartz; 7% each albite and anorthite; 4% wollastonite; 2% each ilmenite and troilite. (Troilite in the norm assumes the presence of S, which was not analyzed for, in the K unknown material. The troilite inclusion in the center of the K-rich area shown in Figure IIB-32, and the presence of disseminated reflective particles, probably also troilite, throughout the K-rich area, support this assumption.)

The K-rich areas may be glass (apart from the reflective particles just noted) or may be a fine-grained polymineralic assemblage similar to the norm cited above. They could even be an hitherto undescribed mineral. We have not been able to obtain an x-ray diffraction pattern of this material; this supports the possibility of glass. On the other hand, the material has a finely granulated appearance in thin section; however, this could be entirely due to the opaque disseminated mineral noted.

The fragments containing K-rich areas are about five times richer in K, overall, than values reported for lunar basalts by LSPET (1969b). The whole question of K abundance in the lunar material is of special importance, because of the critical role this element plays in the heat budget of planets and also in K-Ar dating. The heterogeneity of distribution of K we have noted would render suspect K-Ar dates obtained for lunar fines or soil breccia, unless the material had been thoroughly homogenized before aliquots were taken for K analysis and Ar spectrometry.

Metal and troilite

These minerals occur frequently as accessories in the lunar basalts, in very small grains (a few microns or tens of microns). They may occur as pure metal or pure troilite, allotriomorphic and interstitial in both cases, but usually they occur in association with one another. Typically, the metal occurs as rounded or irregular inclusions in the sulfide (Figure IIB-33). Representative microprobe analyses are shown in Table IIB-VIII. The content of Ni is always very low, which eliminates the possibility that the metal was contributed to the lunar surface material by meteorite infall. Evidently the lunar lava systems evolved in an environment with sufficiently low oxygen fugacity to reduce a small amount of their iron oxide to the metallic state.

Silica minerals

A number of grains of quartz, tridymite, and cristobalite were identified by x-ray diffraction in the fine soil component of our sample, almost all of which derived originally from the lunar basalts. Silica minerals are also visible in thin sections of some fragments (Figure IIB-34); these were confirmed by microprobe analysis but not x-ray diffraction.

Rutile and chromite

These minerals were observed (rutile, frequently; chromite, once) as exsolution lamellae (2-5μ thick) in ilmenite (Figure IIB-35). Microprobe analyses are shown in Table IIB-V. Both identifications are on the basis of appearance in the microscope and microprobe analyses; x-ray diffraction patterns were not attempted.

Bulk Compositions

We estimated the bulk compositions of two medium basalts (Table IIB-IX) by averaging 10 defocussed beam (50μ) microprobe analyses made on each of them. The analyses were randomly placed (at intersections of a grid). This was done mostly in order to draw comparisons between the overall compositions of basalts and anorthosites (Section IIC). We are aware of the limitations of such an approach, yet the analyses turned out to be quite informative. They revealed an anomalously high K content in (18-1); in checking this out, we discovered the fragment contains numerous high-K areas, such as those shown in Figures IIB-30 and -32. They also showed a surprisingly high content of S in both fragments, which drew to our attention the substantial abundance of microscopically visible troilite. Our analyses concur with the spectrographic analyses of Type A rocks presented in LSPET (1969b), except for the high K content of (18-1); a Cr content somewhat less in our analyses than LSPET's; and the S we report, which LSPET did not analyze for. Norms calculated from our analyses (Table IIB-IX) are reasonable, falling within the range of mineral modes observed in lunar basalts (Table IIB-I).

Zirconium

LSPET (1969a, b) reports remarkably high levels of Zr (~1000 ppm) in the Apollo 11 sample, so we searched especially diligently for zirconium minerals. Only one small zircon crystal was found, in the heavy mineral separates. Supposing most of the Zr to be dissolved in the major rock-forming minerals, we microprobed these at the Zr Kα wavelength for sufficiently

long integration periods to obtain statistically significant signals. Our microprobe data are presented in their entirety in Table IIB-X. (Measurements were made with 13 KV accelerating voltage, 0.1 μamp sample current, and 5-min integration times. Background offset wavelengths were chosen to avoid possible interference by the P Kα line at 6.155 Å. Blanks were run to test the efficacy of the background subtraction. Poor results of the first blank run were probably due to the buildup of a thick contamination spot during the 15 min of background-line-background measurement, an effect that is more pronounced on metallic surfaces (such as the Co metal used as a blank) than on silicates (such as the standard and lunar materials). This difficulty was avoided in the second blank run by moving the beam to fresh metal areas between 5-min integrations. No corrections other than the background subtraction were performed; since results are presented to only 1.5 significant figures, the corrections omitted are negligible.)

We found Zr levels in the rock-forming minerals to be considerably lower than 1000 ppm (Table IIB-X). Some ilmenite grains with exceptionally high Zr content were found, but even taking these into account there did not seem to be enough Zr to average out at 1000 ppm in the lunar sample. We then analyzed a number of glasses and soil breccias, homogenized lunar materials that provide a sampling of the overall composition of the lunar surface material, with a defocussed microprobe beam. These materials did not come up to 1000 ppm either. Our results suggest that the Zr content of lunar material at the Apollo landing site is more nearly 400 ppm than 1000 ppm (still almost three times the mean level of Zr in terrestrial basalts (150 ppm – Taylor, 1964)), and that most of the Zr is contained in rock-forming minerals (especially ilmenite), although occasional zirconium minerals are to be found.

## Discussion

As already noted, the basalts described are clearly volcanic flow rocks, fragments of the vast lava flow units that filled Mare Tranquillitatis soon after the formation of the Moon. The fine grain size of most of them, the

chemistry of their pyroxenes, and the geologic setting from which they were taken all point in this direction. The general uniformity of compositions of the basalts provides additional evidence: crystal fractionation in plutonic bodies might be expected to produce more drastic composition differences than we observe. One could argue that the coarsest basalts were derived from shallow intrusive bodies rather than flows, but the fact that a continuous gradation of basalt types exists between the coarsest and the finest makes it seem more likely that all are extrusive rocks, the coarse basalts having crystallized inside particularly thick lava flow units. We observed a few lithic fragments that may represent chilled margins between flow units (Figure IIB-36), though they could also have been formed by complex impact remelting events.

The presence of phenocrysts in many of the basalts testifies to a time of relatively gradual cooling and crystallization before these lavas were extruded onto the lunar surface. Presumably this occurred in subsurface volcanic conduits that fed lava onto the mare surfaces, or at even earlier stages in the history of the lava. There is abundant evidence of a discontinuous cooling rate of the lavas after they were extruded and had ceased flowing, in the form of lithic fragments with bimodal distributions of mineral grain size. This is especially well illustrated by the basalt in Figure IIB-37, in which the interstices between mineral grains of a partly developed ophitic fabric are filled with glass. The integrity of the structure of feldspar and ilmenite crystals makes it seem unlikely that the lava was still flowing when the sudden increase in cooling rate occurred, or that impact remelting was involved.

The order of crystallization of minerals in the basalts was variable, as would be expected in melts of a near-eutectic but somewhat variable bulk composition. The history of crystallization cannot always be read clearly from the fabrics of lunar basalts: Figure IIB-38 provides an interesting example. Pyroxene phenocrysts are surrounded by a fine-grained matrix of pyroxene and feldspar, evidently a near-eutectic liquid that crystallized late and rapidly. But what about the ilmenite? Since it crosscuts pyroxene

phenocrysts, does it predate them? If so, why is it more abundant in the matrix between phenocrysts than in the phenocrysts themselves? And why the preferred orientation of ilmenite plates if they grew directly from the melt, either early or late?

It is likely that some of the finer basalts are not primary igneous rocks, but were remelted by impacts on the lunar surface. Certainly much or all of the lunar glass was formed this way, and all gradations exist between glasses and fine basalts. We cannot say whether a grain-size cutoff exists between primary and remelted basalts, or what the proportion of remelted basalts might be.

The lunar basalts are completely lacking in hydrated minerals. In addition, we have not observed fluid inclusions. Evidently the lunar surface either never contained any appreciable amount of water, or lost it at an early stage.

Table IIB-I. Estimates of relative proportions of major minerals in 12 lunar basalt fragments.

| Fragment number | Grain size | Volume percentages | | |
|---|---|---|---|---|
| | | Clino-pyroxene | Ca-rich feldspar | Ilmenite |
| (18-20) | coarse | 61 | 28 | 11 |
| (18-11) | medium | 51 | 34 | 15 |
| (18-14) | medium | 54 | 29 | 17 |
| (18-16) | medium | 48 | 38 | 14 |
| (18-18) | medium | 56 | 32 | 12 |
| (18-25) | medium | 57 | 25 | 18 |
| (18-27) | medium | 61 | 24 | 15 |
| (18-35) | medium | 50 | 36 | 14 |
| (18-37) | medium | 50 | 42 | 8 |
| (18-38) | medium | 50 | 41 | 9 |
| (18-39) | medium | 55 | 30 | 15 |
| (18-23) | fine | 51 | 22 | 27 |
| Average (vol. %) | | 53 | 32 | 15 |
| Average (wt. %) | | 53 | 26 | 21 |

Table IIB-II. Table of obscure petrographic terms.

Idiomorphic (adj.) Used to describe a mineral grain; means the grain is bounded by its own crystal faces, which press in upon and impinge on neighboring mineral grains. An idiomorphic rock texture is one in which most of the major mineral grains display idiomorphic forms. Crystals are generally idiomorphic because they developed earlier than their neighbors.

Allotriomorphic (adj.) Just the opposite: applied to minerals whose boundaries are those imposed on them by neighboring minerals. An allotriomorphic texture is one in which no crystal faces are strongly developed; mineral interfaces sometimes resemble the soap film walls in a mass of soap bubbles.

Hypidiomorphic (adj.) A condition intermediate to the two above.

Granular (adj.) Descriptive of a rock texture; composed of nearly equidimensional (equant) mineral grains.

Porphyritic (adj.) Descriptive of a rock texture; composed of large mineral grains (phenocrysts; usually idiomorphic) in a groundmass or matrix of finer-grained rock.

Ophitic (adj.) Descriptive of a rock texture. Composed of elongated, lath-like feldspar crystals embedded in pyroxene, the dimension of single crystal pyroxene domains being substantially greater than the dimensions of feldspar crystals. Subophitic if the disparity in dimensions is not so impressive.

Table IIB-III. Representative electron microprobe analyses of pyroxenes in lunar basalts.

Weight percentages of elements

| | Coarse | | | | | Medium | | | | Fine | |
|---|---|---|---|---|---|---|---|---|---|---|---|
| | A | B | C | D | E | F | G | H | I | J | K |
| Si | 23.5 | 24.2 | 23.3 | 24.2 | 24.6 | 21.3 | 22.7 | 21.8 | 22.2 | 22.3 | 22.0 |
| Ti | 0.9 | 0.5 | 1.6 | 0.9 | 0.5 | 3.4 | 2.8 | 2.9 | 2.3 | 3.9 | 1.6 |
| Al | 0.9 | 0.4 | 1.5 | 0.9 | 0.4 | 3.0 | 1.8 | 3.3 | 0.9 | 3.4 | 1.9 |
| Cr | 0.2 | 0.1 | 0.4 | 0.2 | 0.2 | 0.4 | 0.8 | 0.3 | 0.0 | 0.8 | 0.4 |
| $Fe^{L}$ | 15.1 | 17.3 | 8.4 | 11.4 | 11.6 | 8.1 | 8.2 | 10.1 | 23.4 | 9.6 | 12.2 |
| Mn | 0.3 | 0.3 | 0.1 | 0.3 | 0.4 | 0.2 | 0.1 | 0.2 | 0.4 | 0.2 | 0.1 |
| Mg | 10.3 | 10.4 | 9.1 | 9.4 | 10.1 | 7.0 | 8.9 | 7.3 | 5.8 | 8.2 | 7.4 |
| Ca | 6.1 | 4.6 | 12.4 | 10.0 | 9.3 | 13.9 | 12.4 | 12.7 | 6.2 | 10.6 | 10.3 |
| Na | 0.1 | 0.0 | 0.0 | 0.0 | 0.0 | 0.3 | 0.0 | 0.0 | 0.0 | 0.1 | 0.0 |
| $O^{M}$ | 42.0 | 42.1 | 42.9 | 43.0 | 42.6 | 42.2 | 43.2 | 43.0 | 41.0 | 43.9 | 40.5 |
| Sum | 99.4 | 100.0 | 99.9 | 100.3 | 99.6 | 99.8 | 100.9 | 101.6 | 102.3 | 103.1 | 96.5 |

Atoms per six oxygen atoms

| | | | | | | | | | | | |
|---|---|---|---|---|---|---|---|---|---|---|---|
| Si | 1.91 | 1.96 | 1.86 | 1.92 | 1.98 | 1.73 | 1.81 | 1.73 | 1.85 | 1.74 | 1.86 |
| $Al^{N}$ | 0.08 | 0.03 | 0.13 | 0.07 | 0.02 | 0.26 | 0.15 | 0.27 | 0.08 | 0.26 | 0.14 |
| $Al^{P}$ | 0.00 | 0.00 | 0.00 | 0.00 | 0.01 | 0.00 | 0.00 | 0.00 | 0.00 | 0.02 | 0.03 |
| Ti | 0.04 | 0.02 | 0.07 | 0.04 | 0.02 | 0.16 | 0.13 | 0.14 | 0.11 | 0.18 | 0.08 |
| Cr | 0.01 | 0.01 | 0.02 | 0.01 | 0.01 | 0.02 | 0.03 | 0.01 | 0.00 | 0.03 | 0.02 |
| $Fe^{L}$ | 0.62 | 0.71 | 0.34 | 0.45 | 0.47 | 0.34 | 0.33 | 0.40 | 0.98 | 0.38 | 0.52 |
| Mn | 0.01 | 0.01 | 0.00 | 0.01 | 0.01 | 0.01 | 0.00 | 0.01 | 0.02 | 0.01 | 0.00 |
| Mg | 0.97 | 0.97 | 0.84 | 0.86 | 0.94 | 0.66 | 0.81 | 0.67 | 0.56 | 0.74 | 0.72 |
| Ca | 0.35 | 0.26 | 0.69 | 0.56 | 0.52 | 0.79 | 0.69 | 0.71 | 0.36 | 0.58 | 0.61 |
| Na | 0.00 | 0.00 | 0.00 | 0.00 | 0.00 | 0.03 | 0.01 | 0.00 | 0.00 | 0.01 | 0.00 |
| $cations^{Q}$ | 2.00 | 1.99 | 1.96 | 1.93 | 1.98 | 2.01 | 2.00 | 1.94 | 2.03 | 1.95 | 1.98 |
| $En^{R}$ | 49.7 | 49.8 | 45.0 | 46.0 | 48.3 | 36.9 | 44.3 | 37.7 | 29.5 | 43.5 | 38.9 |
| Fs | 32.4 | 36.9 | 18.2 | 24.1 | 24.9 | 19.0 | 18.0 | 22.5 | 51.6 | 22.4 | 28.1 |
| Wo | 17.9 | 13.3 | 36.8 | 29.9 | 26.8 | 44.1 | 37.7 | 39.8 | 18.9 | 34.1 | 33.0 |

Key

A. Typical coarse basalt (sub-calcic) augite, from (8-28).
B. Pigeonite coexisting with A in (8-28).
C. Center of augite crystal in (2-128).
D. Edge of crystal C (2-128), demonstrating zoning.
E. Augite of particularly low Ti and Al content in (8-4).
F. Augite of particularly high Ti and Al content in (2-27).
G. Center of large augite crystal in (9-18), a bimodal-grain-size basalt similar to Figure IIB-9.
H. Edge of crystal G (9-18), demonstrating zoning.
I. Small pyroxene crystal in zone of late-formed material, in same fragment as two preceding analyses (9-18).
J. Augite in fine basalt (18-11).
K. Augite in fine basalt (18-23).

L. All Fe assumed in +2 state.
M. Oxygen abundance calculated from stoichiometry.
N. Al in tetrahedral coordination.
P. Al in octahedral coordination.
Q. Total number of cations in octahedral coordination; should equal 2.
R. Mole percentages of the pyroxene end-members of enstatite (En), ferrosilite (Fs), and wollastonite (Wo), recalculated to sum 100%.

Table IIB-IV. Representative electron microprobe analyses of plagioclase feldspars in lunar basalts.

| | Weight percentages of elements | | | | | | |
|---|---|---|---|---|---|---|---|
| | Coarse | | | Medium | | | Fine |
| | A | B | C | D | E | F | G |
| Si | 22.4 | 23.9 | 20.6 | 21.4 | 24.1 | 25.7 | 25.3 |
| Ti | 0.0 | 0.0 | 0.0 | 0.1 | 0.1 | 0.1 | 0.1 |
| Al | 16.9 | 15.7 | 19.0 | 17.3 | 15.4 | 14.7 | 15.4 |
| Fe | 0.4 | 0.6 | 0.2 | 0.3 | 1.1 | 1.3 | 0.9 |
| Ca | 11.1 | 9.5 | 13.1 | 12.6 | 10.8 | 10.7 | 10.4 |
| Na | 1.6 | 2.9 | 0.4 | 0.7 | 1.3 | 1.1 | 1.8 |
| K | 0.2 | 0.5 | 0.0 | 0.0 | 0.1 | 0.1 | 0.3 |
| O[H] | 45.8 | 46.3 | 45.9 | 45.1 | 46.3 | 47.5 | 47.8 |
| Sum | 98.4 | 99.4 | 99.2 | 97.5 | 99.2 | 101.2 | 102.0 |
| | Atoms per eight oxygen atoms | | | | | | |
| Si | 2.23 | 2.35 | 2.04 | 2.16 | 2.38 | 2.46 | 2.41 |
| Al | 1.74 | 1.61 | 1.96 | 1.82 | 1.58 | 1.47 | 1.53 |
| Ti | 0.00 | 0.00 | 0.00 | 0.01 | 0.01 | 0.01 | 0.01 |
| Fe | 0.02 | 0.03 | 0.01 | 0.01 | 0.06 | 0.06 | 0.04 |
| Ca | 0.77 | 0.65 | 0.91 | 0.89 | 0.74 | 0.72 | 0.69 |
| Na | 0.20 | 0.35 | 0.05 | 0.09 | 0.16 | 0.13 | 0.21 |
| K | 0.01 | 0.03 | 0.00 | 0.00 | 0.01 | 0.01 | 0.02 |
| Sum | 4.97 | 5.02 | 4.97 | 4.98 | 4.94 | 4.86 | 4.91 |
| Ab[I] | 20.2 | 33.8 | 5.2 | 8.7 | 17.3 | 15.1 | 22.6 |
| An | 78.6 | 63.0 | 94.8 | 91.3 | 81.8 | 84.0 | 75.1 |
| Or | 1.2 | 3.2 | 0.0 | 0.0 | 0.9 | 0.9 | 2.3 |

Key

A. Center of plagioclase lath in coarse basalt (8-4): bytownite.

B. Edge of lath A (8-4) (labradorite), displaying zoning.

C. Center of anorthite lath in (8-4), same fragment as above analyses; one of our most calcic feldspars.

D. Center of plagioclase phenocryst in medium basalt (18-38).

E. Edge of phenocryst D (18-38), displaying zoning.

F. Fine-grained late-formed feldspar in same fragment as D and E (18-38).

G. Plagioclase feldspar in fine basalt (18-11).

H. Oxygen abundance calculated from stoichiometry.

I. Mole percentages of the feldspar end-members albite (Ab), anorthite (An), and orthoclase (Or).

Table IIB-V. Representative electron microprobe analyses of oxide minerals in lunar basalts.

| | Weight percentages of elements | | | | | | |
|---|---|---|---|---|---|---|---|
| | A | B | C | D | E | F | G |
| Ni | 0.0 | | | | | 0.0 | |
| Fe | 27.5 | 36.0 | 32.6 | 4.6 | 24.6 | 11.3 | 11.4 |
| Mn | 0.3 | | | | | 0.1 | 0.1 |
| Cr | 1.4 | 0.4 | 0.5 | 0.9 | 22.4 | 1.3 | 1.5 |
| Ti | 33.5 | 31.2 | 32.5 | 54.4 | 10.3 | 44.6 | 44.6 |
| Ca | 0.1 | | | | | 0.1 | 0.0 |
| Si | 0.0 | | | | | 0.0 | 0.1 |
| Al | 0.1 | 0.0 | 0.0 | 0.1 | 8.4 | 1.1 | 0.9 |
| Mg | 4.6 | 0.5 | 2.2 | 0.4 | 2.5 | 4.5 | 4.2 |
| $O^H$ | 34.4 | 31.7 | 32.8 | 38.5 | 33.4 | 37.9 | 37.7 |
| Sum | 101.9 | 99.8 | 100.6 | 98.9 | 101.6 | 100.9 | 100.5 |

Key

A. Ilmenite phenocryst in ultrafine basalt (9-23).

B. Ilmenite in coarse basalt (8-4).

C. Another ilmenite grain in (8-4); host to D and E below.

D. Rutile exsolution lamella in ilmenite C (8-4).

E. Cr-rich exsolution lamella, apparently chromite, in ilmenite C (8-4). Analyzed volume probably includes some of adjacent ilmenite; analysis should show somewhat more Cr and less Ti. Al and Fe contents are typical of many terrestrial chromites.

F. Pseudobrookite phenocryst in (9-23), same fragment as A above.

G. Pseudobrookite in medium basalt (2-29).

H. Oxygen abundance calculated from stoichiometry.

Table IIB-VI. Representative electron microprobe analyses of olivines in lunar basalts.

| | Weight percentages of elements | | | | |
|---|---|---|---|---|---|
| | A | B | C | D | E |
| Si | 16.9 | 17.4 | 16.4 | 18.3 | 18.1 |
| Ti | 0.1 | 0.1 | 0.1 | 0.1 | 0.1 |
| Al | 0.0 | 0.0 | 0.0 | 0.0 | 0.0 |
| Cr | 0.1 | 0.1 | 0.1 | 0.2 | 0.2 |
| Fe | 24.2 | 20.8 | 20.9 | 18.9 | 19.3 |
| Mn | 0.3 | 0.3 | 0.2 | 0.4 | 0.3 |
| Mg | 18.8 | 21.0 | 21.9 | 20.7 | 20.9 |
| Ca | 0.2 | 0.2 | 0.3 | 0.2 | 0.3 |
| Ni | 0.0 | | 0.0 | | |
| O[F] | 38.8 | 39.9 | 40.3 | 41.0 | 41.1 |
| Sum | 99.4 | 99.8 | 100.2 | 99.8 | 100.3 |
| Fa[G] | 36.0 | 30.7 | 29.4 | 28.4 | 28.7 |
| Fo | 64.0 | 69.3 | 70.6 | 71.6 | 71.3 |

Key

A. Olivine in coarse basalt (8-28); coexisting pyroxenes shown in Table IIB-III.

B. Olivine in medium basalt (17-2).

C. Olivine in medium basalt (9-18); coexisting pyroxenes shown in Table IIB-III.

D. Center of olivine phenocryst in fine basalt (9-23).

E. Edge of olivine phenocryst D in (9-23), demonstrating feeble zoning.

F. Oxygen abundance calculated from stoichiometry.

G. Mole percentages of the olivine end-members fayalite (Fa) and forsterite (Fo).

Table IIB-VII. Electron microprobe analyses of K-rich areas in lunar basalts.

| | Weight percentages of elements | | | |
|---|---|---|---|---|
| | A | B | C | D |
| Na | 0.2 | 0.7 | 0.4 | 0.6 |
| Al | 5.5 | 6.4 | 5.3 | 6.4 |
| Si | 32.4 | 33.8 | 32.3 | 32.7 |
| K | 4.4 | 6.0 | 5.4 | 6.1 |
| Ca | 1.8 | 1.0 | 5.0 | 0.6 |
| Ti | 0.7 | 0.6 | 0.5 | 0.6 |
| Fe | 6.1 | 1.9 | 1.1 | 2.3 |
| O[E] | 45.8 | 47.0 | 45.4 | 45.7 |
| Sum | 96.9 | 97.4 | 95.4 | 95.0 |

Key

A. K-rich area in (18-1) – point x in Figure IIB-30.

B-D. K-rich areas in (2-103).

E. Oxygen abundance calculated from stoichiometry.

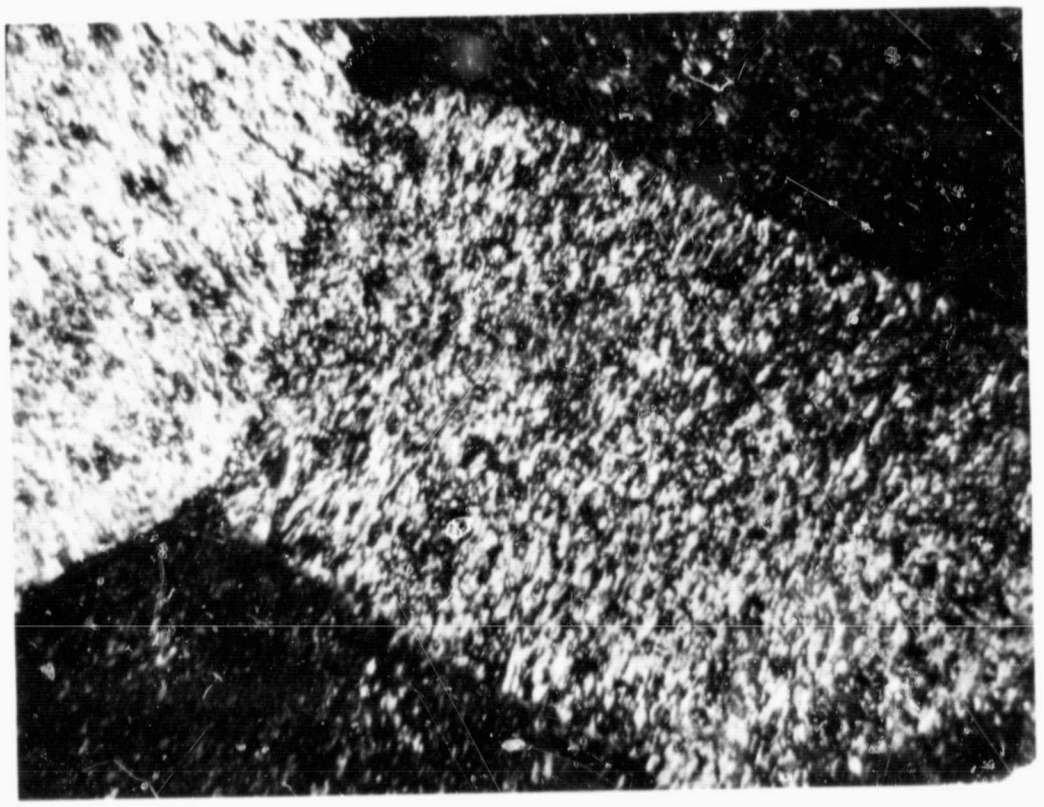



Figure III-7. The twin planes are still evident in this plagioclase crystal, but the original twins have been broken down into tiny, anisotropic units. The dark twins are nearly isotropic. Crossed nicols.

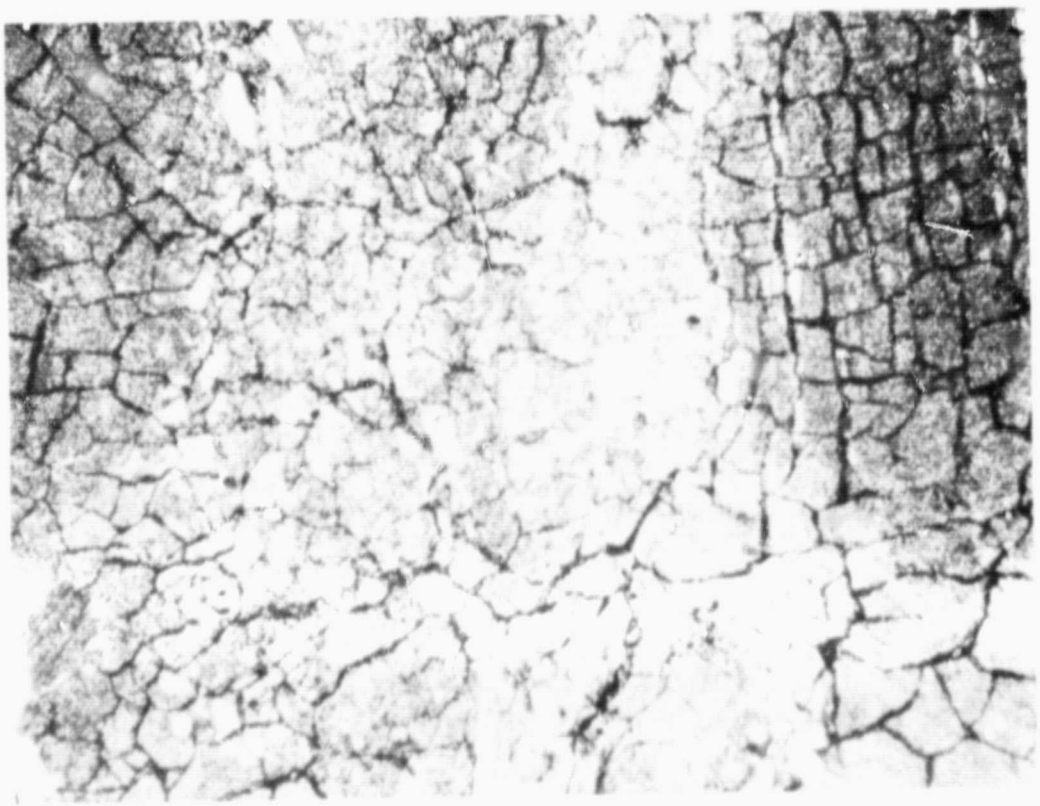



Figure III-8. Partly fused gabbroic anorthosite or anorthositic gabbro. Note the overall polygonal fracture pattern. The darker parts are nearly isotropic. The lighter, more feldspathic part in the center was not fused. Unpolarized light.

Table IIB-VIII. Representative electron microprobe analyses of metal and troilite grains in the lunar basalts.

| | Weight percentages of elements | | | |
|---|---|---|---|---|
| | A | B | C | D |
| Fe | 65.4 | 65.7 | 97.7 | 98.1 |
| Ni | 0.0 | | 0.2 | 0.3 |
| Ti | 0.1 | 0.1 | 0.0 | 0.4 |
| S | 33.9 | 34.5 | 0.1 | 1.3 |
| Sum | 99.4 | 100.4 | 98.0 | 100.1 |

Key

A. Troilite in coarse basalt (8-28).

B. Troilite in coarse basalt (8-4).

C. Rounded metal inclusion (12μ diameter) in troilite A above (8-28).

D. Rounded metal inclusion (6μ diameter) in troilite A (8-28).

Table IIB-IX. Bulk compositions of two lunar medium-grained basalts.

| | Weight percent of oxides | | | C. I. P. W. Norms (wt. %) | |
|---|---|---|---|---|---|
| | (18-1) | (18-38) | | (18-1) | (18-38) |
| $SiO_2$ | 42.7 | 41.7 | Quartz | 3.4 | 2.2 |
| $TiO_2$ | 11.1 | 8.0 | Orthoclase | 4.3 | 1.6 |
| $Al_2O_3$ | 11.0 | 14.8 | Plagioclase | 27.8 | 39.5 |
| $Cr_2O_3$ | 0.5 | 0.2 | Diopside | 21.2 | 18.6 |
| FeO | 16.7 | 15.8 | Hypersthene | 24.3 | 22.4 |
| MnO | 0.3 | 0.3 | Olivine | 0.0 | 0.0 |
| MgO | 8.9 | 6.2 | Chromite | 0.7 | 0.3 |
| CaO | 10.8 | 12.5 | Ilmenite | 21.1 | 15.2 |
| $Na_2O$ | 0.6 | 0.6 | (Other) | 1.7 | 1.7 |
| $K_2O$ | 0.7 | 0.3 | | | |
| NiO | 0.0 | 0.0 | | | |
| S | 0.4 | 0.4 | | | |
| Sum | 103.7 | 100.8 | | | |

## Table IIB-X. Zr measurements in lunar materials.

| Fragment | Material | Beam* | Background counts at 6,260 Å | Background counts at 5,943 Å | Background interpolated to 6,070 Å ± counting statistics | Counts recorded at 6,070 Å | Counts above background | Zr content (ppm) |
|---|---|---|---|---|---|---|---|---|
| (18-36) | Pyroxene | F | 493 | 1,333 | 997 ± 32 | 1,149 | 152 | 200 |
| (18-36) | Feldspar | F | 417 | 1,050 | 827 ± 29 | 973 | 146 | 200 |
| (18-36) | Ilmenite | F | 864 | 1,717 | 1,376 ± 37 | 1,651 | 275 | 400 |
| (18-35) | Pyroxene | F | 392 | 1,041 | 782 ± 28 | 895 | 113 | 150 |
| (18-35) | Feldspar | F | 396 | 924 | 713 ± 27 | 857 | 144 | 200 |
| (18-35) | Ilmenite 1 | F | 465 | 1,469 | 1,067 ± 33 | 2,202 | 1,135 | 1,500 |
| (18-35) | Ilmenite 2 | F | 482 | 1,443 | 1,060 ± 33 | 2,280 | 1,220 | 1,500 |
| (18-37) | Ilmenite | F | 617 | 1,492 | 1,142 ± 34 | 1,423 | 281 | 400 |
| (18-39) | Ilmenite | F | 699 | 1,515 | 1,189 ± 35 | 1,627 | 438 | 600 |
| | Co metal (blank) | F | 1,007 | 2,389 | 1,835 ± 43 | 1,955 | 120 | (150) |
| | Zircon standard | F | 730 | 2,870 | 2,013 ± 45 | 354,460 | 352,447 | (500,000) |
| | Zircon standard | D | 440 | 2,600 | 1,736 ± 42 | 354,820 | 353,084 | (500,000) |
| (18-21) | Orange glass | D | 639 | 1,165 | 955 ± 36 | 1,418 | 463 | 650 |
| (18-32) | Soil breccia | D | 566 | 1,022 | 840 ± 29 | 937 | 97 | 200 |
| | Zircon standard | D | 1,020 | 3,530 | 2,526 ± 50 | 431,850 | 429,324 | (500,000) |
| | Co metal (blank) | D | 1,125 | 2,553 | 1,980 ± 45 | 1,987 | 7 | (0) |
| (16-1) | Soil breccia | D | 317 | 955 | 700 ± 26 | 1,019 | 319 | 350 |
| (16-2) | Orange glass | D | 578 | 1,123 | 906 ± 30 | 1,257 | 351 | 400 |
| (16-3) | Anorthosite breccia | D | 493 | 1,168 | 897 ± 30 | 1,008 | 111 | 150 |
| (16-4) | Soil breccia | D | 384 | 885 | 685 ± 26 | 1,146 | 461 | 550 |
| (16-5) | Yellow glass | D | 505 | 1,207 | 927 ± 30 | 1,369 | 442 | 500 |
| (16-23) | Brown glass | D | 556 | 1,272 | 986 ± 31 | 1,263 | 277 | 300 |
| (16-36) | Orange glass | D | 587 | 1,490 | 1,128 ± 34 | 1,464 | 336 | 400 |
| (16-40) | Tan glass | D | 696 | 1,318 | 1,069 ± 33 | 1,416 | 347 | 400 |
| (16-29) | Orange glass | D | 532 | 1,319 | 1,003 ± 32 | 1,395 | 392 | 450 |

*F, point focus; D, defocussed (50μ diameter).

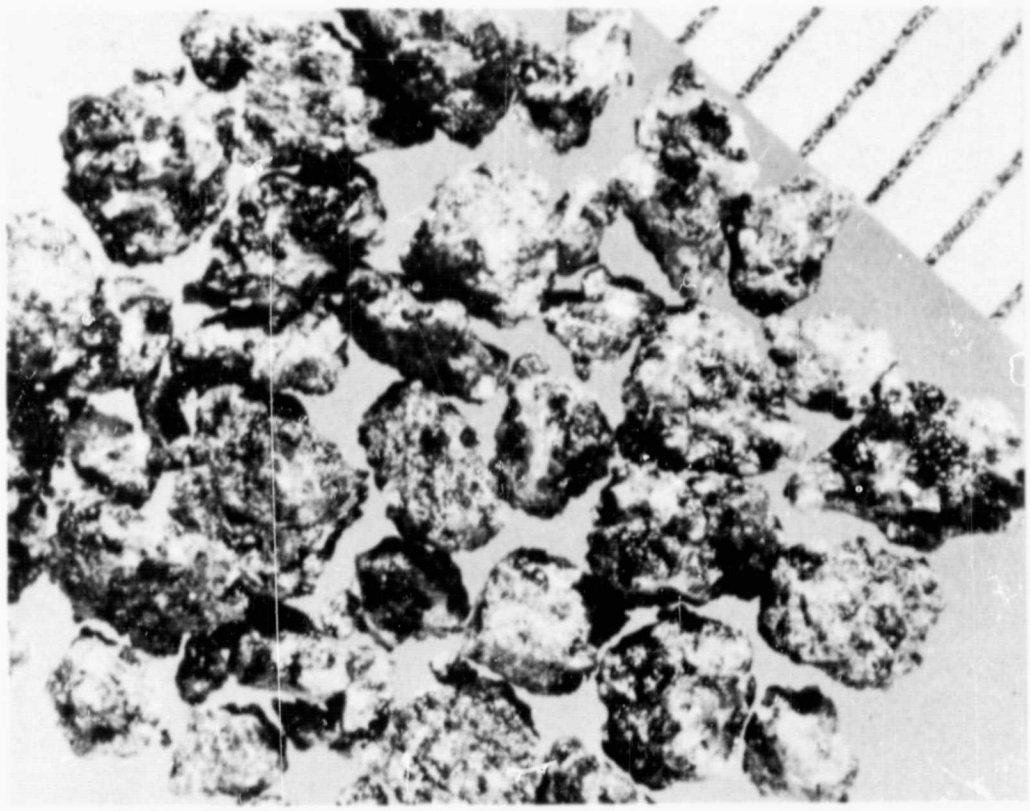


Figure IIB-1. Macroscopic view of coarse basalt fragments, with millimeter scale. The three principal mineral components are plainly visible.



Figure IIB-2. Fragment of medium basalt.

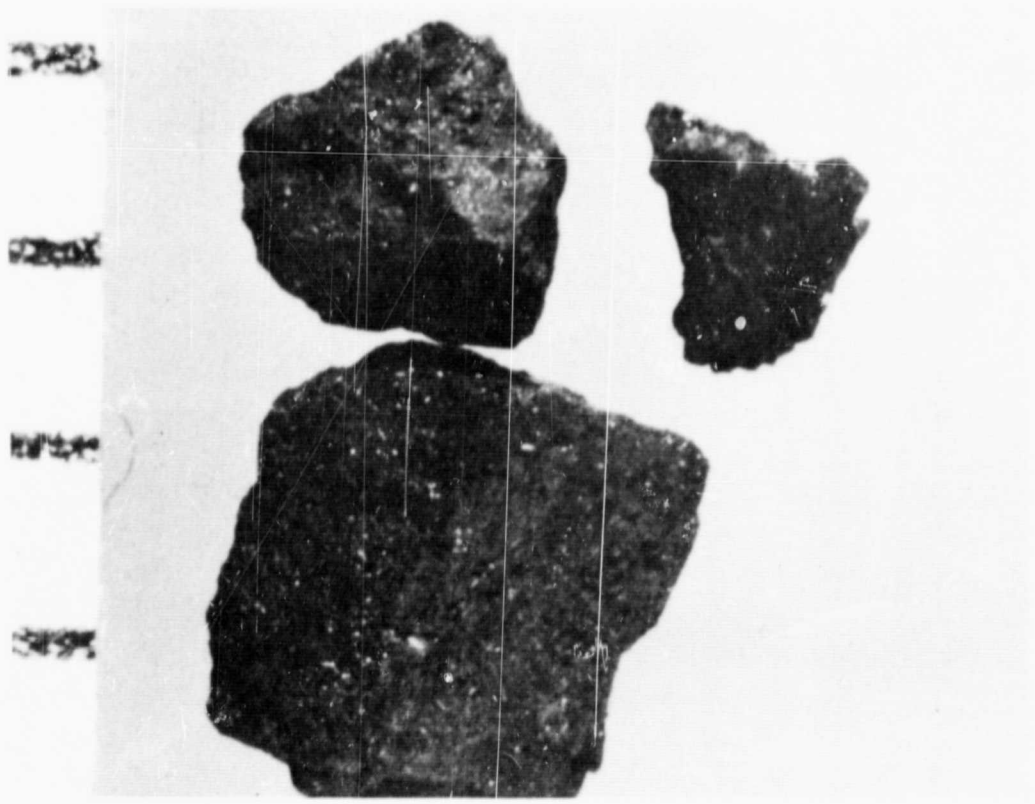
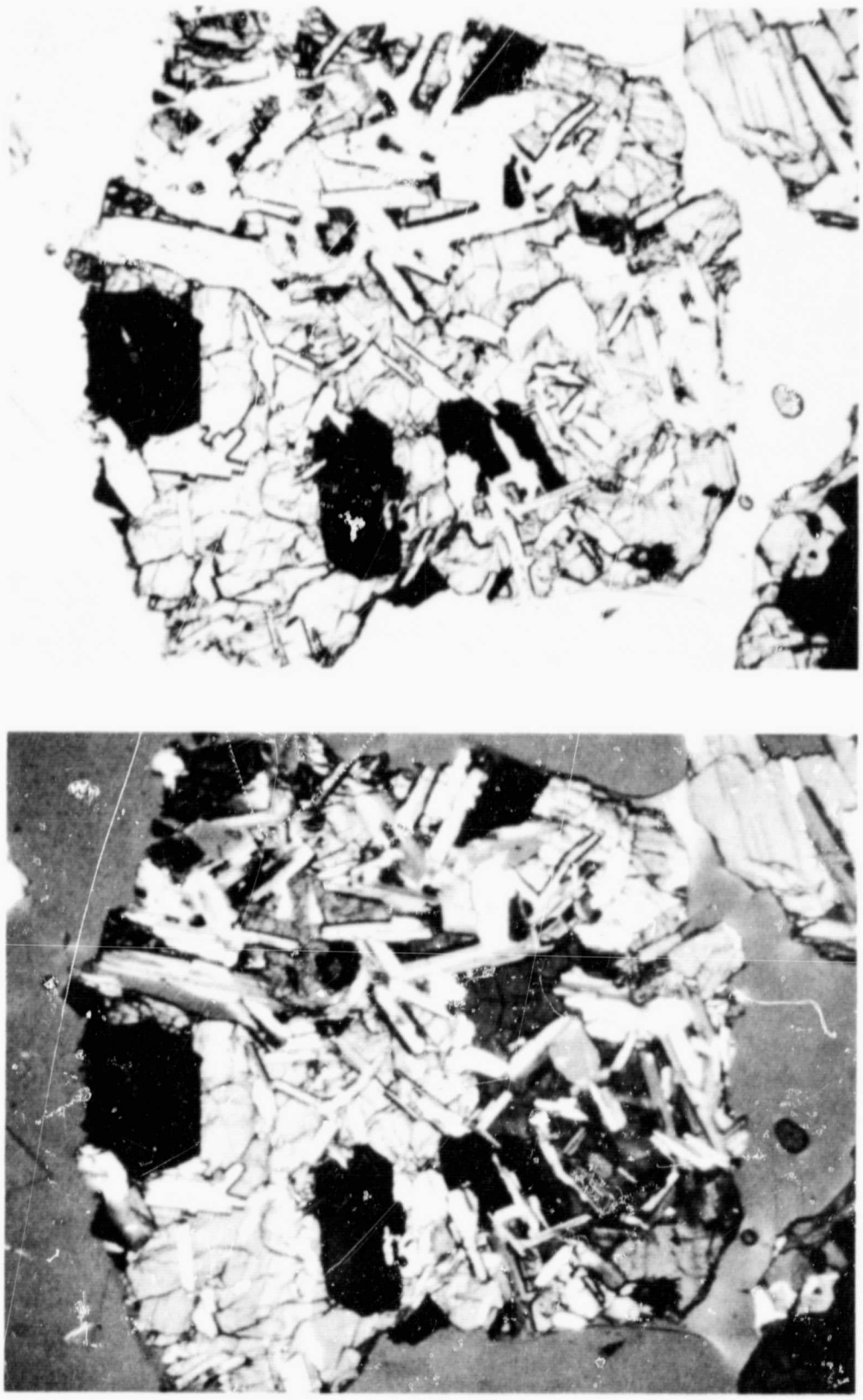


Figure IIB-3. Fragments of fine-grained basalt, with millimeter scale.



1mm

Figure IIB-4. Thin section of typical coarse basalt grain. Above, plain light: clear white crystals, calcic plagioclase feldspar; black crystals, ilmenite; medium-gray crystals, pyroxene. Below, partly polarized light (to show extent of domains of optical continuity of pyroxenes — single crystals).

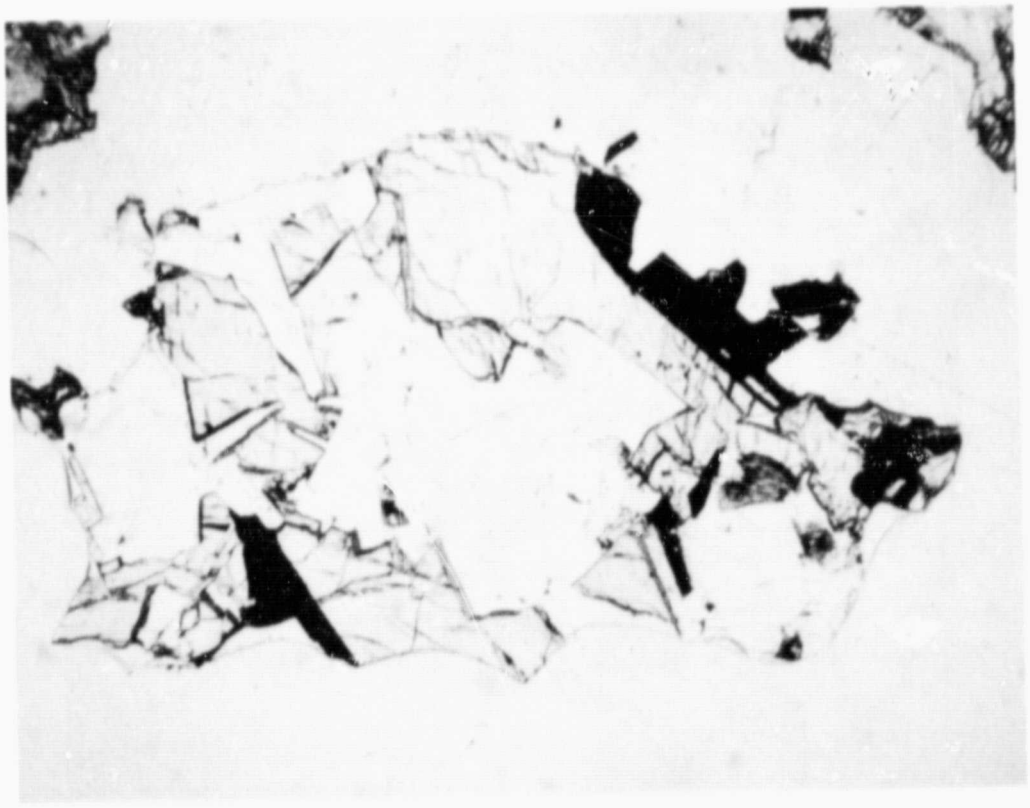



Figure IIB-5. Basalt fragment with coarser and less ophitic texture than Figure IIB-4. This is representative of the coarsest grained rocks we encountered.

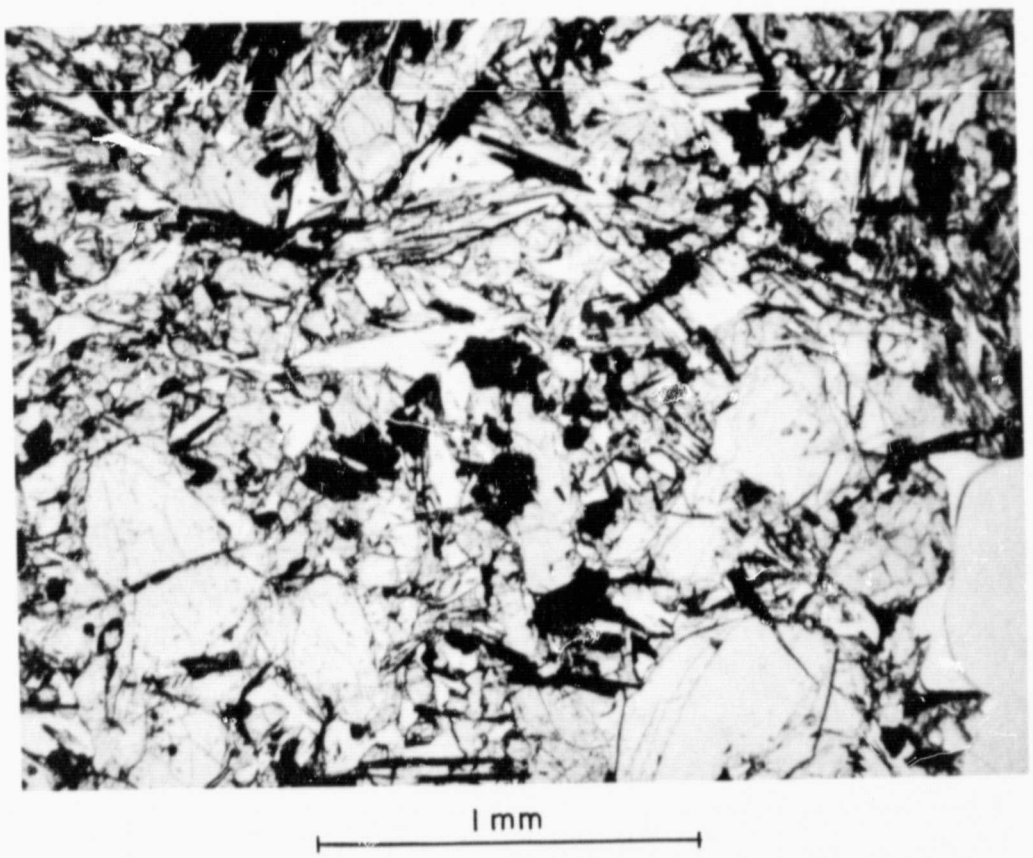



Figure IIB-6. Coarse olivine basalt. Three 0.5-mm olivine crystals, light gray in color, are visible in the lower half of the figure.

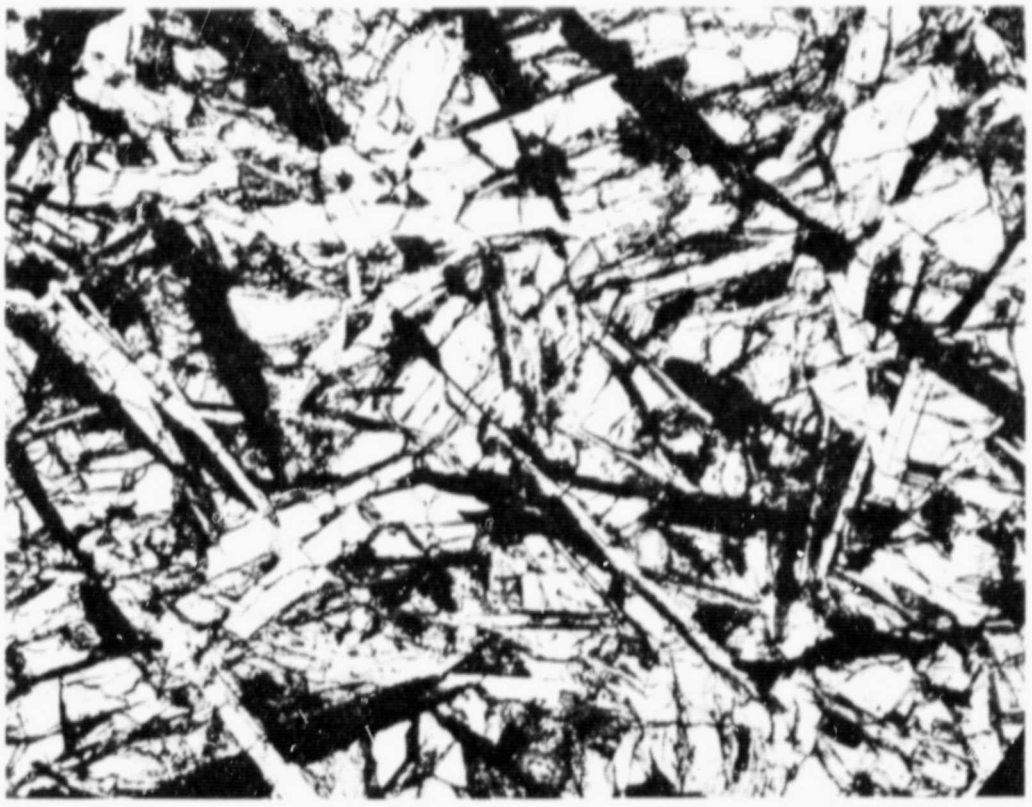



Figure IIB-7. Medium basalt fragment (22-4) with pronounced ophitic texture. Ilmenite as well as plagioclase occurs in elongated crystals.

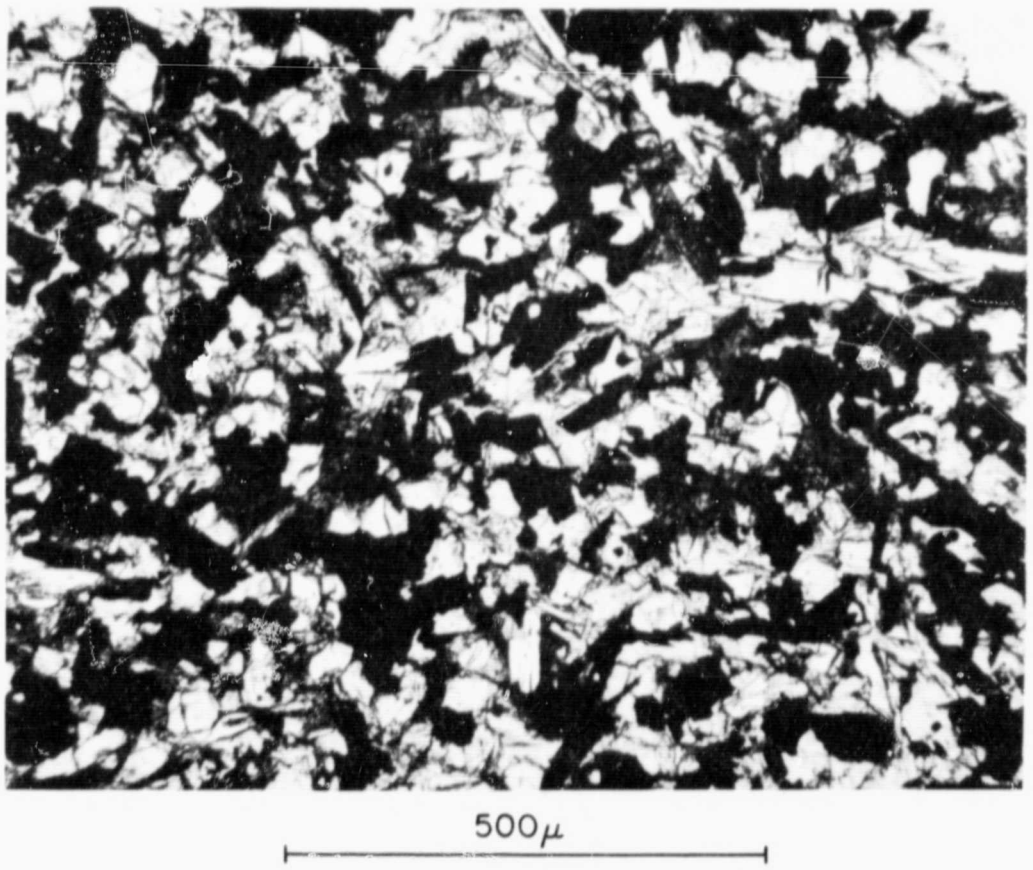



Figure IIB-8. Medium basalt fragment (18-1) with more nearly equidimensional crystalline texture.




Figure IIB-9. Medium basalt fragment (18-38) with bimodal distribution of crystal sizes. Relatively coarse crystals of feldspar, pyroxene, and ilmenite are visible, as well as fine-grained sheafs of fibers or blades of all three minerals (presumably last to crystallize).

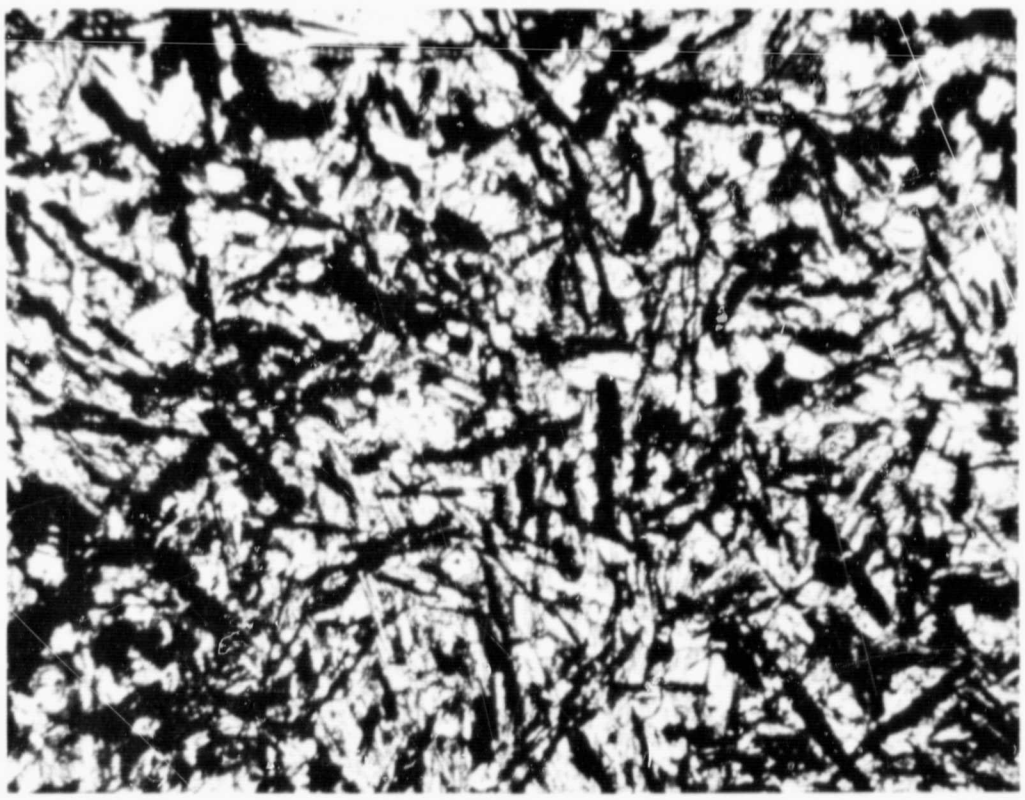



Figure IIB-10. Fine basalt fragment (18-11).

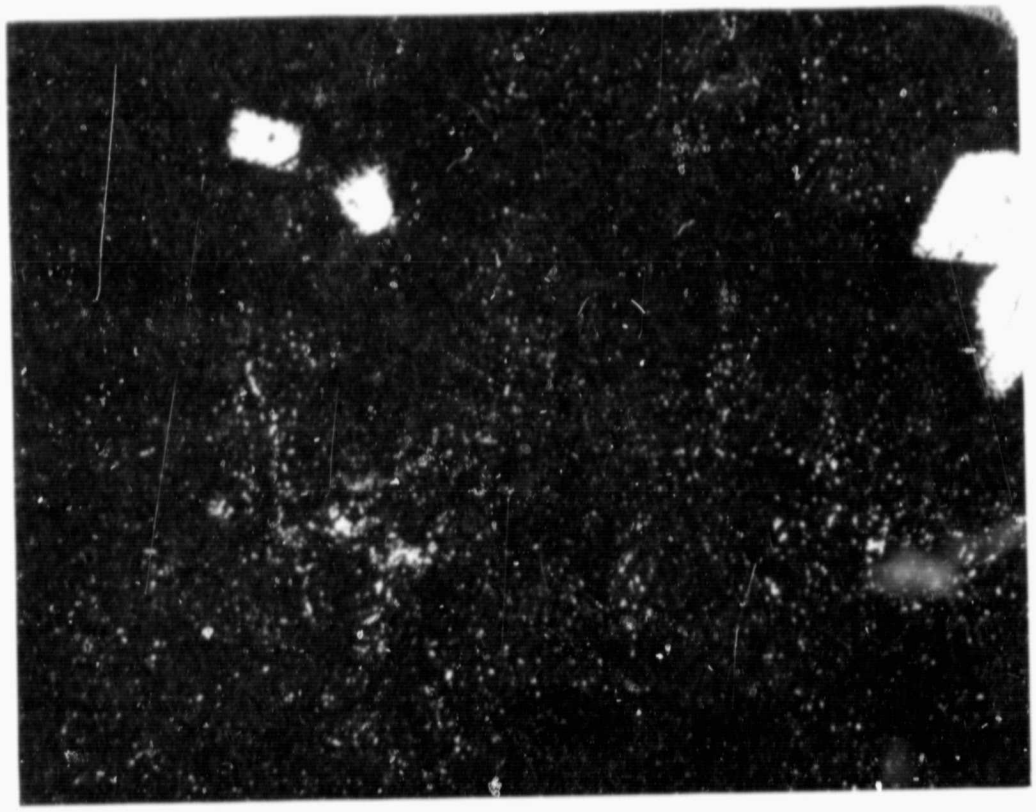



Figure IIB-11. Very fine basalt fragment (18-23), by transmitted light. Section is rendered almost opaque by ilmenite crystallites of dimension smaller than thickness of the section. White phenocrysts, olivine.

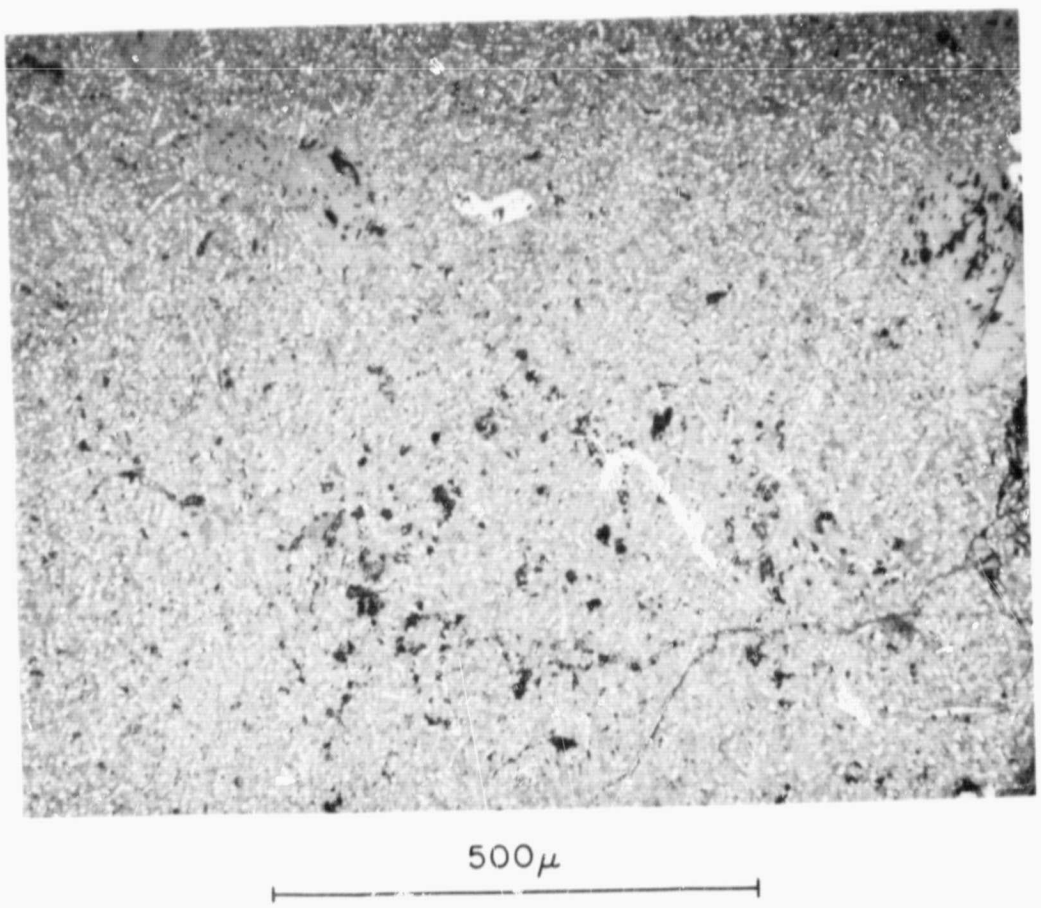



Figure IIB-12. Same field as above, by reflected light.

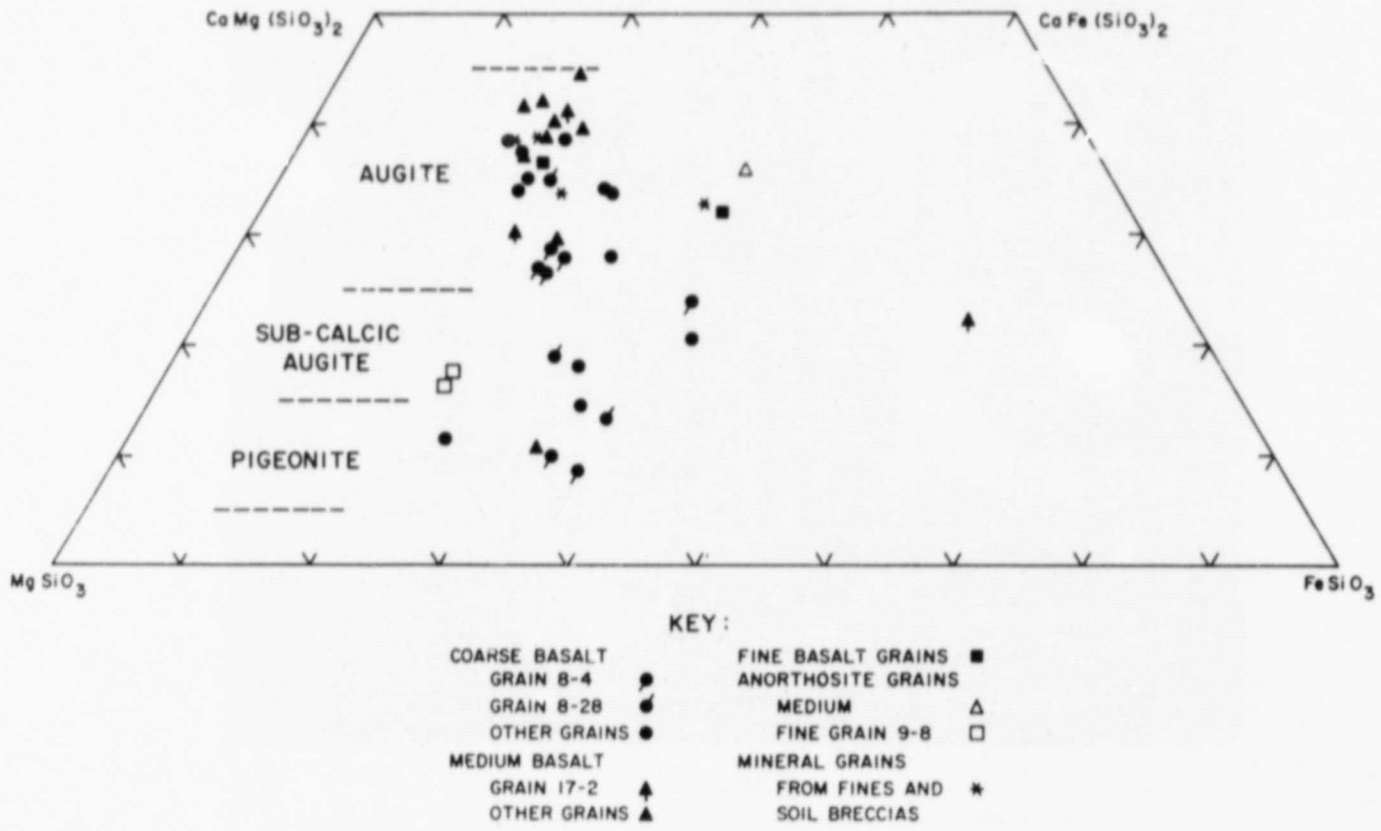



Figure IIB-13. Compositions of lunar pyroxenes analyzed, plotted on a conventional triangular diagram showing molar proportions Mg, Fe, and Ca pyroxene end-members. Only superior analyses ($\sum$ = 98.5 - 101.0%) are entered. Analyses were recalculated on a Ti, Al free basis.

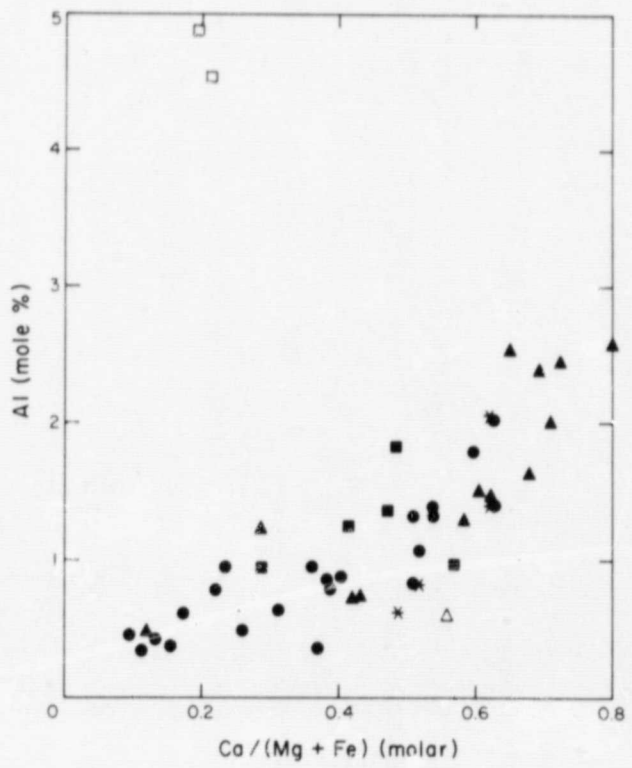



Figure IIB-14. Relation of Al to Ca content of lunar pyroxenes. Same pyroxene analyses and symbols as in Figure IIB-13, except coexisting pyroxenes are not indicated.

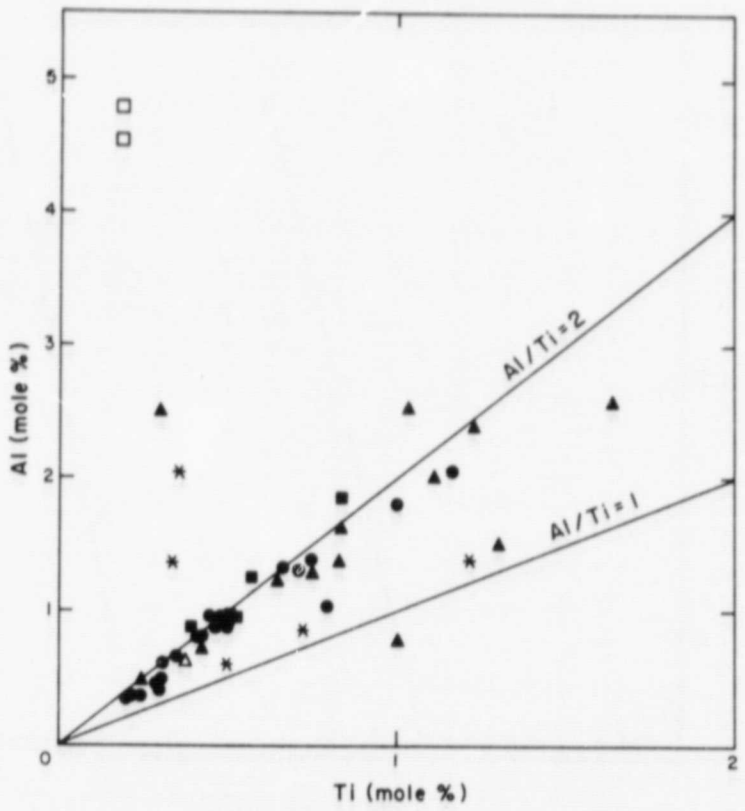



Figure IIB-15. Relation of Ti to Al content of lunar pyroxenes. Same pyroxene analyses and symbols as in Figure IIB-13, except coexisting pyroxenes are not indicated.

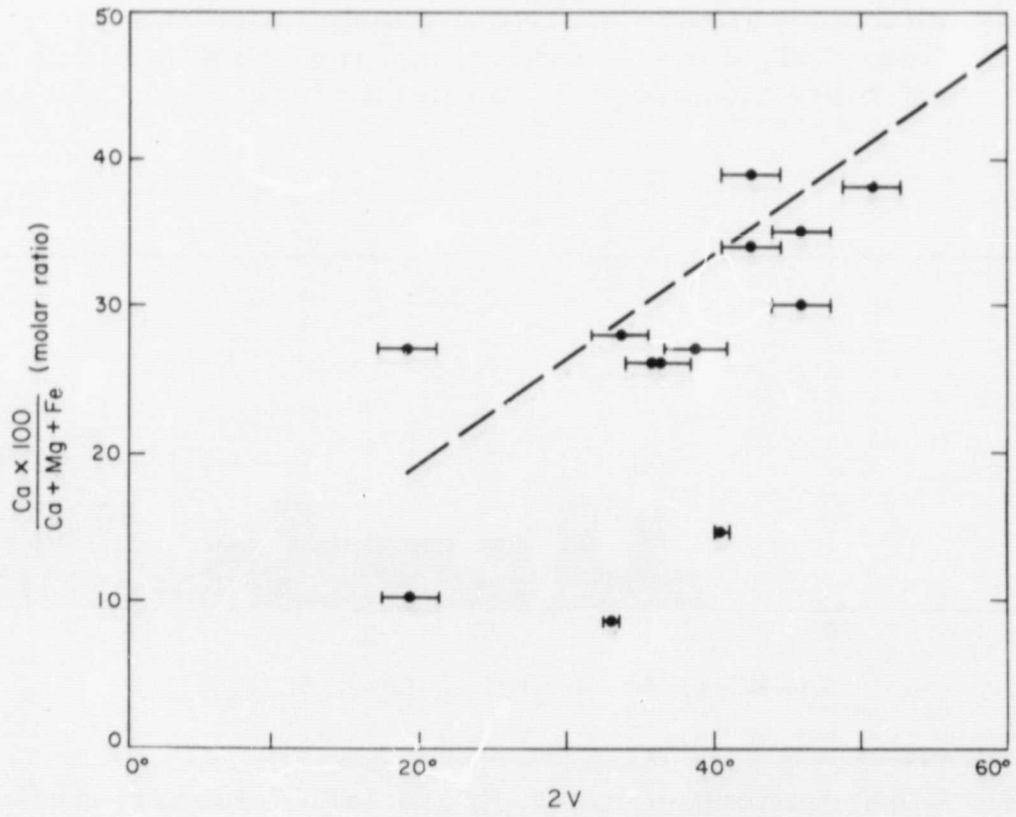



Figure IIB-16. Observed relationship between optic angle (2V) and Ca content of lunar basaltic pyroxenes. Dashed line shows approximate variation of 2V with Ca for terrestrial clinopyroxenes along the join $Di_{55}Hd_{45}$ - $En_{55}Fs_{45}$ (Deer, Howie, and Zussman, 1962).

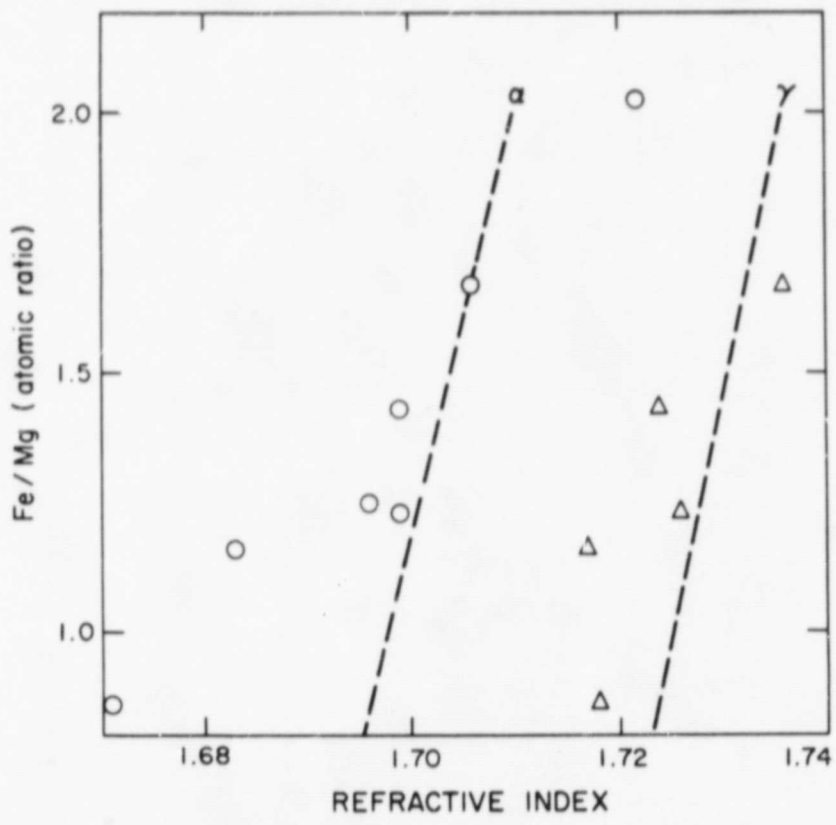



Figure IIB-17. Refractive indices of clinopyroxenes. Circles: minimum indices. Triangles: maximum indices. The dashed lines show, for comparison, variation of maximum and minimum index along the diopside-hedenbergite join in terrestrial pyroxenes (based on Deer, Howie, and Zussman, Volume 2, Figure 22, 1963). Deviations are attributable to less calcic and more titaniferous compositions of lunar pyroxenes.

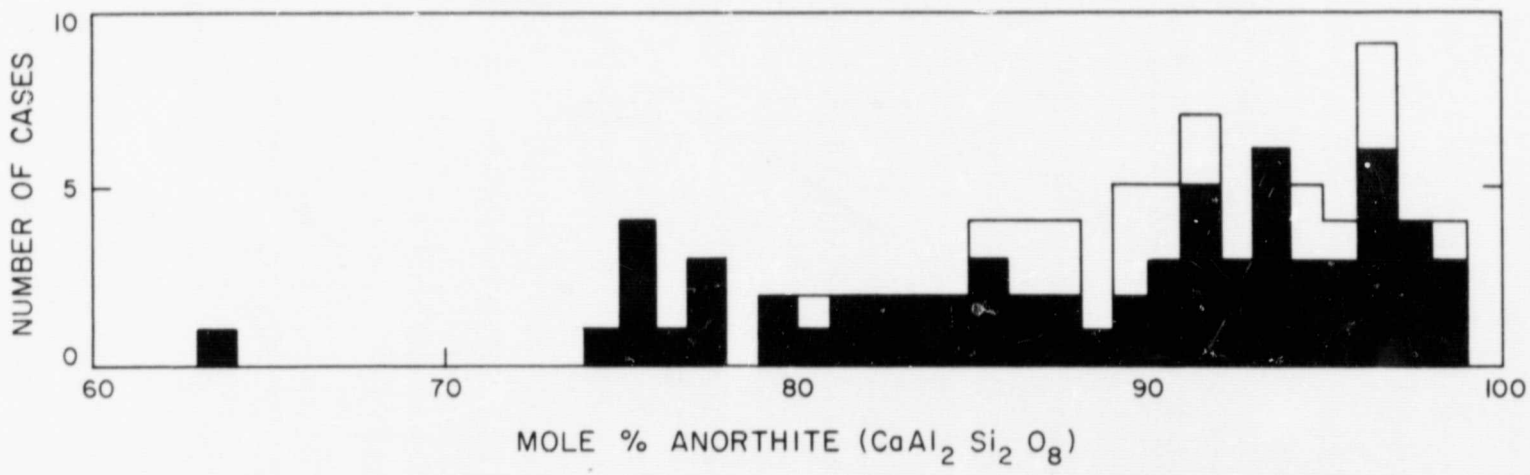



Figure IIB-18. Compositions of lunar plagioclase feldspars analyzed. Only superior analyses are reported ($\sum$ = 98.5 to 101.0%). Black, basalt grains; white, anorthosites.

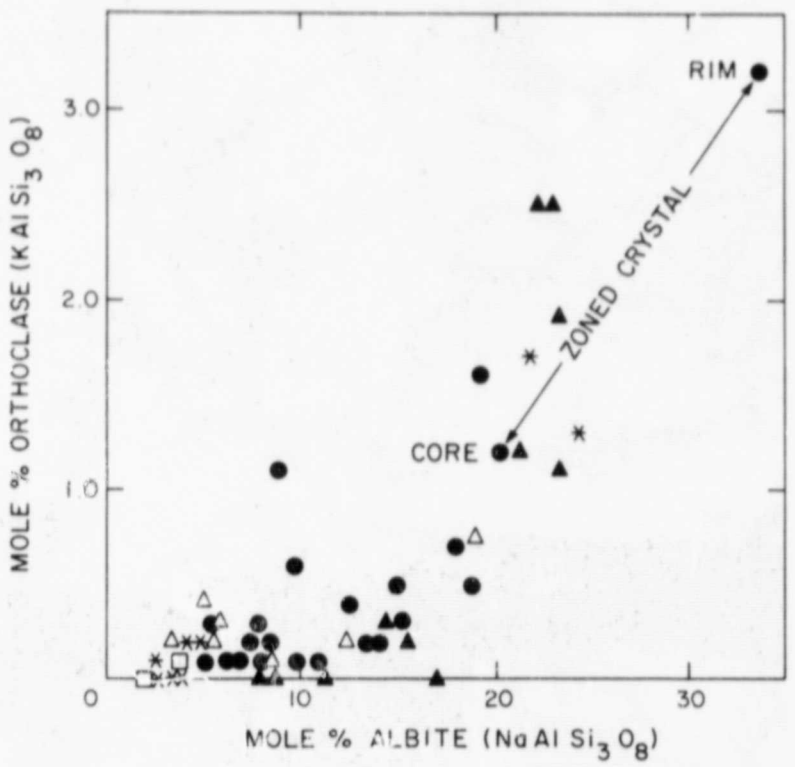



Figure IIB-19. Relation of K to Na content (expressed as albite to orthoclase) of lunar plagioclase feldspars. Only superior analyses are reported. Symbols are defined in Figure IIB-13.

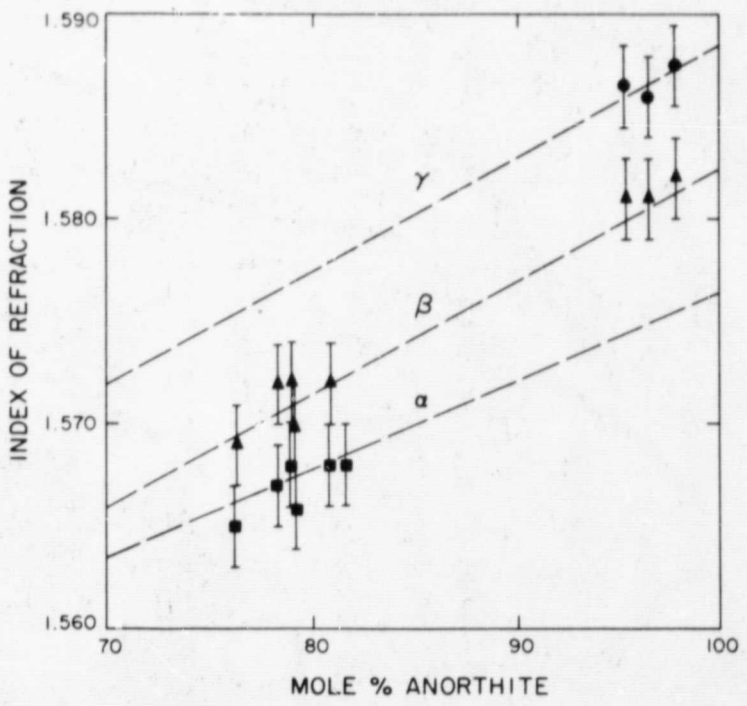



Figure IIB-20. Refractive indices of plagioclase crystals from the +200, -100 mesh size fraction of the particulate sample vs. mole percent $CaAl_2Si_2O_8$ (composition by electron microprobe). Dashed lines show refractive index variation of high temperature terrestrial plagioclases (data from Deer, Howie, and Zussman, 1962).




Figure IIB-21. Complexly twinned plagioclase feldspar in coarse basalt (25-17).




Figure IIB-22. Extremely elongated feldspar crystals in medium basalt (29-6). Atypical.

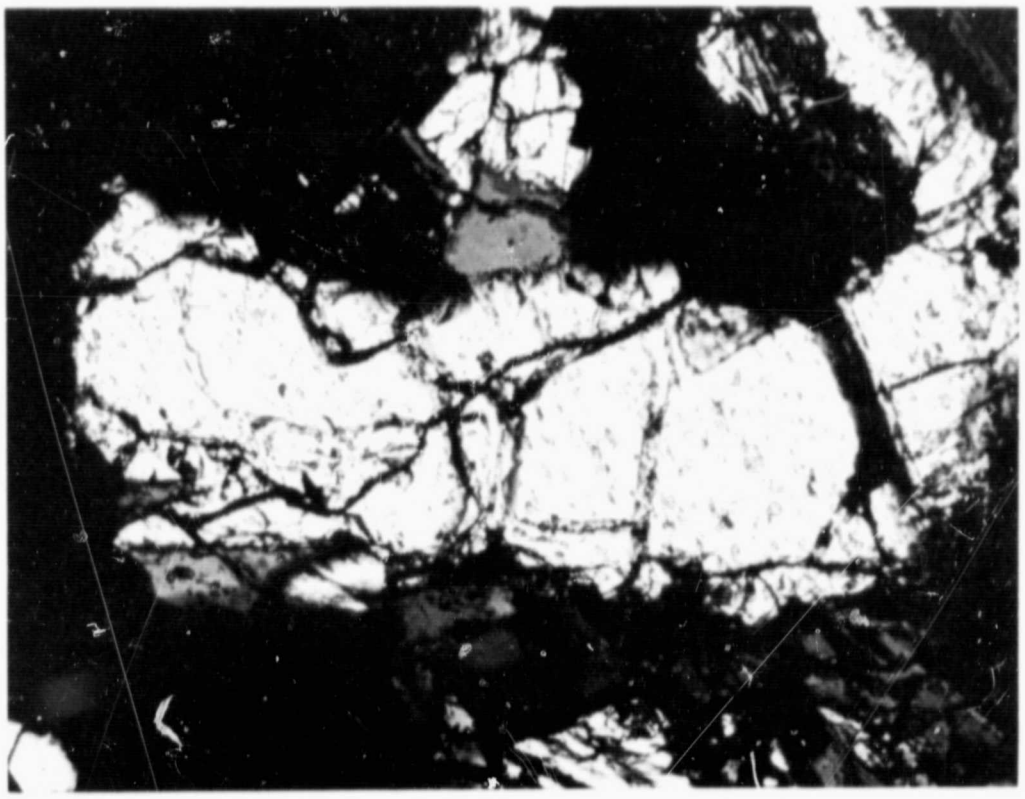



Figure IIB-23. Feldspar crystal containing inclusions of (apparently) pyroxene; in coarse basalt (20-45). Crossed nichols.

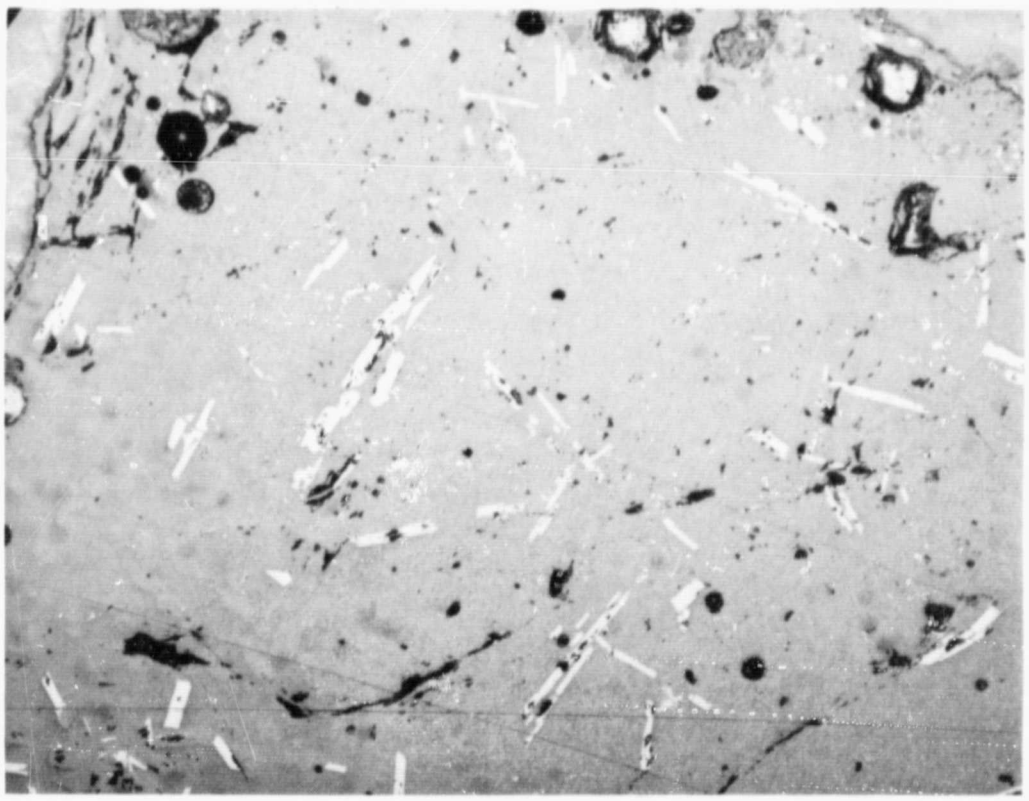



Figure IIB-24. Yellow glass containing phenocrysts of ilmenite and (less visible) pyroxene; by reflected light. Glass, probably shock-melted basalt, demonstrates that ilmenite, much of which survived melting, is a relatively refractory constituent. Fragment (18-21).

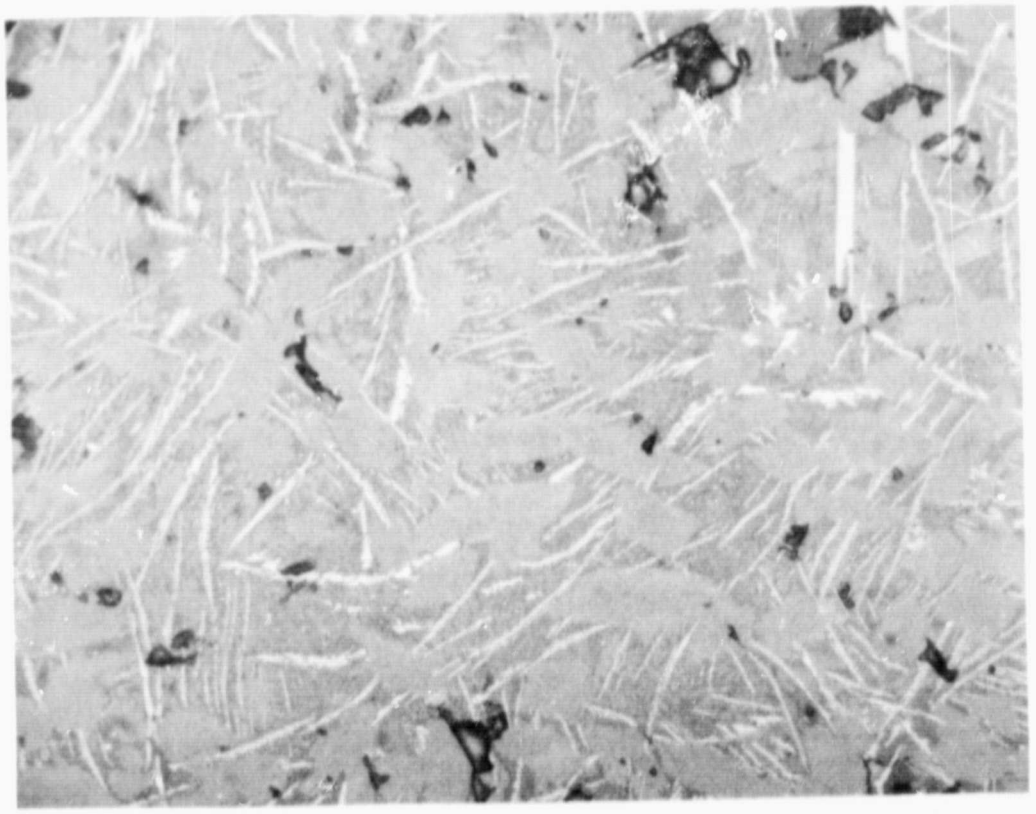



Figure IIB-25. Fine basalt fragment in which pyroxene clearly crystallized first, followed by essentially simultaneous crystallization of feldspar, pyroxene, and ilmenite (the latter two minerals in dendritic or feathery structures) in the melt liquid remaining.

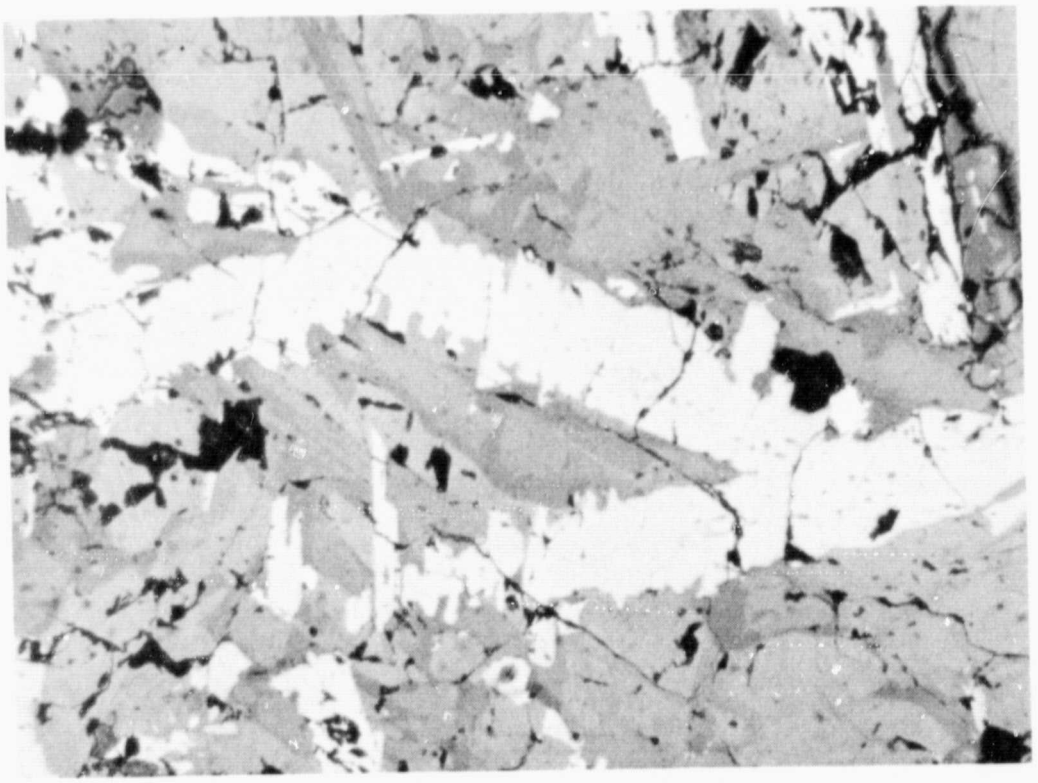



Figure IIB-26. Ilmenite crystals, apparently resorbed, in a coarse olivine basalt.

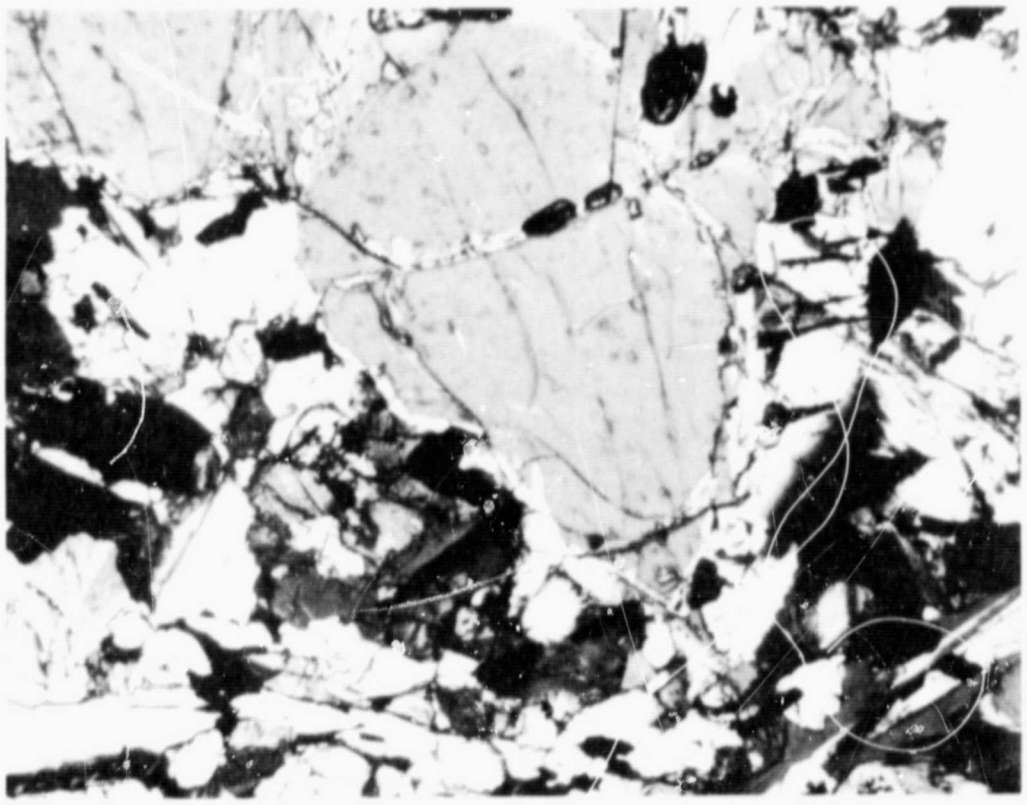



Figure IIB-27. Resorbed olivine crystal (large, medium gray) in coarse olivine basalt.




Figure IIB-28. Phenocrysts of ilmenite (light gray), pseudobrookite (darker), and olivine (darkest) in a matrix of ultrafine "basalt" in which feathery crystallites of ilmenite are visible.

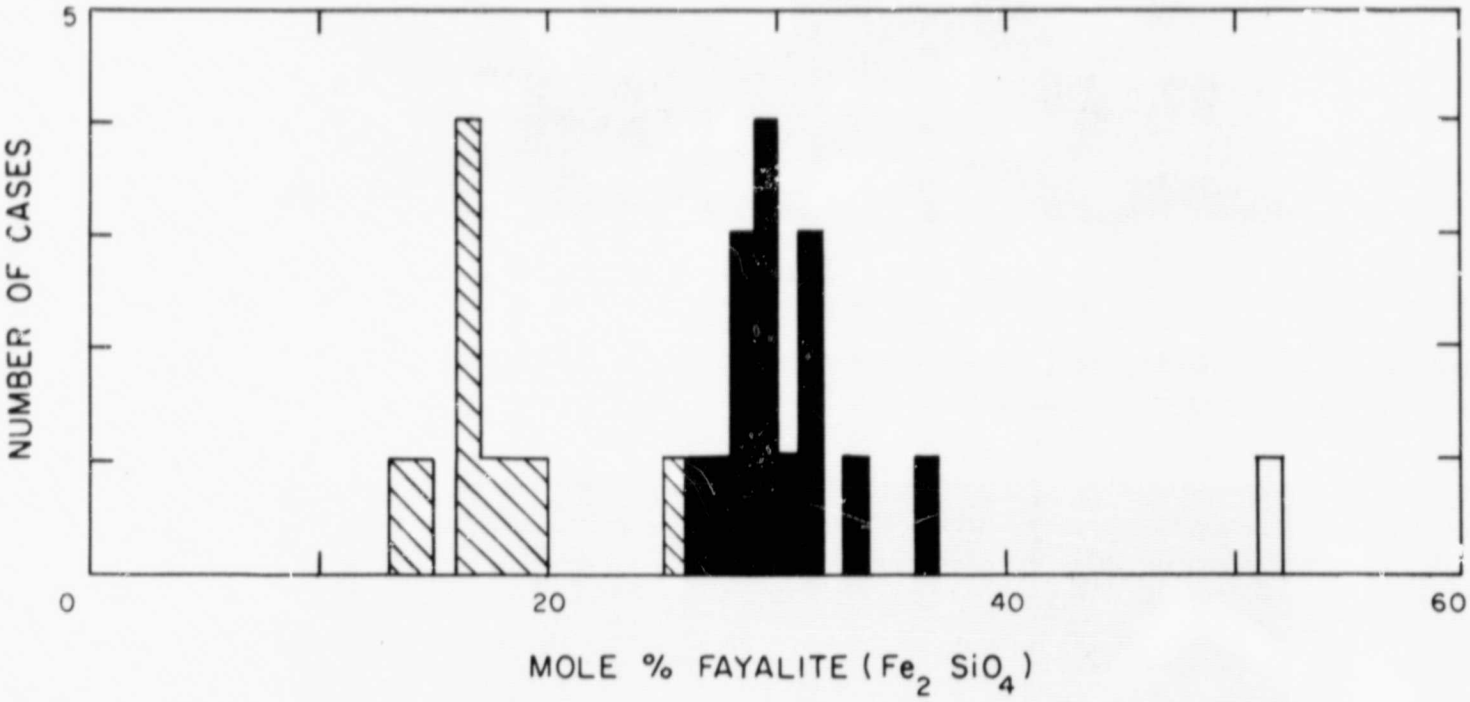
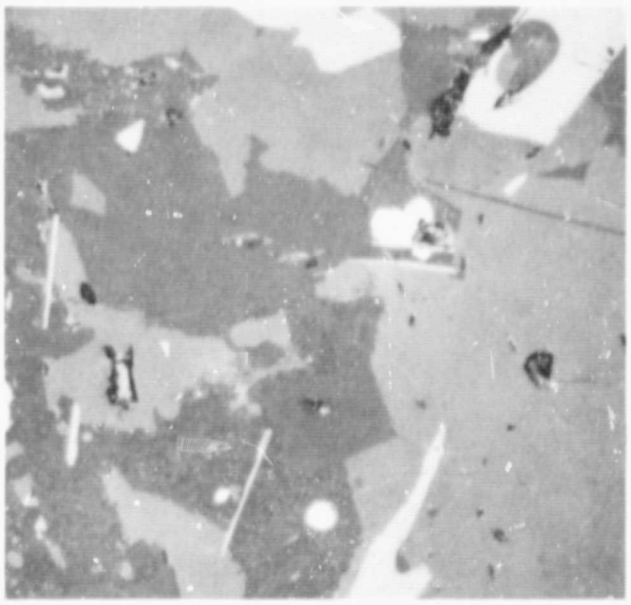


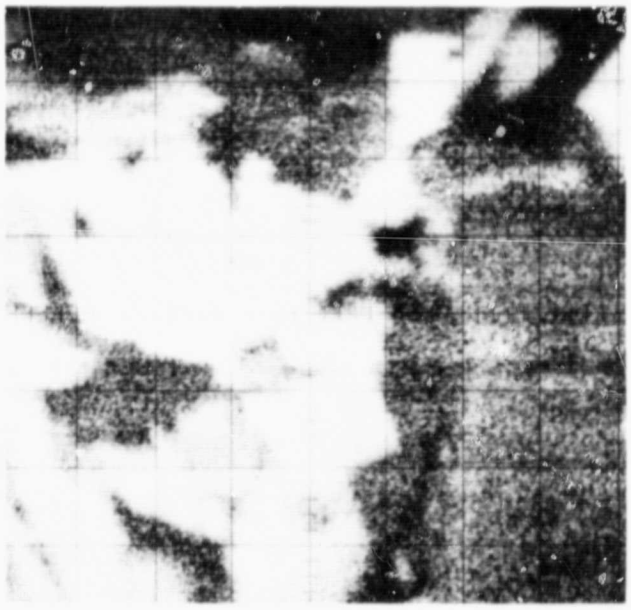

Figure IIB-29. Histogram of lunar olivine compositions determined by microprobe analysis. Black, lunar basalts; hatched, problematical fragment (8-36) discussed in Section IIE; white, anorthosite.



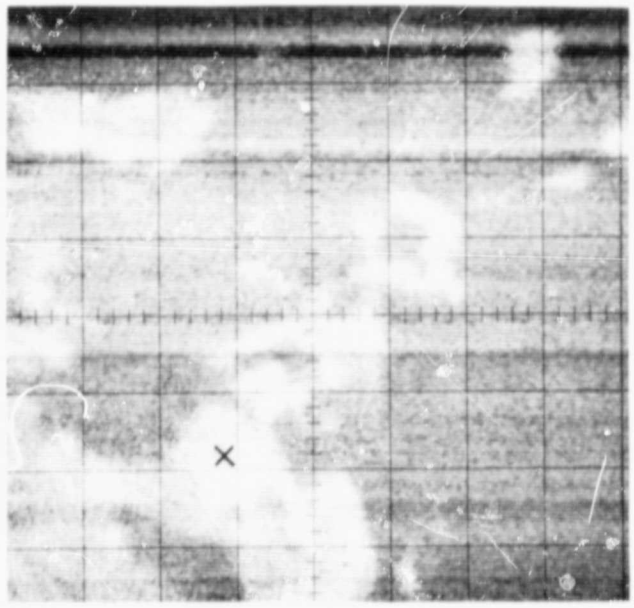
Reflected light



Sample current



Al $k_a$ x-rays



K $k_a$ x-rays

200$\mu$

Figure IIB-30. K-rich area in medium basalt (18-1), by reflected-light microscopy and electron-microprobe beam scanning displays. Al $k_a$ display shows general distribution of feldspar; K $k_a$ display shows that not all these areas are K-rich. Quantitative analysis at point x appears elsewhere in this section.




Figure IIB-31. Pseudobrookite plate (medium gray) surrounded by a rim of ilmenite (lighter gray), in medium basalt (9-19). Reflected light, oil immersion.




Figure IIB-32. K-rich area shown in Figure IIB-30 (medium basalt 18-1), more highly magnified and with oil immersion. K, polyminerallic, K-rich zone; T, troilite; C, calcic feldspar; I, ilmenite; other medium gray areas, pyroxene.

20μ

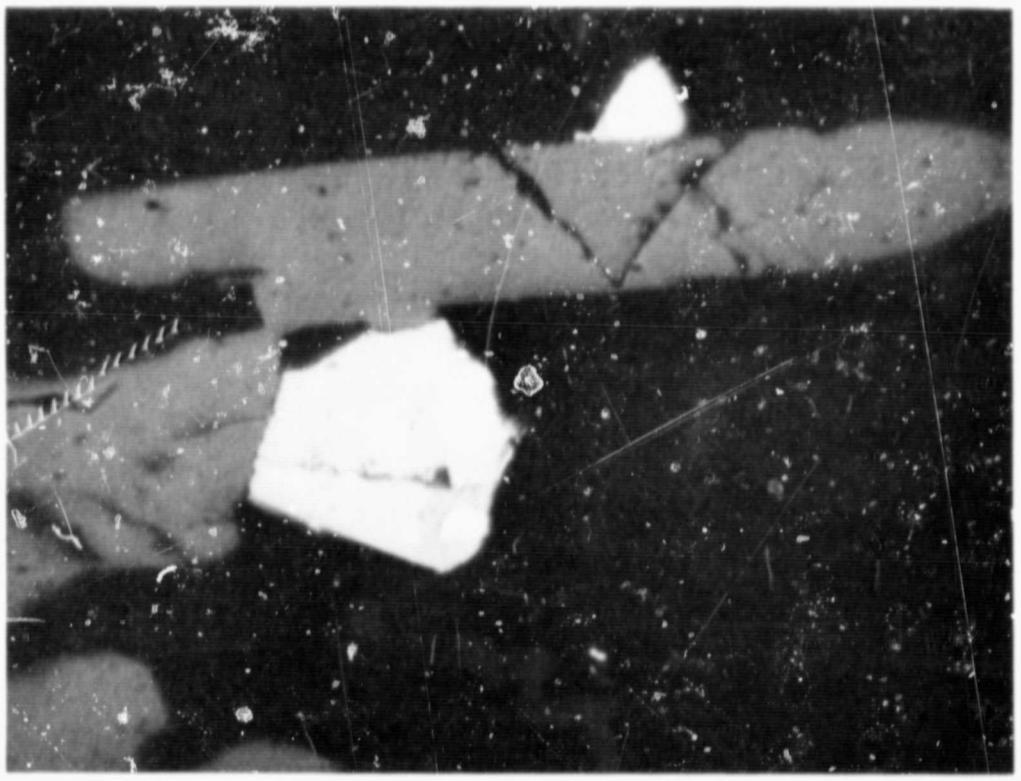



Figure IIB-33. Metal-troilite aggregation in a coarse basalt; typical occurrence. Reflected light. White, metallic iron; light gray, troilite; dark gray, ilmenite.

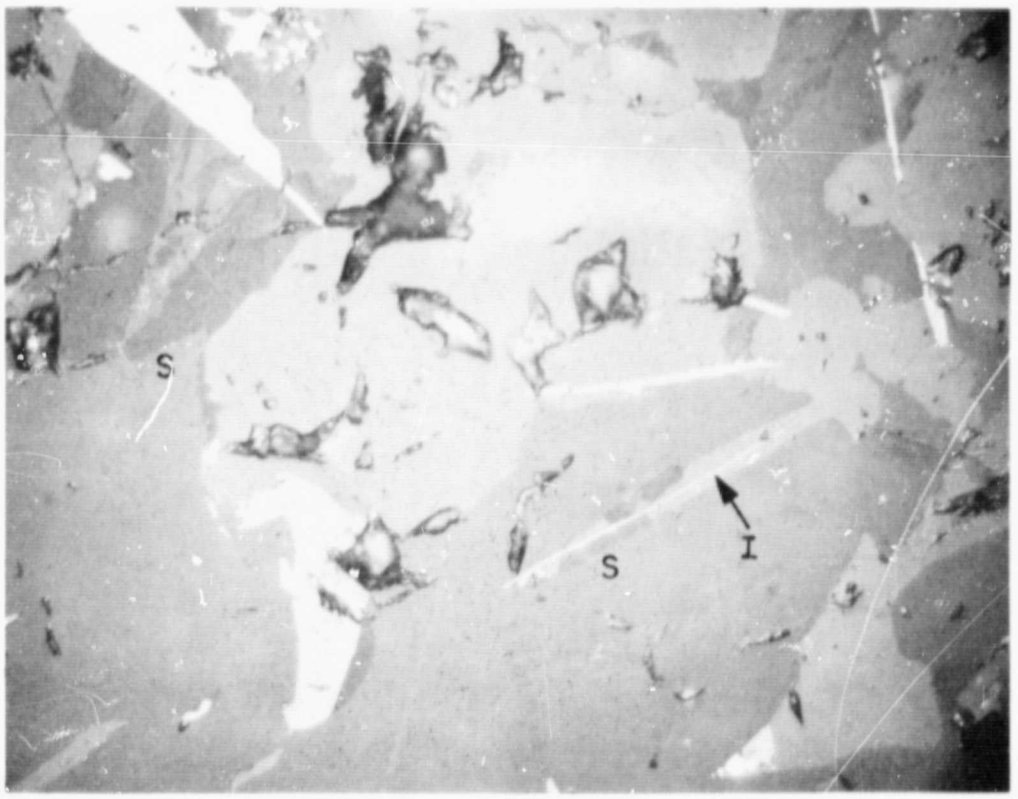



Figure IIB-34. Silica mineral in coarse basalt (18-22), by reflected light. White, ilmenite (flake I appears dark brown in thin section); light gray, calcic feldspar; medium gray, pyroxene; darker gray (S), silica mineral.

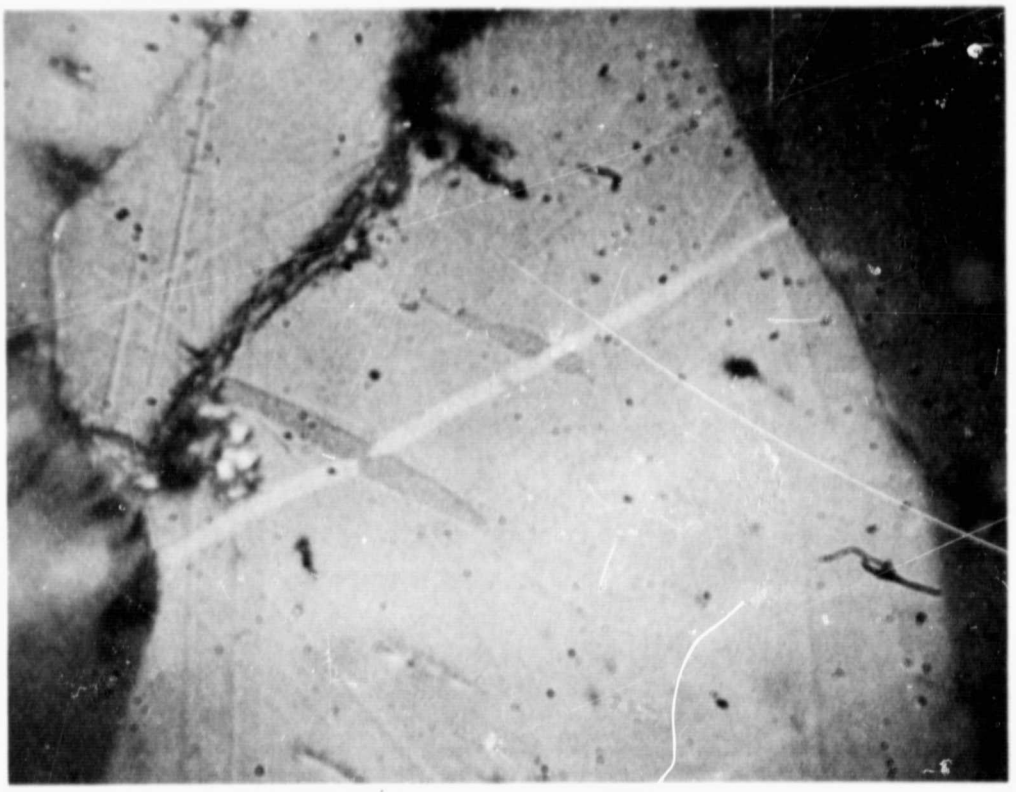



Figure IIB-35. Exsolution lamellae of rutile (light) and chromite (dark) in ilmenite in coarse basalt (8-4). Microprobe analyses of phases appear in Table IIB-V.

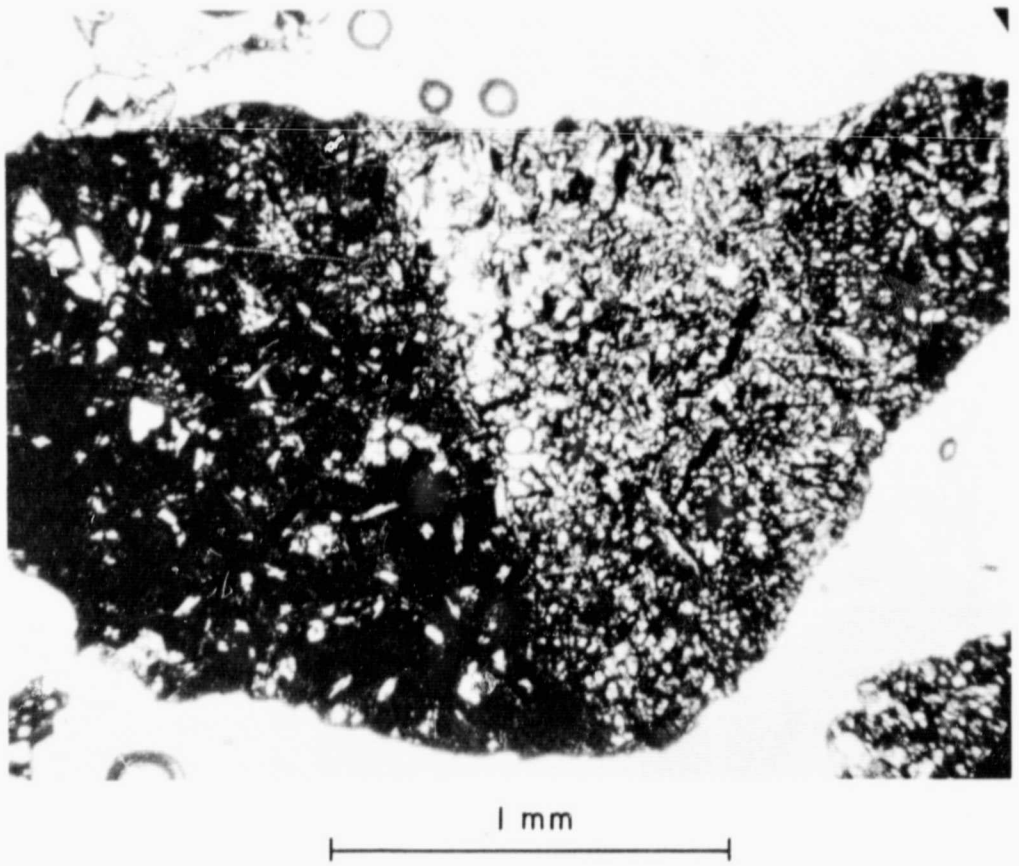



Figure IIB-36. Contact between fine and very fine basalts, in fragment (20-29); possibly the chilled margin of a lunar volcanic flow unit.

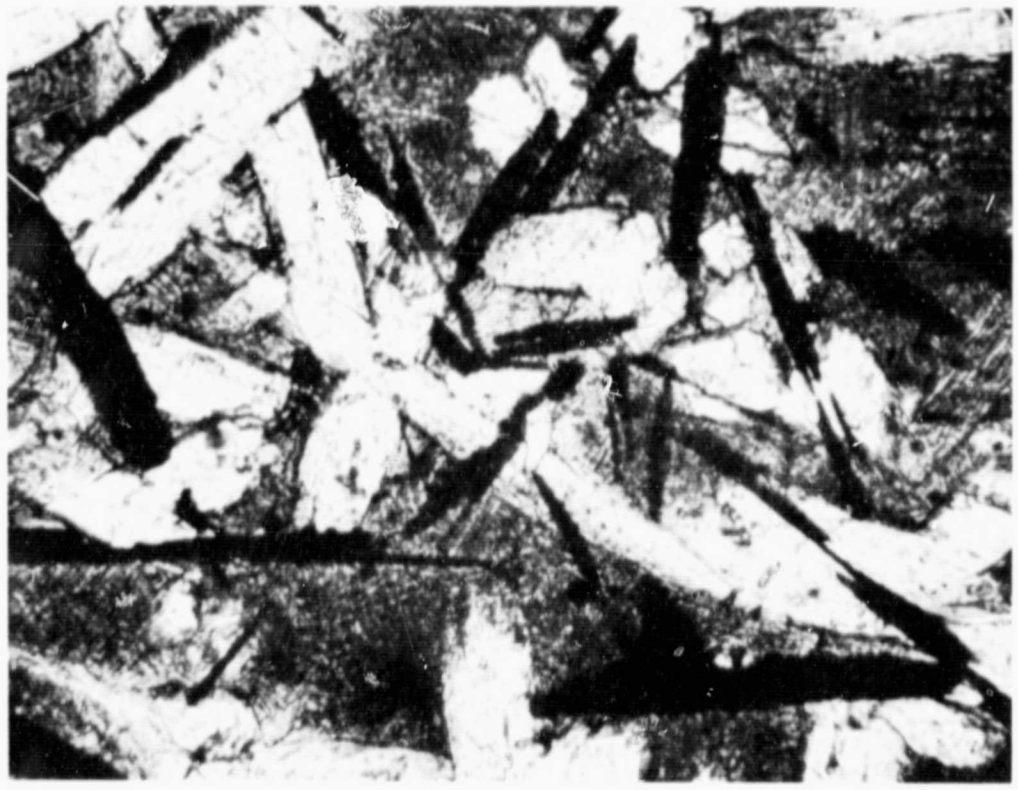



Figure IIB-37. Medium basalt (26-6), showing feldspar laths and ilmenite plates in a glassy groundmass.

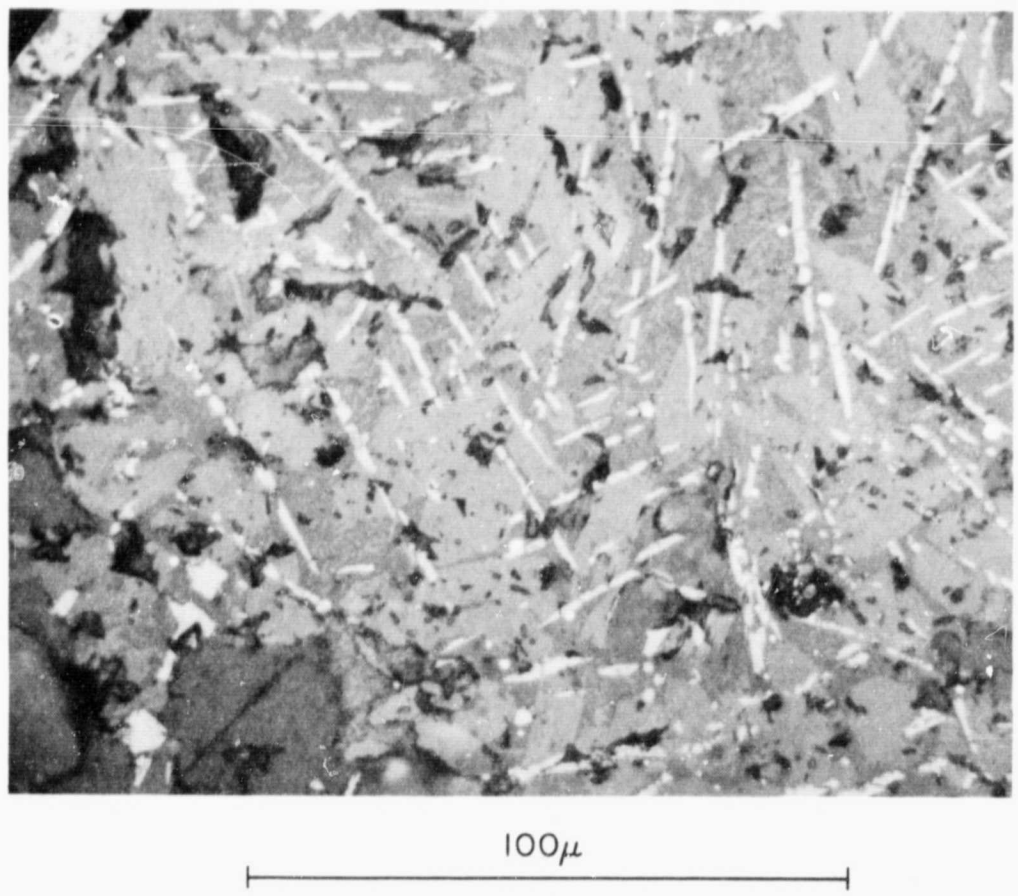



Figure IIB-38. Fine basalt (28-32), showing enigmatic arrangement of ilmenite plates.

## IIC. Anorthositic Rocks

A small proportion (4%) of lithic fragments in the Apollo 11 particulate sample are leucocratic rocks ranging from anorthosites to anorthositic gabbros (Figures IIC-1 and -2). These rocks differ from the dark, Ti-rich basalts in composition, density, and texture. They are Ti-poor and rich in Ca and Al. Their dominant constituent is anorthite, and consequently their densities are less than 2.9 gm/cm$^3$. (Densities measured on three particles were 2.88, 2.88, and 2.84 gm/cm$^3$.) Typically they contain equant, subidiomorphic crystals. Some specimens are ophitic, others are composed of closely interlocking crystals. We have found examples of true anorthosites (plagioclase > 90%), gabbroic anorthosites (77% < plagioclase < 90%), and anorthositic gabbros (plagioclase < 77%). The gabbroic anorthosites are the most common fragments in this group. Most of these fragments have suffered shock metamorphism and display some degree of cataclasis, isotropization, or fusion. The shock features will be reviewed in Section III. The descriptions below are of apparently unshocked specimens.

True anorthosites are rare in the sample. They consist (Figure IIC-3) of tightly packed anorthite polyhedra with less than 2% of other phases. (The accessory phases are minute crystals of olivine and opaque minerals.) The anorthite crystals ($An_{96-98}$) are generally untwinned and homogeneous. These true anorthosites occur as clots within a particular variety of gabbroic anorthosite (Figure IIC-4) that contains small (10μ) olivine crystals ($Fa_{49}$) lying along the contacts between anorthite polyhedra.

The true anorthosite is an adcumulate* formed by accumulation of plagioclase crystals (by settling or, perhaps, flotation). After accumulation the plagioclase crystals continued to grow and, in doing so, expelled all of the mafic, intercumulus liquid.* The associated gabbroic anorthosite is a mesocumulate,* in which some of the intercumulus liquid precipitated as olivine between the growing plagioclase crystals.

Other examples of true anorthosites and gabbroic anorthosites are slightly more confused but reflect similar origins. The feldspar crystals are, typically, blocky subhedra which are both complexly twinned and zoned. In some crystals (Figure IIC-5) the zoning is ocillatory. Olivine and, rarely, clinopyroxene join plagioclase as primary precipitates in some of the gabbroic anorthosites. Analyzed pyroxenes from these rocks (Table IIC-II) (Figures IIB-13, -14, and -15) are magnesian pigeonites with high Al/Ti ratios. Troilite, titaniferous chromite, ilmenite, and kamacite have been found as minor accessories.

The anorthositic gabbros contain subhedral plagioclase, olivine, and clinopyroxene phenocrysts in a mafic groundmass. In some specimens (Figures IIC-6 and -7, Table IIC-III) the mafic intercumulus liquid crystallized as large (up to 1 mm) clinopyroxene crystals, creating an ophitic texture. These gabbros are (or approach) orthocumulates* and, therefore, approach the composition of the contemporaneous magma.

---

*The following terms, defined by Wager, Brown, and Wadsworth (1960), are used here:

Cumulate: an igneous rock formed by crystal accumulation.

Intercumulus liquid: liquid in the interstices between primary precipitate crystals.

Orthocumulate: cumulate consisting of primary precipitate crystals and the crystalline products of the intercumulus liquid.

Adcumulate: cumulate in which the crystalline products of the intercumulus liquid are inconspicuous or absent. The pore space has been filled by adcumulus growth of primary precipitate crystals.

Mesocumulate: cumulate containing a small amount of interstitial material – i.e., intermediate between orthocumulate and adcumulate.

The anorthosite and anorthositic gabbro fragments are products of fractional crystallization under plutonic, hypabyssal, or stagnant volcanic conditions. By terrestrial standards they are fine-grained rocks, but this may have been caused more by the absence of volatiles than by rapid cooling. There is no close genetic relationship between these rocks and the more common, Ti-rich basalts. If they are consanguinous – that is, if the basalts are residual liquids from differentiated magmas from which the anorthosites and anorthositic gabbros were early differentiates – a variety of intermediate compositions, representing intermediate liquids between the original magma and the residual basalt, should be present in the intercumulus materials. We have yet to find such intermediate compositions. In particular, the intercumulus materials are much less titaniferous than the basalts.

These lunar anorthosites are more calcic than any terrestrial anorthosites. This is another manifestation of the low alkali content of the Apollo 11 sample. It is worth noting that of the two types of terrestrial anorthosites (Buddington, 1939), the Adirondack type and the stratiform type, the latter are the more calcic and have textures of a more certainly accumulative origin. These stratiform anorthosites occur as layers in the differentiated plutons such as the Bushveld and Stillwater igneous complexes. The Adirondack type anorthosites occur as domical massifs in high grade metamorphic terranes, and although they may have originated as cumulates their textures are no longer easily recognizable as cumulative. On compositional as well as textural grounds, therefore, these lunar anorthosites and gabbros are more closely related to the stratiform-type anorthosites.

Table IIC-I. Bulk compositions of anorthositic particles.

| | Weight Percent | | | Atomic Percent | | | C. I. P. W. Norm | |
|---|---|---|---|---|---|---|---|---|
| | a | b | | a | b | | a | b |
| $SiO_2$ | 46.0 | 45.4 | Si | 16.2 | 15.9 | Qz | 0.00 | 0.71 |
| $TiO_2$ | 0.3 | * | Ti | 0.07 | * | Co | 1.24 | 1.29 |
| $Al_2O_3$ | 27.3 | 33.8 | Al | 11.3 | 14.0 | Or | 0.24 | 0.06 |
| $Cr_2O_3$ | 0.2 | * | Cr | 0.05 | * | Plag | 71.75 | 90.07 |
| FeO | 6.2 | 2.8 | Fe | 1.8 | 0.84 | Opx | 22.36 | 9.56 |
| MnO | 0.1 | 0.1 | Mn | 0.03 | 0.3 | OL | 5.94 | 0.00 |
| MgO | 7.9 | 1.7 | Mg | 4.1 | 0.90 | Cr | 0.25 | 0.06 |
| CaO | 14.1 | 17.5 | Ca | 5.31 | 6.60 | Ilm | 0.53 | 0.06 |
| $Na_2O$ | 0.3 | 0.4 | Na | 0.2 | 0.2 | Rest | 0.16 | 0.00 |
| $K_2O$ | * | * | K | * | * | | | |
| NiO | * | 0.0 | Ni | * | 0.0 | | | |
| $SO_3$ | 0.1 | 0.0 | S | 0.02 | 0.0 | | | |
| | | | O | 60.92 | 61.42 | | | |
| Sum | 102.5 | 101.7 | | 100.00 | 100.16 | | 102.46 | 101.79 |

Key

a. Anorthositic gabbro (9-8). Average of 10 defocussed beam analyses.

b. Anorthosite-gabbroic anorthosite (37-1). Average of seven defocussed beam analyses.

* Detected.

Table IIC-II. Compositions of minerals in anorthositic particles.

| | a | b | c | d | e | f | g | h | i | j | k |
|---|---|---|---|---|---|---|---|---|---|---|---|
| Si | 16.3 | 20.7 | 0.1 | 0.5 | 0.3 | 0.1 | * | 21.3 | 24.3 | 25.9 | 22.0 |
| Ti | 0.0 | 0.0 | 4.3 | 0.0 | 0.0 | 0.0 | 32.7 | * | 0.4 | 0.9 | 0.4 |
| Al | 0.1 | 19.5 | 5.7 | 1.4 | 0.1 | 0.1 | 0.1 | 18.7 | 0.4 | 0.6 | 6.0 |
| Cr | 0.0 | 0.0 | 30.3 | 0.6 | 0.0 | 0.1 | 0.2 | 0.0 | 0.2 | 0.6 | 0.4 |
| Fe | 31.2 | 0.2 | 28.9 | 62.6 | 63.5 | 93.1 | 29.5 | 0.1 | 13.4 | 11.3 | 9.7 |
| Mn | 0.3 | 0.0 | 0.4 | 0.0 | 0.0 | 0.0 | 0.3 | 0.0 | 0.3 | 0.2 | 0.2 |
| Mg | 14.5 | 0.1 | 1.2 | 0.2 | 0.1 | 0.2 | 3.6 | 0.1 | 14.0 | 15.3 | 11.8 |
| Ca | 0.2 | 13.8 | 0.3 | 0.4 | 0.1 | 0.1 | * | 12.6 | 2.6 | 1.5 | 5.2 |
| Na | 0.0 | 0.2 | 0.1 | 0.0 | 0.8 | 0.3 | 0.0 | 0.9 | 0.0 | 0.0 | 0.1 |
| K | 0.0 | 0.0 | 0.0 | 0.0 | 0.0 | 0.0 | 0.0 | 0.2 | 0.0 | – | – |
| Ni | 0.0 | 0.0 | 0.0 | 0.0 | 0.0 | 5.9 | 0.0 | 0.0 | 0.0 | – | – |
| S | 0.0 | 0.0 | 0.0 | 32.5 | 33.7 | 0.0 | 0.0 | 0.0 | – | – | – |
| O | 37.2 | 46.5 | 31.4 | 0.0 | 0.0 | 0.0 | 32.9 | 46.4 | 42.6 | 45.5 | 43.9 |
| Sum | 99.8 | 101.0 | 102.7 | 98.2 | 98.6 | 99.9 | 99.3 | 100.3 | 98.2 | 101.8 | 99.7 |

Key

a. Olivine ($Fo_{51}$) in gabbroic anorthosite (37-1).
b. Plagioclase ($An_{98}$) in gabbroic anorthosite (37-1).
c. Ti-rich chromite in gabbroic anorthosite (37-1).
d. Troilite in gabbroic anorthosite (37-1).
e. Troilite in gabbroic anorthosite (37-2).
f. Kamacite in gabbroic anorthosite (37-2).
g. Ilmenite in gabbroic anorthosite (37-2).
h. Plagioclase ($An_{90}$) in gabbroic anorthosite (37-2). (Average of 11 analyses.)
i. Interstitial pigeonite in gabbroic anorthosite (19-1).
j. Interstitial pigeonite in gabbroic anorthosite (9-29).
k. Sub-calcic augite lath in subophitic anorthositic gabbro (9-8).
* Detected.

Table IIC-III. Compositions of minerals in anorthositic gabbro (38-1).

| | a | b | c | d | e | f |
|---|---|---|---|---|---|---|
| Si | 16.8 | 17.9 | 20.6 | 25.0 | 0.1 | 0.1 |
| Ti | 0.0 | * | 0.0 | 0.5 | 0.0 | 0.0 |
| Al | * | * | 19.6 | 0.5 | 0.1 | 0.1 |
| Fe | 19.3 | 20.8 | 0.1 | 12.7 | 62.4 | 67.2 |
| Mn | 0.2 | 0.2 | 0.0 | 0.2 | 0.0 | 0.0 |
| Mg | 23.1 | 21.0 | 0.1 | 14.4 | 0.1 | 0.2 |
| Ca | 0.1 | 0.3 | 13.6 | 3.1 | 0.4 | 0.2 |
| Na | 0.3 | * | 0.3 | 0.1 | 0.4 | 0.3 |
| K | * | 0.0 | * | 0.0 | 0.0 | 0.0 |
| Ni | 0.0 | * | * | * | 0.1 | 28.6 |
| S | * | * | 0.0 | 0.0 | 34.4 | 0.1 |
| O | 40.2 | 40.5 | 46.6 | 43.8 | ** | ** |
| Total | 100.0 | 100.7 | 100.9 | 100.3 | 98.0 | 96.8 |

Key

a. Olivine ($Fa_{27}$) inclusion within cumulus plagioclase crystal (Fig. IIC-8) of anorthositic gabbro (38-1).

b. Cumulus olivine ($Fa_{30}$) crystal in anorthositic gabbro (38-1). (Figs. IIC-6, IIC-7).

c. Cumulus plagioclase ($An_{96}$) crystal in anorthositic gabbro (38-1) (Fig. IIC-8). Host to olivine of analysis a.

d. Groundmass (intercumulus) pigeonite of anorthositic gabbro (38-1) (Figs. IIC-6, IIC-7).

e. Accessory troilite in anorthositic gabbro (38-1).

f. Accessory taenite occurring with troilite in anorthositic gabbro (38-1).

* Detected.

** Oxygen assumed to be absent.



Figure IIC-1. Fragments of lunar anorthositic rock, showing characteristic light color. Millimeter scale.

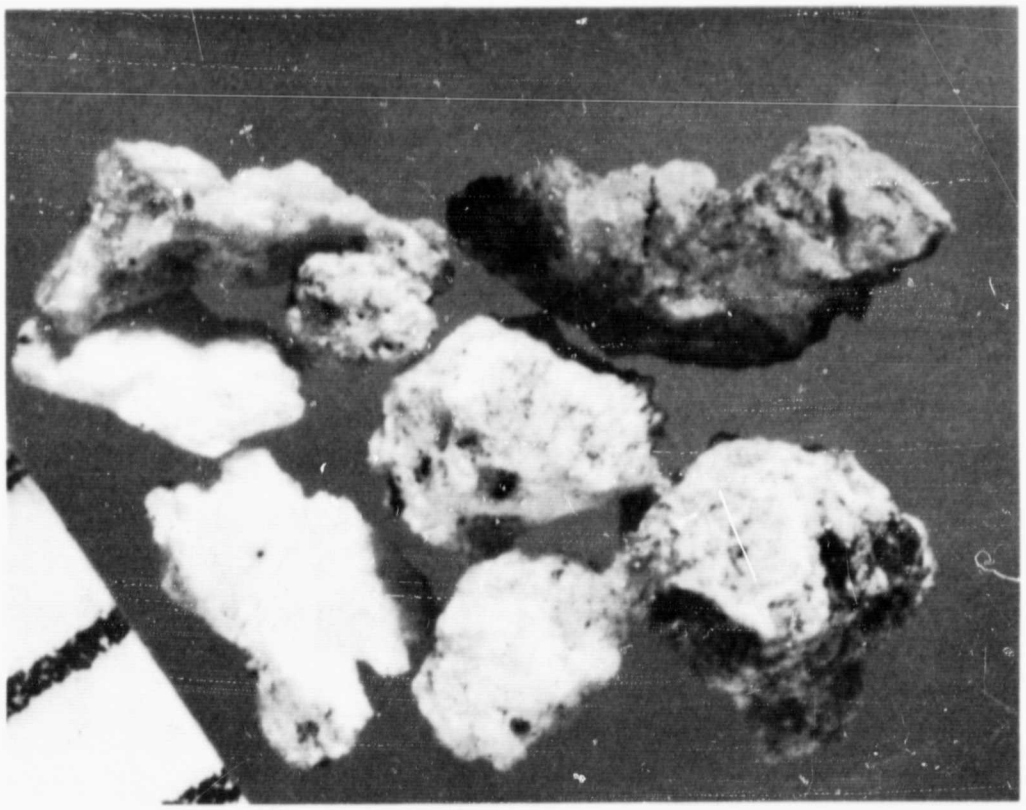


Figure IIC-2. Anorthositic fragments, some displaying characteristic chalky appearance of highly shocked material. Millimeter scale.

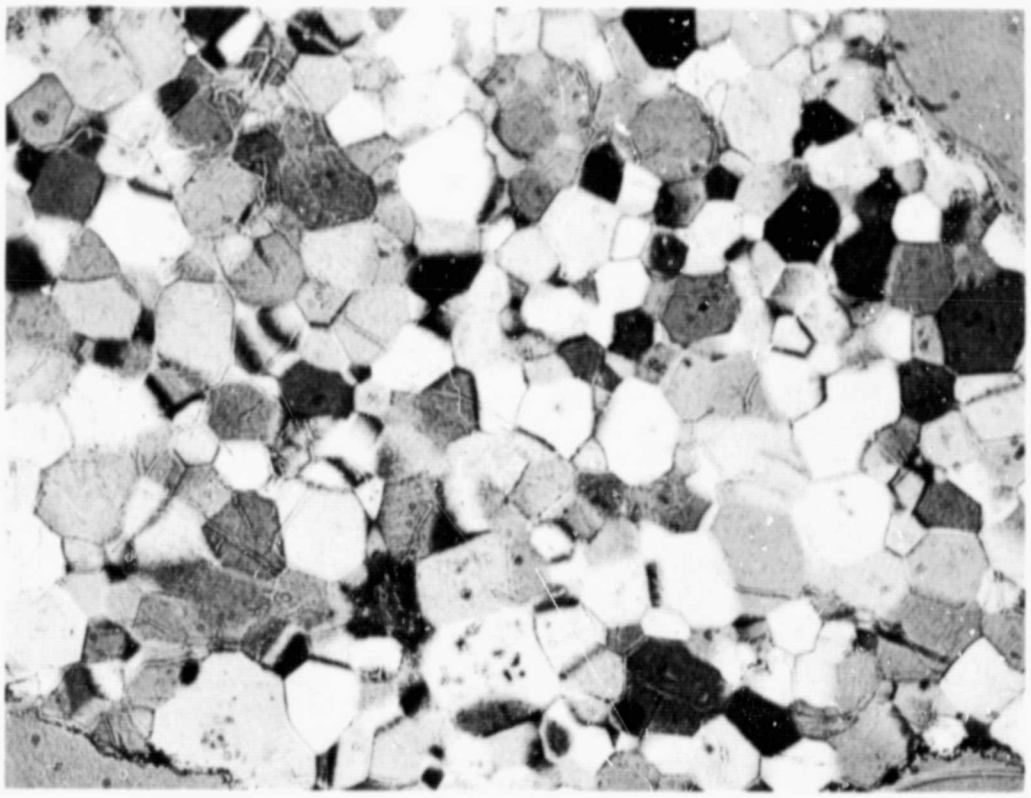



Figure IIC-3. Anorthosite (37-1) composed almost entirely of polygonal crystals of anorthite. Oblique nicols.

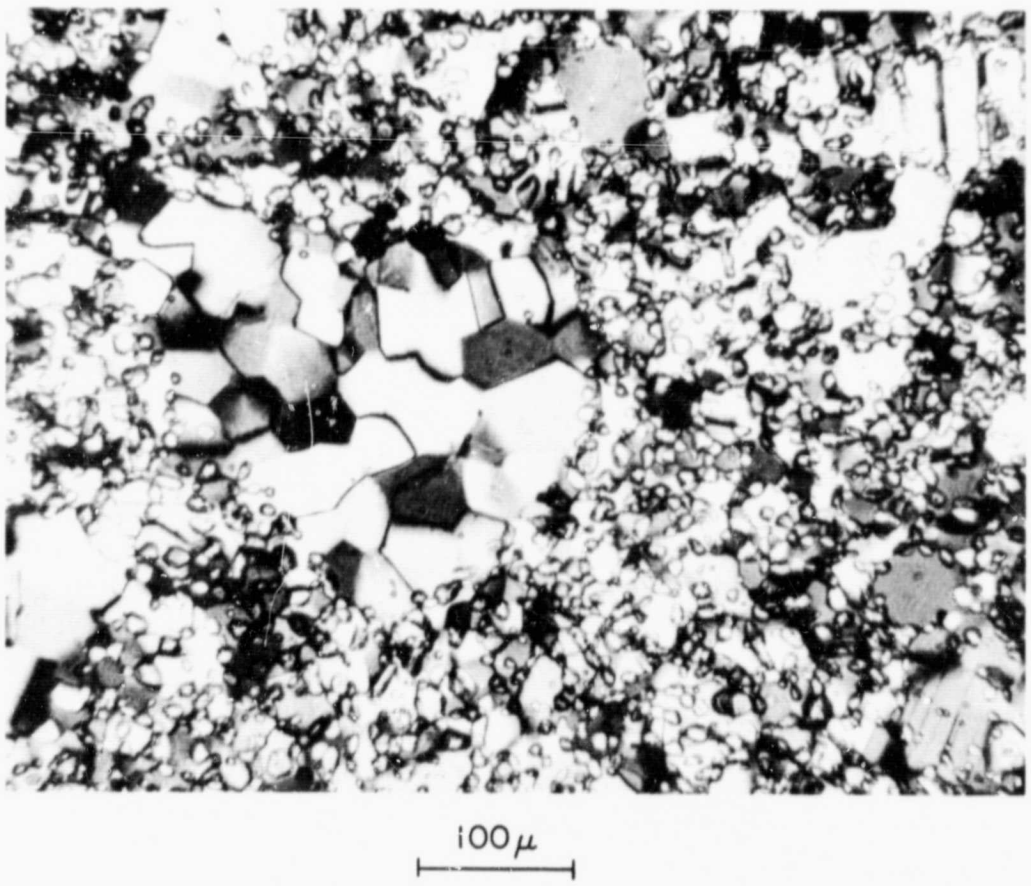



Figure IIC-4. Gabbroic anorthosite(37-2) composed of idiomorphic olivine crystals lying in a closely packed matrix of anorthite polyhedra. Note that the olivines tend to outline the anorthite crystals. Oblique nicols.

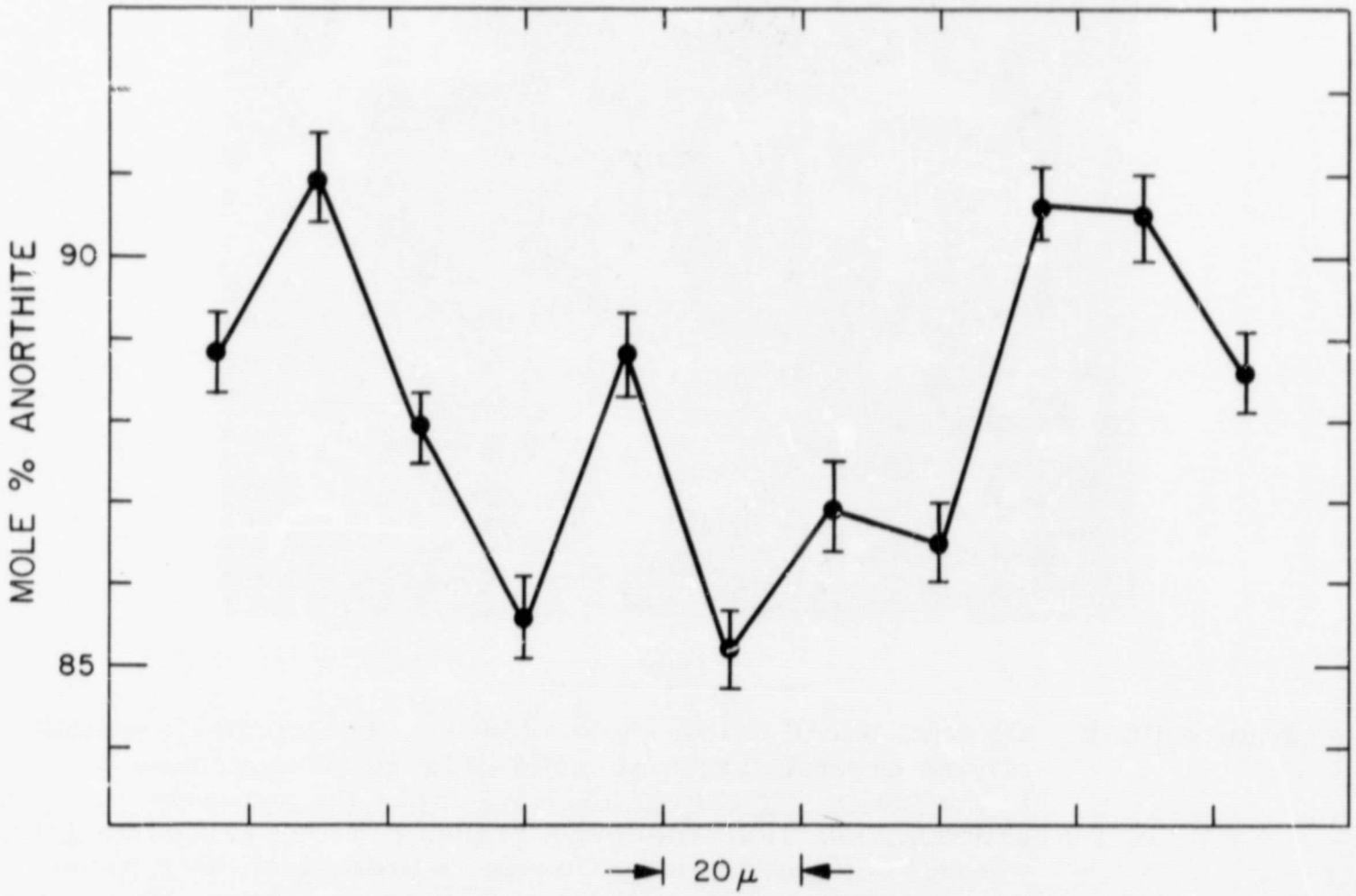



Figure IIC-5. Variation of anorthite content across a zoned plagioclase crystal in a gabbroic anorthosite (37-2). Analyses by electron microprobe.

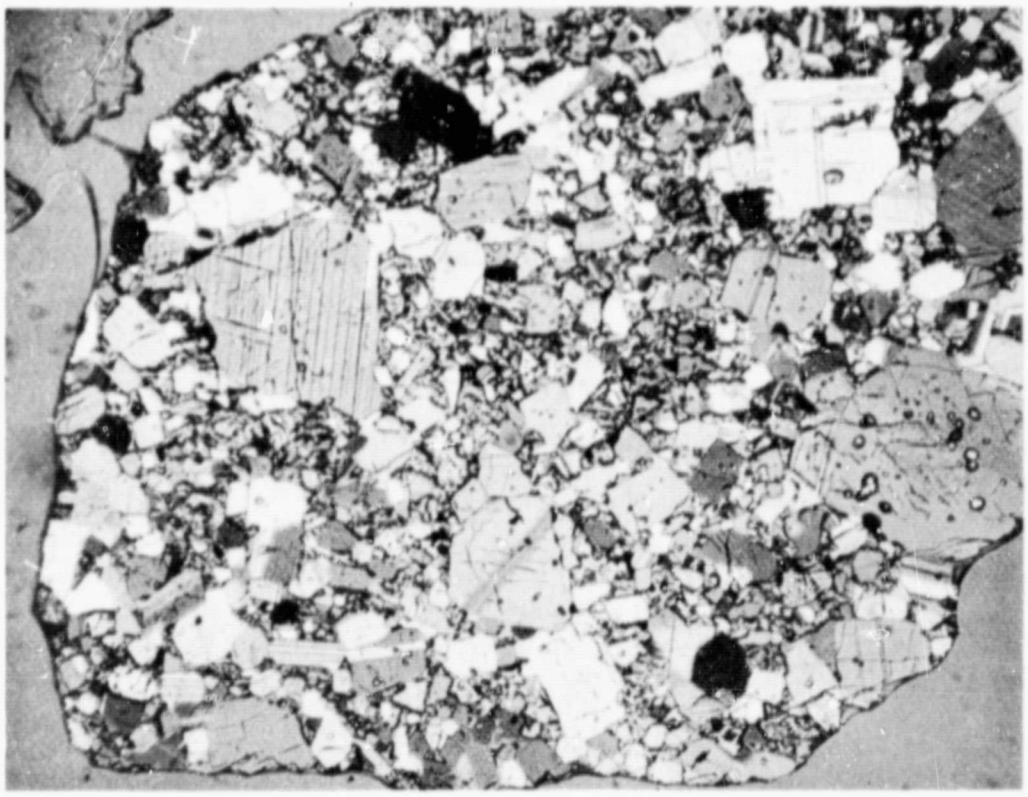



Figure IIC-6. Ophitic, anorthositic gabbro (38-1). The plagioclase and olivine crystals are embedded in large clinopyroxenes. In the lower left corner the rock lacks the pyroxene groundmass. The specimen grades from an orthocumulate, where the groundmass pyroxene is prominent, to a mesocumulate where the pyroxene is inconspicuous. The subidiomorphic plagioclases and olivine have undergone little adcumulus growth. Oblique nicols.

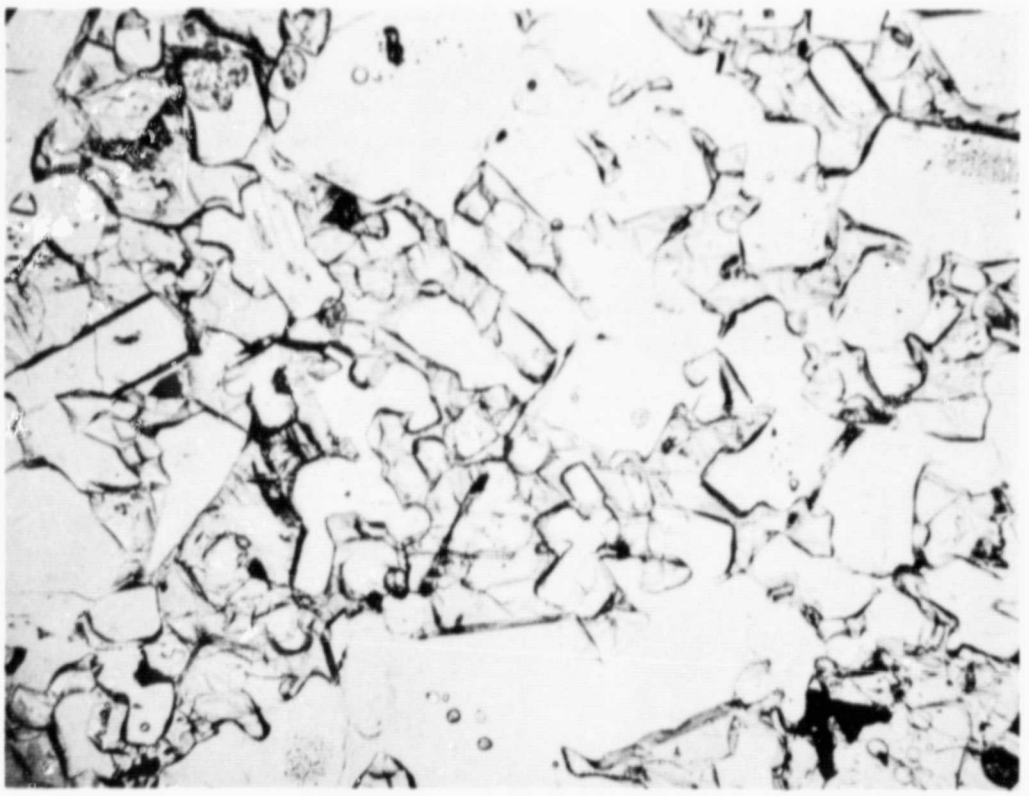



Figure IIC-7. Detailed relationships in the ophitic, anorthositic gabbro (38-1). The plagioclase and olivine crystals (low relief) lie in a matrix of optically continuous clinopyroxene (high relief). Unpolarized light.

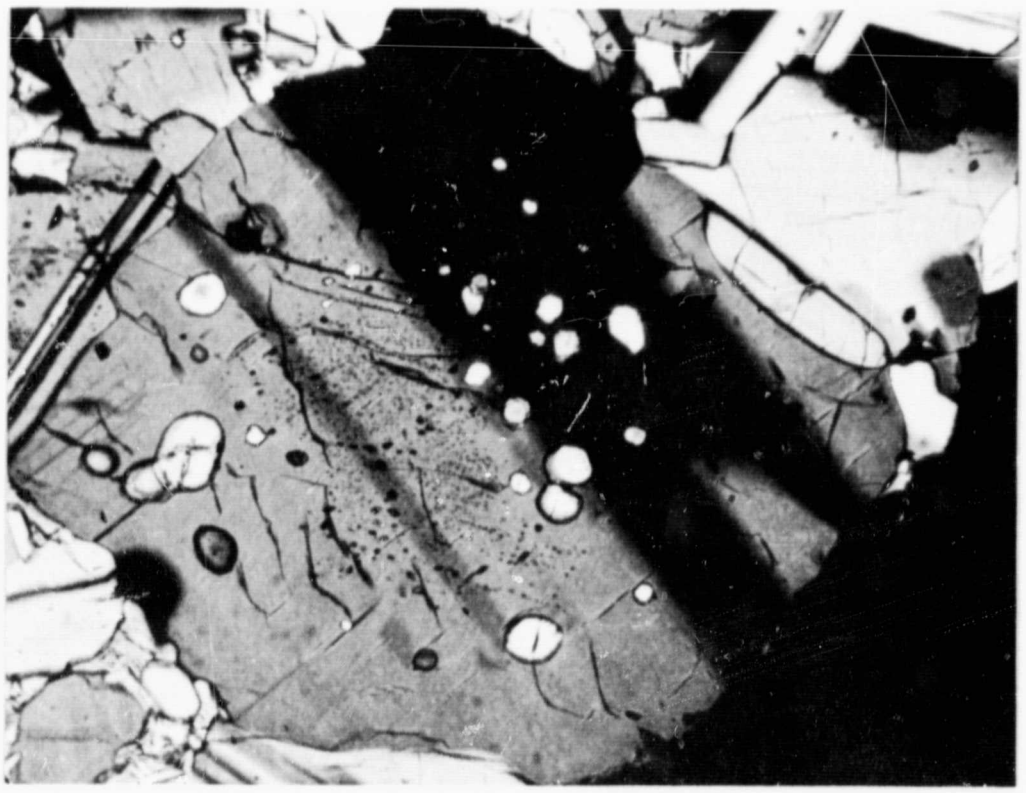



Figure IIC-8. Olivine crystals included within a plagioclase phenocryst in an anorthositic gabbro (38-1). Crossed nicols.

## IID. Glasses

As initially reported by LSPET (1969a, b) and verified in our study (Section IIA), the most abundant phase in the lunar "fines" is glass. Some originated as primary igneous glass: as noted in Section IIB, glass occasionally occurs in small amounts in the otherwise crystalline medium- and fine-grained basalts. This glass is dirty brown in color, commonly contains minute crystallites, and occurs as a matrix, interstitial to euhedral feldspar crystals (Figure IIB-37). Glass occurrences of this sort, resulting from quenching of a mush of crystallized minerals and late-stage residual melt, are not uncommon in terrestrial lavas. The great majority of glass particles in the lunar soil sample, however, are undoubtedly of impact origin. (One can argue that they might just as well be of volcanic origin, pyroclastic ejecta particles. But the ubiquitous evidence of severe shock effects in the lunar material, and especially the not uncommon occurrences of partly vitrified soil breccias where the vitrification obviously took place in situ, make it clear that impact melting is by far the more likely explanation. LSPET (1969b) has also pointed out that the inhomogeneity of many of the glass particles is a feature not generally observed in terrestrial volcanic glasses. We know from both observation and astronomical considerations that hypervelocity impact is a continuing process on the lunar surface; lunar vulcanism, especially in latter aeons, is at best conjectural.) The present section will be wholly concerned with these secondary impact glasses.

### Morphology

The most striking aspect of the lunar glasses is the wide variety of form, color, optical properties, and chemistry that they display. The glass fragments range in shape from sharply angular to scoriaceous (Figure IID-1 and -2) to nearly perfectly spherical (Figure IID-3), and in size from > 2 mm to less than 1μ. Many of the larger fragments have highly irregular, branching shapes and contain abundant vesicles (Figure IID-2). All of the soil breccias contain glasses, frequently of several varieties. The fine matrices of the soil breccias consist largely of tiny glass particles, and fragments

and spherules of glass are embedded in the breccias along with mineral and rock fragments. In addition, irregular swirls and veinlets of glass, evidently formed in situ or introduced along fractures (see Figures IIA-4 and -5), are visible in some cases. Many of the lithic fragments in the soil sample are partly coated with spatters of glassy material. Although most soil breccia fragments contain a heterogeneous aggregation of constituents, two fragments were noted in which some 90% of the identifiable particles consist of orange glass of uniform color (Plate 2, F; Figure IIA-7).

Many of the lunar glasses are very homogeneous in color and clarity (Figure IID-3), while others are heterogeneous, some to a remarkable degree. The latter often show swirls of alternating dark and light color (Figures IIA-5, IID-4) and/or abundant vesicles. Commonly, angular to sub-round fragments of silicate crystals and of the mare basalts and soil breccias are present as inclusions in heterogeneous glasses (Figures IIA-8, IID-2 and -5). Some of the larger glass fragments contain minute acicular crystallites of birefringent and/or opaque minerals, presumably the result of devitrification (Figure IID-6). Occasionally these acicular crystals, commonly arranged in divergent patterns, reach sizes of 20μ or more in width and some 200μ in length (Figure IID-7). Crystals of such size are probably too large to be devitrification products and may have resulted from partial crystallization from the molten state during very rapid cooling rather than from diffusion in the solid state. In one fragment two stages of liquid immiscibility are displayed in a droplet of Fe metal and troilite contained in a silicate matrix of tiny crystallites and glass (Figures IID-6 and -8). The spherical form of the opaque droplet reflects immiscibility between silicate and Fe-plus-sulfide liquids; inside it, sub-droplets of Fe metal in the sulfide (and vice versa) reflect immiscibility between metal and sulfide liquids.

A few intriguing lithic fragments were observed to consist of pyroxene, plagioclase and ilmenite crystal fragments suspended in heterogeneous swirly glass (Figure IID-9). Virtually all the crystals are rounded, many to a high degree. Flow lines are distinctly visible in the glassy matrix,

commonly following the contours of the suspended crystal fragments. This curious texture strongly suggests partial fusion of an otherwise typical lunar basalt.

The wide range of glass colors reported by LSPET (1969a, b) was verified in our study. In 30μ sections, glasses of all shades of brown, reddish-brown, orange, yellow, and pale green are visible; macroscopically, these colored glasses usually appear to be black and opaque (Plate 1). Colorless glasses are also present in the thin sections. Macroscopically, most of these have a pale green color, not unlike forsterite.

As would be expected from the color variability, a wide range of refractive index was observed in the glasses. In this study we measured indices ranging from 1.490 to 1.750. LSPET (1969a) reported the range ~1.6 to 1.8.

Chemistry

Microprobe analyses of more than 75 glass particles revealed a wide range in chemical composition. Table IID-I lists a few of these analyses, to give an indication of the range and to illustrate typical and unusual compositions. In general, it can be said that both Al and Ca content of the glasses decrease with increasing content of Fe and Ti. Mg and heavier metals such as Cr and Mn appear to follow Fe and Ti in this trend and Si to follow Al and Ca, although this latter relationship is not so clearly defined. There is a clear correlation between refractive index and Fe content (Figure IID-11). A similar correlation exists between Ti content and refractive index (Figure IID-12), but Fe probably exerts the greater influence on refractive index, since it is more abundant in the glasses than Ti.

Figure IID-13 illustrates the relationship between Ti and Al abundances, and color. The glasses plotted in this diagram were classified by the Munsell (1966) color system, according to their appearance by transmitted light in 30μ sections. In general, the more highly-colored glasses (mainly

shades of red-orange-yellow) are rich in Fe, Mg and Ti. The colorless glasses tend to be deficient in these elements and relatively rich in Al and Ca (Figure IID-13 and Table IID-I).

Formation of the Glasses

C. I. P. W. norms calculated from the analyses of Table IID-I are listed in Table IID-II. From these, it can be seen that the chemical trends described above can also be couched in terms of relative amounts of plagioclase feldspar vs. mafic minerals (clinopyroxene, olivine, and ilmenite). One is tempted to conclude that the observed range of glasses is due to the incorporation in melted ejecta droplets of variable proportions of the minerals that comprised the target rock struck by cratering impacts. Thus if the target rock was a coarse gabbro, we might picture an occasional impact-vitrified droplet as having been derived almost entirely from one of the plagioclase crystals in the gabbro. This droplet would now be a feldspathic glass. Highly mafic droplets would also be produced. The trouble is, this mechanism predicts a continuous distribution of glass compositions between feldspathic and mafic extremes, corresponding to cases where target feldspar and target mafic minerals were incorporated in various proportions; and the distribution of lunar compositions is not continuous but bimodal (Figure IID-13). This makes it appear that the compositional range is not a "memory" of the mineralogical range in a single parent target rock (basalt/gabbro), but that two different parent rock types were involved.

Compositions of colored glasses in the main cluster of Figure IID-13 are very similar to compositions of the two most abundant materials found at the Apollo 11 site, lunar basalt and soil breccia (Table IID-III), and it seems clear that the colored glasses are formed by impact melting of these materials. In order to confirm that glasses produced in this manner would resemble the lunar glasses in color, we melted very small samples of lunar soil and basalt in a resistence-heated tungsten boat, in a bell jar vacuum. The glasses produced (Figure IID-10) were thin sectioned. The product of the basalt run was a clear, homogeneous yellow-orange glass of Munsell

code 7.5 YR, 7/12, the most common shade observed among the lunar yellow glasses. The product of the soil run was an inhomogeneous swirly yellow-orange glass (Munsell code 7.5 YR, 6/12) containing numerous vesicles and small (50μ) rounded silicate crystal fragments (Figure IIA-9). Inhomogeneities in the latter case were more likely due to a less vigorous heating of the charge than to any fundamental difference between basaltic and breccia starting materials. In both cases, the colors were perfect matches to lunar glasses.

Compositions of colorless glasses in the secondary cluster of Figure IID-13 are similar to compositions of the anorthositic rock fragments described in Section IIC (Table IIC-I). It is reasonable to suppose that the former are shock-vitrified forms of the latter.

Table IID-I. Compositions of representative lunar glasses. The analyses also demonstrate the range for most elements.

| | A | B | C | D | E | F | G | H | I | J | K | L |
|---|---|---|---|---|---|---|---|---|---|---|---|---|
| Si | 24.3 | 21.5 | 21.2 | 21.6 | 21.7 | 23.1 | 20.2 | 16.7 | 21.2 | 19.7 | 17.4 | 17.2 |
| Ti | 0.1 | – | – | 0.8 | 0.2 | 1.2 | 4.1 | 3.3 | 3.2 | 5.2 | 5.7 | 5.8 |
| Al | 17.1 | 18.7 | 18.8 | 12.5 | 13.2 | 9.1 | 7.0 | 10.5 | 5.5 | 6.0 | 3.3 | 3.0 |
| Cr | – | – | – | 0.1 | 0.1 | 0.2 | 0.3 | 0.1 | 0.4 | 0.3 | 0.4 | 0.5 |
| Fe[1] | – | – | – | 5.3 | 4.3 | 8.6 | 11.6 | 11.5 | 12.2 | 13.5 | 18.2 | 18.0 |
| Mn | – | – | – | 0.1 | – | 0.1 | 0.2 | 0.2 | 0.2 | 0.2 | 0.3 | 0.3 |
| Mg | 0.1 | 0.1 | 0.1 | 4.4 | 4.7 | 5.8 | 4.6 | 6.3 | 7.0 | 4.3 | 8.7 | 8.5 |
| Ca | 9.2 | 12.9 | 13.9 | 9.7 | 10.5 | 7.0 | 8.3 | 9.9 | 6.7 | 7.6 | 5.1 | 5.2 |
| Na | 2.1 | 0.9 | 0.5 | 0.4 | 0.1 | 0.2 | 0.4 | – | 0.1 | 0.5 | 0.2 | 0.4 |
| K | 0.8 | – | – | 0.1 | – | 0.2 | 0.1 | – | – | 0.2 | – | 0.1 |
| Ni | – | – | – | – | – | – | – | – | – | – | – | – |
| S | – | – | – | 0.1 | – | – | 0.1 | – | 0.3 | 0.2 | – | – |
| O[2] | 47.6 | 46.7 | 46.4 | 45.0 | 45.2 | 44.6 | 42.2 | 42.3 | 42.5 | 41.7 | 39.9 | 39.8 |
| Total | 101.3 | 100.8 | 100.9 | 100.1 | 100.0 | 100.1 | 99.1 | 100.8 | 99.3 | 99.4 | 99.2 | 98.8 |
| R.I.[3] | 1.562 | 1.568 | | | 1.593 | 1.620 | | | 1.661 | | 1.740 | |
| hue[4] | | | 7.5YR | 5YR | | | 7.5YR | 10YR | | 7.5YR | | 10YR |
| value/chroma[4] | | | 9/2 | 2/4 | | | 7/10 | 8/8 | | 7/12 | | 8/12 |
| general color | colorless | colorless | colorless | dark brown | | | orange-yellow | yellow | | orange-yellow | | yellow |

[1] All Fe is assumed to be in the +2 state.

[2] Oxygen calculated by stoichiometry; see note 1.

[3] Refractive Index; uncertainty is ± 0.001.

[4] Hue, value and chroma are color designations according to the scheme presented in the Munsell Book of Color, Munsell Color Company, Inc., Baltimore, Md. Estimates were made in thin sections of standard thickness (30μ).

– Means concentration level less than twice the total estimated uncertainty, generally < 0.04 wt. %.

Key

A. Calcic feldspar glass; see Figure IID-11.

B. Calcic feldspar glass, with less Na; see Figure IID-11.

C. Calcic feldspar glass, with even less Na; see Figure IID-13 (2-26).

D. Dark brown, inhomogeneous glass; see Figure IID-13 (2-11).

E. Glass with feldspar-rich composition and appreciable ferro-magnesian component; see Figure IID-11.

F. Typical glass with feldspar plus ferro-magnesian composition and appreciable Ti; see Figure IID-11.

G. Clear orange-yellow glass; see Figure IID-13 (2-10).

H. Clear yellow glass spherule; see Figure IID-13 (2-30).

I. Glass with high ferro-magnesian content and high Ti; see Figure IID-11.

J. Clear orange-yellow glass with large silicate mineral inclusions; see Figure IID-13 (2-8).

K. Glass with high ferro-magnesian and Ti contents; see Figure IID-11.

L. Clear yellow glass with high Ti content; see Figure IID-13 (2-28).

Table IID-II. C. I. P. W. norms calculated for the analyses in Table IID-I.

| | A | B | C | D | E | F | G | H | I | J | K | L |
|---|---|---|---|---|---|---|---|---|---|---|---|---|
| Quartz[1] | 4.74 | 0.13 | 1.43 | – | – | 4.77 | 2.24 | – | 2.57 | 3.07 | – | – |
| Corundum[1] | 3.48 | 0.58 | 0.68 | – | – | – | – | – | – | – | - | – |
| Orthoclase | 5.79 | 0.06 | 0.24 | 0.47 | 0.24 | 1.71 | 0.89 | – | 0.24 | 1.48 | 0.30 | 0.47 |
| Albite | 22.67 | 10.00 | 5.10 | 3.02 | 0.76 | 1.78 | 2.09 | – | – | 2.27 | 1.73 | 3.92 |
| Anorthite | 64.00 | 89.50 | 92.23 | 62.61 | 67.48 | 45.32 | 34.36 | 54.22 | 28.42 | 28.78 | 16.04 | 13.21 |
| Diopside (Wo) | – | – | – | 2.03 | 2.32 | 1.48 | 9.75 | | 7.52 | 9.98 | 8.13 | 9.61 |
| Diopside (En) | – | – | – | 1.22 | 1.45 | 0.83 | 5.05 | | 4.25 | 4.84 | 4.46 | 5.22 |
| Diopside (Fs) | – | – | – | 0.71 | 0.73 | 0.59 | 4.43 | | 2.96 | 4.97 | 3.38 | 4.05 |
| Enstatite | 0.27 | 0.45 | 0.47 | 16.62 | 16.21 | 23.00 | 14.00 | | 24.62 | 12.96 | 11.71 | 8.49 |
| Ferrosilite | – | 0.05 | 0.11 | 9.68 | 8.20 | 16.46 | 12.27 | | 17.17 | 13.31 | 8.89 | 6.60 |
| Forsterite | – | – | – | 0.35 | 1.22 | – | – | 18.15 | – | – | 13.96 | 14.86 |
| Fayalite | – | – | – | 0.22 | 0.68 | – | – | 14.57 | – | – | 11.68 | 12.72 |
| Chromite | – | – | 0.06 | 0.24 | 0.25 | 0.37 | 0.53 | 0.24 | 0.80 | 0.54 | 0.94 | 1.10 |
| Ilmenite | 0.15 | 0.13 | – | 2.45 | 0.57 | 3.86 | 12.86 | 10.37 | 9.97 | 16.50 | 17.93 | 18.35 |
| Residues[2] | 0.23 | – | – | 0.37 | 0.16 | 0.16 | 0.60 | (3.29) | 0.83 | 0.85 | 0.04 | 0.11 |
| Total | 101.35 | 100.92 | 100.33 | 99.99 | 100.26 | 100.34 | 99.06 | 100.84 | 99.35 | 99.57 | 99.19 | 98.71 |
| R.I. | 1.562 | 1.568 | | | 1.593 | 1.620 | | | 1.661 | | 1.740 | |

[1] Quartz and corundum in norms of feldspar-rich analyses probably result from alkali loss (principally Na). Normative quartz by itself (without corundum) does not result from this artifact. In the case of these glasses some alkali loss may have occurred at the time the glass was formed.

[2] Residues include any S allotted to thenardite ($Na_2SO_4$). Residue for analysis H is entirely larnite, $Ca_2SiO_4$; the analysis for Si may be somewhat low and/or Ca, somewhat high.

Table IID-III. Defocussed beam analyses on medium-grained dark basalt (B), soil breccia (C), and gabbroic anorthosite (D) compared to typical yellow (A) and colorless (E) glasses.

| | A | B | C | D | E |
|---|---|---|---|---|---|
| $SiO_2$ | 41.4 | 42.7 | 44.5 | 45.4 | 44.4 |
| $TiO_2$ | 11.2 | 11.1 | 3.2 | – | – |
| $Al_2O_3$ | 9.6 | 10.9 | 20.5 | 33.8 | 34.9 |
| $Cr_2O_3$ | 0.6 | 0.5 | 0.3 | – | – |
| FeO[1] | 18.4 | 16.7 | 10.6 | 2.8 | 0.1 |
| MnO | 0.2 | 0.3 | 0.2 | 0.1 | – |
| MgO | 7.3 | 8.9 | 7.9 | 1.7 | 0.2 |
| CaO | 11.6 | 10.9 | 12.8 | 17.5 | 17.5 |
| $Na_2O$ | 0.6 | 0.6 | 0.5 | 0.4 | 1.2 |
| $K_2O$ | 0.1 | 0.7 | 0.2 | – | 0.1 |
| NiO | – | – | – | – | – |
| $SO_3$ | 0.4 | 1.1 | 0.2 | – | – |
| Total | 101.4 | 104.4 | 100.9 | 101.7 | 98.4 |

[1] All Fe assumed to be in the +2 state; oxygen calculated by stoichiometry and element contents recalculated to weight percentage(s) of the oxides.

– Means concentration less than twice the total estimated uncertainty, i.e., < 0.04 wt.%.

Key

A. Yellow glass, defocussed beam analysis (18-21).

B. Average of 10 defocussed beam analyses on a medium-grained basalt lithic fragment (18-1).

C. Average of four defocussed beam analyses on soil breccia (section 27).

D. Average of seven defocussed beam analyses on gabbroic anorthosite (from Table IIC-I).

E. Colorless glass (focussed beam analysis).



Figure IID-1. Typical scoriaceous glass fragments from the Apollo 11 sample, millimeter scale. Note vesicles, dark color.

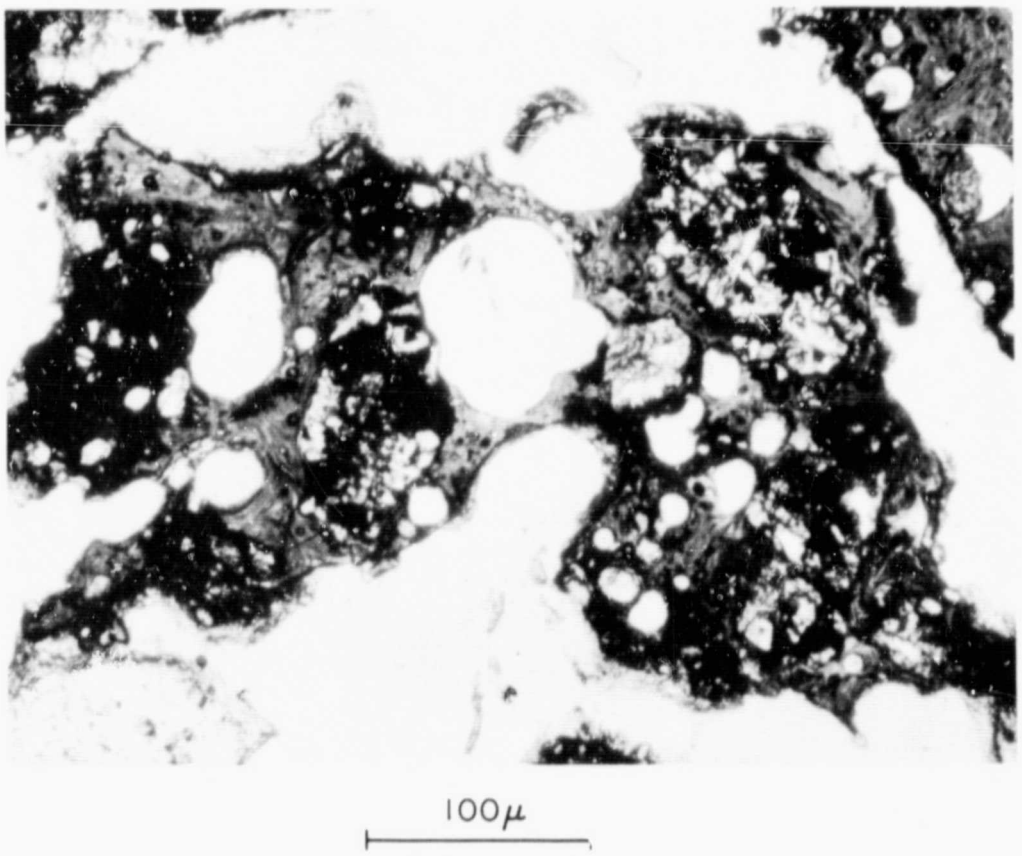



Figure IID-2. Inhomogeneous swirly glass fragment, of highly irregular shape. Note abundant vesicles and included rock and crystal fragments.

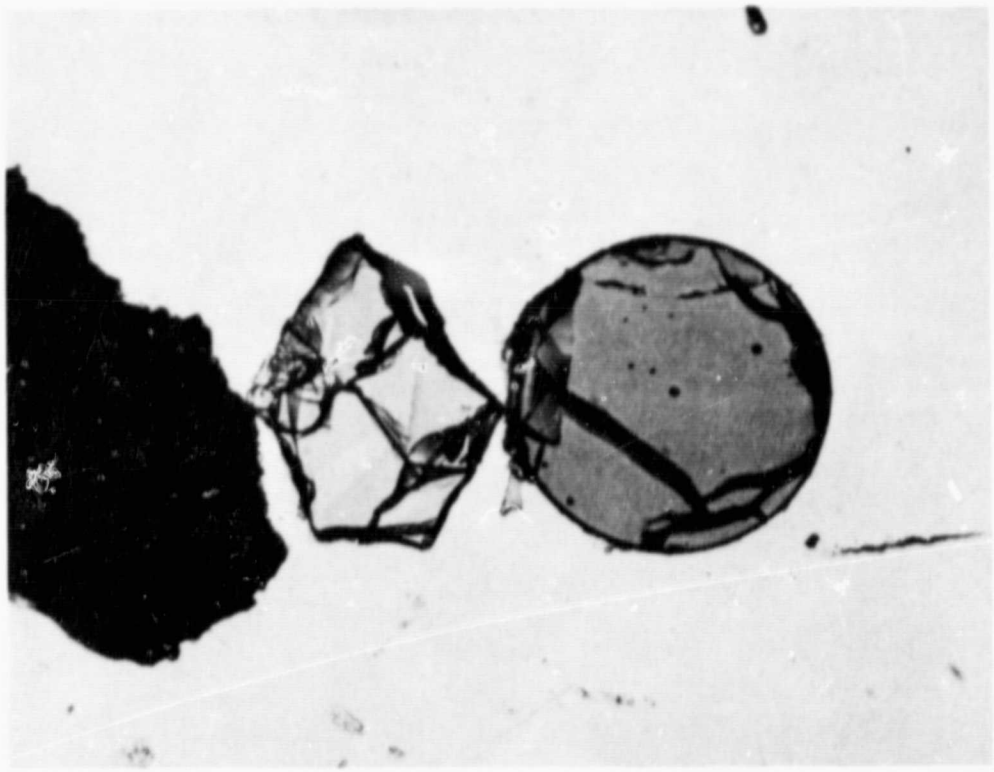



Figure IID-3. Angular and spherical particles of clear, homogeneous glass. (Section 13.)

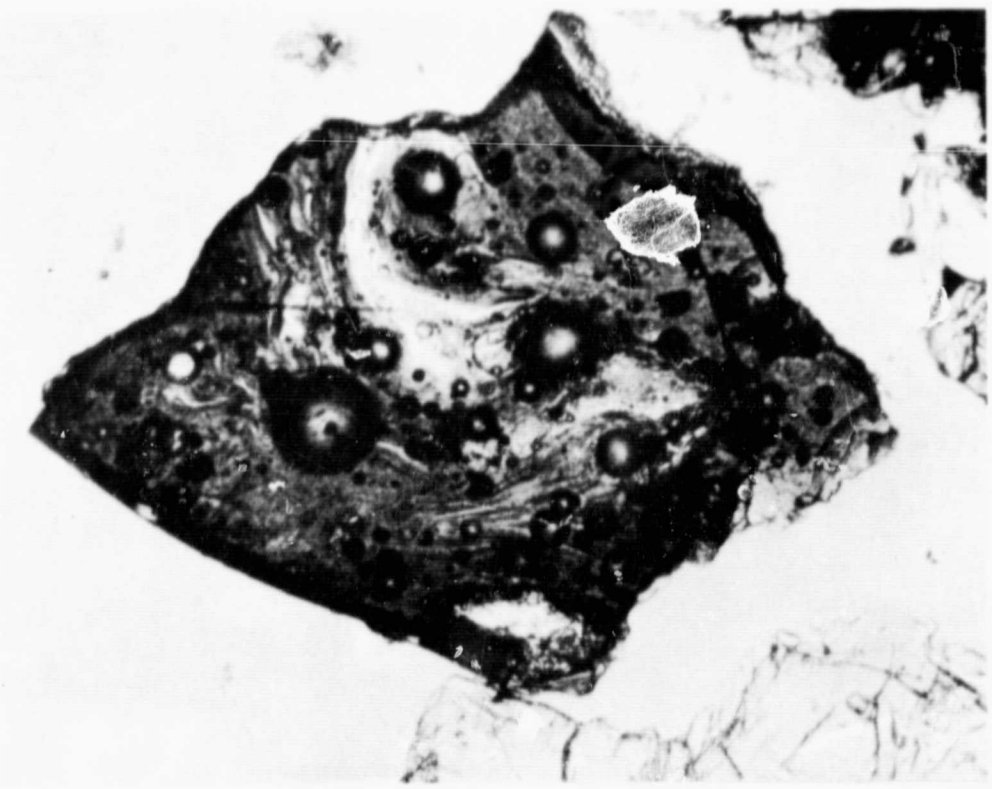



Figure IID-4. Inhomogeneous vesicular brown glass with pronounced color swirls. (Section 4.)

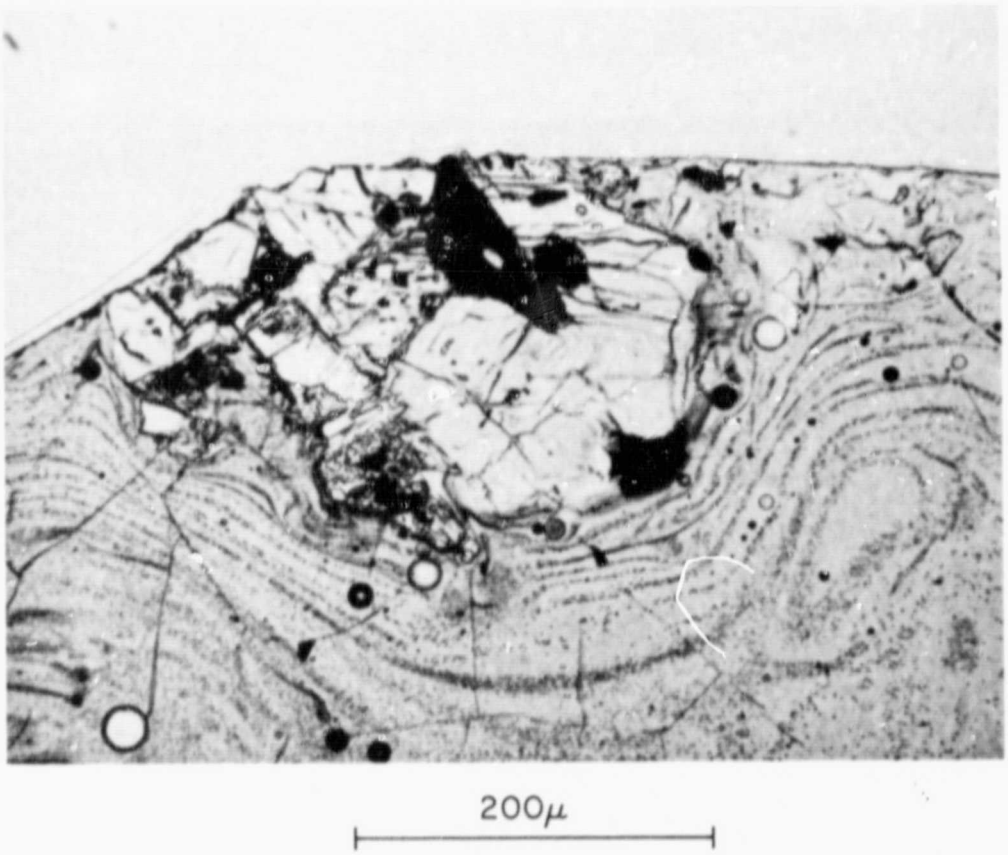



Figure IID-5. Lithic fragment of typical lunar basalt suspended in heterogeneous swirly yellow glass. Dark swirls are due to concentrations of opaque spherules.

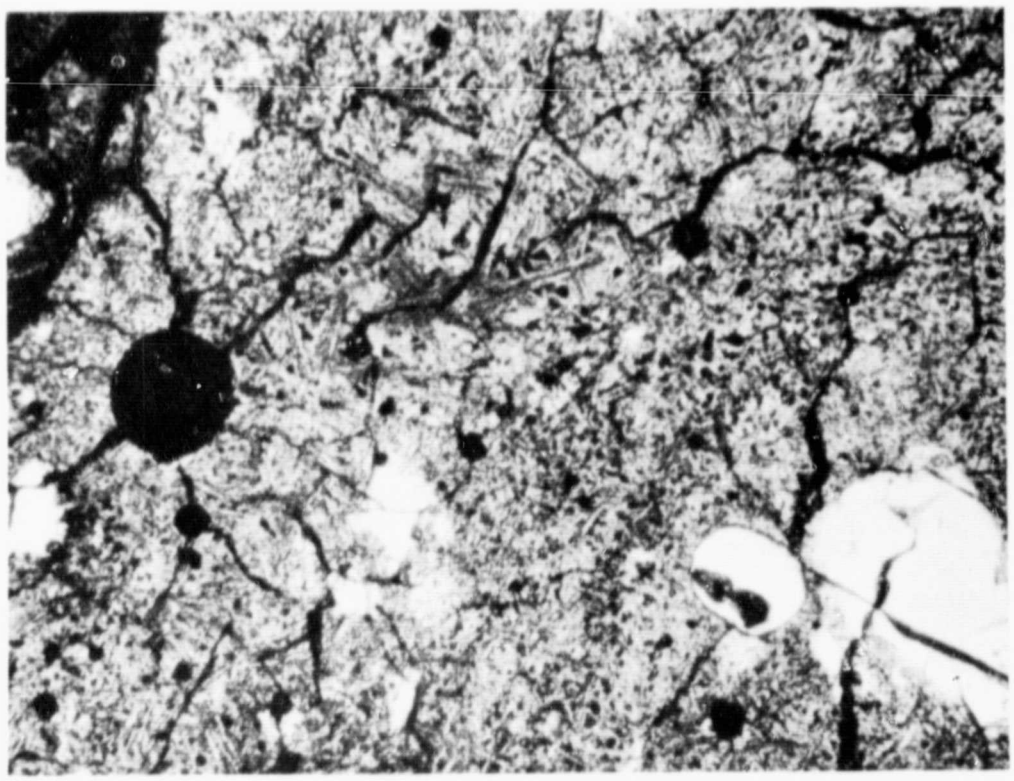



Figure IID-6. Minute silicate crystallites in a glassy matrix, possibly resulting from devitrification. The large opaque sphere is a fine mixture of Fe metal and FeS (see Figure IID-8). (Section 17.)

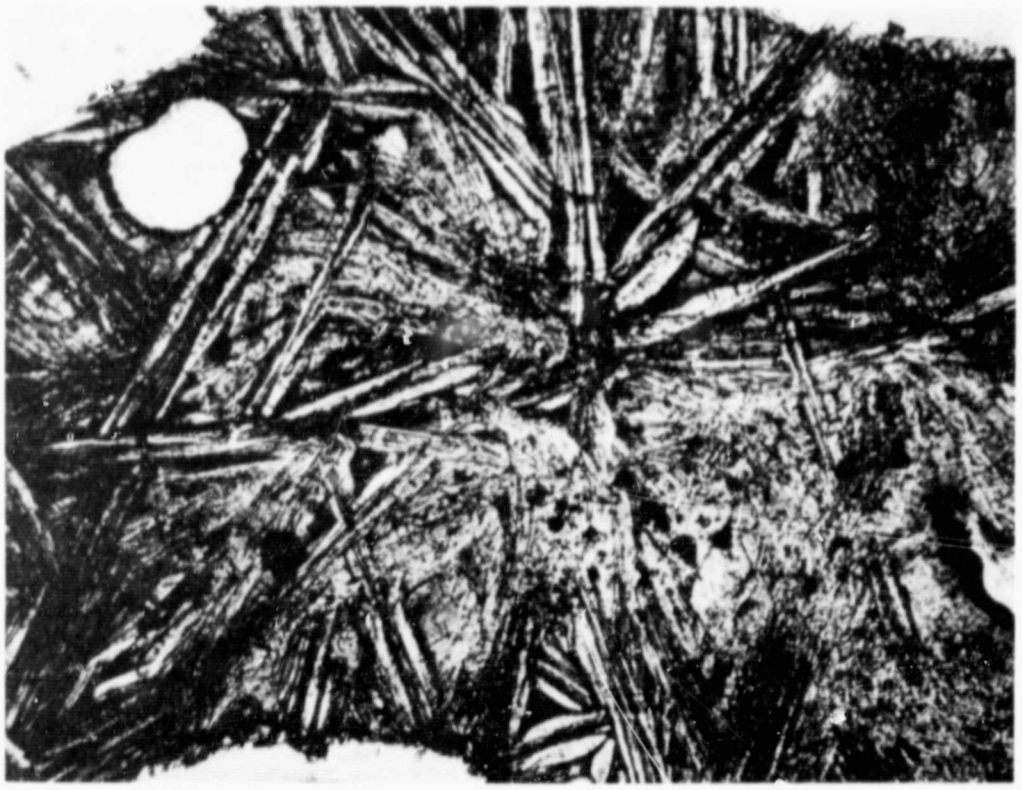



Figure IID-7. Radiating acicular plagioclase crystals in a glassy matrix, presumably a quench texture; compare to the much smaller crystallites in Figure IID-6. (Section 16.)

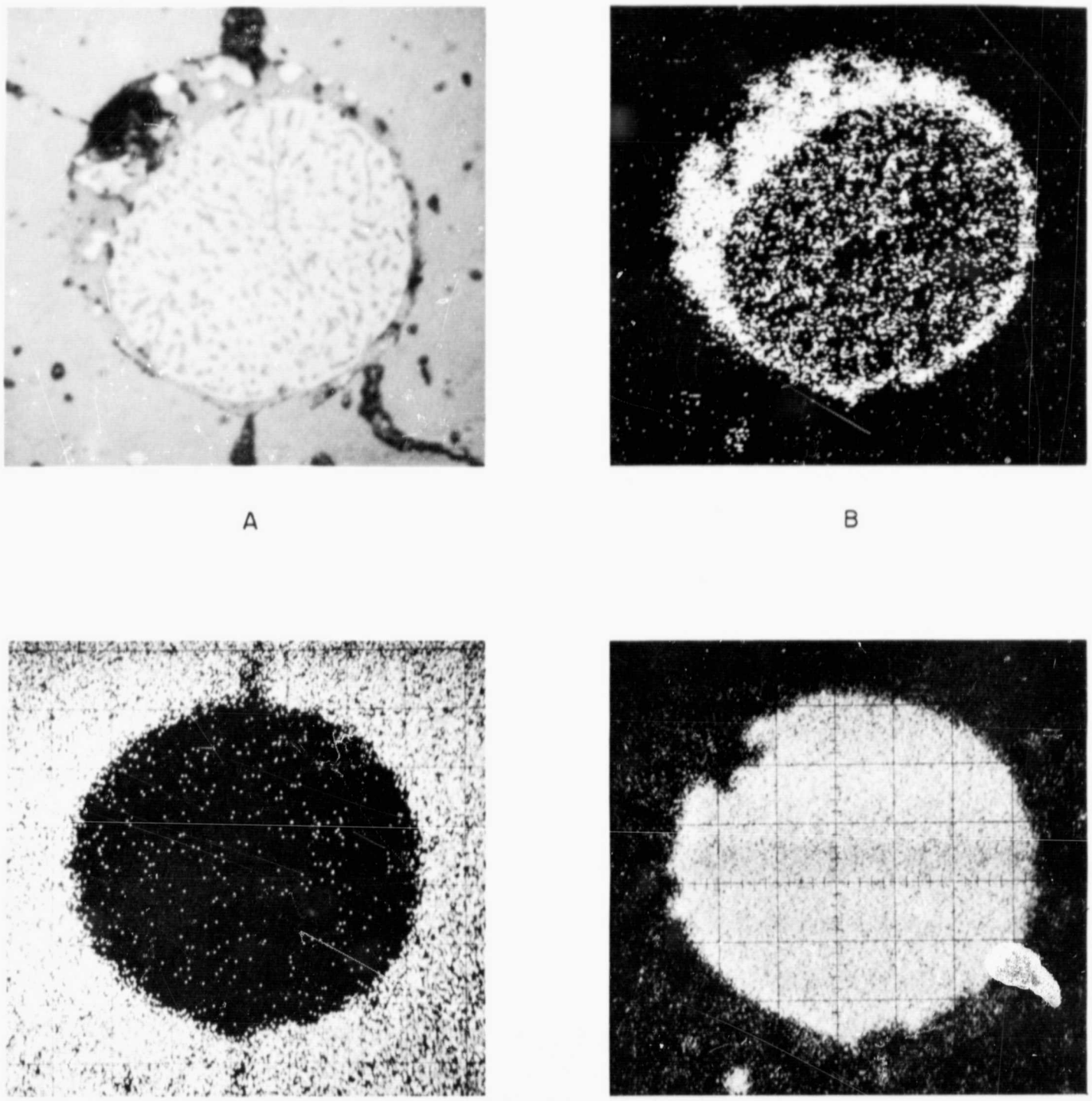



Figure IID-8. Two stages of liquid immiscibility in a heterogeneous, devitrified glass (see Figure IID-6). (A). Spherical droplet of Fe metal (light gray) and FeS (associated darker gray) surrounded by devitrified silicate glass (reflected light). (B). S Kα x-ray display, microprobe beam scanning. (C). Si Kα x-ray display. (D). Fe Kα x-ray display. (Section 17.).

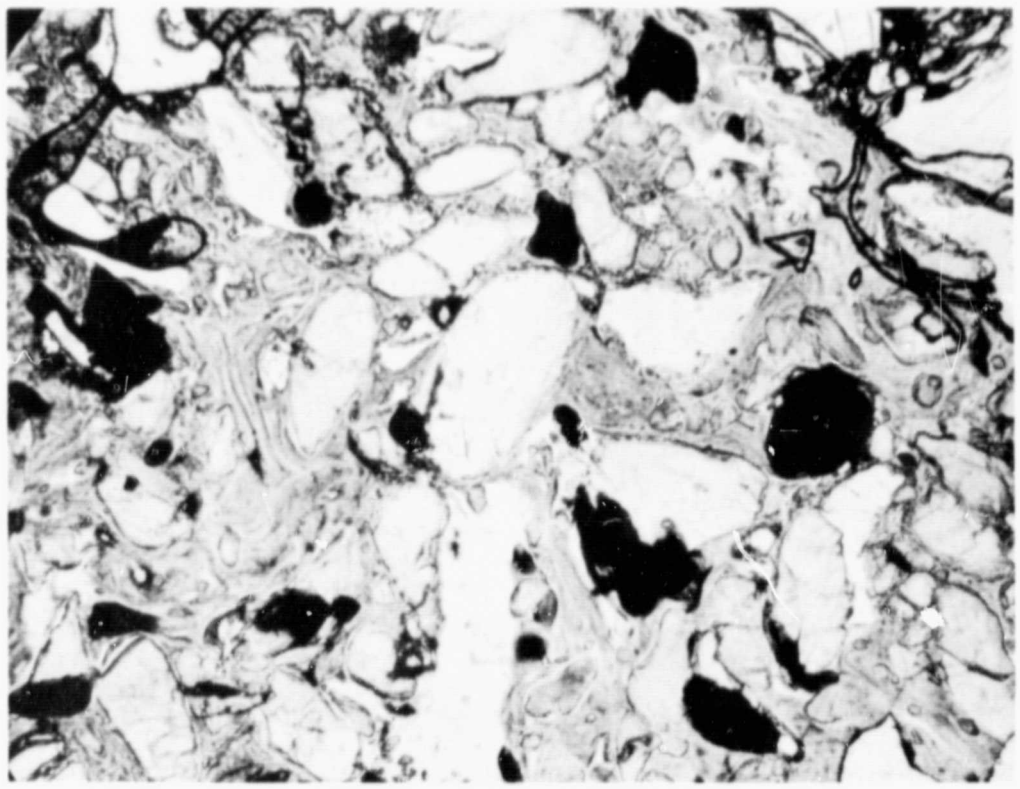



Figure IID-9. Rounded grains of pyroxene (medium gray), plagioclase (light gray) and ilmenite (black) in glassy matrix. Note flow lines in the glass, presumably the result of partial fusion and quenching of a typical lunar coarse basalt. (Section 26.)

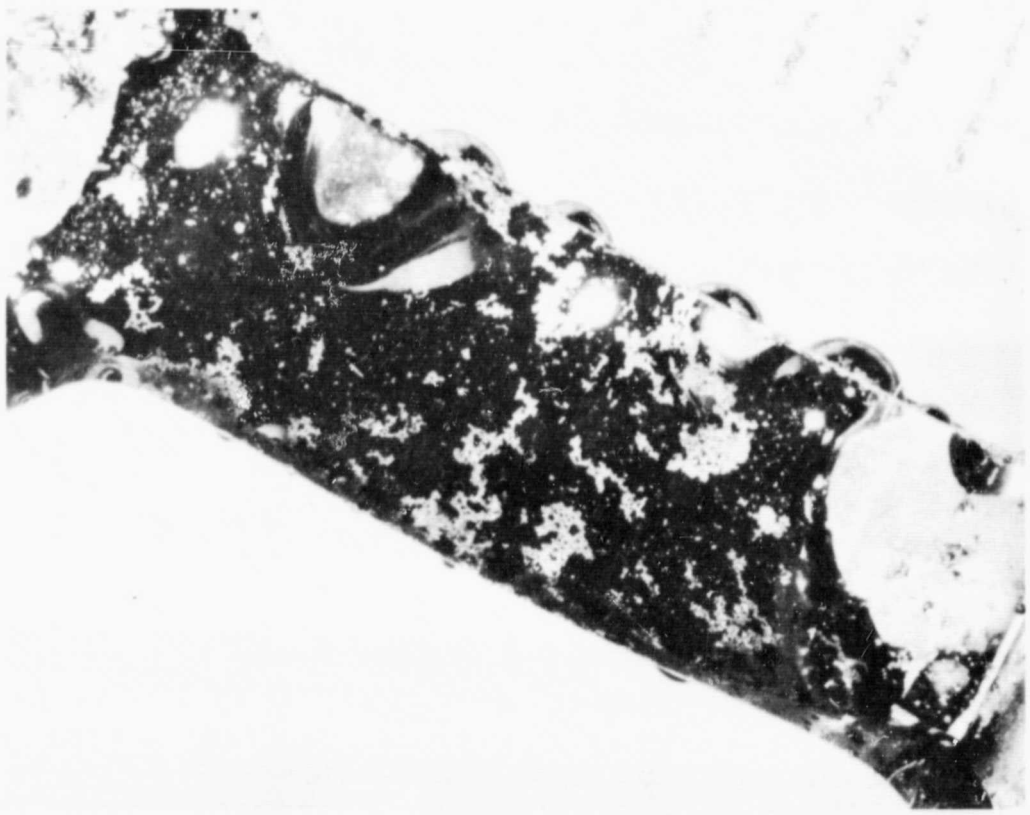


Figure IID-10. Tungsten boat containing artificially melted lunar soil; scale in millimeters. Character of lichen-like scum on glass surface is unknown; this deposit is also present on lunar glasses (fragment to lower right in Figure IID-1).

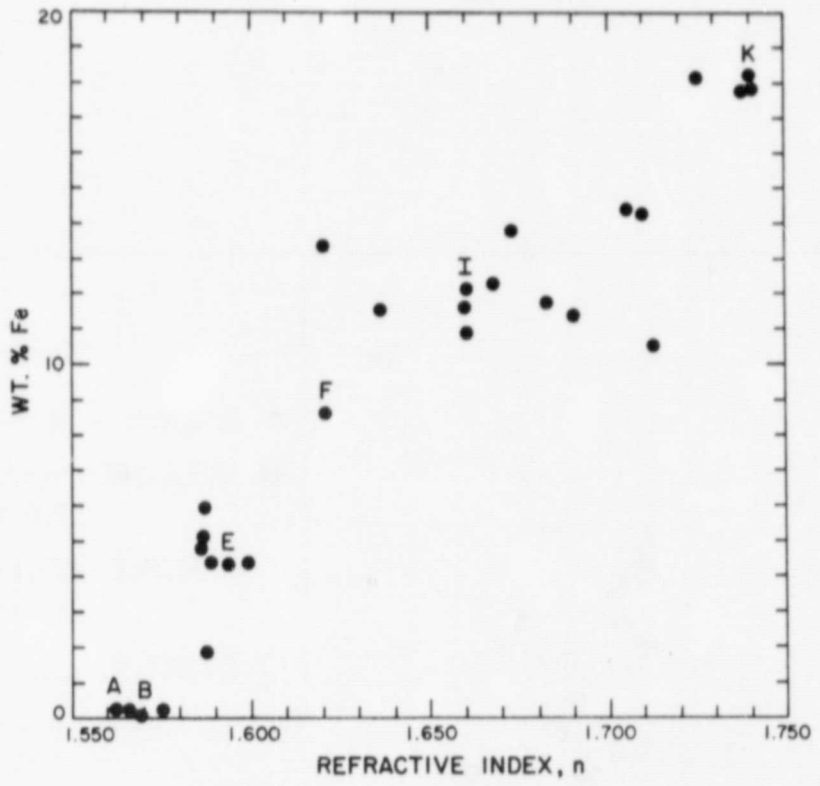



Figure IID-11. Refractive index plotted as a function of wt. % Fe in lunar glasses. Lettered points refer to analyses listed in their entirety in Table IID-I. Analyses in this diagram sum to between 97. 5 and 102. 0 wt. %.

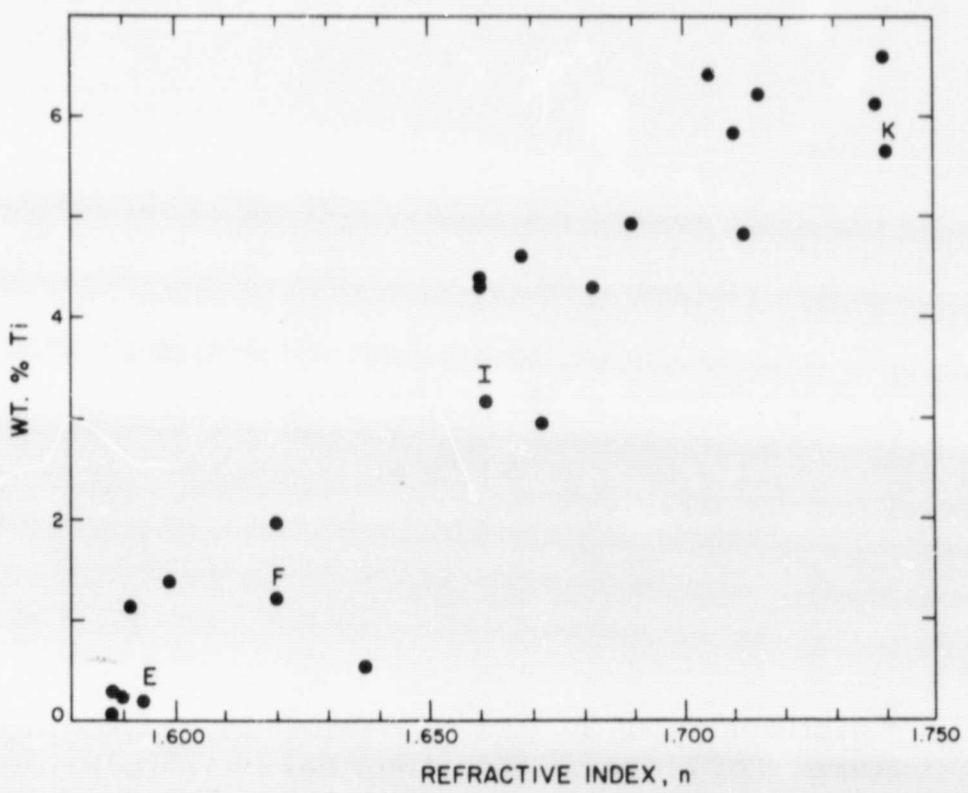



Figure IID-12. Refractive index plotted as a function of wt. % Ti in lunar glasses. Lettered points indicate analyses listed in their entirety in Table IID-I. Analyses plotted in this diagram sum to between 97. 5 and 102. 0 wt. %.

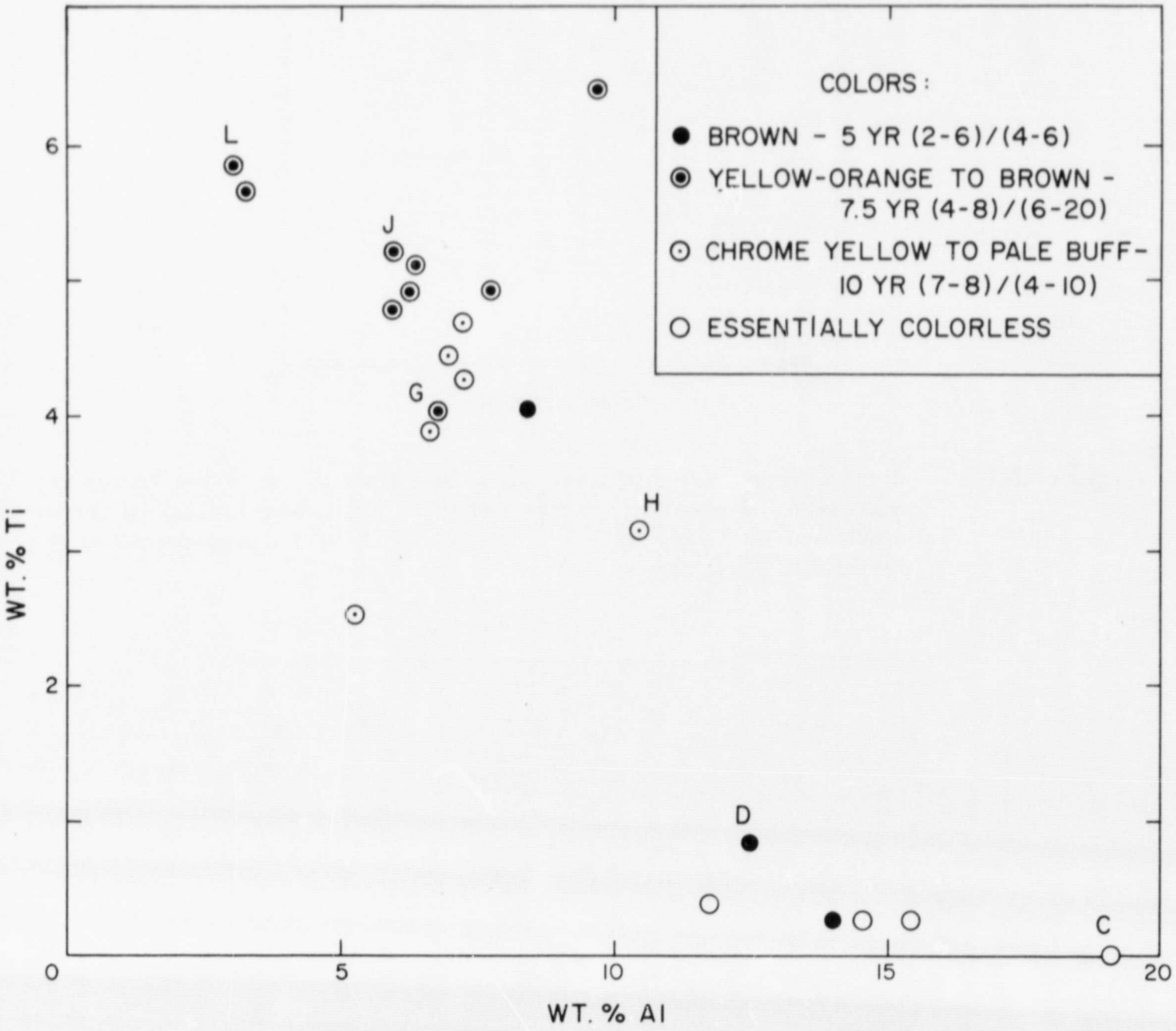



Figure IID-13. Relationship of Ti and Al content and color in lunar glasses. Ranges of Munsell color numbers are indicated. Lettered points are analyses listed in Table IID-I. Sums of all analyses entered fall between 97.5 and 102.0 wt.%.

## IIE. "Meteorites"

In view of the ample evidence of extensive meteorite bombardment of the lunar surface, including abundant impact craters and the common occurrence in the lunar sample of shock-produced and shock-related features, it would not be surprising to find some remnants of the impacting objects in a lunar soil sample. Nor would it be surprising if they were recognizably similar to some examples in terrestrial meteorite collections. One would not expect extralunar meteoritic material to be particularly abundant on the lunar surface, however, since the projectile/target ratio in the rubble produced by experimental high-velocity impacts is typically very low (e. g., Gault et al. (1963)).

We have observed in the soil sample a small number of fragments having features distinctly dissimilar to the typical lunar basalts and glasses described in previous sections. Further, their characteristics are similar enough to known meteorite types to warrant discussion.

### Ni-Fe Metal (Irons)

Particles of metallic iron are not uncommon in the fragments of soil breccia. The metal grains are generally irregular in shape and are frequently angular (Figures IIE-1 and -2). Metallic iron frequently occurs in the lunar mare basalts (Section IIB) and would therefore be expected to occur in the soil breccias along with the other constituents of the basalts. Some of the metal particles in the soil breccias, however, are at least an order of magnitude greater in size than the largest observed basalt metal grains. More important, the former frequently contain Ni in abundances of 5 wt. % or more (Table IIE-I), while the basaltic metal grains characteristically contain <0. 5 wt. % Ni.

Clearly the Ni-rich metal grains in the soil breccias do not have an origin in the mare basalts, which are in the bulk very low in Ni and Co. It is probable, although not certain, that they are not indigenous to any portion of the lunar surface. Therefore, they must have an origin either at some depth below the lunar surface or in an extralunar environment. The fact that the Ni levels observed are typical of some iron meteorites (hexahedrites) and of meteoritic kamacite (body-centered cubic α-iron) in general, coupled with the apparent absence of a (high density) core in the Moon, strongly suggests an extralunar origin for the high-Ni metal particles. It seems most likely that these metal fragments are pieces of iron (or stony iron) meteorites broken up during impact with the lunar surface. We estimate their abundance in the soil sample to be very approximately 0.1% by volume. This is no more than an order of magnitude estimate.

Stony-Iron Fragment (Mesosiderite?)

A most intriguing fragment some 3 mm in diameter, possessing several features notably dissimilar to other lunar material and to lunar basaltic rocks in particular, was found in the lunar soil sample. This fragment consists of approximately 70% (by volume) metallic Ni-Fe and 30% silicate phases (Figures IIE-3 and -4). In addition to its great abundance relative to associated silicates, the metal has a high Ni content compared to metal in lunar mare basalts (Table IIE-I). The metal consists primarily of kamacite with 6.9 wt.% Ni and contains minor amounts of taenite with Ni content ranging from 14 to >30 wt.%. The kamacite is polycrystalline and contains abundant Neumann bands (deformational twinning) (Figure IIE-5). Taenite masses are typically very irregular in form (Figure IIE-6). Metal-silicate interfaces are highly irregular and intricate in shape (Figure IIE-4), suggesting a more intimate relationship than would be produced by mechanical mixing of materials on the lunar surface.

The silicate assemblage in this fragment consists (in order of decreasing abundance) of low-Ca clinopyroxene (pigeonite), calcic plagioclase feldspar, olivine, and augite. Ilmenite, chromite, and troilite occur as opaque accessories (along with Ni-Fe metal) within the silicate masses, all in <1 vol.%

abundance. The chromite occurs as discrete grains and not as exsolution lamellae in ilmenite (which is its occurrence – when rarely observed at all – in the lunar basalts). Typical compositions of the various phases are listed in Table IIE-II.

Superficially, the non-metallic mineral assemblage appears similar to that of typical lunar basalts. However, there are several important differences. Pigeonite, which has low abundance in some lunar basalts and is absent in most, is the dominant pyroxene in the above assemblage. On the other hand augite, which dominates in the lunar basalts, occurs only as minute (<3μ) exsolution lamellae in pigeonite in the stony-iron fragment (Figure IIE-7). This latter pyroxene relationship – which is commonly observed in terrestrial basic rocks and is typical of basaltic achondrite (Duke and Silver, 1967) and mesosiderite meteorites (Powell, 1969a, c) – was nowhere observed in the lunar basalts. Another possible distinction can be seen in the Ti and Al contents of the pyroxenes in this particle (Table IIE-II), which are lower than in the typical lunar basalt pyroxenes (Section IIB), although not outside the compositional ranges of the latter. A typical pigeonite from the Crab Orchard mesosiderite is shown in Table IIE-II for comparison. The compositions of the feldspar and olivine in the stony-iron fragment are typical of those in mesosiderites, but are also not significantly different from those in the lunar basalts.

The abundance of metallic iron and its high Ni content, the nature of the pyroxene assemblage, the low abundance of ilmenite (and of Ti in general), and the presence of discrete chromite grains are features unique to this fragment among lunar materials observed in this study. On the other hand, the fragment is strikingly similar to mesosiderites (themselves unique among meteorites – Powell and Weiblen, 1967; Powell, 1969b) in mineralogy and chemistry. We believe that this fragment may be a piece of mesosiderite. Whether such material had a genetic origin within the Moon as has been suggested (Powell, 1969b) or whether its origin is extralunar is unknown. If the former were true, its origin must have been at some depth within the Moon, judging from mesosiderite metal cooling rate estimates (Powell, 1969b) and considering what is currently being revealed about the nature of

the lunar surface materials. Clearly some material from beneath the lunar surface has been brought to the surface by meteorite impact, the depth of "sampling" depending on the magnitude of the impact event.

Olivine Porphyry (Chondrite )

A unique lithic fragment consisting of euhedral olivine phenocrysts set in a very fine-grained semi-opaque matrix was observed in the lunar soil sample (Figure IIE-8). The abundance of olivine (~40 vol. %) as well as the texture are features totally unlike the lunar basalts and other lunar surface materials. Table IIE-III lists the compositions of olivine phenocrysts (A, B, C) and matrix (D, E) along with a typical lunar mare basalt olivine for comparison (I).

As can be seen in Figure IIE-8 many of the olivine phenocrysts are skeletal, which together with the extremely fine-grained nature of the matrix, suggests the bulk material was quenched from the molten state. The olivines are strongly zoned with Fe enrichment in the rims (Table IIE-III), also suggestive of very rapid cooling. Considering the possibility that this unique material may represent a portion of a meteorite melted and quenched upon impact with the lunar surface, an experiment was devised to simulate the process. A few milligrams of the Murray carbonaceous chondrite were placed in a tungsten boat and melted and quenched by the procedure described in Section IID. (A carbonaceous chondrite was used because the absence of Fe metal in the olivine porphyry and the high levels of Ni in the olivine compared to lunar basaltic olivine and most meteoritic olivine (see, for example, Buseck and Goldstein, 1969) suggested a relatively highly oxidized starting material. Murray was chosen because of its availability.) The resulting material consisted of olivine phenocrysts contained in a glassy matrix. Many of the olivine phenocrysts are acicular in habit and form a criss-cross, decussate texture (Figure IIE-9); others are more nearly equidimensional, frequently euhedral and skeletal (Figure IIE-10). In this latter habit the olivines strongly resemble the phenocrysts in the lunar olivine porphyry.

Microprobe analyses of the melted Murray material reveal further similarities to the olivine porphyry (Table IIE-III). In both materials the olivines are strongly zoned. Also in both, the elements Si, Fe, Al, and Ca (the latter two strongly) are concentrated in the fine matrices relative to the olivine and Mg is strongly depleted in the matrices. (This Al and Ca distribution is not surprising in view of the low abundances of these elements in olivines in general.) The same can be said regarding the concentration of Na in the matrix of the olivine porphyry. That this effect was not observed in the melted Murray material is unexplained. (Possibly almost all the chondritic Na was volatilized during the bell jar melting.) This experiment does not establish that the lunar olivine porphyry is a fragment of a chondrite (carbonaceous or otherwise) melted and quenched during lunar impact, but it does establish that such textures and compositional features can be produced by melting and quenching of ultrabasic rock materials.

The uniqueness of texture and composition of the olivine porphyry indicates either that this material is of extralunar origin or that it comes from a part of the Moon totally unlike Mare Tranquillitatis.

Table IIE-I. A comparison of the compositions of metal particles from the lunar soil sample with the composition of metal from typical lunar basalts.

| | A[1] | B[2] | C | D | E |
|---|---|---|---|---|---|
| Fe | 97.7 | 94.1 | 91.7 | 88.7 | 84.0 |
| Co | N. D. | 0.49 | N. D. | N. D. | N. D. |
| Ni | 0.22 | 5.8 | 6.9 | 14.1 | 20.6 |
| Sum | 97.9 | 100.3 | 98.6 | 102.8 | 104.6 |

[1] Total estimated analytical uncertainty (see Section VC) for Fe is 0.4 wt. %; for Ni, 0.04 wt. %.

[2] Total estimated analytical uncertainty for Fe is 1.0 wt. %; for Co, 0.06 wt. %; for Ni, 0.2 wt. %.

N. D.: Not determined.

Key

A. Composition of a typical Fe metal grain in lunar basalt (8-28).

B. Composition of isolated Ni-Fe metal fragment in lunar soil breccia.

C. Composition of kamacite in stony-iron "meteorite" fragment in the lunar soil sample.

D, E. Compositions of taenite in stony-iron "meteorite" fragment in the lunar soil sample.

Table IIE-III. Compositions of olivine phenocrysts and fine-grained matrices in unique olivine porphyry from the lunar soil sample, and in an artificially melted and quenched carbonaceous chondrite sample (Murray).

| | A | B | C | D | E | F | G | H | I |
|---|---|---|---|---|---|---|---|---|---|
| Si | 18.2 | 18.6 | 17.6 | 19.7 | 20.3 | 18.1 | 17.7 | 19.4 | 17.6 |
| Ti | – | – | – | 0.4 | 0.3 | 0.1 | 0.1 | 0.2 | 0.1 |
| Al[1] | 0.06 | 0.09 | 0.05 | 7.0 | 7.1 | 0.2 | 0.3 | 3.8 | – |
| Cr | 0.2 | 0.2 | 0.2 | – | – | 0.2 | 0.4 | 0.3 | 0.1 |
| Fe[2] | 12.8 | 11.8 | 18.5 | 19.9 | 20.6 | 15.3 | 23.5 | 23.3 | 21.4 |
| Mn | 0.2 | 0.2 | 0.2 | 0.4 | 0.3 | N.D. | N.D. | N.D. | 0.2 |
| Mg | 25.7 | 26.5 | 23.4 | 0.5 | 0.9 | 24.2 | 17.4 | 5.5 | 20.0 |
| Ca[3] | 0.13 | 0.14 | 0.16 | 8.2 | 6.5 | 0.37 | 0.40 | 2.9 | 0.21 |
| Na | – | – | – | 2.4 | 2.2 | – | – | – | – |
| K | – | – | – | 0.3 | 0.3 | – | – | – | – |
| Ni[4] | 0.16 | 0.10 | 0.12 | – | – | – | – | – | <0.06 |
| O[5] | 41.6 | 42.4 | 41.2 | 40.0 | 40.3 | 41.4 | 39.1 | 37.1 | 39.6 |
| Total | 99.1 | 100.0 | 101.4 | 98.8 | 98.8 | 99.9 | 98.9 | 92.4 | 99.2 |
| Cations per 4 oxygens | 3.00 | 2.99 | 3.02 | | | 2.99 | 2.95 | | 2.98 |
| Mole % Fo | 82.2 | 83.7 | 74.4 | | | 78.4 | 63.0 | | 68.2 |
| Mole % Fa | 17.8 | 16.3 | 25.6 | | | 21.6 | 37.0 | | 31.8 |

[1] Total estimated uncertainty (see Section VC) on Al analyses in olivine ± 0.01 wt. %.

[2] All iron assumed to be in the +2 state.

[3] Total estimated uncertainty on Ca analyses in olivine ± 0.01 wt. %.

[4] Total estimated uncertainty on Ni analyses in olivine ± 0.03 wt. %.

[5] Oxygen calculated on the basis of stoichiometry (see note 2).

– Means concentration level is less than twice the total estimated uncertainty, i.e., < 0.04 wt. %.

Key

A. Core of olivine phenocryst in olivine prophyry, fragment (8-36).

B. Another olivine phenocryst core composition from (8-36).

C. Rim of olivine phenocryst (B above) from (8-36).

D, E. Fine-grained semi-opaque matrix in olivine porphyry (8-36).

F. Core of olivine phenocryst in artificially melted and quenched carbonaceous chondrite sample (Murray). (See Figure IIE-10.)

G. Rim of olivine phenocryst (see F above and Figure IIE-10).

H. Fine-grained glassy matrix in artificially melted Murray carbonaceous chondrite (see Figure IIE-9).

I. Typical olivine composition from coarse lunar basalt (8-28).

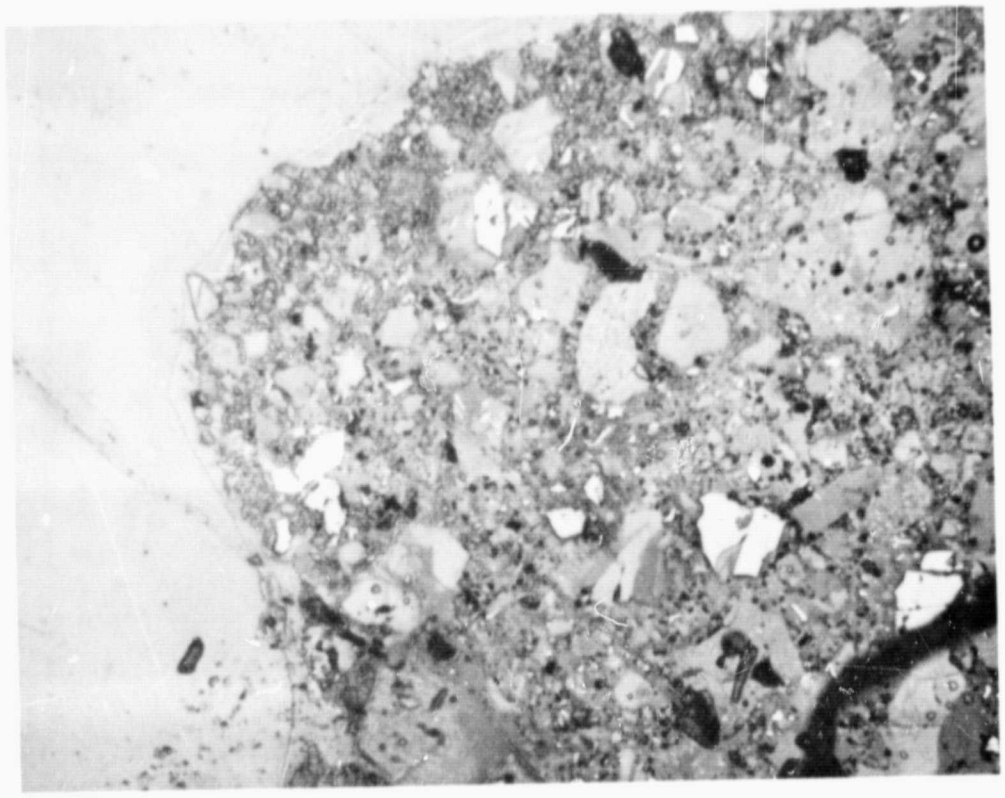



Figure IIE-1. Particle of metallic Ni-Fe (bright white grain near margin of fragment) in soil breccia; reflected light.




Figure IIE-2. Large angular particle of Ni-Fe metal in soil breccia; réflected light.

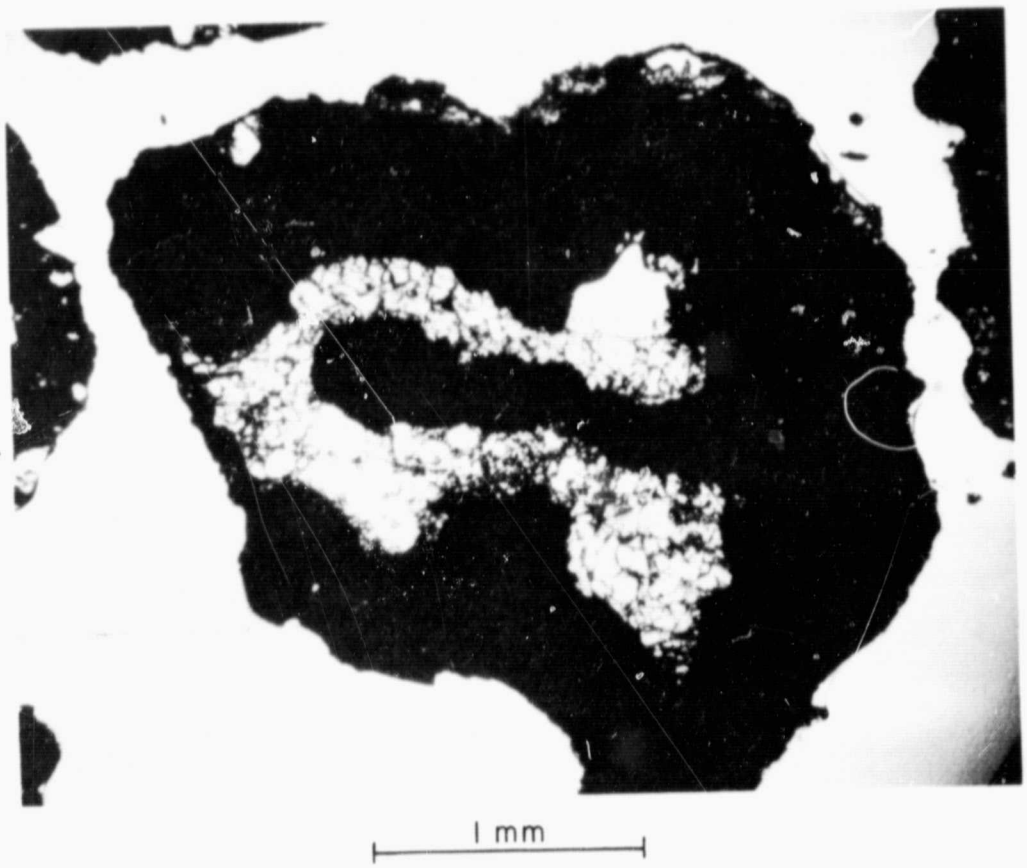



Figure IIE-3. Stony-iron "meteorite" fragment from the lunar soil, consisting of approximately 70% (by volume) Ni-Fe metal (black) and 30% silicates (light colored); transmitted light.

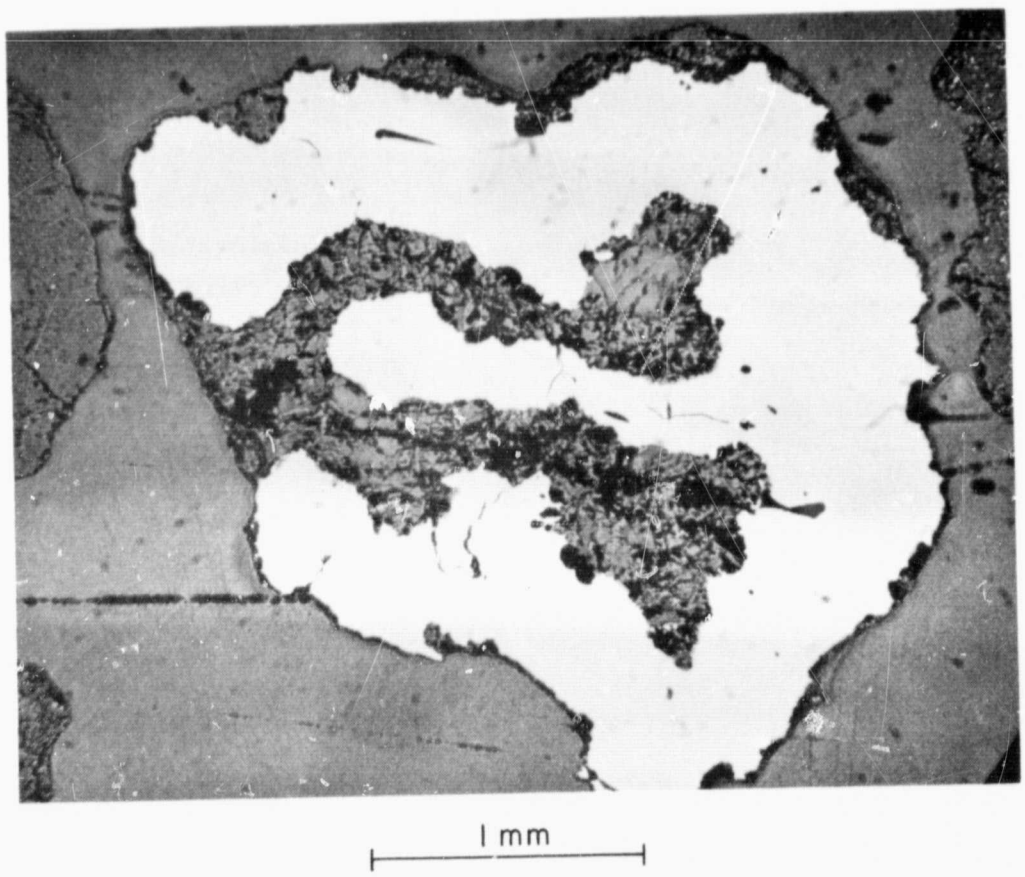



Figure IIE-4. Same field as Figure IIE-3, by reflected light. Ni-Fe metal is light gray; silicates are dark gray.

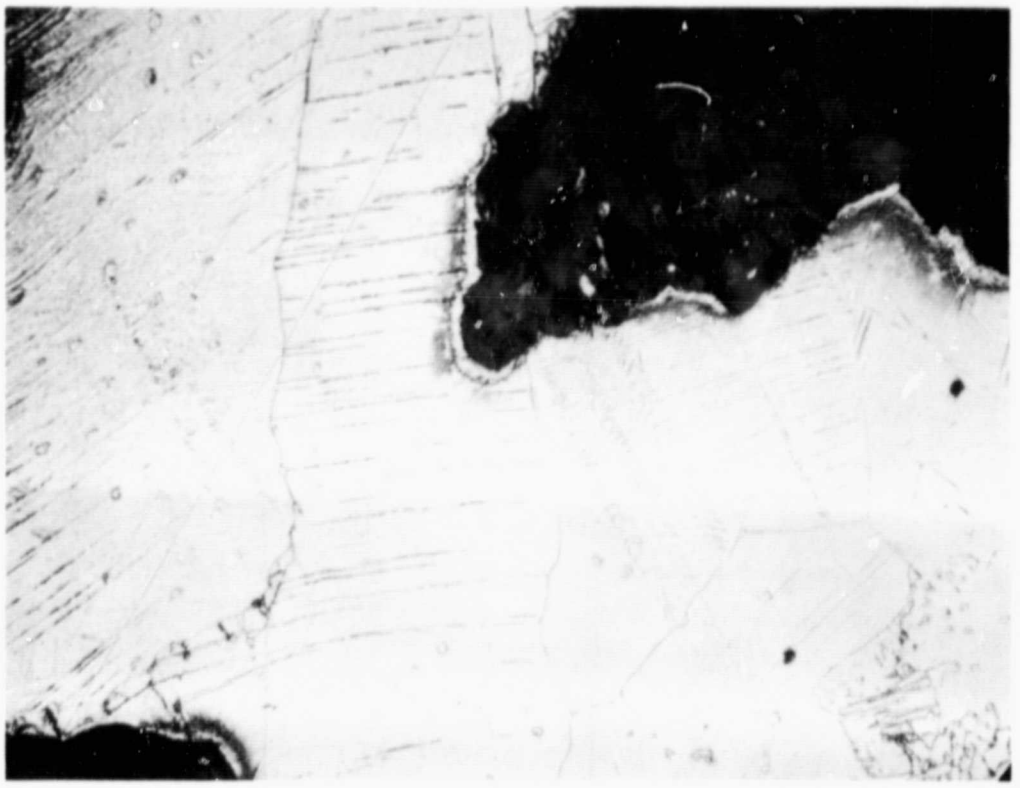



Figure IIE-5. Neumann bands in polycrystalline kamacite in stony-iron fragment; silicates are dark gray. Note grain boundaries in kamacite. Reflected light; 4% nital etch.

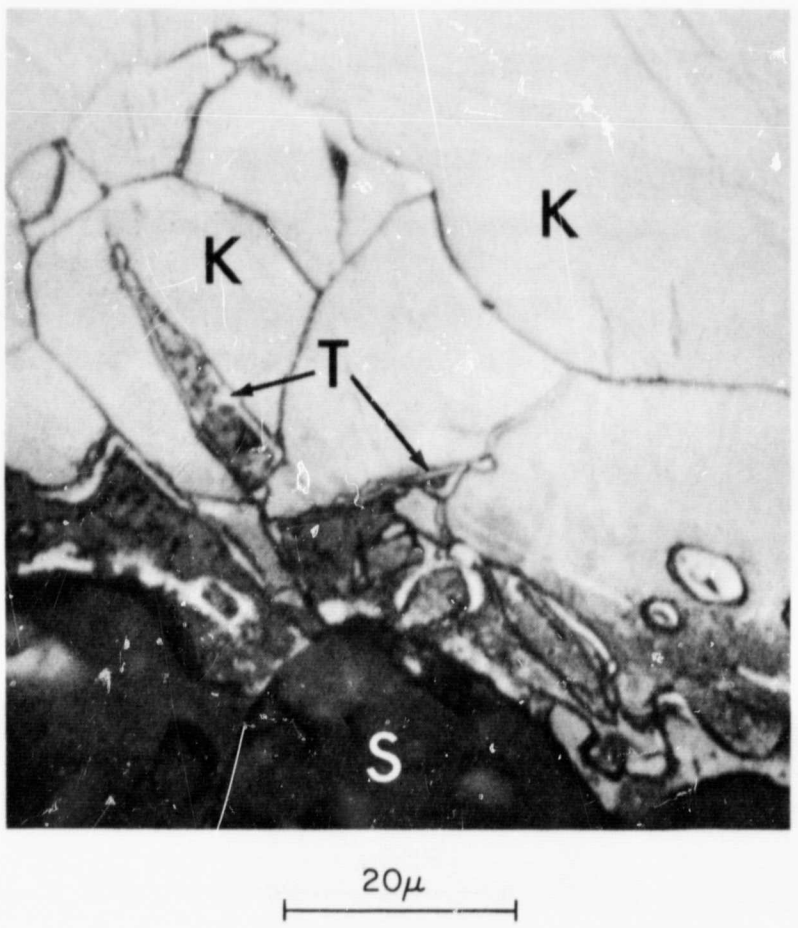



Figure IIE-6. Kamacite (K) and taenite (T) in stony-iron fragment. Grain boundaries are visible in kamacite; S = silicates. Reflected light; 4% nital etch.

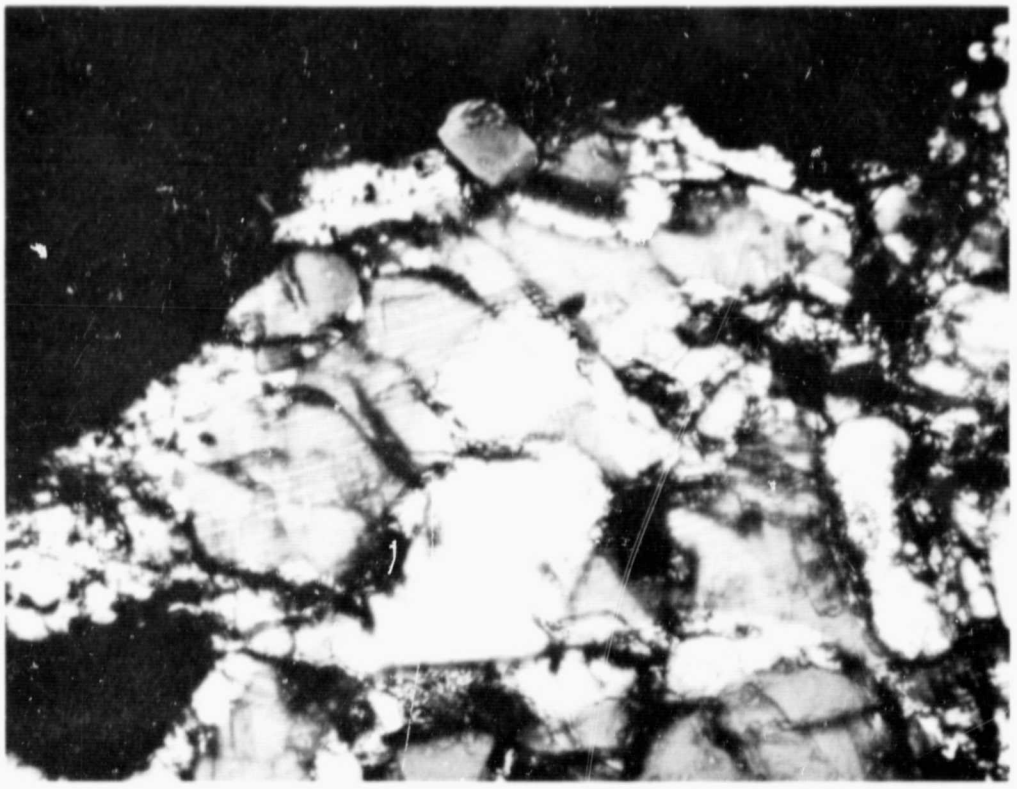



Figure IIE-7. Augite exsolution lamellae (light lines) in pigeonite in stony-iron fragment. Polarized transmitted light.

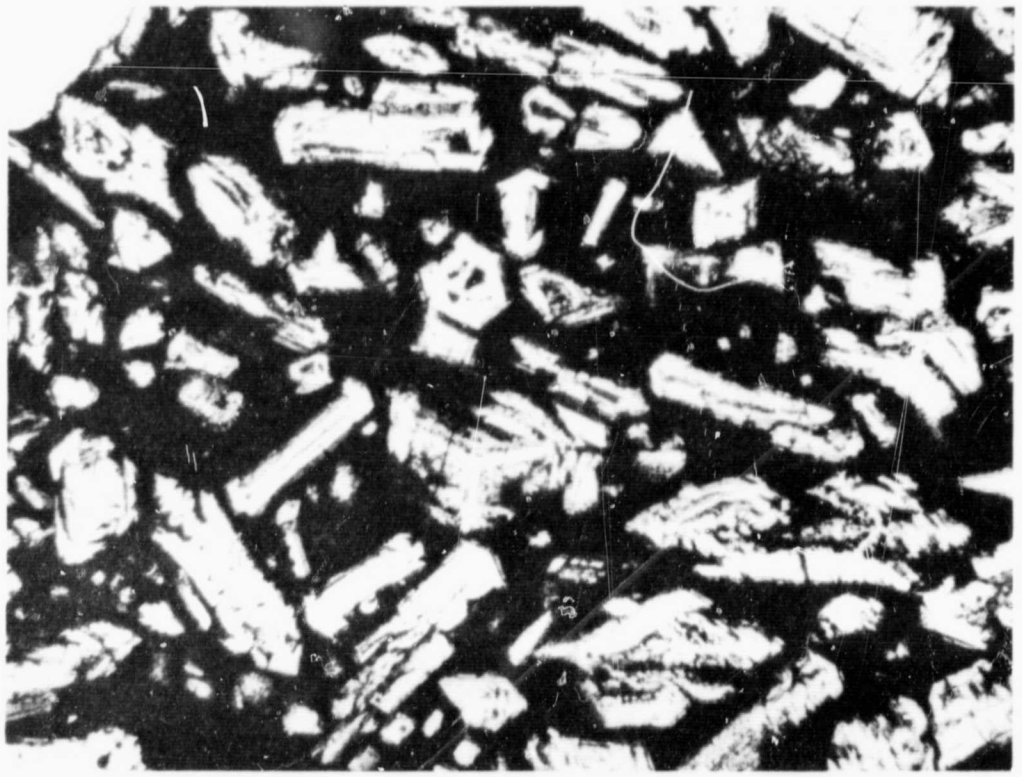



Figure IIE-8. Euhedral olivine phenocrysts in a very fine-grained semi-opaque matrix in unique olivine porphyry from the lunar soil. Note the skeletal form of many of the olivine crystals; transmitted light.




Figure IIE-9. Acicular olivine phenocrysts in glassy matrix in artificially melted Murray carbonaceous chondrite. H indicates analysis point on glassy matrix (see Table IIE-3).

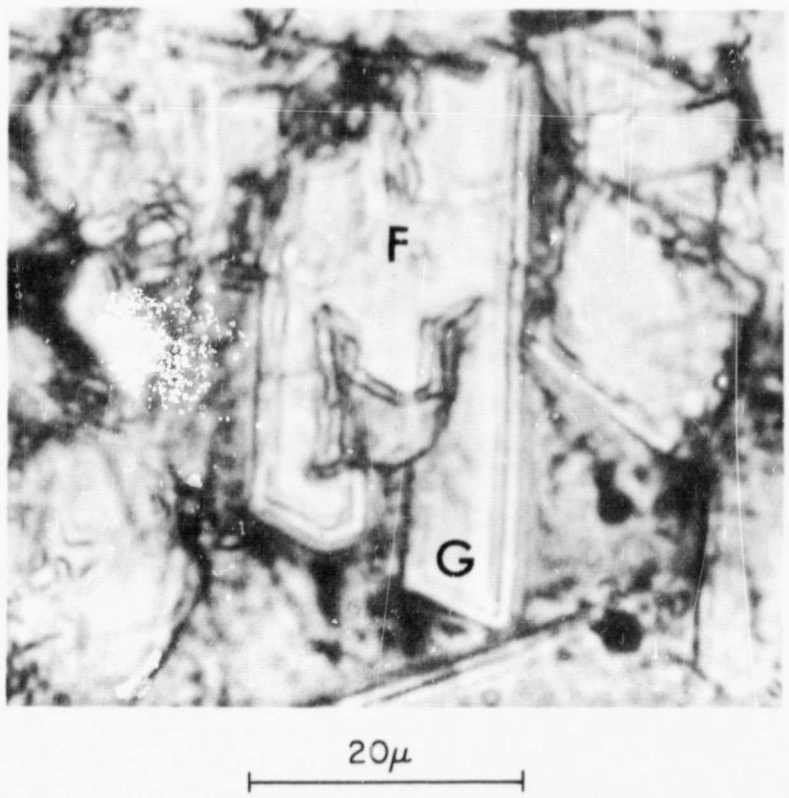



Figure IIE-10. Skeletal euhedral olivine phenocryst in artificially melted Murray carbonaceous chondrite; note zoning. Compare to Figure IIE-8. F and G are analysis points listed in Table IIE-III.

## III. SHOCK METAMORPHISM

Upon the airless, arid lunar surface ordinary erosive and weathering phenomena are absent or inconspicuous; instead the pervasive agents of change are impact cratering and shock metamorphism due to meteorite bombardment. Shock metamorphism is apparent in about 75% of the particles we examined. Of the different rocks in the Apollo 11 particulate sample the anorthosites, anorthositic gabbros, and the breccias show the most severe shock effects; the dark, Ti-rich basalts are, typically, less affected. We find three general forms of shock metamorphism: cataclasis and microdeformation, solid-state isotropization, and fusion.

Under cataclasis and microdeformation we include gross fracturing and disruption of rocks and deformation of individual crystals. Figure III-1 illustrates a grabbroic anorthosite that has been fractured and granulated by shock. The deformation of crystals ranges from the development of planar features (Figure III-2) to more severe fracturing and bending (Figures III-3 and -4).

More intense shock conditions cause solid-state isotropization of crystals. In Figure III-5 a nearly isotropic plagioclase crystal contains myriad tiny oriented bodies, which appear to be feldspathic glass. Such arrays of glassy inclusions are present in many shocked feldspars. Some larger, twinned plagioclase crystals (Figures III-6 and -7) have been transformed into complex aggregates of small, anisotropic units. This repeated subdivision and disruption eventually renders the crystal isotropic.

As we have noted above, the small particle size fraction of the Apollo 11 bulk sample contains abundant glass ($\simeq$ 50% by volume). Some of these glasses, particularly those with monomineralic compositions, were produced by solid-state isotropization, but most were once liquids formed by intense, shock-induced heating. Effects of this rock fusion appear in many

forms, ranging from a scattering of glass blebs along crystal interfaces to rounded, relict crystals, immersed in swirling, brown glass (Figure IID-9). Many of the glassy fragments containing quench crystals (Figure IID-7) may have been fused during shock events. In the anorthositic rocks shock melting is manifested (Figure III-8) by light brown, isotropic or finely devitrified glass broken by a polygonal system of shrinkage cracks. In some of these rocks (Figure III-9 and -10) only the more mafic, lower melting parts have fused. In such examples, as in the case of incipient, intergranular melting, the heat pulse was obviously not extreme, and fusion was probably not caused directly by a shock wave but by heat conducted away from the shocked region.

The partly fused soil breccias (Section IIA, Figure III-11) are possibly the most extraordinary rocks in the sample. In many respects they resemble terrestrial welded tuffs; however, the presence of glass spherules and a heterogeneous assemblage of rock fragments shows that they are lunar soils, not products of explosive volcanism. Spherules and shreds of glass are common in the breccias, and many have glassy matrices. These breccias were probably created by repeated shock melting and mixing; but their formation remains somewhat obscure, for there is nothing like them on Earth.

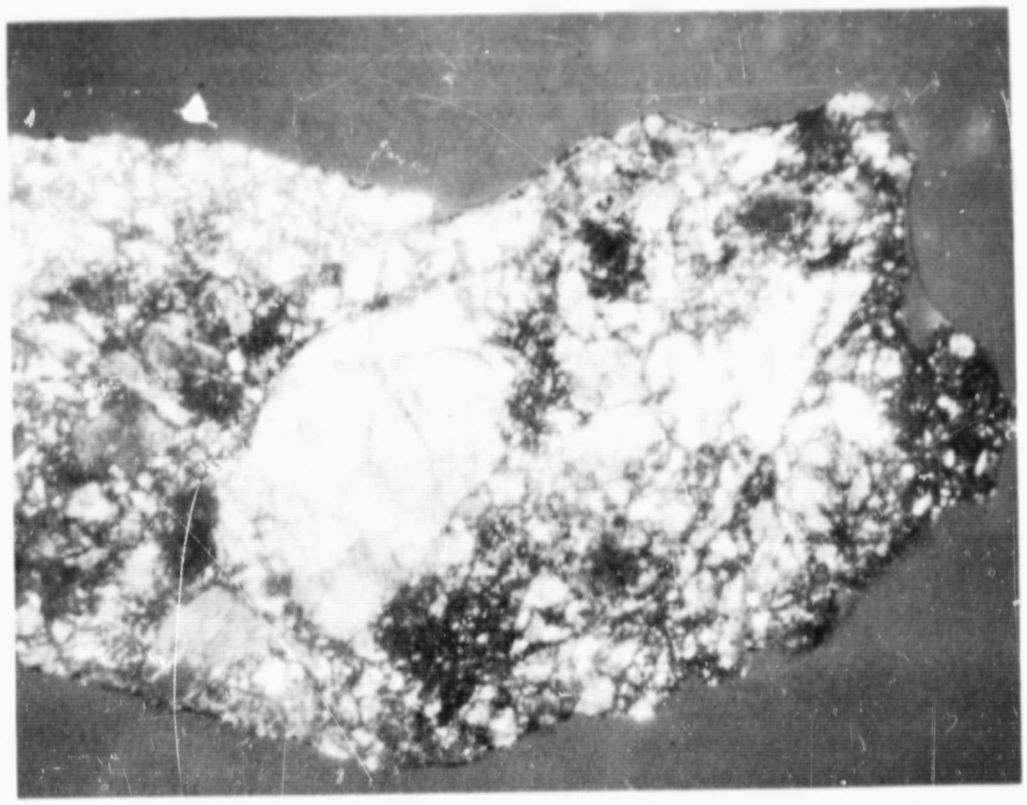



Figure III-1. Fractured, granulated, gabbroic anorthosite. Oblique nicols.

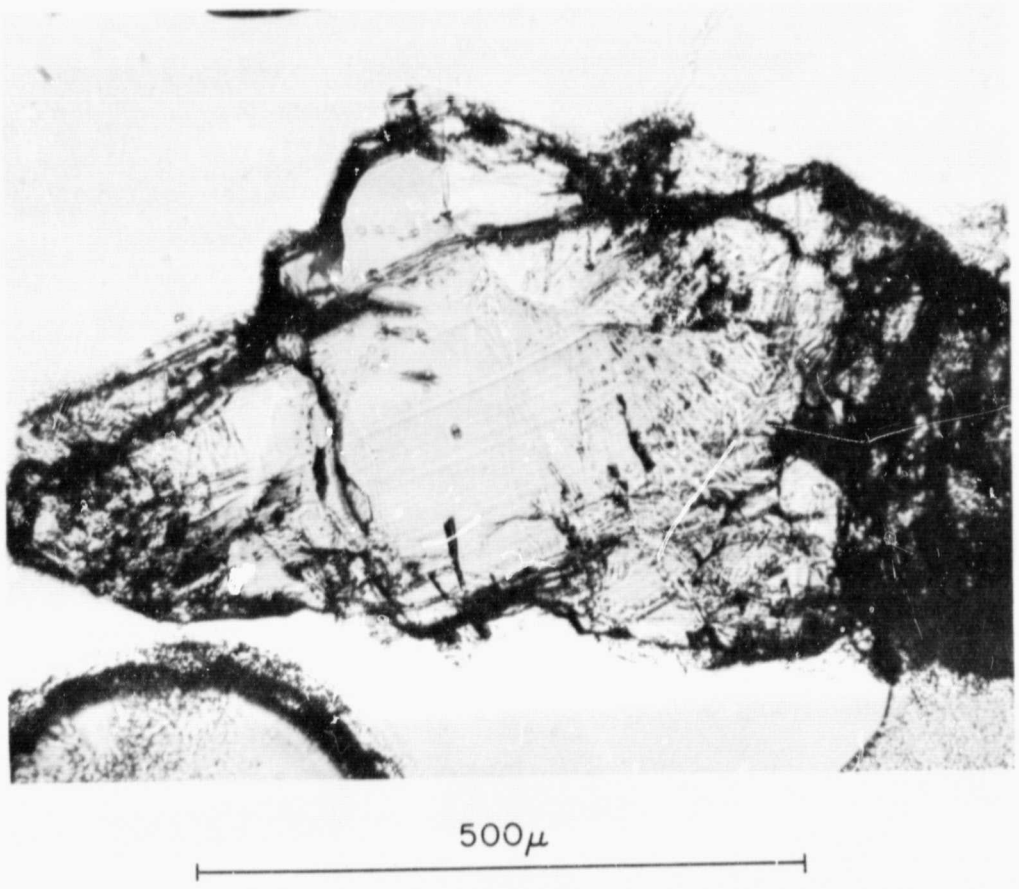



Figure III-2. Clinopyroxene crystal (in a soil breccia) with a set of fine, parallel, planar features. Unpolarized light.

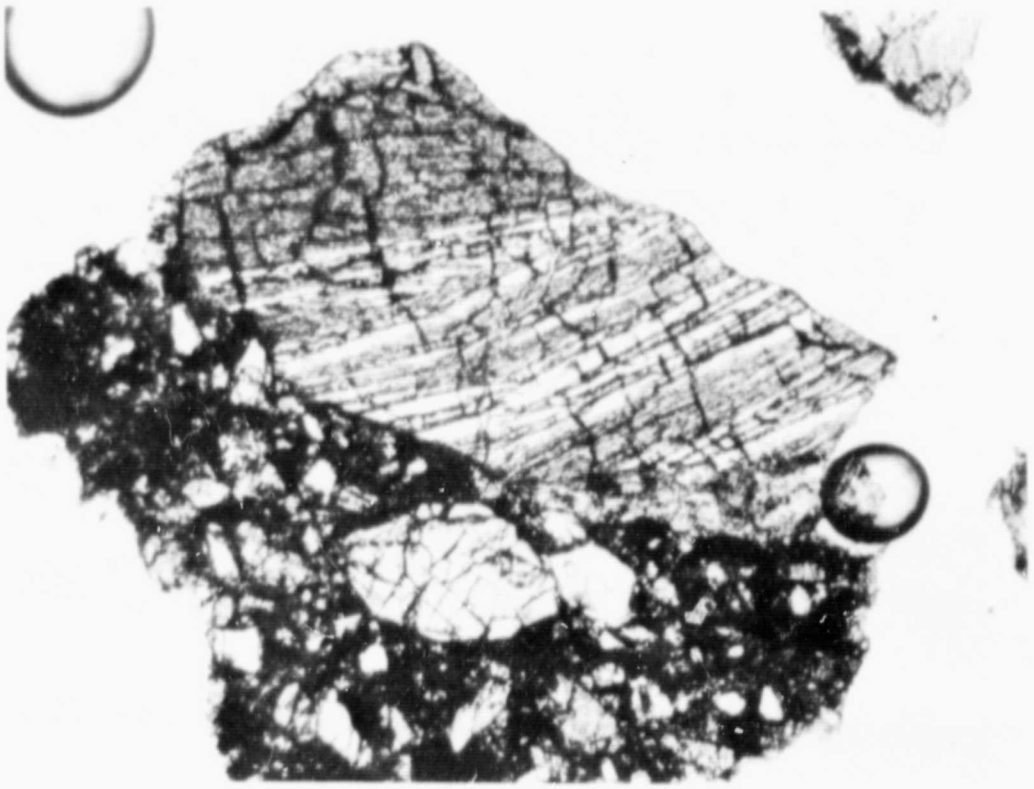



Figure III-3. Plagioclase crystal (in a soil breccia) with two superimposed fracture systems: an older, blocky fracture system and a younger, laminar fracture system. The darker parts of the crystal have become partly isotropic. Unpolarized light.

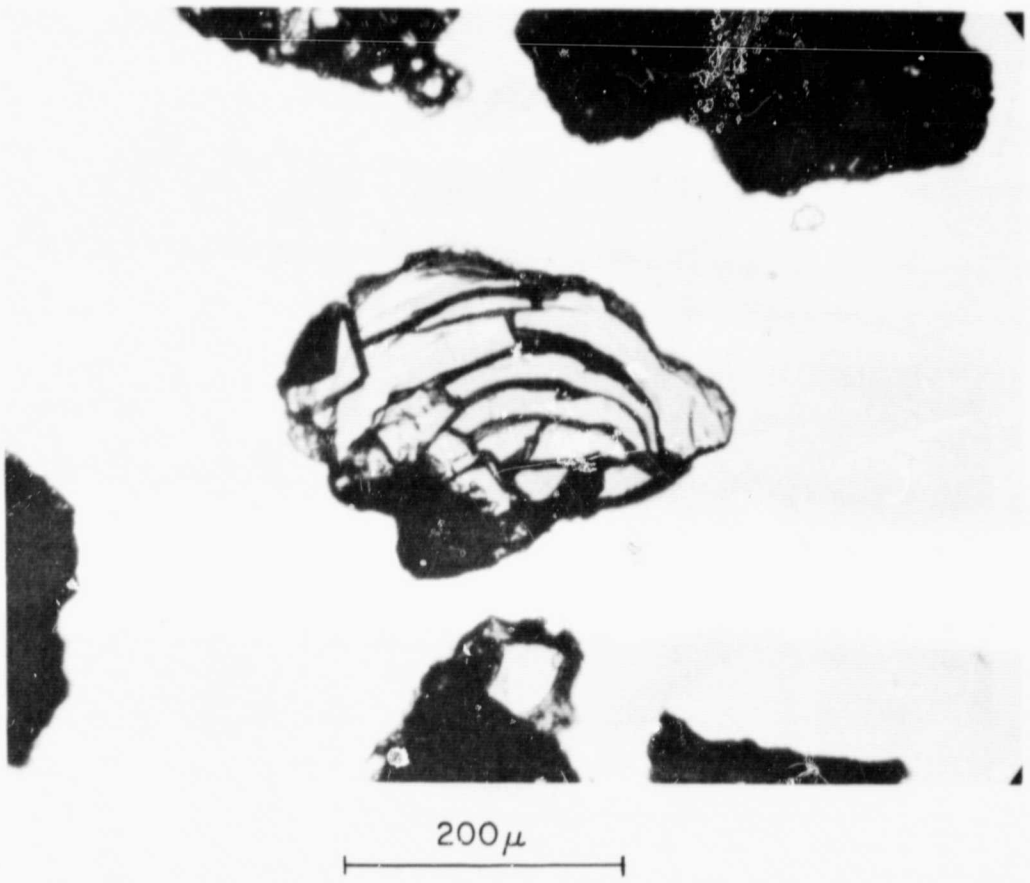



Figure III-4. Bent clinopyroxene crystal. Note the planar features normal to the curved fractures. Unpolarized light.

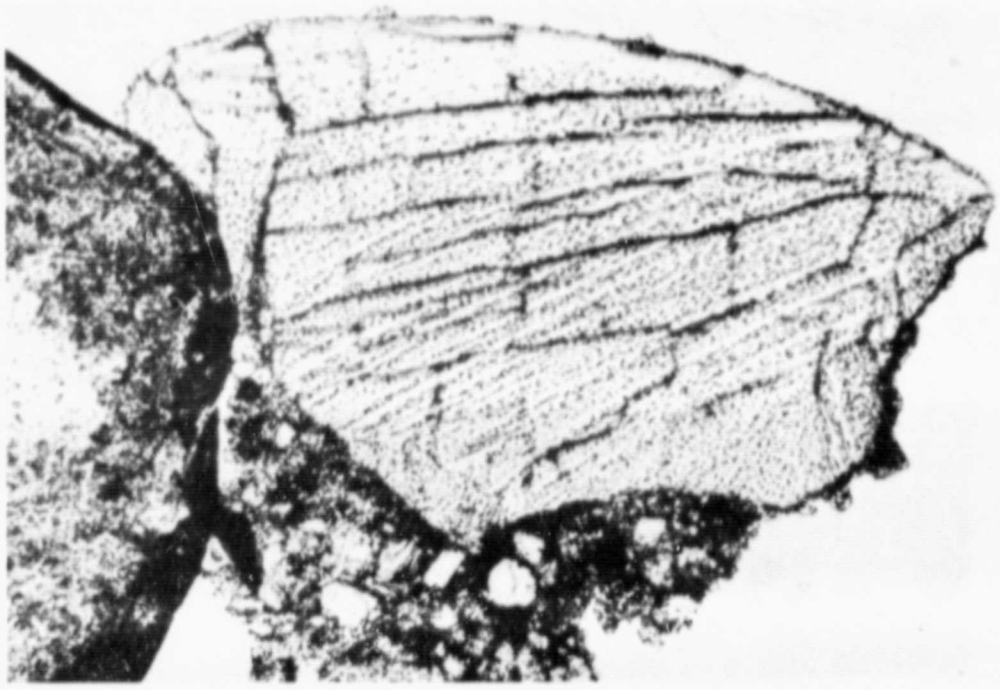



Figure III-5. Plagioclase crystal (in a soil breccia) with oriented inclusions of feldspathic glass (?). The crystal itself is largely isotropic. Unpolarized light.

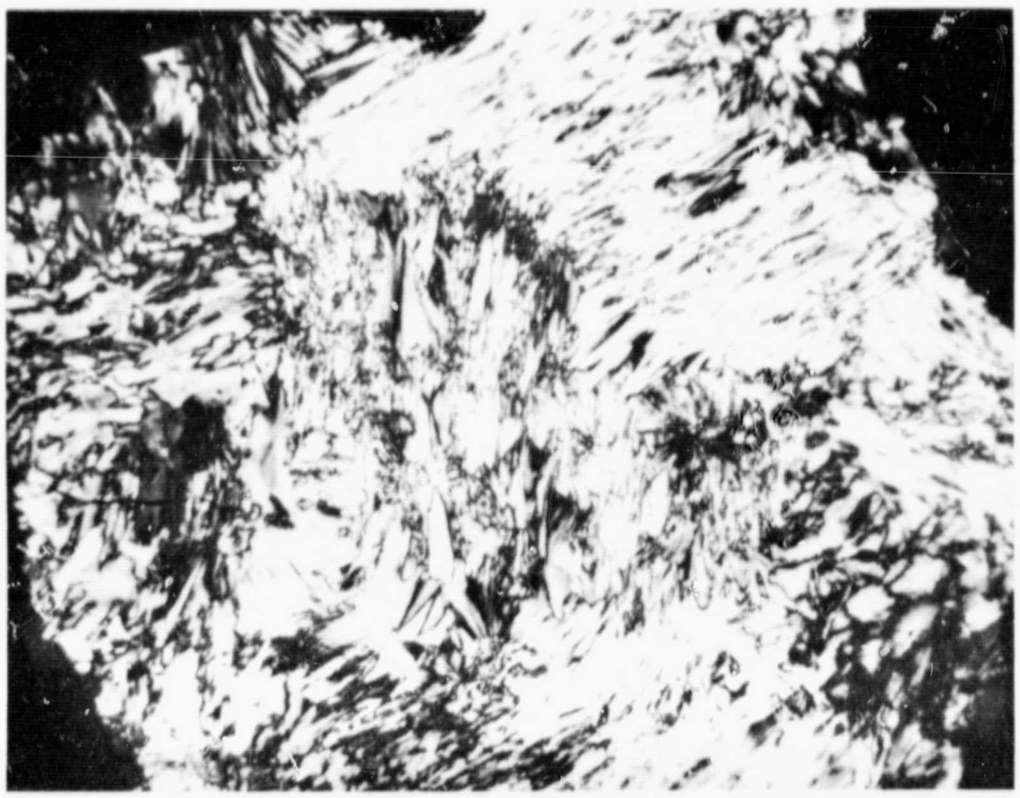



Figure III-6. An aggregate of coarse, twinned plagioclase crystals that has been sheared and disrupted into anisotropic shreds. Crossed nicols.

Table IIE-II. Mineral compositions in stony-iron "meteorite" fragment from the lunar soil sample.

| | A | B | C | D | E | F | G |
|---|---|---|---|---|---|---|---|
| Si | 24.0 | 23.4 | 23.6 | 19.8 | 16.9 | 0.2 | – |
| Ti | 0.5 | 0.1 | 0.5 | – | – | 3.4 | 33.5 |
| Al | 0.5 | 0.5 | 0.9 | 19.3 | – | 6.9 | – |
| Cr | 0.4 | 0.3 | 0.4 | – | – | 29.9 | 0.2 |
| Fe[1] | 16.4 | 21.8 | 11.4 | 0.2 | 23.4 | 24.9 | 30.9 |
| Mn | 0.3 | 0.9 | 0.2 | – | 0.3 | 0.2 | 0.3 |
| Mg | 12.9 | 9.4 | 11.0 | 0.1 | 19.9 | 2.6 | 3.0 |
| Ca | 2.7 | 3.3 | 8.8 | 13.9 | 0.1 | 0.1 | – |
| Na | 0.2 | N.D. | – | 0.3 | – | 0.2 | – |
| K[2] | – | N.D. | – | 0.05 | – | – | – |
| Ni | – | N.D. | – | – | – | – | – |
| O[3] | 42.6 | 41.7 | 42.3 | 45.6 | 39.3 | 31.4 | 33.4 |
| Total | 100.5 | 101.4 | 99.1 | 99.3 | 99.9 | 99.8 | 101.3 |
| Cations[4] | 2.03 | 2.03 | 2.02 | 5.02 | 3.01 | 3.01 | 1.99 |
| Mole % En | 59.0 | 44.5 | 51.6 | Mole % Ab 3.6 | Mole % Fo 66.2 | | |
| Mole % Fs | 33.5 | 46.2 | 23.5 | Mole % An 96.0 | Mole % Fa 33.8 | | |
| Mole % Wo | 7.5 | 9.3 | 24.9 | Mole % Or 0.4 | | | |

[1] All iron assumed to be in the +2 state.

[2] Total estimated uncertainty ± 0.01 wt. % for analysis D.

[3] Oxygen calculated on the basis of stoichiometry (see note 1).

[4] Total octahedral cations for pyroxene analyses. Total cations per eight oxygens for plagioclase, per four oxygens for olivine and chromite, per three oxygens for ilmenite.

– Means concentration level is less than twice the total estimated uncertainty, generally < 0.04 wt. %.

Key

A. Pigeonite in stony-iron lithic fragment in the lunar soil sample.

B. Typical pigeonite from the Crab Orchard mesosiderite meteorite.

C. Augite exsolution lamella in pigeonite A above. The true Ca content is doubtless somewhat higher (and Fe, Mg lower) than indicated, as the analysis probably includes some of the host pigeonite: the lamella is not much larger than the microprobe spot size.

D. Plagioclase in the stony-iron fragment (see A above).

E. Olivine in the stony-iron fragment (see A above).

F. Chromite in the stony-iron fragment (see A above).

G. Ilmenite in the stony-iron fragment (see A above).

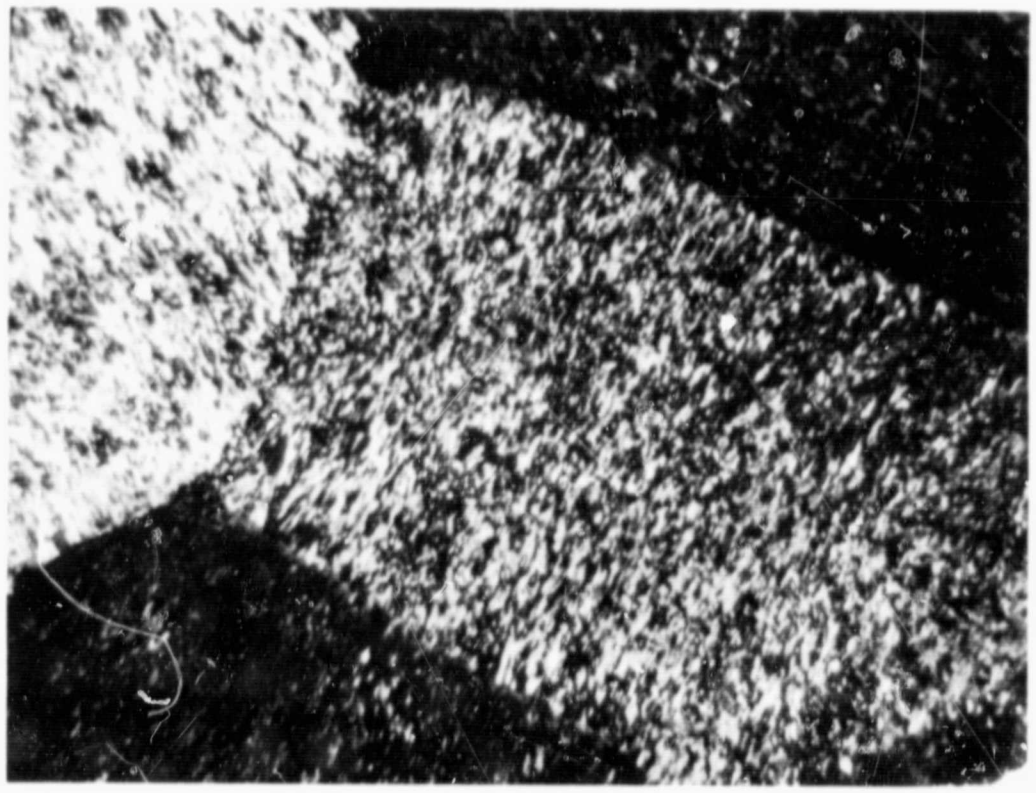



Figure III-7. The twin planes are still evident in this plagioclase crystal, but the original twins have been broken down into tiny, anisotropic units. The dark twins are nearly isotropic. Crossed nicols.

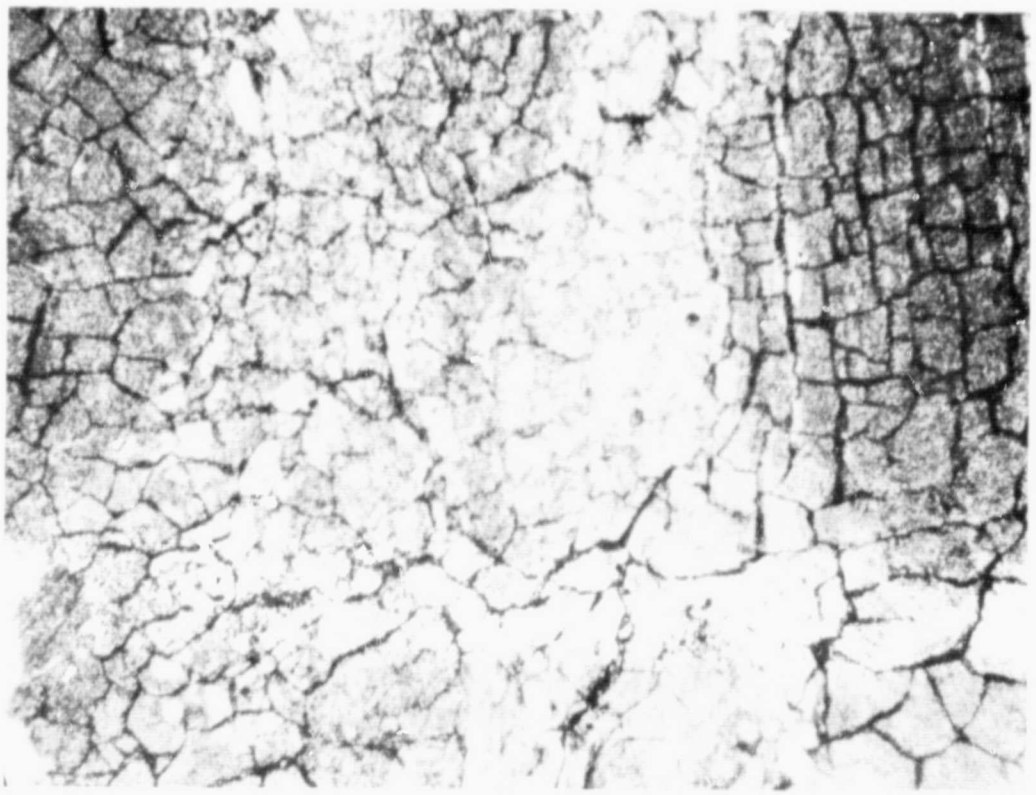



Figure III-8. Partly fused gabbroic anorthosite or anorthositic gabbro. Note the overall polygonal fracture pattern. The darker parts are nearly isotropic. The lighter, more feldspathic part in the center was not fused. Unpolarized light.

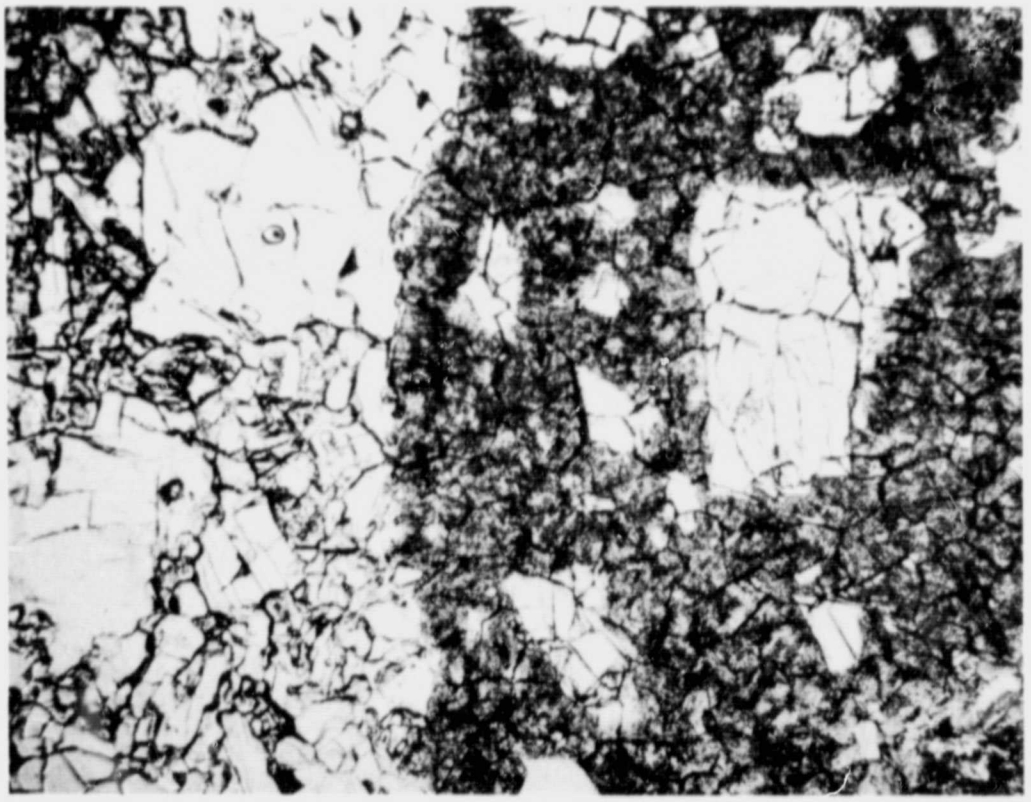



Figure III-9. Selective fusion in a fragment composed of anorthositic gabbro and gabbroic anorthosite. The gabbro was melted, but the anorthosite was only deformed. Note the unfused islands of anorthosite within the gabbroic part. Unpolarized light.

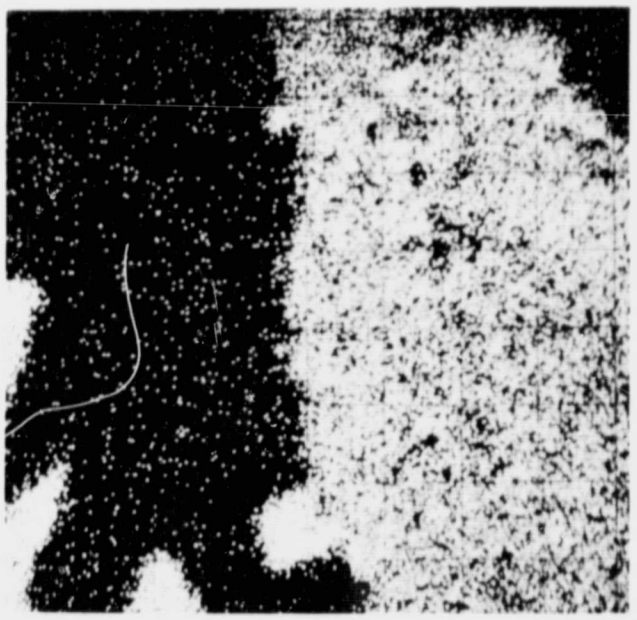



Figure III-10. A display of Mg Kα x-radiation emitted along the gabbro-anorthosite contact shown in Figure III-9. (Light points indicate Mg concentration.) The Mg concentration corresponds precisely with the field of fused gabbro and demonstrates the more mafic composition of the shock-melted zone. A similar pattern was observed for Fe.

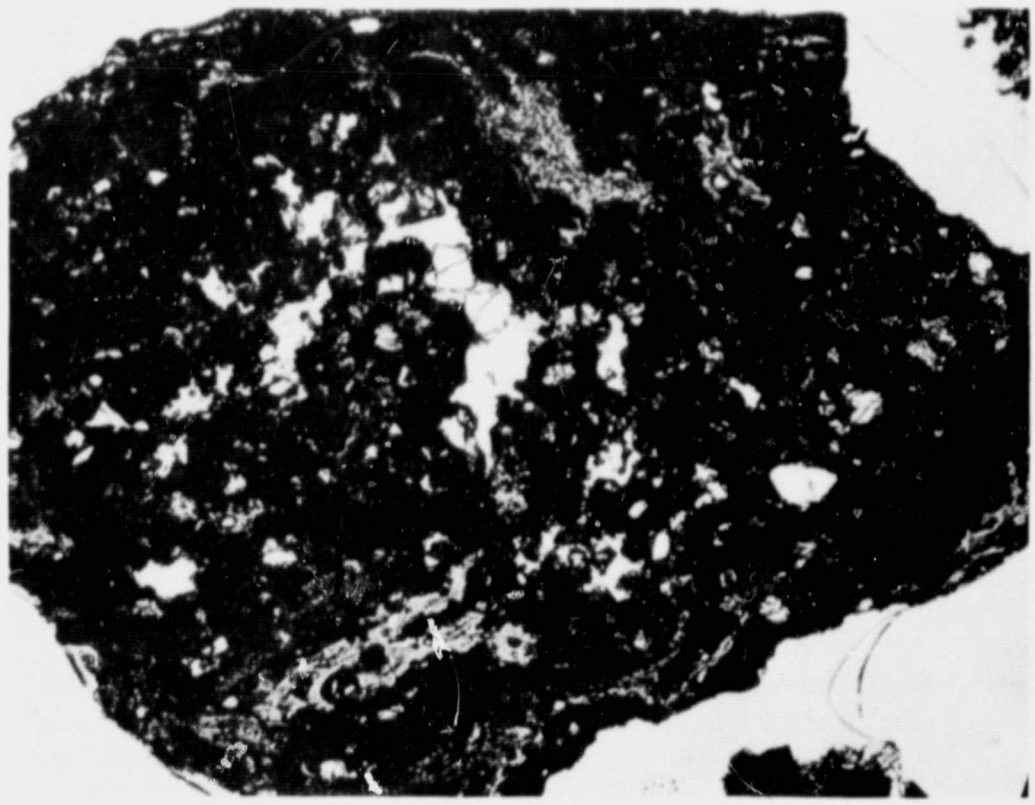



Figure III-11. Partly fused soil breccia. Note the shreds of brown glass and crystal fragments. Unpolarized light.

## IV. DISCUSSION AND INTERPRETATION

The interpretation of most of the types of fragments we have observed is straightforward enough. The basalts in the Apollo 11 sample (Section IIB) are clearly pieces of Mare Tranquillitatis itself, the bedrock underfoot. It has long been believed by most selenologists that the maria are vast lava plains, and mafic lavas (basalts) have usually been favored because of the dark color of the maria (Baldwin, 1949; Urey, 1952; Kuiper, 1954). Only the detailed chemical composition and high density of the Tranquillitatis lavas have provided surprises. A finely ground and thoroughly mixed surface "soil" layer including particles of both the Moon and the meteoritic projectiles that did the grinding was also predicted in earlier publications (Gault et al., 1966; Rennilson et al., 1966; Quaide and Oberbeck, 1968). Our observation of ~ 0.1 vol.% iron meteorite material in the Apollo 11 sample (Section IIE), although probably accompanied by at least 10 times that much stony meteorite material largely in unrecognizable form, falls somewhat short of Öpik's (1969) calculation of ~3% meteoritic component. The phenomenon of shock vitrification of silicate materials was already well known from studies of meteorites and terrestrial meteorite craters, and by hindsight it seems obvious that we should have foreseen abundant impact-melted glasses on the lunar surface (Section IID), although in fact this point was largely overlooked.

### Anorthosites as Highlands Material

Our most interesting and unexpected observation, we feel, is the presence of a substantial component (4%) of gabbroic anorthosite fragments in our sample (Section IIC). Sixty-one such fragments were observed: they are distinctly different from the mare basalts; no rock types transitional between mare basalt and anorthosite were observed among the lithic fragments studied. These rocks are substantially less dense than the mare basalts (~2.9 vs. ~3.3 gm/cm$^3$; these numbers are taken as representative

of the two anorthosite densities reported in Section IIC and the basalt densities reported in Section IIB and in LSPET (1969a, b)). They are also distinctly lighter in color (Plate 1; Figures IIC-1 and -2 vs. Figures IIB-1, -2, and -3) mostly because of the total absence of the mineral ilmenite, which is black and opaque, from the anorthosites. The anorthosites are chemically quite different from the basalts, especially in their lower content of Ti and Fe. Most interesting of all, the bulk chemical compositions of the most common anorthosite type, estimated by us on the basis of multiple defocussed-beam electron microprobe analyses, are in good agreement with the composition of lunar material at the Surveyor VII landing site on the ejecta blanket of the crater Tycho, as determined by the alpha-scattering instrument carried by Surveyor VII (Patterson et al., 1969). The comparison is drawn in Table IV-I.

Table IV-I. Apollo 11 anorthositic gabbro (9-8) vs. Tycho ejecta: a comparison of chemical compositions (atomic percent).

| Element | Fragment (9-8) | Tycho ejecta |
|---|---|---|
| C | -- | <2 |
| O | 60.9 | 58 ± 5 |
| Na | 0.2 | <3 |
| Mg | 4.1 | 4 ± 3 |
| Al | 11.3 | 9 ± 3 |
| Si | 16.2 | 18 ± 4 |
| "Ca"[a] | 5.4 | 6 ± 2 |
| "Fe"[b] | 2.0 | 2 ± 1 |

[a]All elements in the range of mass numbers 30 to 47, including P, S, K, and Ca.

[b]All elements of mass numbers 47 to 65, including Ti, Cr, Mn, Fe, and Ni.

Tycho is in the lunar highlands, and as is well known, the highlands are lighter in color (higher albedo) than the lunar maria. It is very hard to resist drawing the conclusion that the anorthosite fragments in the Apollo 11 sample are pieces of the highlands, tossed onto Mare Tranquillitatis by cratering events in the highlands. The Apollo 11 landing site is only some 50 km from the edge of the highlands, and as was noted in Section I, rays of ejecta from the highlands craters Theophilus and Alfraganus (or possibly Tycho itself) can be seen on Mare Tranquillitatis close to the landing site. It would be surprising if the Apollo 11 bulk sample did not contain a highlands component amounting to several percent, and the anorthositic fraction described is the best candidate by any criterion. Finally, it is worth reiterating that the anorthositic fragments often display evidence of severe shock damage and sometimes contain inclusions of iron meteorites, as would be expected if they had suffered through impact events violent enough to propel them 50 km or more from their sources. The concept of anorthositic highlands is indeed novel and unexpected; anorthosite is one of the few rock types that have not been previously proposed by one writer or another as the substance of the lunar surface. The most commonly held idea has probably been that the highlands are ultramafic in composition (Vinogradov et al., 1967; Urey's conception of the Moon as a largely unmelted body of undifferentiated (solar) composition implies ultramafic highlands, though this is not explicitly stated).

## A Model of Lunar Structure and Evolution

We propose that the simplest model of the lunar near-surface region consists of a "crust" of anorthosite floating on denser Ti gabbro (now solid). Presumably this crust was continuous in the Moon's earlier epochs, as it still is on the far side of the Moon, but was early punctured by impacts of very large meteoroids or planetesimals, with the bombardment occurring preferentially (for a reason not known) on the face of the Moon that is now aligned toward the Earth. The holes (maria) were filled by Ti basalt lava that welled up from below.

It is easy to see why the highlands would be "high" in such a model; they are buoyed up by deep root zones that, like the anorthosites we have sampled, are less dense than the basic rock material they "float" in. O'Keefe (1968) has noted that the lunar surface must be in a state of near-isostatic compensation, from which the mascons observed by Muller and Sjogren (1968) constitute a relatively minor deviation. On average the highlands stand about 3 km above the mare surfaces (Lamar and McGann, 1966); assuming that buoyant equilibrium prevails, we can calculate that a crust of 2.9 gm/cm$^3$ material would have to be about 25 km thick in order to support highlands 3 km above the surface of a "bath" of 3.3 gm/cm$^3$ material. (The mare basalts are quite variable in density, and few density measurements have been reported; for purposes of the computation just noted, one could wish for a more reliable estimate of the mean density of mare basalts.)

How can such a layered structure have been created? If we are willing to entertain the possibility that the Moon was largely melted in early times and that as it cooled it comprised one vast magma chamber in which crystal fractionation operated according to the classic petrologic pattern, we can see how such a structure might have been created quite straightforwardly. Given a body of composition not grossly different from the cosmic abundance tables (except unaccountably deficient in Na and reduced siderophile elements), an intense heat source, and a mechanism of cooling (discussed below), we can predict that the earliest minerals to crystallize in abundance would be olivine and anorthitic feldspar. (If melting had not been complete, the surviving minerals would again be the most refractory compounds, olivine and anorthite, so in either case these minerals would be present during early stages of the cooling cycle.) The density of anorthitic feldspar is 2.76 gm/cm$^3$ or less; olivine ranges from 3.21 (forsterite) to 4.39 gm/cm$^3$ (fayalite). (Density values are taken from the Handbook of Physical Constants, Clark (1966).) If we assume they were immersed in a gabbroic melt of composition similar to that of the mare basalt (3.3 gm/cm$^3$ solid, so assuming a 10% volume expansion on melting, as is representative of terrestrial diabases (Clark (1966), p. 93), the liquid density is about 3.0 gm/cm$^3$), the anorthite crystals would tend to float up to the surface and olivine crystals to sink.

Of course the melt phase in earliest times was not equivalent to the present mare basalt compositions; presumably the latter is a composition the melt phase was evolving toward, by removal of the elements that are used in crystallizing olivine and anorthite. But the early composition would have differed in being more basic, more nearly like the cosmic abundance table, poorer in Si and hence no less dense than the 3.0 gm/cm$^3$ value just assumed; so it seems certain that anorthite would have floated at all stages of evolution of the magma. On the other hand, it is hard to postulate a silicate magma so dense as to float olivine crystals separating from it; these must have sunk, unless they were attached to and rafted upward by larger anorthite crystals.

Continued cooling, crystallization, floating, and sinking would produce a planetary structure (sketched in Figure IV-1) consisting of a surface layer of floating anorthite crystals (plus interstitial magma of more general composition), a "core" or inner region of sunken olivine crystals and/or pyroxenes (to which olivine may be transformed by reaction with the melt phase during later stages of cooling) plus interstitial magma, and a zone between of gabbroic rock, of composition near the eutectic value for the substance of the Moon as a whole. If this interpretation is correct, we have to conclude that in the case of the Moon, Ti is greatly enriched in the eutectic or low-melting fraction; it is hard to evaluate the likelihood of this, but reconnaissance studies of the behavior of Ti in magmatic systems (MacGregor, 1969) tend to support it.

The trend of feldspar compositions in the lunar material, as reported in Figure IIB-18, is what we might reasonably expect to be produced by the magmatic process just sketched. The first plagioclase feldspar to separate from terrestrial silicate melts (natural and laboratory) is the poorest in Na; with decreasing temperature and continued crystallization, the plagioclase feldspar crystallizing becomes more sodic and less calcic. Thus, according to our model, feldspar crystals in the highlands or crustal cumulate, being the earliest to separate from the melt, ought to be poorer in Na than feldspars in the mare basalts, which were the last of the lunar magma system to

crystallize. And while none of the lunar feldspars are very generously endowed with Na, this relationship does seem to hold: 31% of the basaltic feldspars reported in Figure IIB-18 are more sodic than $An_{85}$, while only 5% of anorthositic feldspars are.

Anorthosites (90 to 100% feldspar), gabbroic anorthosites (77.5 to 90% feldspar) and anorthositic gabbros (65 to 77.5% feldspar) occur terrestrially, forming huge (and enigmatic) igneous masses principally in eastern North America and Scandinavia (Buddington, 1939). One cannot help drawing parallels between these systems and the lunar rocks. Olsen (1969) drew attention to the similarity in composition (even Ti content) between the Surveyor V analysis of lunar mare basalt and pyroxene gabbros associated with anorthosite systems on Earth, even before the Apollo 11 sample was returned. The lunar material differs from terrestrial anorthositic and associated rocks only in its lower content of alkalis and its smaller grain size.

The origin of terrestrial anorthosites has been a source of controversy. Some writers have concluded they are cumulates of feldspar crystals from more basic parent magmas – our lunar model follows this precedent; others postulate the existence of an anorthositic magma. Herz (1969) has noted that terrestrial anorthosites are spatially and temporally localized in occurrence (anorthosite ages cluster about $1.3 \pm 0.2 \times 10^9$ years) and suggests they were formed by a unique cataclysmic event. As he points out, one possibility is that the Moon was captured by the Earth at that time. Tidal friction in the Earth transfers angular momentum from the Earth to the Moon, and this has the effect of steadily increasing the Moon's distance from the Earth: MacDonald (1964) calculates (assuming a constant phase lag in the Earth's tidal bulge) that the Moon must have been very close to the Earth and suffered drastic changes in orbital parameters, just $1.79 \times 10^9$ years ago. Presumably it was captured at that time. Conceivably, the similarity between this date and the ages of terrestrial anorthosites is not a coincidence. There are difficulties, however: the lunar rocks are much older than $1.3 \times 10^9$ years (LSPET, 1969a, b), and it is hard to see how an event violent enough to

transfer anorthosite from the Moon to the Earth could fail to reset the radiometric clock on the Moon.

It is interesting to note that the mare basalt is less dense than olivine while in the molten state – hence olivine sinks through it – but more dense than the more Mg-rich olivines once it crystallizes. Thus, a partly melted Moon, in which the melt phase is similar to mare basalts in composition and density, offers the possibility of achieving through gravity crystal fractionation a density reversal – a central region or "core" that is less dense than the overlying layers (once these have crystallized)! An actual density reversal may have been prevented in the Moon by the Fe content of the olivine that would have separated and by pressure effects in the lunar interior; but we see that a density distribution that increases very little with depth (below the crust in the Moon) is certainly possible. Fortunately so, for the mean density of the Moon as a whole (3.35 $gm/cm^3$) is so nearly the same as measured densities of mare basalts that there can be no significant increase of density with depth. Note that crystal fractionation and olivine settling are essential to the establishment of a near-constant density profile: if the Moon consisted entirely of mare basalt, its density at depth would be higher than at the surface because pressures in the lunar interior are sufficient to transform the feldspar in the basalt to higher density minerals (Wetherill, 1968). Pressure at the center of the Moon (about 50 kbar) is not high enough to transform olivine or pyroxenes, however, so a cumulate of these minerals with minor amounts of interstitial feldspar would be no denser at the center of the Moon than at the surface. (Simple compression of the crystals by the lunar central pressure is approximately offset by thermal expansion attributable to reasonable central temperatures.)

## Melting of the Moon

We feel the concept of wholesale early melting of the Moon is more than just an interesting and self-consistent explanation of our data; we believe it is the only mechanism that would supply the required layerings of rock types. Extensive lunar melting has been advocated earlier by Kuiper (1954)

and Menzel (1967). Meteorite studies show that some of these objects are products of magmatic fractionation, yet they cooled too early in the history of the solar system to have been melted by decay of long-lived radionuclides (which generate heat slowly) and too near the surfaces of their parent planets for long-lived radionuclides in reasonable abundances to have been capable of effecting the melting. A potent but short-lived heat source must have operated in the newly formed meteorite planets, and Fish et al. (1960) have argued persuasively that $Al^{26}$ is the most likely candidate. Presumably some of this short-lived radionuclide (half-life, 720,000 years), generated by nucleosynthetic events that preceded solar-system formation, was incorporated in the planets when they accreted, and it provided a brief pulse of internal heat as it decayed. Wood (1967) has pointed out that if this early heat source was powerful enough to melt the parent meteorite planets, which were small (asteroidal dimensions) and therefore poor conservers of heat, then it should have affected the larger terrestrial planets (including the Moon) even more profoundly. From this point of view, it is hard to see how the Moon could have helped being melted.

However, in the words of Menzel, "This concept of lunar evolution has not been in favor during recent times." Hot, melted planets have been unfashionable since the appearance of Urey's treatise on The Planets (1952). Urey et al. (1959) argue that the present observed differences in the Moon's moment of inertia about three orthogonal axes are due to a non-isostatically adjusted distribution of densities in the Moon and that interior material would have to be fairly cool in order to be strong enough to support this disequilibrium state for all of geologic time. (However, there are other ways of understanding the moment-of-inertia data; Lamar and McGann (1966) point out that temperature inhomogeneities in a weak, isostatically adjusted Moon would also suffice. Material beneath the highlands would have to be 100 to 250° C hotter than sub-mare material.) Ness (1969) observes that the electrical conductivity of the lunar interior, as inferred from a study of the propagation of discontinuities in the interplanetary magnetic field through the Moon, requires a relatively cool interior (less than about 1000°C).

On the other hand, these objections to a hot Moon are based on the properties of that object now, not $4.7 \times 10^9$ years ago when we postulate melting in the Moon. Numerous studies of heat-flow in the Moon have been carried out (see, for example, MacDonald (1962) and Levin (1962)), and these indicate that heat loss from the Moon is sufficiently sluggish to prevent the interior from cooling significantly beneath the solidification temperature in $4.7 \times 10^9$ years. This would leave the lunar interior embarrassingly hot from the point of view of Ness' requirement. However, much uncertainty is associated with planetary heat-flow calculations, especially in the matter of the radiative transfer of heat. This process is not well understood, and the value of optical opacity most favored in heat-flow computations ($10\ cm^{-1}$) could easily be inappropriate for the deep lunar interior. Figure IV-4 shows that an opacity of $1\ cm^{-1}$ is more than adequate to cool the center of the Moon to less than 1000°C.

The early high-temperature episode we picture probably did not melt the substance of the Moon completely, nor did the lunar interior remain liquid for very long. Planetary melting is a self-defeating process because of the accident of geochemistry that all the heat-generating nuclides ($K^{40}$, $Th^{232}$, the U isotopes, and even $Al^{26}$) tend to concentrate in the low-melting fraction of silicate systems, the first liquid to appear as temperature rises; this liquid, being less dense than the unmelted silicates, makes its way to the upper reaches of the planet, carrying the heat sources to a position where they are less effective in heating the planet than they had been, much of their heat output being dissipated at the surface.

The substance of the Moon would have become mobile when it was about half or two-thirds melted, and at this point density differences would have rearranged the lunar constituents, probably less than 100% efficiently, into the three layers sketched in Figure IV-1. After this stage, temperatures would not continue to increase significantly, since heat generated in the liquid layer (B) could be efficiently conveyed upward by fluid convection, and the solid crust (A) was relatively thin. When the decay of $Al^{26}$ was completed or the early heat source of whatever nature turned off, layer (B) would have

continued to cool efficiently by convection while heavy and light minerals crystallized and, respectively, sank or floated. After final solidification of layer (B), heat transfer would everywhere be dependent on solid conduction, and the subsequent decrease of temperature in the Moon would be slow (Figure IV-4).

## Lunar Mascons

One of the most interesting recent observations of the nature of the Moon has been Muller and Sjogren's (1968) discovery of positive gravity anomalies, amounting to some 150 mgal in magnitude, centered on the more sharply defined maria, i. e., those bounded by mountain ramparts (Imbrium, Senenitatis, Crisium). Anomalies are lacking over the more ill-defined and presumably older maria such as Tranquiilitatis. The material under the maria displaying anomalies must somehow contain more mass – more grams per square centimeter of surface area – than material under the surrounding areas. This means the maria containing "mascons" are not in isostatic equilibrium with their surroundings; they "bear down" harder on underlying rock at a given distance from the center of the Moon than do their surroundings. Maintainance of this state of affairs requires that the rock beneath the mascon maria has possessed some strength since the time of formation of the mascons, but the stress differences involved are modest (30 to 50 bars) and do not exclude temperatures at this depth approaching the melting point (O'Keefe, 1968).

A number of ingenious explanations for the mascons have been proposed (Stipe, 1968; Conel and Holstrom, 1968; O'Keefe, 1968; Baldwin, 1968; Urey, 1968). We wish to point out that the simple model of lunar structure proposed in this paper offers an opportunity to understand the lunar gravity anomalies without recourse to buried meteorites, additional (hidden) rock types, mantle relief, density reversals, or sedimentation. It relies on the fact (noted above) that basalt is about 10% less dense when melted than it is in the solid state.

It is generally agreed that the maria are giant craters excavated in the lunar surface by impacts of major planetesimals in early times. Consider the formation of a crater of this type in a 25 km thick, 2.9 gm/cm$^3$ crust, at a time when the material underlying it was still partly molten. Suppose the substrate lava is able to flow into the crater, either through constricted fissures in the crater floor or as a result of the planetesimal impact having punched cleanly through the crust (Figure IV-2). Lava floods will tend to fill the crater until the substrates beneath mare and crust are in hydrostatic equilibrium. While the lava is liquid (3.0 gm/cm$^3$), the surface of the mare should stand at Level I in Figure IV-2, about 1 km lower than the mean surface elevation of the surrounding crust (highlands), when hydrostatic equilibrium is achieved. When the lava has solidified, on the other hand, the equilibrium mare surface should stand about 3 km below the mean crustal surface (Level II, Figure IV-2), since the mare density has increased to 3.3 gm/cm$^3$.

We can see several ways in which the mare surface might have dropped by 2 km. Perhaps ingress to the crater was restricted, and just enough lava was admitted into it at the outset to fill it to Level I, after which it was effectively sealed off from lava sources. Then no matter how the lava in the crater cooled and crystallized, shrinkage would be bound to drop the upper surface to Level II. Or possibly the bottom of the crater was not sealed to lava sources, but after filling to Level I crystallization proceeded in an orderly manner from the top surface downward. There are difficulties with this scheme, because once a lava crust hardens it becomes denser than the liquid under it and ought to sink; but conceivably this was prevented by the difficulty lava would have getting around and on top of the sinking crustal plate. Perhaps every time the lava crust cracked and tried to founder, lava rising through the cracks froze and healed them, leaving the crust to thicken and grow in strength, perched on top of lighter molten basalt. In this case, hydrostatic equilibrium would have required that as the lava crust thickened, it moved downward like a piston, along peripheral graben fault planes, until by the time it had crystallized to the depth of the base of the 2.9 gm/cm$^3$ crust, the surface level had dropped to Level II. Although

basalt liquid was free to come and go at the base of this system, there would have been no pressure differential to drive such a flow. In both cases just cited, no material would have been added to (or removed from) the mare system after hydrostatic equilibrium had first been established, hence there would be no mascon and no gravity anomaly. Possibly the formation of the ragged, non-mascon maria was related to one of these mechanisms.

But there is another possible filling mechanism, and it is not particularly improbable. Suppose the mare crater had filled, either in one flood or in a series of flows (Figure IV-3), to Level I and subsided during solidification to Level II, resulting in hydrostatic equilibrium between solid basalt in the mare and solid anorthosite in the crust and no gravity anomaly; but suppose also that through faults, shrinkage cracks, or otherwise, subcrustal magma sources of limited extent were still in communication with the mare surface, still had a means of egress. So far as the liquids under the crust were concerned, the equilibrium level at which their free surface would have wanted to stand was still Level I; there a 3.0 gm/cm$^3$ liquid would be in buoyant equilibrium with the crustal layer that overlay the magma zone. If the lava could find a channel to the surface and space there below Level I to fill, fill it it would.

If the volume between Levels I and II were filled with lavas derived from the root zone directly beneath the mare, this would not create a gravity anomaly. The solid part of the mare would slip down to fill the space vacated by the lava extruded; the process would amount to nothing but an exchange of hot material at depth for cooler, shallower material. This might be the means of eliminating fairly promptly any melted zones from beneath the mare and leaving it in solid contact with reasonably strong substrate rock.

If lava from beneath the highlands surrounding the mare were extruded onto the mare surface between Levels I and II, however, we would have the interesting situation where additional mass from elsewhere (laterally) in the Moon was being added to the mare, and this would constitute a mascon. It would, that is, unless there were still liquid material under the mare,

which the additional load on the mare could inject laterally back out under the highlands, replacing the lava extruded. But it is possible, as noted in the last paragraph, that sub-mare magmas would be squeezed out and permanently eliminated after a finite number of lava flows had topped Level II and pressed the mare down. After this, the mare would rest on a fairly firm foundation, and additional lavas extruded between Levels I and II would not be wholly successful in driving the mare down to a new isostatically compensated position. These uncompensated lavas would cause a gravity anomaly, the magnitude of which is easily calculated by use of the infinite-slab approximation:

$$g_z(\text{mgal}) = 41.9\,\rho L \quad ,$$

where L is the slab thickness in kilometers. (The depth of the slab is immaterial.) The situation described could have generated as much as 2 km (the interval between Levels I and II) of uncompensated basalt of density 3.3 gm/cm$^3$, which, from the above formula, would give rise to a 276 mgal positive gravity anomaly. This is almost twice the magnitude of the anomalies observed, so we can afford to concede that the maria did not overfill all the way up to Level I and/or that the material beneath was not completely successful in supporting these uncompensated loads.

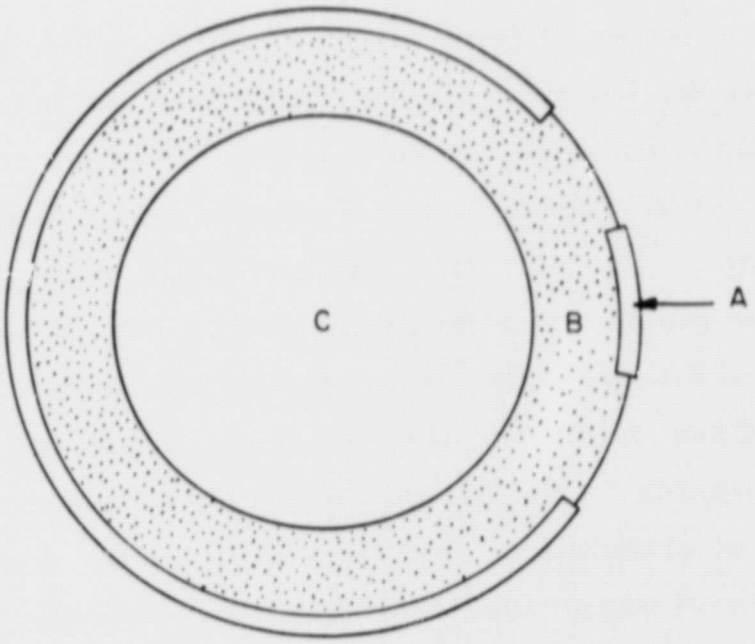
We wish to stress that this mechanism postulates no tricks in the behavior of basalt liquids: all the motions of liquids discussed are in the direction of achievement of hydrostatic equilibrium. A gravity anomaly cannot be created without some kind of disequilibrium, however; in the case at hand, the disequilibrium is between rock pressure beneath the mare vs. that beneath the highlands. The former exceeds the latter, so sub-mare material would like to flow out laterally under the highlands, but is presumably prevented by its own mechanical strength from doing so.

## Origin of the Moon

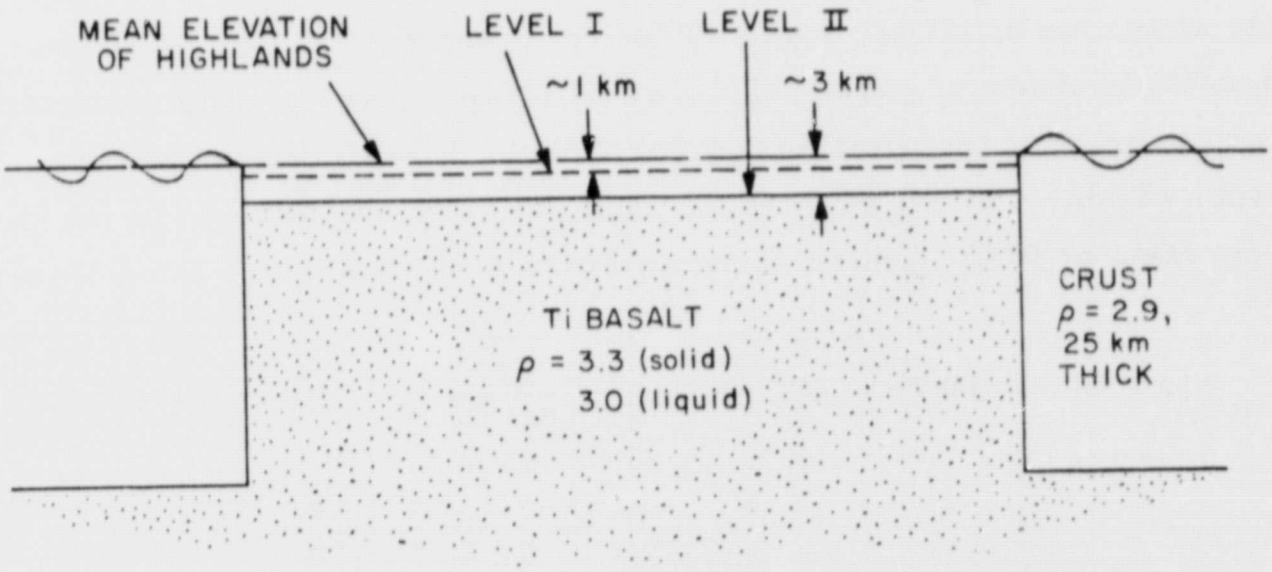
It is not apparent to us that the observations in this report offer the means of confirming or rejecting any one of the three possible modes of formation of the Moon: capture, fission from the Earth, or accretion in place.

Figure IV-1, -2, and -3. (1), proposed lunar model. In an extensively melted Moon, crystallizing anorthite ($\rho$ = 2.76) would tend to float and olivine ($\rho$ = 3.21 to 4.39) or pyroxene ($\rho$ = 3.19 to 3.55) to sink, from a residual low-melting basaltic liquid ($\rho \sim$ 3.0). Floating anorthite would form a "crust" (A) and sunken olivine/pyroxene a "core" (C), separated by liquid basalt (B), which would rise into holes torn in the crust by major cratering impacts. (2), surface levels of basalt in such a hole: buoyant equilibrium requires a surface at Level I while the basalt is a liquid, but at Level II after it crystallizes and becomes denser. (3), crater-filling by repeated lava eruptions. Even after the crater is filled to Level II with solid basalt, additional lava – in hydrostatic equilibrium with subsurface lava sources – can be laid on top of it, up to Level I. This "overfilling" of basalt would produce a positive gravity anomaly. All drawings are schematic.

1


C
B
A

2


MEAN ELEVATION
OF HIGHLANDS
LEVEL I
~1 km
LEVEL II
~3 km
Ti BASALT
ρ = 3.3 (solid)
3.0 (liquid)
CRUST
ρ = 2.9,
25 km
THICK

3

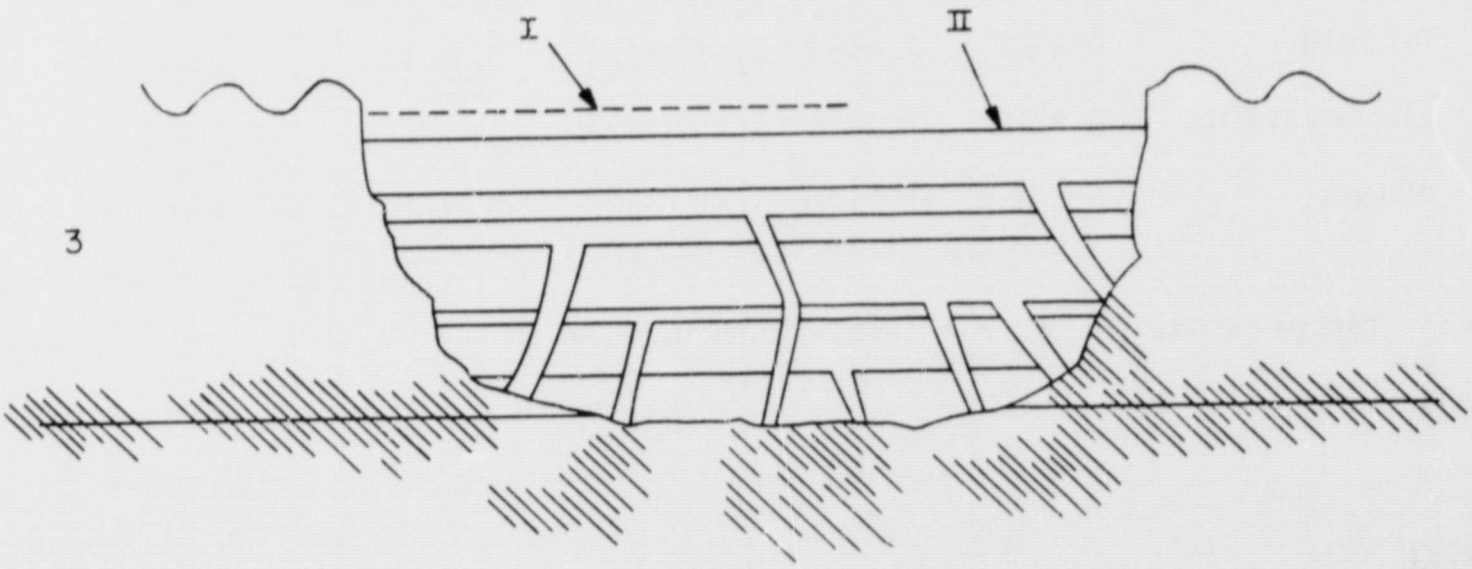
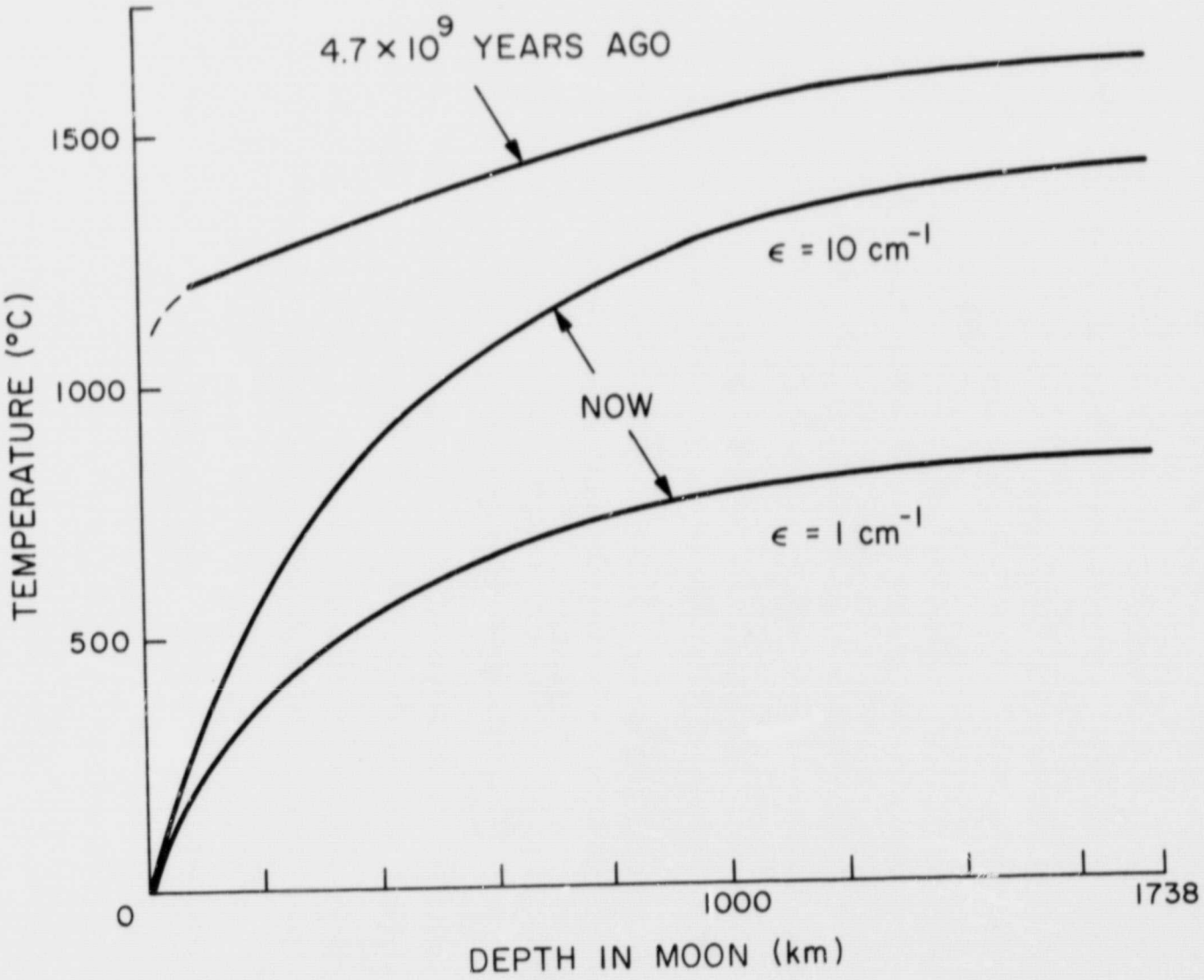

I
II

Figure IV-4. Evolution of temperature profile in an initially melted and differentiated Moon, for two different assumed values of optical opacity ($\epsilon$). Heat-flow calculations were carried out on the Rice University Burroughs 5500 computer, while one of us (JAW) was a guest of the Lunar Science Institute, Houston. The computational procedure employed 250,000-year time increments and divided the lunar radius into 20 space increments. The Moon was assumed to be differentiated into two layers. The outer layer contained 21% of the volume of the Moon and consisted of equal parts of anorthite and diopside. The Moon's overall content of K, U, and Th was taken to be that of chondrites, but all was concentrated in the upper layer. (Thus the validity of assuming chondritic radioactivity is relatively unimportant. Radioactive heat generation so near the surface of the Moon does not figure importantly in the thermal evolution investigated, which consists mostly of losses of initial heat.) The inner layer consisted of olivine and clinoenstatite in equal parts. The initial temperature profile assumed is taken to represent the melting temperature of basalt, which increases with pressure (Yoder and Tilley, 1962). Surface temperature on the Moon was held constant at 0° C. Thermal parameters employed were the following:

$$C_p = [a + b(T \times 10^{-3}) + c(T^{-2} \times 10^{5})] \frac{\text{cal}}{\text{gm °K}} ; \qquad K = [d + eT] \frac{\text{cal}}{\text{cm sec °K}}$$

| | a | b | c | d | e |
|---|---|---|---|---|---|
| anorthite | 0.232 | 0.0492 | -0.0607 | 0.00380 | 0.0000012 |
| diopside | 0.244 | 0.0362 | -0.0727 | 0.0133 | -0.0000110 |
| clinoenstatite | 0.244 | 0.0472 | -0.0626 | 0.0141 | -0.0000110 |
| olivine | 0.252 | 0.0300 | -0.0637 | 0.0144 | -0.0000070 |

(T = temperature in °K; K = lattice conductivity.)


4.7 × 10^9 YEARS AGO
1500
ε = 10 cm^-1
NOW
1000
TEMPERATURE (°C)
ε = 1 cm^-1
500
0
1000
1738
DEPTH IN MOON (km)

# V. ANALYTICAL PROCEDURES

## VA. Preliminary Sample Treatment

The sample, as received from NASA Manned Spacecraft Center, comprised two size fractions screened in the Lunar Receiving Laboratory with stainless-steel sieves. One fraction (10084,108) consisted of particles < 1 mm in size, the other (10085,24) nominally of particles > 1 mm, < 1 cm.

The first step in the preliminary sample treatment was accurate weighing of the two separates. A Chain-o-matic analytical balance was used, indicating the following: 10084,108 (5.057 gm); 10085,24 (11.094 gm). The two separates were then photographed under the binocular microscope before further treatment. Subsequent preliminary sample treatment procedures are displayed schematically in Figures VA-1 and -2. A general discussion relating to these procedures follows.

The fine sample (10084) was dry sieved through 100 mesh (149μ) nitex screen (Figure VA-1), the bulk of the < 100 mesh material (3.095 gm) receiving no further treatment other than weighing. An aliquot (~ 110 mgm) of the -100 fraction was then wet sieved (acetone, 99 mole % pure) through 200 mesh (74μ) nitex in an ultrasonic bath; the +200 -100 fraction (107.7 mgm) was air dried to be used for fiber mounting (see Section VD). The > 100 mesh fraction from the dry sieving was rinsed in acetone to remove adhering ultrafine particles that were not removable by dry sieving. The -100 washings were then collected with the -200 washings and stored to permit complete settling from the acetone before decanting the latter. The various fractions of sample 10084 (except washings) were weighed on a Cahn electrobalance and labeled.

The coarse sample (10085) after initial weighing was dry sieved through 100 mesh nitex to remove most of the adhering finer material not completely

removed in the Lunar Receiving Laboratory and produced by disaggregation of larger particles in transit. The < 100 mesh dry product received no further preliminary treatment other than weighing. The > 100 mesh fraction was then rinsed in acetone in the ultrasonic cleaner to complete removal of the finer particles. The > 100 mesh separate was extensively photographed and once more sieved (100 mesh, dry) to remove minor fines produced during sample handling. The remaining +100 fraction was screened (with acetone) successively through 10 mesh (2.00 mm) bronze wire and 30, 60, and 100 mesh (595, 250, 149μ, respectively) nitex sieves (Figure VA-2). The > 10 mesh material (4.5650 gm) was hand-separated into 10 approximate size fractions (for ease in later thin-section preparation). A portion of the -10 +30 fraction was hand-separated into 15 categories on the basis of superficial lithology, the remainder left unpicked prior to sectioning. All material < 10 mesh and > 100 mesh was ultimately made into thin sections (see Section VB). The -100 washings were allowed to settle in acetone before decanting the latter. The various separates (except washings) were weighted on the electrobalance and labeled as the final step in the preliminary sample treatment.

Table VA-I describes the materials left unused at the time of writing.

Table VA-I. Unused lunar soil sample (as of 12/30/69).

| Sample No. | Subsample | Mesh | Remaining weight (gm) |
|---|---|---|---|
| 10084,108 | FI | >100 | 0.9549 |
| | FII | <200, >100 | 0.1039 |
| | FIV | <100, dry | 3.0953 |
| TOTAL | | | 4.1641 |
| 10085,24 | Ci | <100, dry | 0.5875 |
| | Ciii | unsized | 0.0073 |
| | Civ | unsized | 0.0457 |
| | Cvi-xv | >10 | 4.1960 |
| | Cv | <100 | 0.0160 |
| TOTAL | | | 4.8525 |

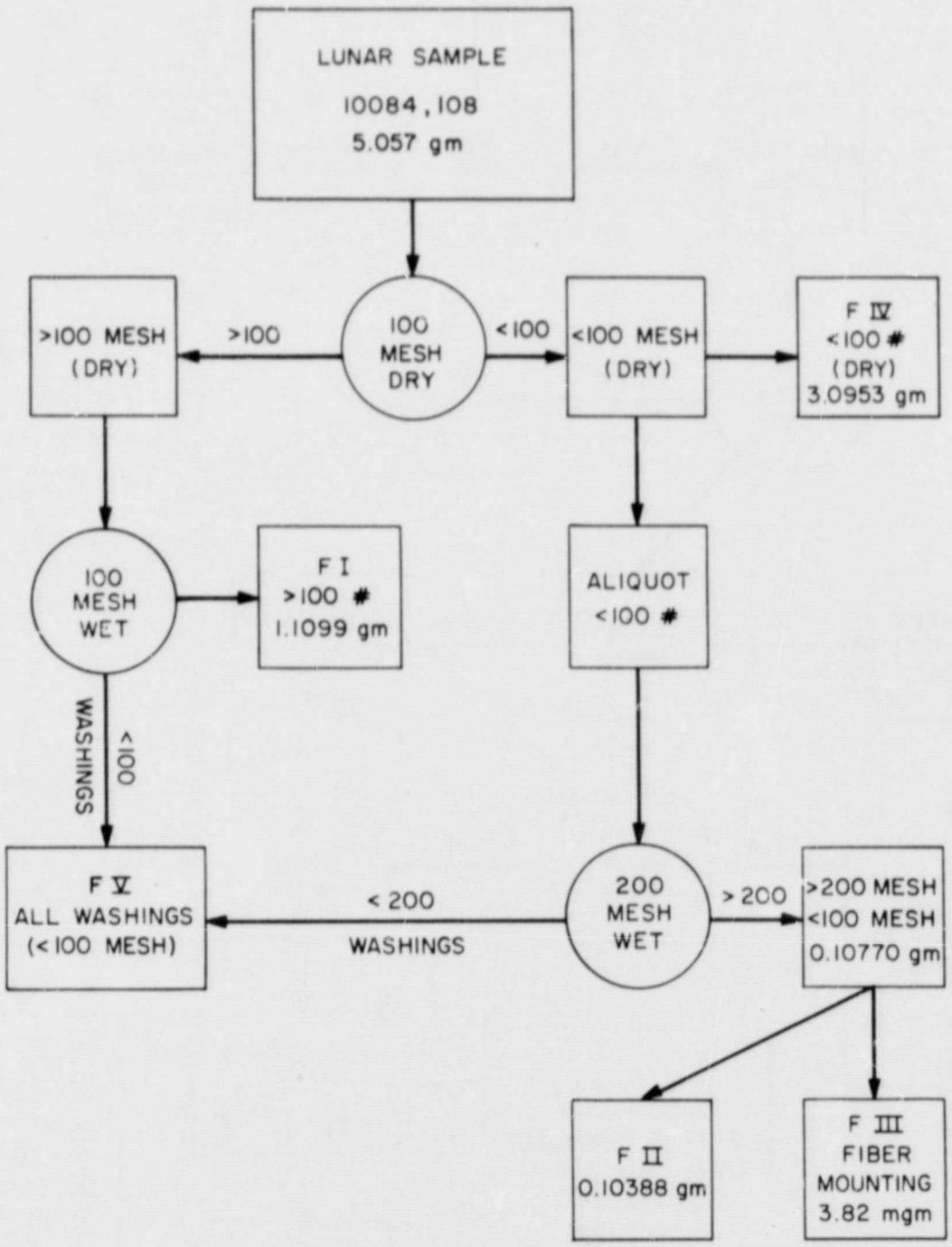



Figure VA-1. Schematic diagram of preliminary sample treatment procedures applied to the fine sample, No. 10084,108.

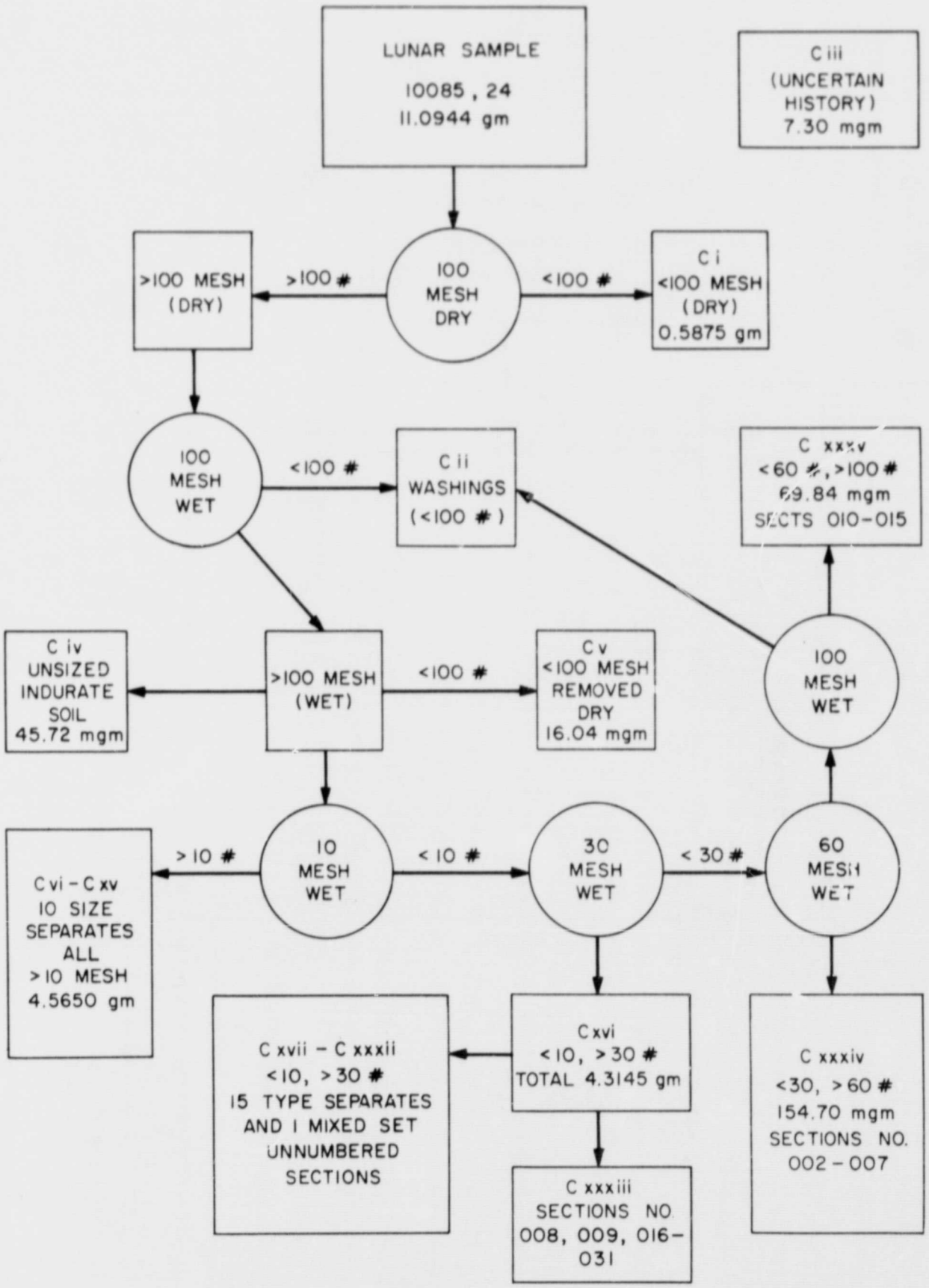



Figure VA-2. Schematic diagram of preliminary sample treatment procedures applied to the coarse sample, No. 10085, 24.

## VB. Thin-Section Preparation

The procedure followed in making thin sections of lithic fragments was essentially that outlined by Moreland (1968). Groups of lithic fragments (up to ~ 50) of similar size were arranged on a teflon plate, impregnated with epoxy (Araldite AY105 and Hardener 935F) diluted 3/1 with toluene, and cured for one hour at 100°C; then ring forms were placed over the groups and filled with Buehler Epoxide. After removal from the forms, the basal surface of each Epoxide plug, where the samples were embedded, was ground on carborundum paper (or 3μ loose abrasive in water on an iron lap, which produces a flatter surface) until the centers of the lithic fragments were exposed, then polished with 0.3μ alumina.

Each plug was then cemented to a glass slide (standard petrographic slide, 27 × 46 mm), using Araldite epoxy AY105 and Hardener 935F, approximately in the manner described by Moreland. We would add to Moreland's account that (1) not just any epoxy will do — we found that Buehler Expoxide and Cargille Araldite 6005 developed shrinkage voids during curing, and did not adhere strongly enough to the glass slide (tending to pull away during polishing); and (2) differences in thermal contraction of glass slide and epoxied-on Epoxide plug during cooling from the high-temperature (100°C) mounting procedure specified by Moreland are actually great enough to shatter the glass slide. To prevent this, as soon as plugs were epoxied to slides they were transferred to a 100°C oven; after a half hour at this temperature to complete curing, the oven temperature was decreased to 50°C and the plugs were left overnight to "anneal."

Surplus plug material was then sawed off with a 0.02-in. diamond blade, and the remaining plug-plus-lithic fragments ground down with a cup diamond wheel until feldspar interference colors were yellow-to-gray. We departed from Moreland's practice by using a DoAll Model DH-612 surface grinder (Figure VB-1) instead of Ingraham equipment for these operations, for reasons of economy. Saw blades and grinding wheels can be interchanged on the same machine, which we fitted with a splash shield and vacuum chuck.

Of great assistance in the final machine-grinding stages was a machinist's depth gauge (Figure VB-2), which we adapted to the job of measuring the thickness of section material remaining on the glass slide. The feet of the gauge stand on the blank ends of the slide, and a feeler in the center presses on the surface of the ground-off plug. The measurement can be made between passes of the grinding wheel, without removing the section from the chuck. The gauge reading can be translated directly into the number of divisions the advance wheel of the surface grinder needs to be rotated, in order to leave about 50μ of material on the slide.

In order to insure parallelism between the polished plug surface glued to the slide and the surface being ground down by the cup wheel, the grinding machine was used to "dress" each blank slide, by grinding once down the face of it with the cup wheel, before the plug was epoxied on.

Finally, sections (held in a Buehler petrographic slide holder, 30-8005) were fine-ground by hand, using a 3M extra-fine metal-backed diamond disk, or in some cases No. 600 carborundum paper, until the desired interference colors were obtained, then polished with 0.3μ alumina on a Buehler Texmet-covered lap.

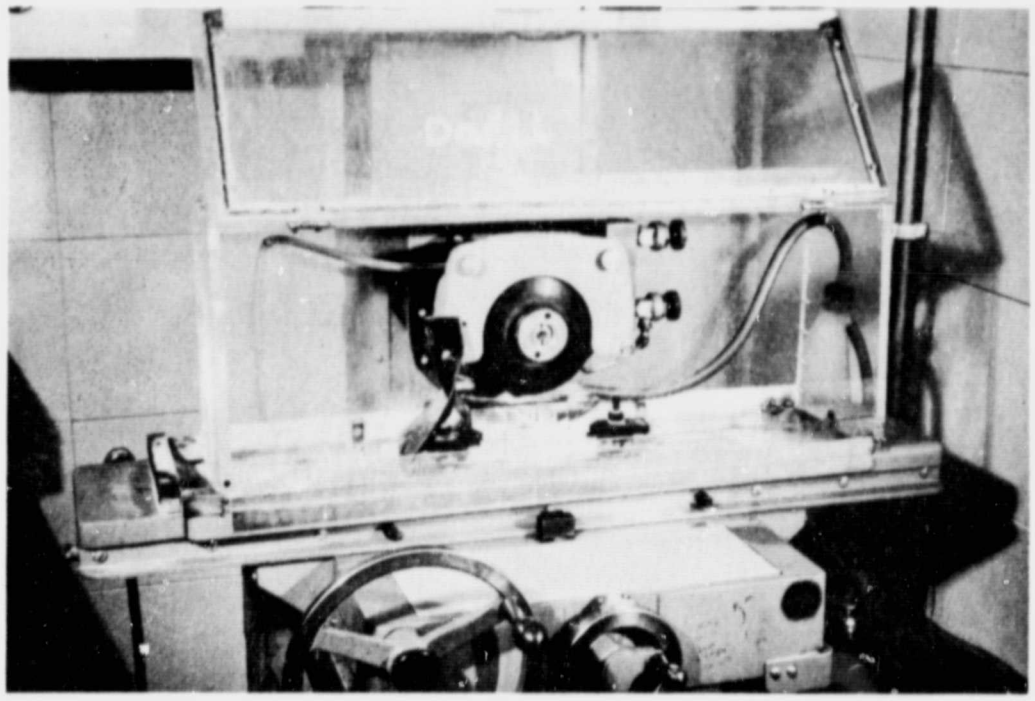


Figure VB-1. Surface grinder adapted for making thin sections.

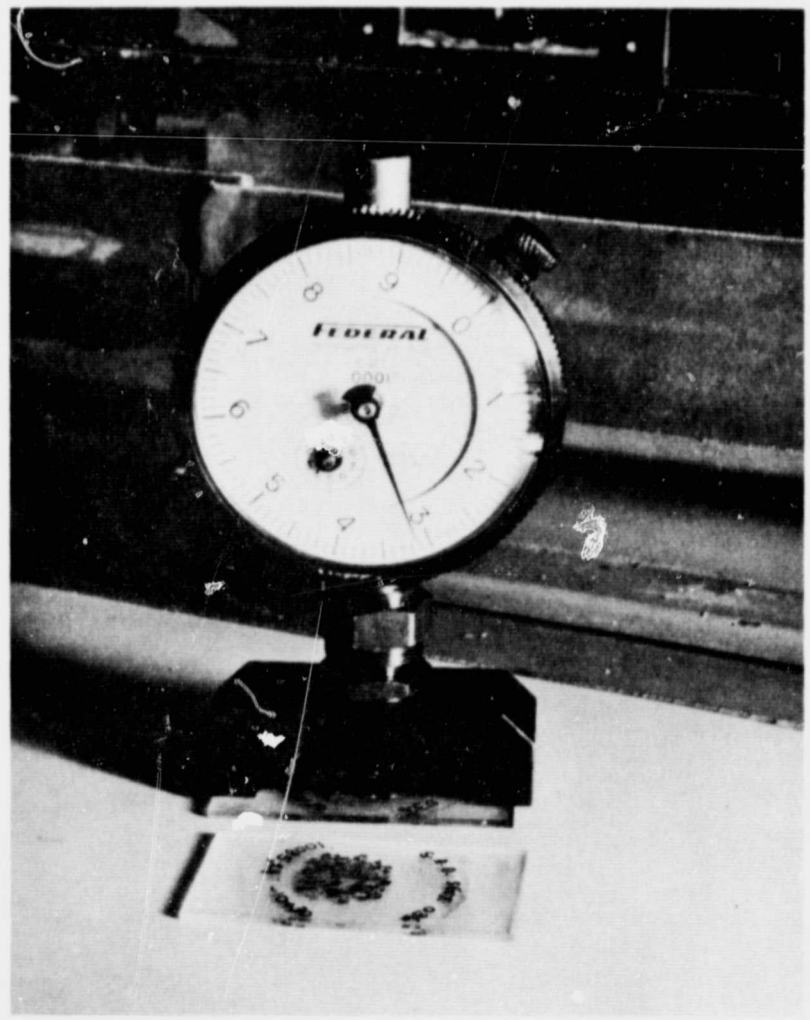



Figure VB-2. Depth gauge, adapted to measure thickness of material remaining on a glass slide during sectioning. In practice, measurement is made while section remains attached to vacuum chuck.

## VC. Microprobe Analysis

### Procedures

All microprobe analyses reported in this study were made with a MAC Model 400 electron microprobe analyzer equipped with transmitted as well as reflected light optics. Operating conditions routinely employed were 20 KV accelerating voltage and 0.010 to 0.025 μamp specimen current. Some Na and K analyses were made with 10 KV and 0.030 μamps. Thirty-second counting times were routinely used.

The three spectrometers of the MAC 400 were used simultaneously for three different elements. Detectors and analyzing crystals used for various elements are indicated in Table VC-I. For all elements pulse-height analysis (integral mode) was employed. Minerals were analyzed for all major and most minor elements (except oxygen, see below), with up to 12 elements being analyzed in most silicates. This procedure of course requires more than one run on a given analysis point. Polaroid photomicrographs taken through a Zeiss polarizing microscope in transmitted and reflected light were used to aid in relocating analysis points and for relating analyses to textures. Chemically analyzed natural and synthetic minerals were used as element standards along with certain pure metals (Fe, Ni, Co).

For the majority of analyses a focussed electron beam with a diameter of approximately 1μ was used. A few analyses were made utilizing a defocussed beam (50μ diameter). When this was done, standards as well as unknowns were analyzed with the defocussed beam. Although the standard microprobe correction procedures are partly invalidated when heterogeneous areas are analyzed with a broad beam, we found this procedure useful for estimating the bulk composition of fine-grained materials.

Data reduction was performed by a CDC 6400 computer using a program devised by one of us (JAW). This program performs the usual theoretical

corrections on both standards and unknowns. Whenever possible, standards close to the composition of the unknowns were used for major elements, to minimize the magnitude of corrections. For example, augite standards were used for Ca-rich clinopyroxene analyses (Fe, Mg, Ca, Si), an olivine standard for olivine analyses (Fe, Mg, Si), troilite for iron sulfide analyses (Fe, S), anorthite or bytownite for calcic-plagioclase analyses, etc. For an element of minor abundance in an unknown, a standard rich in that element was employed on the assumption that the uncertainty in corrections made would be less than the uncertainty in the chemical analysis for minor elements in a more realistic standard. For example, rutile was used as a Ti standard for pyroxene analyses rather than a pyroxene standard supposedly containing some 1 wt. % $TiO_2$.

The data-reduction program is iterative, repeatedly performing corrections on the raw data (using the composition arrived at in the last step to compute $f(\chi)$, etc.) until the result differs from the previous computation by less than 0.05 wt. % for all elements. The procedure used for making fluorescence corrections is basically that of Castaing, as discussed by Koopman (1968). Absorption corrections are made according to the procedure outlined by Adler and Goldstein (1965), using mass absorption coefficients compiled by Heinrich (1968). Atomic number corrections are made according to the procedure of Duncumb and Reed (1968).

In addition to matrix corrections, the data-reduction program makes corrections for detector dead-time and for specimen current drift and background. Specimen current drift is assumed to be linear between standardizations, and a time-proportionate correction is applied to all analyses made between standard readings; provisions are made for irregular time lapses during data collection when they are noted.

Background intensities are assumed to result from backscattered electrons and "white" radiation generated in the target (sample) material. Two methods of background determination were employed, depending on the intensity of the characteristic peak of an element in the unknown. For

elements with a peak/background ratio $>\sim 7$, the count rate was measured on a substance with known mean atomic number containing no elements that produce characteristic radiation of any kind at the wavelength in question. The program then calculates the background as a function of mean atomic number for standards and unknowns. For elements with a peak/background ratio $<\sim 7$, the background was estimated at each analysis point by off-setting the spectrometer symmetrically above and below the wavelength in question and averaging the two readings.

In addition to those elements actually analyzed for in an unknown, the data-reduction program is able to take account of other elements known to be present in certain stoichiometric proportions to the analyzed elements, especially oxygen. For purposes of this stoichiometric computation we assumed all Fe in silicates and oxides to be in the ferrous state. The relatively reduced nature of the lunar rocks makes this assumption reasonable.

Analytical Reliability

Our data-reduction program makes an estimate of the total uncertainty attached to each measurement, according to the formula

$$U = \sqrt{\sum_{i=1}^{\sigma} U_i^2}$$

where

$U_1$ = uncertainty due to counting statistics ($1\sigma$),

$U_2$ = 50% of the beam current drift correction,

$U_3$ = 200% of the background counting error ($1\sigma$),

$U_4$ = 25% of the absorption correction,

$U_5$ = 50% of the fluorescence correction,

$U_6$ = 15% of the atomic number correction.

Clearly the weighting factors applied to each of these various sources of uncertainty are arbitrary. They are intended to represent our best estimate as to the relative contribution to total uncertainty made by each source. For all analyses tabulated in this study this total estimated uncertainty term was used as a guide in assembling the tables of microprobe data in this report. In general we report analyses to one decimal place: we believe this to be a realistic expression of the general reliability of our analyses. The total estimated uncertainty is given in tables where exceptions to this rule occur.

Obviously there are several sources of uncertainty that are not taken into account in U. These include such things as uncertainty in the chemical analysis of a standard, imprecision in relocating analysis points during multiple runs, the possible polymineralic nature of the small volume represented by a given analysis point, etc. Such factors are difficult or impossible to evaluate quantitatively. Therefore, two criteria were applied in judging the acceptability of an analysis. First, the sum of the analysis was required to be within 98.5 to 101.0 wt. %, on the assumption that a good analysis may sum to slightly $<100\%$ because of undetermined minor elements. This criterion was applied to all analyses plotted in diagrams and to most tabulated analyses. Some exceptions appear in tables where better sums were not obtained for a particular type of analysis (usually on very fine-grained material). In these cases the sum is always presented in the table.

A second criterion for reliability was applied to silicate and some oxide analyses. The analyses were recalculated by computer to atomic percents of the various elements (including oxygen) and cation abundances relative to oxygen were calculated according to the ideal stoichiometry of the mineral. For example, in a stoichiometric pyroxene there should be two tetrahedral cations (Si plus some Al) and two octahedral cations (Mg, Fe, Ti, Cr, Mn, Al, etc.) for every six oxygens. Similarly, in a stoichiometric feldspar there should be five cations (Na, K, Ca, Al, Si, etc.) for every eight oxygens. The results of such calculations are presented with tabulated analyses where applied. They are considered to provide some measure of the reliability of the analysis (since compensating errors can still result in a good sum of elemental percentages) and of the mineralogical "purity" of the analysis (an analysis could be nearly perfect but be of a mixture of two or more phases).

Table VC-I. Detectors and analyzing crystals used in microprobe analysis.

| Elements, spectral line | Detector | Analyzing crystal |
|---|---|---|
| Na, Mg, Al, Si $K_a$ | Gas-flow proportional (90% argon, 10% methane) | KAP |
| S, K, Ca, Ti $K_a$ | | PET |
| Zr $L_a$ | | |
| Cr, Mn, Fe, Co, Ni $K_a$ | Sealed proportional (xenon) | LiF |

PRECEDING PAGE BLANK NOT FILMED.

## VD. Grain Mounting for Optical and X-Ray Measurements

In planning our procedures, our goal was to mount tiny grains on the tips of thin fibers in order to determine their optical properties in immersion media on a spindle stage, then to x-ray them, and finally to arrange them in a microprobe mount while on the same fiber. These manipulations require a light but strong fiber and tenacious glue, both of which must be transparent to x-rays and insoluble in immersion oils and rinsing media. After weeks of experimentation with fibers and binders, our assistant, Miss Wendy A. Frank, found the answer in thin glass fibers, 10μ in diameter, and Hysol Epoxi-patch. Clasped in a micromanipulator under a binocular microscope, the glass rod is tipped with a minute amount of the epoxy, which remains fluid long enough for picking up one edge or tip of a small particle. The glass rod is then transferred to a small, numbered hole drilled in a plastic bar cemented in a numbered plastic box. Each box has holes for 10 rods and when all are filled, the box is left overnight in an oven at a temperature of 60 to 70°C to cure the epoxy. These procedures have proved remarkably satisfactory so long as very careful handling at all times is the order of the day.

PRECEDING PAGE BLANK NOT FILMED.

## VE. Refractive Index and Optic Axial Angle Measurements

Refractive indices were determined by the immersion method using "sodium" monochromatic light (produced by an interference filter, $\lambda = 5890$ Å). Final matches were obtained by mixing oils, which were immediately afterward calibrated with a Leitz Abbé refractometer. Temperature gradients between microscope and refractometer were negligible. Maximum and minimum indices of anisotropic crystals were observed by rotating fiber-mounted specimens on a single-axis spindle stage, mounted horizontally on the microscope stage. After a match was obtained, the oil was drawn out of the covered specimen well with a capillary tube and transferred directly to the refractometer. Because many of the lunar crystals are distorted and clouded, their refractive indices are difficult to ascertain. In general, the precision of our measurements on crystals is ±0.002. On glasses, our precision approaches ±0.001.

The optic axial angle (2V) of biaxial crystals was measured conoscopically, whenever possible, on a five-axis universal stage by use of a Leitz conoscopic u-stage apparatus. In some instances, the measurement was made orthoscopically. Whenever possible, hemispheres of refractive index close to that of the central glass plate (n = 1.554) were used with appropriate refraction corrections for the mean index of the mineral. Precision of the measurement depends on the size of the angle: for conoscopic measurements of $2V < 40°$ the precision is ±0.5°, for $40° < 2V < 60°$ it is ±1°, for $60° < 2V$ it is ±3°. The orthoscopic precision is approximately twice the conoscopic precision.

PRECEDING PAGE BLANK NOT FILMED.

## VF. Density Determinations

Each particle was placed in Clerici solution (aqueous solution of thallium malonate and thallium formate), the specific gravity of which was adjusted until the particle hung suspended in the liquid. The specific gravity of the Clerici solution was then determined by weighing the liquid in a 2 ml or 10 ml pycnometer that had been previously calibrated with distilled water. The precision of the measurement is better than $\pm$ 0.003 gm/cm$^3$.

PRECEDING PAGE BLANK NOT FILMED.

## VG. X-Ray Diffraction Procedures

For study of the fine-grained lunar soils, we acquired an Advanced Metals Research, Inc., x-ray microfocus generator that puts out a small, very high intensity beam (Figure VG-1). A focal spot of 40 × 60μ was measured at a distance of 8 cm from the window. The x-ray head has two windows and interchangeable anodes of Cu and Fe. We used only Ni-filtered Cu radiation for the lunar particles.

With this generator we use two Enraf-Nonius Universal camera bases and three interchangeable film cassettes: one standard 114.6-mm diameter Debye-Scherrer type cassette, one 57.3-mm Debye-Scherrer type, and one 57.3-mm diameter rotation camera. The camera bases are equipped with two kinds of sample holders: one precision goniometer head, and one two-axis rotator designed by us and made in the Harvard College Observatory Model Shop (Figure VG-2).

Single crystals mounted on this rotator produce excellent powder patterns. Those on the goniometer rotate about only one axis and therefore produce spotty patterns. The goniometer mount was used mainly for powder rods and grains that appeared finely polycrystalline, or shocked. Most soil particles mounted on the goniometer yielded somewhat grainy but clearly identifiable patterns.

Exposure times of 3 to 4 hr are sufficient for identification purposes of most mineral grains down to a size of about 30μ, and these periods can be shortened by use of a helium path. Many of the lunar grains are partly glassy, however, and require longer exposures to register the included crystalline materials.

A specially designed mini-camera for holding films 52 mm long, punched for obtaining powder patterns of the Straumanis type, has been fitted into a

spare cover for our 57.3-mm Debye-Scherrer camera. It produces measurable patterns in shorter exposure times. We have developed a computer program for obtaining d spacings, corrected for film shrinkage, from 2θ readings on both of our standard-size films. The program can also be applied to the 52-mm films; it treats them as an extreme case of film shrinkage.

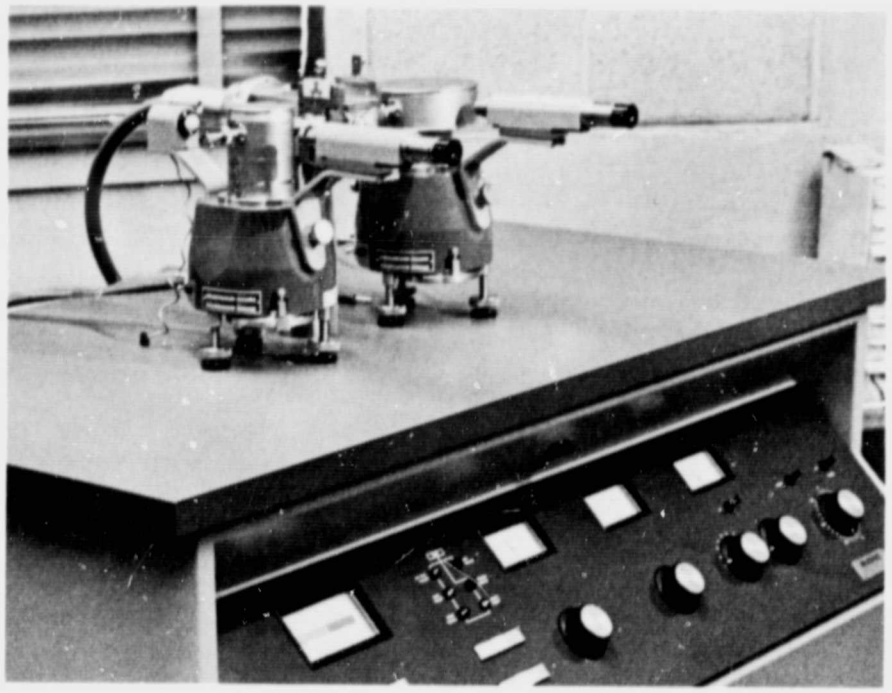


Figure VG-1. X-ray microfocus generator, Advanced Metals Research, Inc., with a camera aligned at each window. The camera bases (Enraf Nonius, Inc.) allow a choice of rotation or oscillation of the mounted crystals. Camera at right is the 114.6-mm Debye-Scherrer type cassette; that at left is the same type, 57.3-mm diameter.

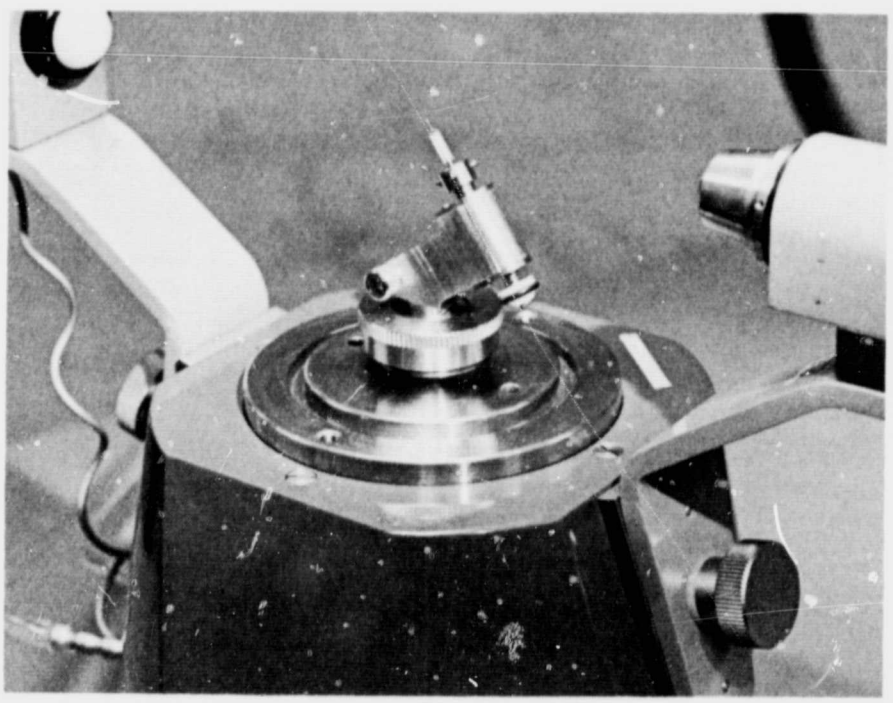


Figure VG-2. The two-axis rotating crystal mount designed by us for obtaining powder patterns from single crystals. The camera motor rotates the central vertical axis while the oblique axis is rotated by an O-ring, which rolls along the inner surface of the cylindrical metal camera base (removed for photograph).

## VI. ACKNOWLEDGMENTS

NASA grant NAS 9-8106 supported the work in this report and paid the salary of one of us (JSD). We are grateful to Fred L. Whipple for stimulating discussions of lunar theory; to Janice F. Bower for microprobe analyses; to Wendy A. Frank for handling and mounting microscopic particles; to the Lunar Science Institute for including JAW in an invaluable Symposium on the Geophysical Interpretation of the Moon (August 1969), and supplying computer facilities for heat-flow calculations; to Ann Phillips for programming the latter; and to Neil A. Armstrong, Michael Collins, and Edwin E. Aldrin, Jr., for important services rendered.

PRECEDING PAGE BLANK NOT FILMED.

## VII. REFERENCES

ADLER, I., and GOLDSTEIN, J.

1965. Absorption tables for electron probe microanalysis. NASA Tech. Note D-2984, 276 pp.

BALDWIN, R. B.

1949. The Face of the Moon. University of Chicago Press, Chicago, Illinois, 239 pp.

1968. Lunar mascons: another interpretation. Science, vol. 162, pp. 1407-1408.

BUDDINGTON, A. F.

1939. Adirondack Igneous Rocks and their Metamorphism. Geol. Soc. Amer. Mem., vol. 7, 354 pp.

BUSECK, P. R., and GOLDSTEIN, J. I.

1969. Olivine compositions and cooling rates of pallasitic meteorites. Geol. Soc. Amer. Bull., vol. 80, pp. 2141-2158.

CLARK, S. P., Jr.

1966. Handbook of Physical Constants. Geol. Soc. Amer. Mem., vol. 97, 587 pp.

CONEL, J. E., and HOLSTROM, G. B.

1968. Lunar mascons: a near-surface interpretation. Science, vol. 162, pp. 1403-1404.

DEER, W. A., HOWIE, R. A., and ZUSSMAN, J.

1962. See Ibid., 1963.

1963. Rock Forming Minerals, vol. 2: Chain Silicates. Longmans, Green & Co. Ltd., London, 379 pp.

DUKE, M. B., and SILVER, L. T.

1967. Petrology of eucrites, howardites, and mesosiderites. Geochim. Cosmochim. Acta, vol. 31, pp. 1637-1665.

DUNCUMB, P., and REED, S. J. B.

1968. The calculation of stopping power and backscatter effects in electron probe microanalysis. In Quantitative Electron Probe Microanalysis, ed. by Heinrich, K. J. F., N.B.S. Special Publication 298, pp. 133-154.

FISH, R. A., GOLES, G. G., and ANDERS, E.

1960. The record in the meteorites. III. On the development of meteorites in asteroidal bodies. Astrophys. Journ., vol. 132, pp. 243-258.

GAULT, D. E., SHOEMAKER, E. M., and MOORE, H. J.

1963. Spray ejected from the lunar surface by meteoroid impact. NASA Tech. Note D-1767, 39 pp.

GAULT, D. E., QUAIDE, W. L., OBERBECK, V. R., and MOORE, H. J.

1966. Luna 9 photographs: evidence for a fragmental surface layer. Science, vol. 153, pp. 985-988.

HEINRICH, K. J. F.

1968. Mass absorption coefficients. In The Electron Microanalyzer and its Applications, ed. by Ziebold, T. O., M.I.T. Summer Session, 1968, pp. S-22-S-34.

HERZ, N.

1969. Anorthosite belts, continental drift, and the anorthosite event. Science, vol. 164, pp. 944-947.

KOOPMAN, N. G.

1968. Fluorescence correction. In The Electron Microanalyzer and its Applications, ed. by Ziebold, T. O., M.I.T. Summer Session, 1968, pp. 70-78.

KUIPER, G. P.

1954. On the origin of the lunar surface features. Proc. U.S. Nat. Acad. Sci., vol. 40, pp. 1096-1112.

LAMAR, D. L., and McGANN, J.

1966. Shape and internal structure of the moon. Icarus, vol. 5, pp. 10-23.

LEVIN, B. J.

1962. Thermal history of the moon. In The Moon, 14th I.A.U. Symposium, Pulkovo, ed. by Kopal, Z. and Mikhailov, Z., pp. 157-167.

LSPET

1969a. Lunar Sample Information Catalogue – Apollo 11. LRL, NASA Manned Spacecraft Center, Houston, Texas.

1969b. Preliminary examination of lunar samples from Apollo 11. Science, vol. 165, pp. 1211-1227.

MacDONALD, G. J. F.

1962. On the internal constitution of the inner planets. Journ. Geophys. Res., vol. 67, pp. 2945-2974.

1964. Earth and Moon: past and future. Science, vol. 145, pp. 881-890.

MacGREGOR, I. D.

1969. The system $MgO-SiO_2-TiO_2$. Amer. Journ. Science, vol. 267A, pp. 342-363.

MENZEL, D. H.

1967. The nature of the surface of the moon, illustrated in part by 3-D slides taken from Ranger photographs. In Interpretation of Lunar Probe Data, vol. 14 of Science and Technology Series, American Astronautical Society, pp. 113-122.

MORELAND, G. C.

1968. Preparation of polished thin sections. Amer. Mineral., vol. 53, pp. 2070-2074.

MULLER, P. M., and SJOGREN, W. L.

1968. Mascons: lunar mass concentrations. Science, vol. 161, pp. 680-684.

MUNSELL COLOR COMPANY

1966. Munsell Book of Color. Munsell Color Company, Inc., Baltimore.

NESS, N. F.

1969. The electrical conductivity and internal temperature of the moon. Preprint, NASA Goddard Space Flight Center Document X-616-69-191.

O'KEEFE, J. A.

1968. Isostasy on the moon. Science, vol. 162, pp. 1405-1406.

OLSEN, E.

1969. Pyroxene gabbro (anorthosite association): similarity to Surveyor V lunar analysis. Science, vol. 166, pp. 401-402.

ÖPIK, E. J.

1969. The Moon's surface. Ann. Rev. Astron. Astrophys., vol. 7, pp. 473-526.

PATTERSON, J. H., FRANZGROTE, E. J., TURKEVICH, A. L., ANDERSON, W. A., ECONOMOU, T. E., GRIFFIN, H. E., GROTCH, S. L., and SOWINSKI, K. P.

1969. Alpha-scattering experiment on Surveyor 7: comparison with Surveyors 5 and 6. Journ. Geophys. Res., vol. 74, pp. 6120-6148.

POWELL, B. N.

1969a. Petrology and chemistry of mesosiderites. Ph.D. Thesis, Columbia University.

1969b. Petrology and chemistry of mesosiderites - I. Textures and composition of nickel-iron. Geochim. Cosmochim. Acta, vol. 33, pp. 789-810.

1969c. Silicates in mesosiderites and their genetic implications. Presented at the 32nd Annual Meeting of the Meteoritical Society, Houston, Texas.

POWELL, B. N., and WEIBLEN, P. W.

1967. On the petrology of mesosiderites. Presented at the 30th Annual Meeting of the Meteoritical Society, Moffett Field, California.

QUAIDE, W. L., and OBERBECK, V. R.

1968. Thickness determinations of the lunar surface layer from lunar impact craters. Journ. Geophys. Res., vol. 73, pp. 5247-5270.

RAMDOHR, P.

1960. Die Erzmineralien und Ihre Verwachsungen. Akademie Verlag, Berlin, 1089 pp.

RENNILSON, J. J., DRAGG, J. L., MORRIS, E. C., SHOEMAKER, E. M., and TURKEVICH, A.

1966. Surveyor I mission report, Part II, Scientific results. Jet Propulsion Lab. Tech. Rept. 32-1023, Pasadena, Calif., pp. 1-44.

STIPE, J. G.

1968. Iron meteorites as mascons. Science, vol. 162, pp. 1402-1403.

TAYLOR, S. R.

1964. Abundance of chemical elements in the continental crust: a new table. Geochim. Cosmochim. Acta, vol. 28, pp. 1273-1285.

UREY, H. C.

1952. The Planets. Yale University Press, New Haven, Connecticut, 245 pp.

UREY, H. C.

1968. Mascons and the history of the moon. Science, vol. 162, pp. 1408-1410.

UREY, H. C., ELSASSER, W. M., and ROCHESTER, M. G.

1959. Notes on the internal structure of the moon. Astrophys. Journ., vol. 129, pp. 842-848.

VINOGRADOV, A. P., SURKOV, Yu. A., CHERNOV, G. M., KIRNOZOV, F. F., and NAZARKINA, G. B.

1967. Paper presented at the 10th meeting of COSPAR, London.

WAGER, L. R., BROWN, G. M., and WADSWORTH, W. J.

1960. Types of igneous cumulates. Journ. Petrol., vol. 1, pp. 73-85.

WETHERILL, G. W.

1968. Lunar interior: constraint on basaltic composition. Science, vol. 160, pp. 1256-1257.

WOOD, J. A.

1967. The early thermal history of planets: evidence from meteorites. In Mantles of the Earth and Terrestrial Planets, ed. by Runcorn, S. K., Interscience Publishers, London, pp. 3-14.

YODER, H. S., Jr., and TILLEY, C. E.

1962. Origin of basalt magmas, and experimental study of natural and synthetic rock systems. Journ. Petrol., vol. 3, pp. 342-532.

## BIOGRAPHICAL NOTES

JOHN A. WOOD received the B.S. degree from Virginia Polytechnic Institute in 1954 and the Ph.D. degree from the Massachusetts Institute of Technology in 1958.

Dr. Wood was a research associate at the Enrico Fermi Institute for Nuclear Studies at the University of Chicago from 1963 to 1965. Since 1965, he has been a geologist at SAO and a research associate at Harvard University.

Dr. Wood's general fields of investigation are chemical analyses and mineralogical studies of meteoritic and lunar material; the study of primitive planetary material, specifically meteorites; and the problem of the origin of the planets and the solar system in general.

URSULA B. MARVIN received the B.A. degree from Tufts University, and the A.M. and Ph.D. degrees from Harvard University in geology.

Her career includes three years of teaching mineralogy and petrology at Tufts University, and six years of laboratory and field investigations of mineral deposits in the United States, Brazil, and West Africa.

Dr. Marvin joined the staff of the Smithsonian Astrophysical Observatory as a geologist in 1961 and became an associate of Harvard in 1965.

Her primary fields of investigation are mineralogical studies of lunar samples, meteorites, and the identification of cosmic dust. She is also interested in impact structures and the geological implications of satellite geodesy.

BENJAMIN N. POWELL was graduated from Amherst College in 1963, with a major in geology. He received the Ph. D. in geology from Columbia University in January 1969, and has been working at SAO since that time.

Dr. Powell is an igneous petrologist, currently specializing in the study of extraterrestrial materials, including meteorites and lunar samples.

JOHN S. DICKEY, Jr. received his Ph. D. in geology from Princeton University in 1969. He has been at SAO since January 1969.

Dr. Dickey is a petrologist, specializing in the chemistry of igneous rocks.

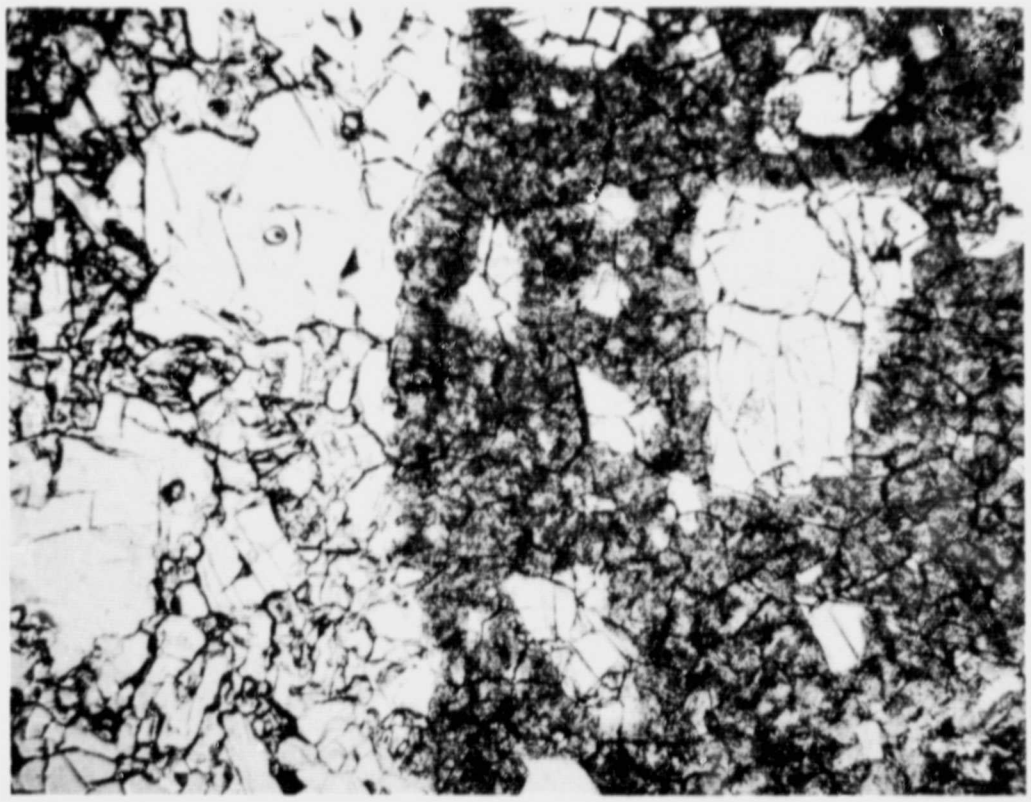



Figure III-9. Selective fusion in a fragment composed of anorthositic gabbro and gabbroic anorthosite. The gabbro was melted, but the anorthosite was only deformed. Note the unfused islands of anorthosite within the gabbroic part. Unpolarized light.

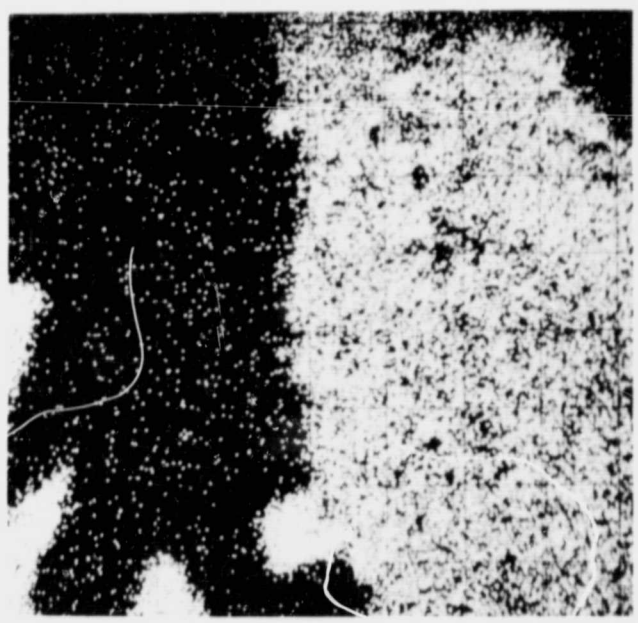



Figure III-10. A display of Mg Kα x-radiation emitted along the gabbro-anorthosite contact shown in Figure III-9. (Light points indicate Mg concentration.) The Mg concentration corresponds precisely with the field of fused gabbro and demonstrates the more mafic composition of the shock-melted zone. A similar pattern was observed for Fe.

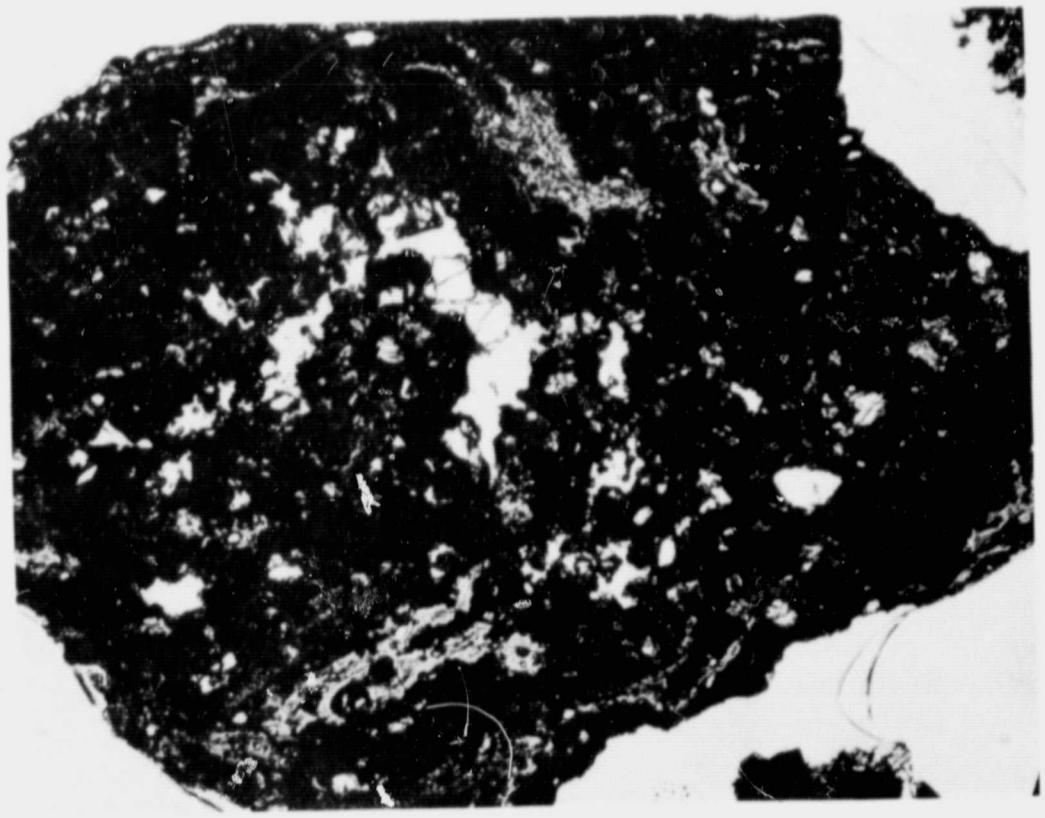



Figure III-11. Partly fused soil breccia. Note the shreds of brown glass and crystal fragments. Unpolarized light.

## IV. DISCUSSION AND INTERPRETATION

The interpretation of most of the types of fragments we have observed is straightforward enough. The basalts in the Apollo 11 sample (Section IIB) are clearly pieces of Mare Tranquillitatis itself, the bedrock underfoot. It has long been believed by most selenologists that the maria are vast lava plains, and mafic lavas (basalts) have usually been favored because of the dark color of the maria (Baldwin, 1949; Urey, 1952; Kuiper, 1954). Only the detailed chemical composition and high density of the Tranquillitatis lavas have provided surprises. A finely ground and thoroughly mixed surface "soil" layer including particles of both the Moon and the meteoritic projectiles that did the grinding was also predicted in earlier publications (Gault et al., 1966; Rennilson et al., 1966; Quaide and Oberbeck, 1968). Our observation of ~ 0.1 vol. % iron meteorite material in the Apollo 11 sample (Section IIE), although probably accompanied by at least 10 times that much stony meteorite material largely in unrecognizable form, falls somewhat short of Öpik's (1969) calculation of ~3% meteoritic component. The phenomenon of shock vitrification of silicate materials was already well known from studies of meteorites and terrestrial meteorite craters, and by hindsight it seems obvious that we should have foreseen abundant impact-melted glasses on the lunar surface (Section IID), although in fact this point was largely overlooked.

### Anorthosites as Highlands Material

Our most interesting and unexpected observation, we feel, is the presence of a substantial component (4%) of gabbroic anorthosite fragments in our sample (Section IIC). Sixty-one such fragments were observed: they are distinctly different from the mare basalts; no rock types transitional between mare basalt and anorthosite were observed among the lithic fragments studied. These rocks are substantially less dense than the mare basalts (~2.9 vs. ~3.3 gm/cm$^3$; these numbers are taken as representative

of the two anorthosite densities reported in Section IIC and the basalt densities reported in Section IIB and in LSPET (1969a, b)). They are also distinctly lighter in color (Plate 1; Figures IIC-1 and -2 vs. Figures IIB-1, -2, and -3) mostly because of the total absence of the mineral ilmenite, which is black and opaque, from the anorthosites. The anorthosites are chemically quite different from the basalts, especially in their lower content of Ti and Fe. Most interesting of all, the bulk chemical compositions of the most common anorthosite type, estimated by us on the basis of multiple defocussed-beam electron microprobe analyses, are in good agreement with the composition of lunar material at the Surveyor VII landing site on the ejecta blanket of the crater Tycho, as determined by the alpha-scattering instrument carried by Surveyor VII (Patterson et al., 1969). The comparison is drawn in Table IV-I.

Table IV-I. Apollo 11 anorthositic gabbro (9-8) vs. Tycho ejecta: a comparison of chemical compositions (atomic percent).

| Element | Fragment (9-8) | Tycho ejecta |
|---|---|---|
| C | -- | <2 |
| O | 60.9 | 58 ± 5 |
| Na | 0.2 | <3 |
| Mg | 4.1 | 4 ± 3 |
| Al | 11.3 | 9 ± 3 |
| Si | 16.2 | 18 ± 4 |
| "Ca"[a] | 5.4 | 6 ± 2 |
| "Fe"[b] | 2.0 | 2 ± 1 |

[a]All elements in the range of mass numbers 30 to 47, including P, S, K, and Ca.

[b]All elements of mass numbers 47 to 65, including Ti, Cr, Mn, Fe, and Ni.

Tycho is in the lunar highlands, and as is well known, the highlands are lighter in color (higher albedo) than the lunar maria. It is very hard to resist drawing the conclusion that the anorthosite fragments in the Apollo 11 sample are pieces of the highlands, tossed onto Mare Tranquillitatis by cratering events in the highlands. The Apollo 11 landing site is only some 50 km from the edge of the highlands, and as was noted in Section I, rays of ejecta from the highlands craters Theophilus and Alfraganus (or possibly Tycho itself) can be seen on Mare Tranquillitatis close to the landing site. It would be surprising if the Apollo 11 bulk sample did not contain a highlands component amounting to several percent, and the anorthositic fraction described is the best candidate by any criterion. Finally, it is worth reiterating that the anorthositic fragments often display evidence of severe shock damage and sometimes contain inclusions of iron meteorites, as would be expected if they had suffered through impact events violent enough to propel them 50 km or more from their sources. The concept of anorthositic highlands is indeed novel and unexpected; anorthosite is one of the few rock types that have not been previously proposed by one writer or another as the substance of the lunar surface. The most commonly held idea has probably been that the highlands are ultramafic in composition (Vinogradov et al., 1967; Urey's conception of the Moon as a largely unmelted body of undifferentiated (solar) composition implies ultramafic highlands, though this is not explicitly stated).

## A Model of Lunar Structure and Evolution

We propose that the simplest model of the lunar near-surface region consists of a "crust" of anorthosite floating on denser Ti gabbro (now solid). Presumably this crust was continuous in the Moon's earlier epochs, as it still is on the far side of the Moon, but was early punctured by impacts of very large meteoroids or planetesimals, with the bombardment occurring preferentially (for a reason not known) on the face of the Moon that is now aligned toward the Earth. The holes (maria) were filled by Ti basalt lava that welled up from below.

It is easy to see why the highlands would be "high" in such a model; they are buoyed up by deep root zones that, like the anorthosites we have sampled, are less dense than the basic rock material they "float" in. O'Keefe (1968) has noted that the lunar surface must be in a state of near-isostatic compensation, from which the mascons observed by Muller and Sjogren (1968) constitute a relatively minor deviation. On average the highlands stand about 3 km above the mare surfaces (Lamar and McGann, 1966); assuming that buoyant equilibrium prevails, we can calculate that a crust of 2.9 gm/cm$^3$ material would have to be about 25 km thick in order to support highlands 3 km above the surface of a "bath" of 3.3 gm/cm$^3$ material. (The mare basalts are quite variable in density, and few density measurements have been reported; for purposes of the computation just noted, one could wish for a more reliable estimate of the mean density of mare basalts.)

How can such a layered structure have been created? If we are willing to entertain the possibility that the Moon was largely melted in early times and that as it cooled it comprised one vast magma chamber in which crystal fractionation operated according to the classic petrologic pattern, we can see how such a structure might have been created quite straightforwardly. Given a body of composition not grossly different from the cosmic abundance tables (except unaccountably deficient in Na and reduced siderophile elements), an intense heat source, and a mechanism of cooling (discussed below), we can predict that the earliest minerals to crystallize in abundance would be olivine and anorthitic feldspar. (If melting had not been complete, the surviving minerals would again be the most refractory compounds, olivine and anorthite, so in either case these minerals would be present during early stages of the cooling cycle.) The density of anorthitic feldspar is 2.76 gm/cm$^3$ or less; olivine ranges from 3.21 (forsterite) to 4.39 gm/cm$^3$ (fayalite). (Density values are taken from the Handbook of Physical Constants, Clark (1966).) If we assume they were immersed in a gabbroic melt of composition similar to that of the mare basalt (3.3 gm/cm$^3$ solid, so assuming a 10% volume expansion on melting, as is representative of terrestrial diabases (Clark (1966), p. 93), the liquid density is about 3.0 gm/cm$^3$), the anorthite crystals would tend to float up to the surface and olivine crystals to sink.

Of course the melt phase in earliest times was not equivalent to the present mare basalt compositions; presumably the latter is a composition the melt phase was evolving toward, by removal of the elements that are used in crystallizing olivine and anorthite. But the early composition would have differed in being more basic, more nearly like the cosmic abundance table, poorer in Si and hence no less dense than the 3.0 gm/cm$^3$ value just assumed; so it seems certain that anorthite would have floated at all stages of evolution of the magma. On the other hand, it is hard to postulate a silicate magma so dense as to float olivine crystals separating from it; these must have sunk, unless they were attached to and rafted upward by larger anorthite crystals.

Continued cooling, crystallization, floating, and sinking would produce a planetary structure (sketched in Figure IV-1) consisting of a surface layer of floating anorthite crystals (plus interstitial magma of more general composition), a "core" or inner region of sunken olivine crystals and/or pyroxenes (to which olivine may be transformed by reaction with the melt phase during later stages of cooling) plus interstitial magma, and a zone between of gabbroic rock, of composition near the eutectic value for the substance of the Moon as a whole. If this interpretation is correct, we have to conclude that in the case of the Moon, Ti is greatly enriched in the eutectic or low-melting fraction; it is hard to evaluate the likelihood of this, but reconnaissance studies of the behavior of Ti in magmatic systems (MacGregor, 1969) tend to support it.

The trend of feldspar compositions in the lunar material, as reported in Figure IIB-18, is what we might reasonably expect to be produced by the magmatic process just sketched. The first plagioclase feldspar to separate from terrestrial silicate melts (natural and laboratory) is the poorest in Na; with decreasing temperature and continued crystallization, the plagioclase feldspar crystallizing becomes more sodic and less calcic. Thus, according to our model, feldspar crystals in the highlands or crustal cumulate, being the earliest to separate from the melt, ought to be poorer in Na than feldspars in the mare basalts, which were the last of the lunar magma system to

crystallize. And while none of the lunar feldspars are very generously endowed with Na, this relationship does seem to hold: 31% of the basaltic feldspars reported in Figure LB-18 are more sodic than $An_{85}$, while only 5% of anorthositic feldspars are.

Anorthosites (90 to 100% feldspar), gabbroic anorthosites (77.5 to 90% feldspar) and anorthositic gabbros (65 to 77.5% feldspar) occur terrestrially, forming huge (and enigmatic) igneous masses principally in eastern North America and Scandinavia (Buddington, 1939). One cannot help drawing parallels between these systems and the lunar rocks. Olsen (1969) drew attention to the similarity in composition (even Ti content) between the Surveyor V analysis of lunar mare basalt and pyroxene gabbros associated with anorthosite systems on Earth, even before the Apollo 11 sample was returned. The lunar material differs from terrestrial anorthositic and associated rocks only in its lower content of alkalis and its smaller grain size.

The origin of terrestrial anorthosites has been a source of controversy. Some writers have concluded they are cumulates of feldspar crystals from more basic parent magmas – our lunar model follows this precedent; others postulate the existence of an anorthositic magma. Herz (1969) has noted that terrestrial anorthosites are spatially and temporally localized in occurrence (anorthosite ages cluster about $1.3 \pm 0.2 \times 10^9$ years) and suggests they were formed by a unique cataclysmic event. As he points out, one possibility is that the Moon was captured by the Earth at that time. Tidal friction in the Earth transfers angular momentum from the Earth to the Moon, and this has the effect of steadily increasing the Moon's distance from the Earth: MacDonald (1964) calculates (assuming a constant phase lag in the Earth's tidal bulge) that the Moon must have been very close to the Earth and suffered drastic changes in orbital parameters, just $1.79 \times 10^9$ years ago. Presumably it was captured at that time. Conceivably, the similarity between this date and the ages of terrestrial anorthosites is not a coincidence. There are difficulties, however: the lunar rocks are much older than $1.3 \times 10^9$ years (LSPET, 1969a, b), and it is hard to see how an event violent enough to

transfer anorthosite from the Moon to the Earth could fail to reset the radiometric clock on the Moon.

It is interesting to note that the mare basalt is less dense than olivine while in the molten state – hence olivine sinks through it – but more dense than the more Mg-rich olivines once it crystallizes. Thus, a partly melted Moon, in which the melt phase is similar to mare basalts in composition and density, offers the possibility of achieving through gravity crystal fractionation a density reversal – a central region or "core" that is less dense than the overlying layers (once these have crystallized)! An actual density reversal may have been prevented in the Moon by the Fe content of the olivine that would have separated and by pressure effects in the lunar interior; but we see that a density distribution that increases very little with depth (below the crust in the Moon) is certainly possible. Fortunately so, for the mean density of the Moon as a whole (3.35 $gm/cm^3$) is so nearly the same as measured densities of mare basalts that there can be no significant increase of density with depth. Note that crystal fractionation and olivine settling are essential to the establishment of a near-constant density profile: if the Moon consisted entirely of mare basalt, its density at depth would be higher than at the surface because pressures in the lunar interior are sufficient to transform the feldspar in the basalt to higher density minerals (Wetherill, 1968). Pressure at the center of the Moon (about 50 kbar) is not high enough to transform olivine or pyroxenes, however, so a cumulate of these minerals with minor amounts of interstitial feldspar would be no denser at the center of the Moon than at the surface. (Simple compression of the crystals by the lunar central pressure is approximately offset by thermal expansion attributable to reasonable central temperatures.)

## Melting of the Moon

We feel the concept of wholesale early melting of the Moon is more than just an interesting and self-consistent explanation of our data; we believe it is the only mechanism that would supply the required layerings of rock types. Extensive lunar melting has been advocated earlier by Kuiper (1954)

and Menzel (1967). Meteorite studies show that some of these objects are products of magmatic fractionation, yet they cooled too early in the history of the solar system to have been melted by decay of long-lived radionuclides (which generate heat slowly) and too near the surfaces of their parent planets for long-lived radionuclides in reasonable abundances to have been capable of effecting the melting. A potent but short-lived heat source must have operated in the newly formed meteorite planets, and Fish et al. (1960) have argued persuasively that $Al^{26}$ is the most likely candidate. Presumably some of this short-lived radionuclide (half-life, 720,000 years), generated by nucleosynthetic events that preceded solar-system formation, was incorporated in the planets when they accreted, and it provided a brief pulse of internal heat as it decayed. Wood (1967) has pointed out that if this early heat source was powerful enough to melt the parent meteorite planets, which were small (asteroidal dimensions) and therefore poor conservers of heat, then it should have affected the larger terrestrial planets (including the Moon) even more profoundly. From this point of view, it is hard to see how the Moon could have helped being melted.

However, in the words of Menzel, "This concept of lunar evolution has not been in favor during recent times." Hot, melted planets have been unfashionable since the appearance of Urey's treatise on The Planets (1952). Urey et al. (1959) argue that the present observed differences in the Moon's moment of inertia about three orthogonal axes are due to a non-isostatically adjusted distribution of densities in the Moon and that interior material would have to be fairly cool in order to be strong enough to support this disequilibrium state for all of geologic time. (However, there are other ways of understanding the moment-of-inertia data; Lamar and McGann (1966) point out that temperature inhomogeneities in a weak, isostatically adjusted Moon would also suffice. Material beneath the highlands would have to be 100 to 250° C hotter than sub-mare material.) Ness (1969) observes that the electrical conductivity of the lunar interior, as inferred from a study of the propagation of discontinuities in the interplanetary magnetic field through the Moon, requires a relatively cool interior (less than about 1000° C).

On the other hand, these objections to a hot Moon are based on the properties of that object now, not $4.7 \times 10^9$ years ago when we postulate melting in the Moon. Numerous studies of heat-flow in the Moon have been carried out (see, for example, MacDonald (1962) and Levin (1962)), and these indicate that heat loss from the Moon is sufficiently sluggish to prevent the interior from cooling significantly beneath the solidification temperature in $4.7 \times 10^9$ years. This would leave the lunar interior embarrassingly hot from the point of view of Ness' requirement. However, much uncertainty is associated with planetary heat-flow calculations, especially in the matter of the radiative transfer of heat. This process is not well understood, and the value of optical opacity most favored in heat-flow computations ($10\ cm^{-1}$) could easily be inappropriate for the deep lunar interior. Figure IV-4 shows that an opacity of $1\ cm^{-1}$ is more than adequate to cool the center of the Moon to less than 1000°C.

The early high-temperature episode we picture probably did not melt the substance of the Moon completely, nor did the lunar interior remain liquid for very long. Planetary melting is a self-defeating process because of the accident of geochemistry that all the heat-generating nuclides ($K^{40}$, $Th^{232}$, the U isotopes, and even $Al^{26}$) tend to concentrate in the low-melting fraction of silicate systems, the first liquid to appear as temperature rises; this liquid, being less dense than the unmelted silicates, makes its way to the upper reaches of the planet, carrying the heat sources to a position where they are less effective in heating the planet than they had been, much of their heat output being dissipated at the surface.

The substance of the Moon would have become mobile when it was about half or two-thirds melted, and at this point density differences would have rearranged the lunar constituents, probably less than 100% efficiently, into the three layers sketched in Figure IV-1. After this stage, temperatures would not continue to increase significantly, since heat generated in the liquid layer (B) could be efficiently conveyed upward by fluid convection, and the solid crust (A) was relatively thin. When the decay of $Al^{26}$ was completed or the early heat source of whatever nature turned off, layer (B) would have

continued to cool efficiently by convection while heavy and light minerals crystallized and, respectively, sank or floated. After final solidification of layer (B), heat transfer would everywhere be dependent on solid conduction, and the subsequent decrease of temperature in the Moon would be slow (Figure IV-4).

## Lunar Mascons

One of the most interesting recent observations of the nature of the Moon has been Muller and Sjogren's (1968) discovery of positive gravity anomalies, amounting to some 150 mgal in magnitude, centered on the more sharply defined maria, i. e., those bounded by mountain ramparts (Imbrium, Senenitatis, Crisium). Anomalies are lacking over the more ill-defined and presumably older maria such as Tranquillitatis. The material under the maria displaying anomalies must somehow contain more mass – more grams per square centimeter of surface area – than material under the surrounding areas. This means the maria containing "mascons" are not in isostatic equilibrium with their surroundings; they "bear down" harder on underlying rock at a given distance from the center of the Moon than do their surroundings. Maintainance of this state of affairs requires that the rock beneath the mascon maria has possessed some strength since the time of formation of the mascons, but the stress differences involved are modest (30 to 50 bars) and do not exclude temperatures at this depth approaching the melting point (O'Keefe, 1968).

A number of ingenious explanations for the mascons have been proposed (Stipe, 1968; Conel and Holstrom, 1968; O'Keefe, 1968; Baldwin, 1968; Urey, 1968). We wish to point out that the simple model of lunar structure proposed in this paper offers an opportunity to understand the lunar gravity anomalies without recourse to buried meteorites, additional (hidden) rock types, mantle relief, density reversals, or sedimentation. It relies on the fact (noted above) that basalt is about 10% less dense when melted than it is in the solid state.

It is generally agreed that the maria are giant craters excavated in the lunar surface by impacts of major planetesimals in early times. Consider the formation of a crater of this type in a 25 km thick, 2.9 gm/cm$^3$ crust, at a time when the material underlying it was still partly molten. Suppose the substrate lava is able to flow into the crater, either through constricted fissures in the crater floor or as a result of the planetesimal impact having punched cleanly through the crust (Figure IV-2). Lava floods will tend to fill the crater until the substrates beneath mare and crust are in hydrostatic equilibrium. While the lava is liquid (3.0 gm/cm$^3$), the surface of the mare should stand at Level I in Figure IV-2, about 1 km lower than the mean surface elevation of the surrounding crust (highlands), when hydrostatic equilibrium is achieved. When the lava has solidified, on the other hand, the equilibrium mare surface should stand about 3 km below the mean crustal surface (Level II, Figure IV-2), since the mare density has increased to 3.3 gm/cm$^3$.

We can see several ways in which the mare surface might have dropped by 2 km. Perhaps ingress to the crater was restricted, and just enough lava was admitted into it at the outset to fill it to Level I, after which it was effectively sealed off from lava sources. Then no matter how the lava in the crater cooled and crystallized, shrinkage would be bound to drop the upper surface to Level II. Or possibly the bottom of the crater was not sealed to lava sources, but after filling to Level I crystallization proceeded in an orderly manner from the top surface downward. There are difficulties with this scheme, because once a lava crust hardens it becomes denser than the liquid under it and ought to sink; but conceivably this was prevented by the difficulty lava would have getting around and on top of the sinking crustal plate. Perhaps every time the lava crust cracked and tried to founder, lava rising through the cracks froze and healed them, leaving the crust to thicken and grow in strength, perched on top of lighter molten basalt. In this case, hydrostatic equilibrium would have required that as the lava crust thickened, it moved downward like a piston, along peripheral graben fault planes, until by the time it had crystallized to the depth of the base of the 2.9 gm/cm$^3$ crust, the surface level had dropped to Level II. Although

basalt liquid was free to come and go at the base of this system, there would have been no pressure differential to drive such a flow. In both cases just cited, no material would have been added to (or removed from) the mare system after hydrostatic equilibrium had first been established, hence there would be no mascon and no gravity anomaly. Possibly the formation of the ragged, non-mascon maria was related to one of these mechanisms.

But there is another possible filling mechanism, and it is not particularly improbable. Suppose the mare crater had filled, either in one flood or in a series of flows (Figure IV-3), to Level I and subsided during solidification to Level II, resulting in hydrostatic equilibrium between solid basalt in the mare and solid anorthosite in the crust and no gravity anomaly; but suppose also that through faults, shrinkage cracks, or otherwise, subcrustal magma sources of limited extent were still in communication with the mare surface, still had a means of egress. So far as the liquids under the crust were concerned, the equilibrium level at which their free surface would have wanted to stand was still Level I; there a 3.0 gm/cm$^3$ liquid would be in buoyant equilibrium with the crustal layer that overlay the magma zone. If the lava could find a channel to the surface and space there below Level I to fill, fill it it would.

If the volume between Levels I and II were filled with lavas derived from the root zone directly beneath the mare, this would not create a gravity anomaly. The solid part of the mare would slip down to fill the space vacated by the lava extruded; the process would amount to nothing but an exchange of hot material at depth for cooler, shallower material. This might be the means of eliminating fairly promptly any melted zones from beneath the mare and leaving it in solid contact with reasonably strong substrate rock.

If lava from beneath the highlands surrounding the mare were extruded onto the mare surface between Levels I and II, however, we would have the interesting situation where additional mass from elsewhere (laterally) in the Moon was being added to the mare, and this would constitute a mascon. It would, that is, unless there were still liquid material under the mare,

which the additional load on the mare could inject laterally back out under the highlands, replacing the lava extruded. But it is possible, as noted in the last paragraph, that sub-mare magmas would be squeezed out and permanently eliminated after a finite number of lava flows had topped Level II and pressed the mare down. After this, the mare would rest on a fairly firm foundation, and additional lavas extruded between Levels I and II would not be wholly successful in driving the mare down to a new isostatically compensated position. These uncompensated lavas would cause a gravity anomaly, the magnitude of which is easily calculated by use of the infinite-slab approximation:

$$g_z(\text{mgal}) = 41.9\,\rho L \quad ,$$

where L is the slab thickness in kilometers. (The depth of the slab is immaterial.) The situation described could have generated as much as 2 km (the interval between Levels I and II) of uncompensated basalt of density 3.3 gm/cm$^3$, which, from the above formula, would give rise to a 276 mgal positive gravity anomaly. This is almost twice the magnitude of the anomalies observed, so we can afford to concede that the maria did not overfill all the way up to Level I and/or that the material beneath was not completely successful in supporting these uncompensated loads.

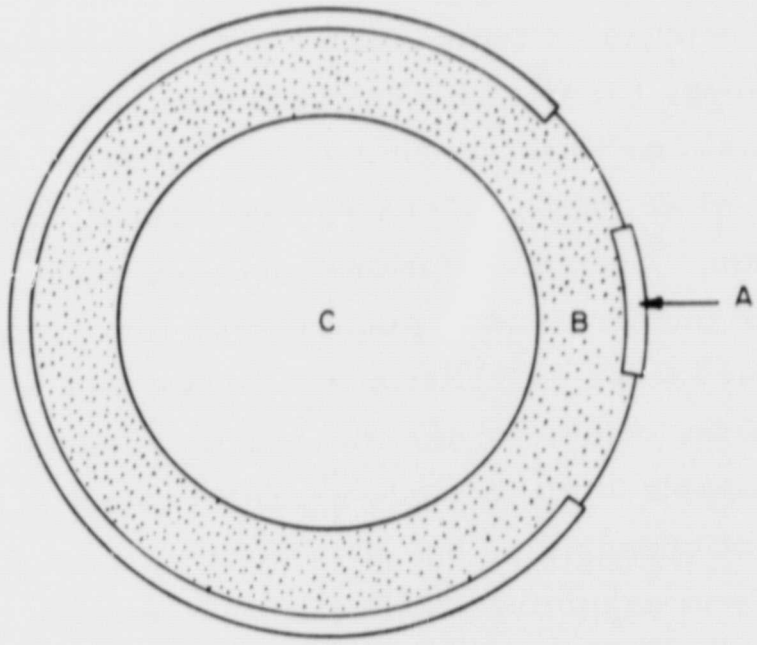
We wish to stress that this mechanism postulates no tricks in the behavior of basalt liquids: all the motions of liquids discussed are in the direction of achievement of hydrostatic equilibrium. A gravity anomaly cannot be created without some kind of disequilibrium, however; in the case at hand, the disequilibrium is between rock pressure beneath the mare vs. that beneath the highlands. The former exceeds the latter, so sub-mare material would like to flow out laterally under the highlands, but is presumably prevented by its own mechanical strength from doing so.

## Origin of the Moon

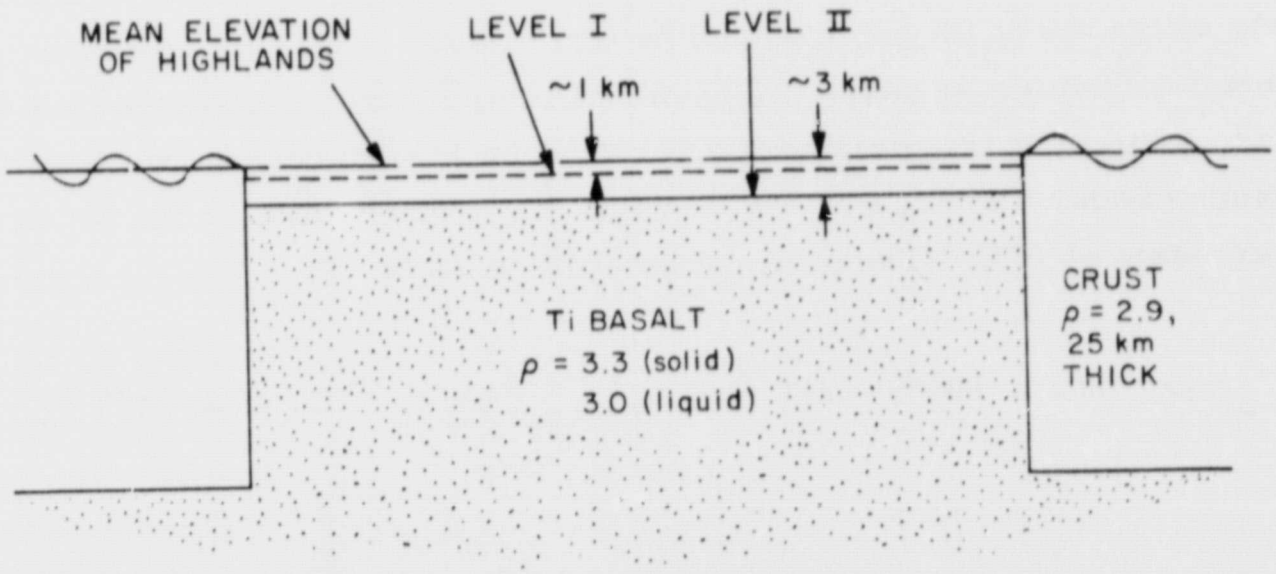
It is not apparent to us that the observations in this report offer the means of confirming or rejecting any one of the three possible modes of formation of the Moon: capture, fission from the Earth, or accretion in place.

Figure IV-1, -2, and -3. (1), proposed lunar model. In an extensively melted Moon, crystallizing anorthite ($\rho$ = 2.76) would tend to float and olivine ($\rho$ = 3.21 to 4.39) or pyroxene ($\rho$ = 3.19 to 3.55) to sink, from a residual low-melting basaltic liquid ($\rho \sim$ 3.0). Floating anorthite would form a "crust" (A) and sunken olivine/pyroxene a "core" (C), separated by liquid basalt (B), which would rise into holes torn in the crust by major cratering impacts. (2), surface levels of basalt in such a hole: buoyant equilibrium requires a surface at Level I while the basalt is a liquid, but at Level II after it crystallizes and becomes denser. (3), crater-filling by repeated lava eruptions. Even after the crater is filled to Level II with solid basalt, additional lava – in hydrostatic equilibrium with subsurface lava sources – can be laid on top of it, up to Level I. This "overfilling" of basalt would produce a positive gravity anomaly. All drawings are schematic.

1


C
B
A

2


MEAN ELEVATION
OF HIGHLANDS
LEVEL I
~1 km
LEVEL II
~3 km
Ti BASALT
ρ = 3.3 (solid)
3.0 (liquid)
CRUST
ρ = 2.9,
25 km
THICK

3

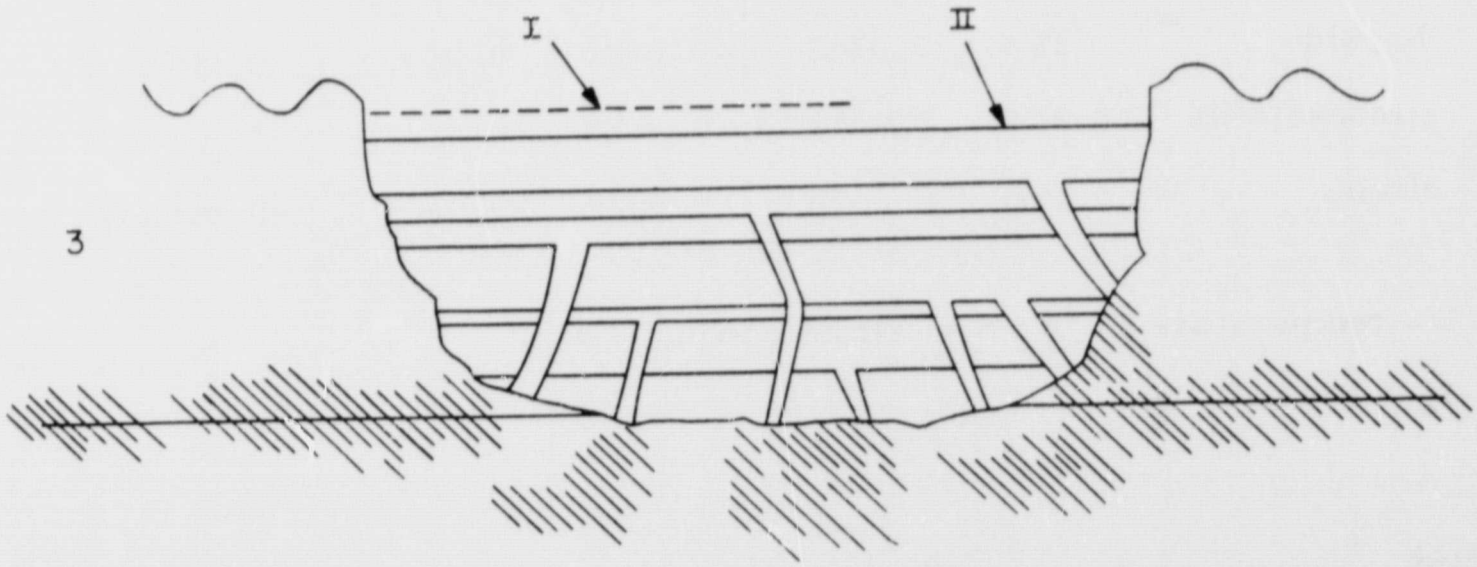
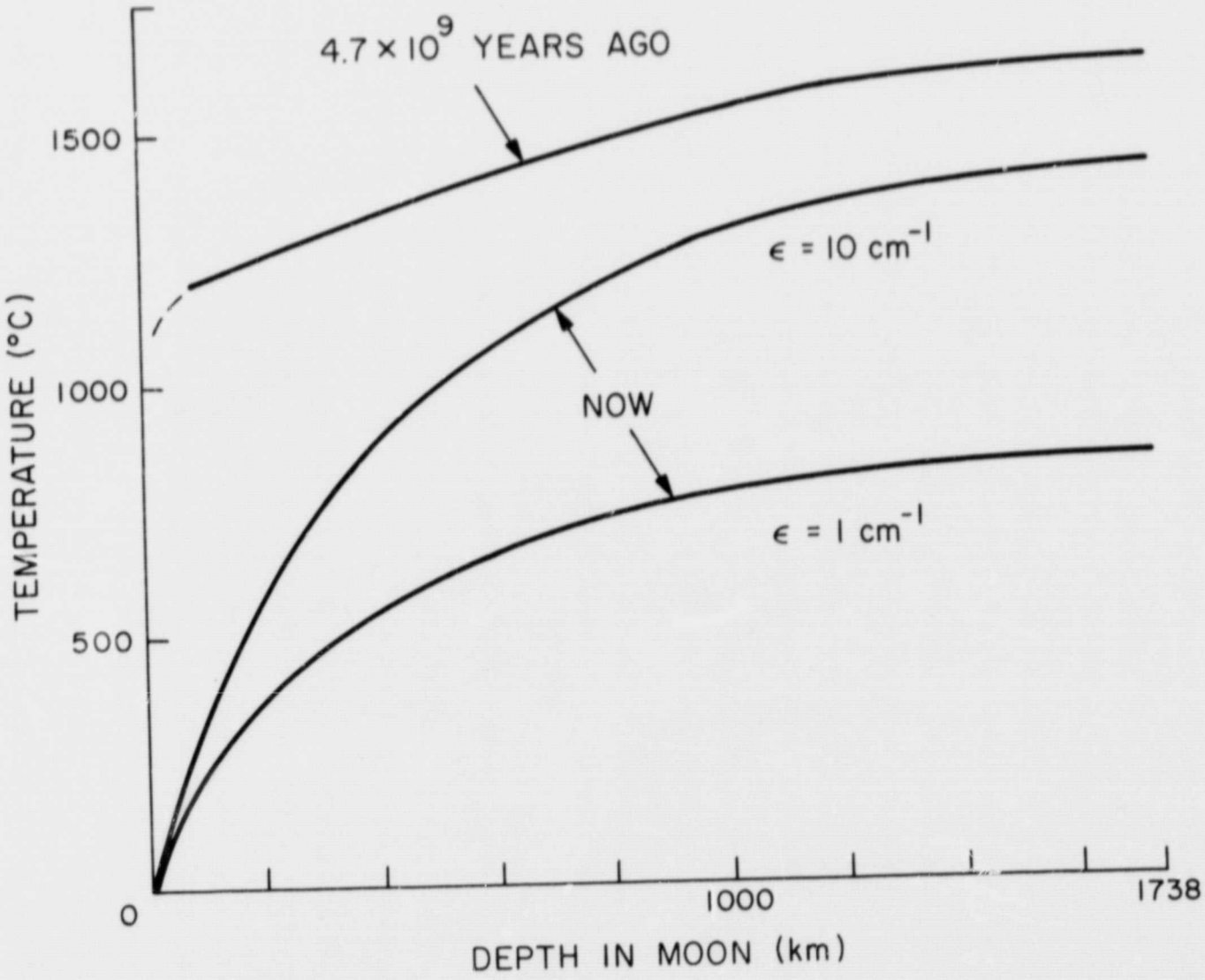

I
II

Figure IV-4. Evolution of temperature profile in an initially melted and differentiated Moon, for two different assumed values of optical opacity ($\epsilon$). Heat-flow calculations were carried out on the Rice University Burroughs 5500 computer, while one of us (JAW) was a guest of the Lunar Science Institute, Houston. The computational procedure employed 250,000-year time increments and divided the lunar radius into 20 space increments. The Moon was assumed to be differentiated into two layers. The outer layer contained 21% of the volume of the Moon and consisted of equal parts of anorthite and diopside. The Moon's overall content of K, U, and Th was taken to be that of chondrites, but all was concentrated in the upper layer. (Thus the validity of assuming chondritic radioactivity is relatively unimportant. Radioactive heat generation so near the surface of the Moon does not figure importantly in the thermal evolution investigated, which consists mostly of losses of initial heat.) The inner layer consisted of olivine and clinoenstatite in equal parts. The initial temperature profile assumed is taken to represent the melting temperature of basalt, which increases with pressure (Yoder and Tilley, 1962). Surface temperature on the Moon was held constant at 0°C. Thermal parameters employed were the following:

$$C_p = [a + b(T \times 10^{-3}) + c(T^{-2} \times 10^{5})] \frac{cal}{gm\ °K}; \qquad K = [d + eT] \frac{cal}{cm\ sec\ °K}$$

| | a | b | c | d | e |
|---|---|---|---|---|---|
| anorthite | 0.232 | 0.0492 | -0.0607 | 0.00380 | 0.0000012 |
| diopside | 0.244 | 0.0362 | -0.0727 | 0.0133 | -0.0000110 |
| clinoenstatite | 0.244 | 0.0472 | -0.0626 | 0.0141 | -0.0000110 |
| olivine | 0.252 | 0.0300 | -0.0637 | 0.0144 | -0.0000070 |

(T = temperature in °K; K = lattice conductivity.)


4.7 × 10^9 YEARS AGO
1500
1000
500
0
TEMPERATURE (°C)
ϵ = 10 cm^-1
NOW
ϵ = 1 cm^-1
1000
1738
DEPTH IN MOON (km)

# V. ANALYTICAL PROCEDURES

## VA. Preliminary Sample Treatment

The sample, as received from NASA Manned Spacecraft Center, comprised two size fractions screened in the Lunar Receiving Laboratory with stainless-steel sieves. One fraction (10084,108) consisted of particles < 1 mm in size, the other (10085,24) nominally of particles > 1 mm, < 1 cm.

The first step in the preliminary sample treatment was accurate weighing of the two separates. A Chain-o-matic analytical balance was used, indicating the following: 10084,108 (5.057 gm); 10085,24 (11.094 gm). The two separates were then photographed under the binocular microscope before further treatment. Subsequent preliminary sample treatment procedures are displayed schematically in Figures VA-1 and -2. A general discussion relating to these procedures follows.

The fine sample (10084) was dry sieved through 100 mesh (149μ) nitex screen (Figure VA-1), the bulk of the < 100 mesh material (3.095 gm) receiving no further treatment other than weighing. An aliquot (~110 mgm) of the -100 fraction was then wet sieved (acetone, 99 mole % pure) through 200 mesh (74μ) nitex in an ultrasonic bath; the +200 -100 fraction (107.7 mgm) was air dried to be used for fiber mounting (see Section VD). The > 100 mesh fraction from the dry sieving was rinsed in acetone to remove adhering ultrafine particles that were not removable by dry sieving. The -100 washings were then collected with the -200 washings and stored to permit complete settling from the acetone before decanting the latter. The various fractions of sample 10084 (except washings) were weighed on a Cahn electrobalance and labeled.

The coarse sample (10085) after initial weighing was dry sieved through 100 mesh nitex to remove most of the adhering finer material not completely

removed in the Lunar Receiving Laboratory and produced by disaggregation of larger particles in transit. The < 100 mesh dry product received no further preliminary treatment other than weighing. The > 100 mesh fraction was then rinsed in acetone in the ultrasonic cleaner to complete removal of the finer particles. The > 100 mesh separate was extensively photographed and once more sieved (100 mesh, dry) to remove minor fines produced during sample handling. The remaining +100 fraction was screened (with acetone) successively through 10 mesh (2.00 mm) bronze wire and 30, 60, and 100 mesh (595, 250, 149μ, respectively) nitex sieves (Figure VA-2). The > 10 mesh material (4.5650 gm) was hand-separated into 10 approximate size fractions (for ease in later thin-section preparation). A portion of the -10 +30 fraction was hand-separated into 15 categories on the basis of superficial lithology, the remainder left unpicked prior to sectioning. All material < 10 mesh and > 100 mesh was ultimately made into thin sections (see Section VB). The -100 washings were allowed to settle in acetone before decanting the latter. The various separates (except washings) were weighted on the electrobalance and labeled as the final step in the preliminary sample treatment.

Table VA-I describes the materials left unused at the time of writing.

Table VA-I. Unused lunar soil sample (as of 12/30/69).

| Sample No. | Subsample | Mesh | Remaining weight (gm) |
|---|---|---|---|
| 10084,108 | FI | >100 | 0.9549 |
| | FII | <200, >100 | 0.1039 |
| | FIV | <100, dry | 3.0953 |
| TOTAL | | | 4.1641 |
| 10085,24 | Ci | <100, dry | 0.5875 |
| | Ciii | unsized | 0.0073 |
| | Civ | unsized | 0.0457 |
| | Cvi-xv | >10 | 4.1960 |
| | Cv | <100 | 0.0160 |
| TOTAL | | | 4.8525 |

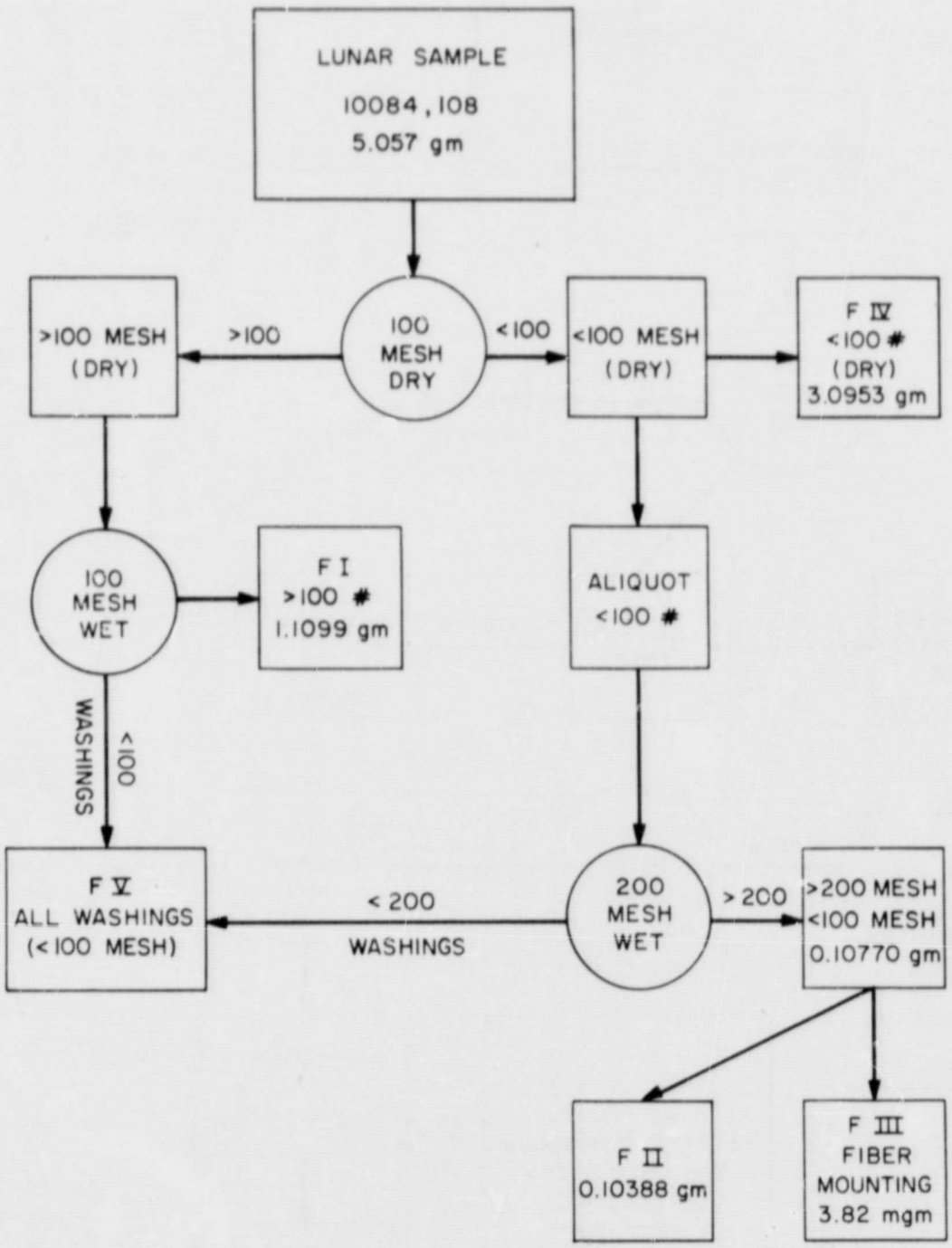



Figure VA-1. Schematic diagram of preliminary sample treatment procedures applied to the fine sample, No. 10084, 108.

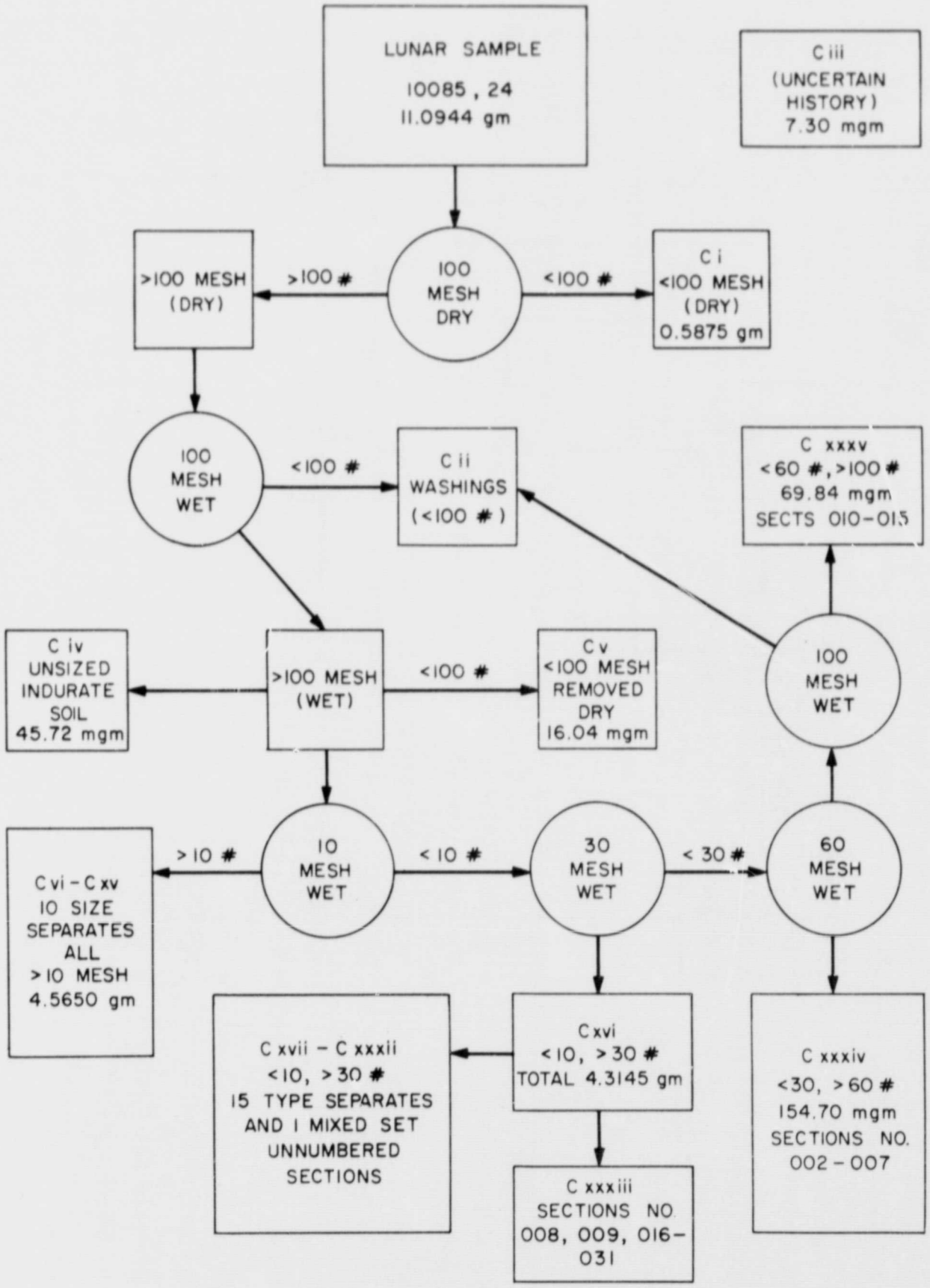



Figure VA-2. Schematic diagram of preliminary sample treatment procedures applied to the coarse sample, No. 10085, 24.

## VB. Thin-Section Preparation

The procedure followed in making thin sections of lithic fragments was essentially that outlined by Moreland (1968). Groups of lithic fragments (up to ~ 50) of similar size were arranged on a teflon plate, impregnated with epoxy (Araldite AY105 and Hardener 935F) diluted 3/1 with toluene, and cured for one hour at 100°C; then ring forms were placed over the groups and filled with Buehler Epoxide. After removal from the forms, the basal surface of each Epoxide plug, where the samples were embedded, was ground on carborundum paper (or 3μ loose abrasive in water on an iron lap, which produces a flatter surface) until the centers of the lithic fragments were exposed, th. .1 polished with 0. 3μ alumina.

Each plug was then cemented to a glass slide (standard petrographic slide, 27 × 46 mm), using Araldite epoxy AY105 and Hardener 935F, approximately in the manner described by Moreland. We would add to Moreland's account that (1) not just any epoxy will do – we found that Buehler Expoxide and Cargille Araldite 6005 developed shrinkage voids during curing, and did not adhere strongly enough to the glass slide (tending to pull away during polishing); and (2) differences in thermal contraction of glass slide and epoxied-on Epoxide plug during cooling from the high-temperature (100°C) mounting procedure specified by Moreland are actually great enough to shatter the glass slide. To prevent this, as soon as plugs were epoxied to slides they were transferred to a 100°C oven; after a half hour at this temperature to complete curing, the oven temperature was decreased to 50°C and the plugs were left overnight to "anneal."

Surplus plug material was then sawed off with a 0.02-in. diamond blade, and the remaining plug-plus-lithic fragments ground down with a cup diamond wheel until feldspar interference colors were yellow-to-gray. We departed from Moreland's practice by using a DoAll Model DH-612 surface grinder (Figure VB-1) instead of Ingraham equipment for these operations, for reasons of economy. Saw blades and grinding wheels can be interchanged on the same machine, which we fitted with a splash shield and vacuum chuck.

Of great assistance in the final machine-grinding stages was a machinist's depth gauge (Figure VB-2), which we adapted to the job of measuring the thickness of section material remaining on the glass slide. The feet of the gauge stand on the blank ends of the slide, and a feeler in the center presses on the surface of the ground-off plug. The measurement can be made between passes of the grinding wheel, without removing the section from the chuck. The gauge reading can be translated directly into the number of divisions the advance wheel of the surface grinder needs to be rotated, in order to leave about 50μ of material on the slide.

In order to insure parallelism between the polished plug surface glued to the slide and the surface being ground down by the cup wheel, the grinding machine was used to "dress" each blank slide, by grinding once down the face of it with the cup wheel, before the plug was epoxied on.

Finally, sections (held in a Buehler petrographic slide holder, 30-8005) were fine-ground by hand, using a 3M extra-fine metal-backed diamond disk, or in some cases No. 600 carborundum paper, until the desired interference colors were obtained, then polished with 0.3μ alumina on a Buehler Texmet-covered lap.

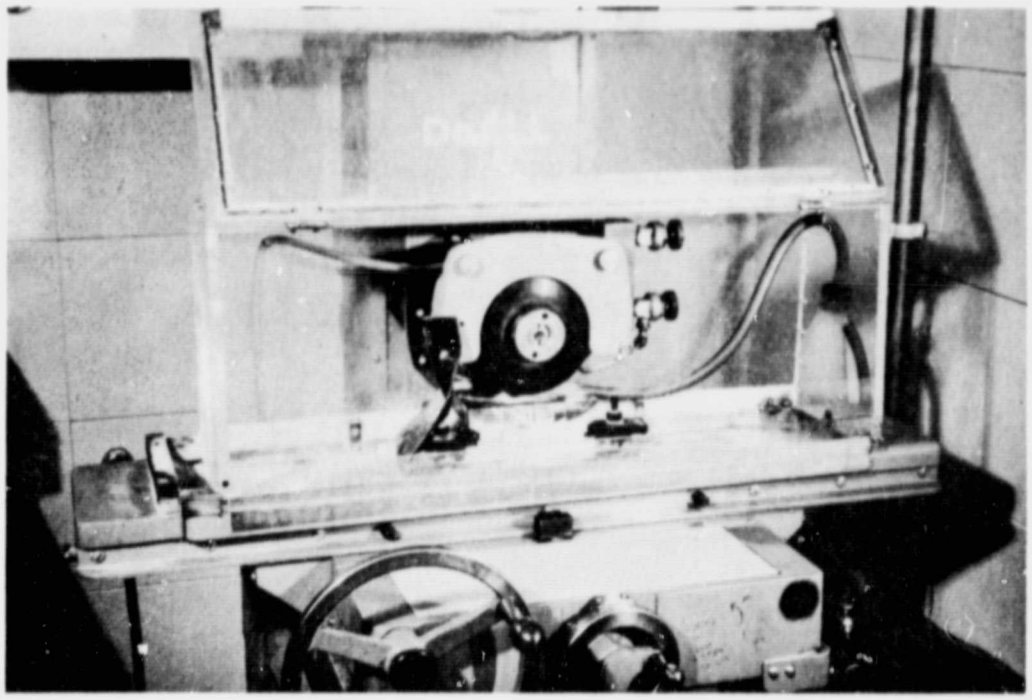


Figure VB-1. Surface grinder adapted for making thin sections.

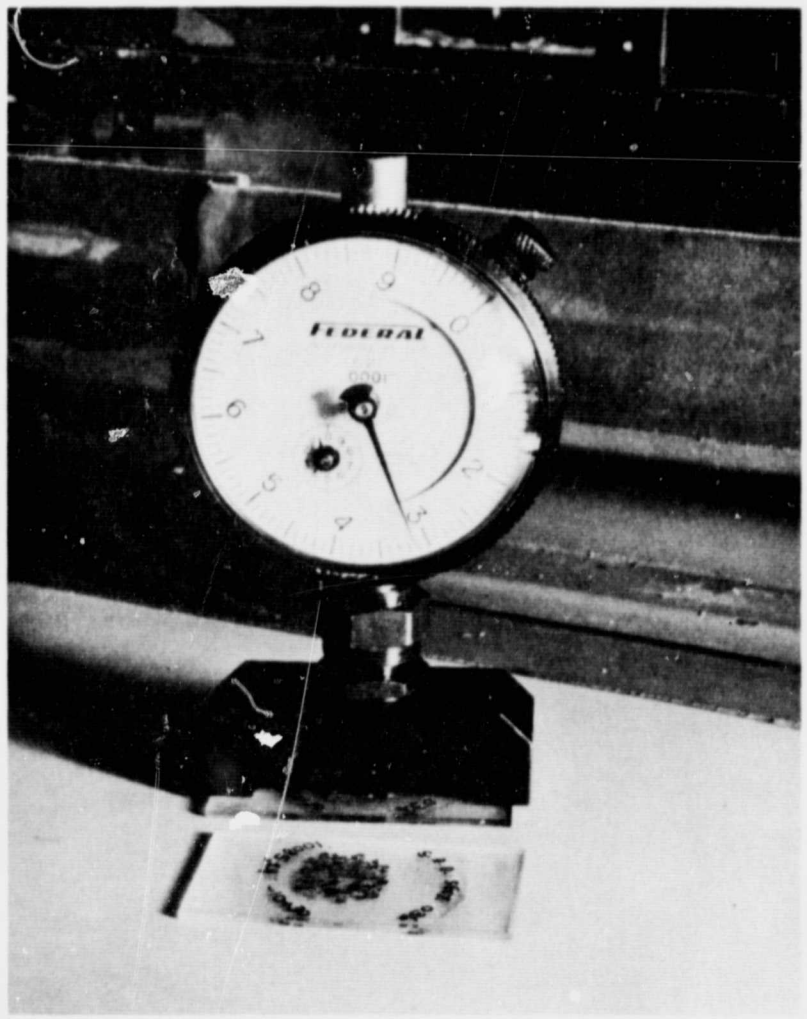



Figure VB-2. Depth gauge, adapted to measure thickness of material remaining on a glass slide during sectioning. In practice, measurement is made while section remains attached to vacuum chuck.

## VC. Microprobe Analysis

### Procedures

All microprobe analyses reported in this study were made with a MAC Model 400 electron microprobe analyzer equipped with transmitted as well as reflected light optics. Operating conditions routinely employed were 20 KV accelerating voltage and 0.010 to 0.025 μamp specimen current. Some Na and K analyses were made with 10 KV and 0.030 μamps. Thirty-second counting times were routinely used.

The three spectrometers of the MAC 400 were used simultaneously for three different elements. Detectors and analyzing crystals used for various elements are indicated in Table VC-I. For all elements pulse-height analysis (integral mode) was employed. Minerals were analyzed for all major and most minor elements (except oxygen, see below), with up to 12 elements being analyzed in most silicates. This procedure of course requires more than one run on a given analysis point. Polaroid photomicrographs taken through a Zeiss polarizing microscope in transmitted and reflected light were used to aid in relocating analysis points and for relating analyses to textures. Chemically analyzed natural and synthetic minerals were used as element standards along with certain pure metals (Fe, Ni, Co).

For the majority of analyses a focussed electron beam with a diameter of approximately 1μ was used. A few analyses were made utilizing a defocussed beam (50μ diameter). When this was done, standards as well as unknowns were analyzed with the defocussed beam. Although the standard microprobe correction procedures are partly invalidated when heterogeneous areas are analyzed with a broad beam, we found this procedure useful for estimating the bulk composition of fine-grained materials.

Data reduction was performed by a CDC 6400 computer using a program devised by one of us (JAW). This program performs the usual theoretical

corrections on both standards and unknowns. Whenever possible, standards close to the composition of the unknowns were used for major elements, to minimize the magnitude of corrections. For example, augite standards were used for Ca-rich clinopyroxene analyses (Fe, Mg, Ca, Si), an olivine standard for olivine analyses (Fe, Mg, Si), troilite for iron sulfide analyses (Fe, S), anorthite or bytownite for calcic-plagioclase analyses, etc. For an element of minor abundance in an unknown, a standard rich in that element was employed on the assumption that the uncertainty in corrections made would be less than the uncertainty in the chemical analysis for minor elements in a more realistic standard. For example, rutile was used as a Ti standard for pyroxene analyses rather than a pyroxene standard supposedly containing some 1 wt. % $TiO_2$.

The data-reduction program is iterative, repeatedly performing corrections on the raw data (using the composition arrived at in the last step to compute $f(\chi)$, etc.) until the result differs from the previous computation by less than 0.05 wt. % for all elements. The procedure used for making fluorescence corrections is basically that of Castaing, as discussed by Koopman (1968). Absorption corrections are made according to the procedure outlined by Adler and Goldstein (1965), using mass absorption coefficients compiled by Heinrich (1968). Atomic number corrections are made according to the procedure of Duncumb and Reed (1968).

In addition to matrix corrections, the data-reduction program makes corrections for detector dead-time and for specimen current drift and background. Specimen current drift is assumed to be linear between standardizations, and a time-proportionate correction is applied to all analyses made between standard readings; provisions are made for irregular time lapses during data collection when they are noted.

Background intensities are assumed to result from backscattered electrons and "white" radiation generated in the target (sample) material. Two methods of background determination were employed, depending on the intensity of the characteristic peak of an element in the unknown. For

elements with a peak/background ratio $>\sim 7$, the count rate was measured on a substance with known mean atomic number containing no elements that produce characteristic radiation of any kind at the wavelength in question. The program then calculates the background as a function of mean atomic number for standards and unknowns. For elements with a peak/background ratio $<\sim 7$, the background was estimated at each analysis point by off-setting the spectrometer symmetrically above and below the wavelength in question and averaging the two readings.

In addition to those elements actually analyzed for in an unknown, the data-reduction program is able to take account of other elements known to be present in certain stoichiometric proportions to the analyzed elements, especially oxygen. For purposes of this stoichiometric computation we assumed all Fe in silicates and oxides to be in the ferrous state. The relatively reduced nature of the lunar rocks makes this assumption reasonable.

Analytical Reliability

Our data-reduction program makes an estimate of the total uncertainty attached to each measurement, according to the formula

$$U = \sqrt{\sum_{i=1}^{\sigma} U_i^2}$$

where

$U_1$ = uncertainty due to counting statistics ($1\sigma$),

$U_2$ = 50% of the beam current drift correction,

$U_3$ = 200% of the background counting error ($1\sigma$),

$U_4$ = 25% of the absorption correction,

$U_5$ = 50% of the fluorescence correction,

$U_6$ = 15% of the atomic number correction.

Clearly the weighting factors applied to each of these various sources of uncertainty are arbitrary. They are intended to represent our best estimate as to the relative contribution to total uncertainty made by each source. For all analyses tabulated in this study this total estimated uncertainty term was used as a guide in assembling the tables of microprobe data in this report. In general we report analyses to one decimal place: we believe this to be a realistic expression of the general reliability of our analyses. The total estimated uncertainty is given in tables where exceptions to this rule occur.

Obviously there are several sources of uncertainty that are not taken into account in U. These include such things as uncertainty in the chemical analysis of a standard, imprecision in relocating analysis points during multiple runs, the possible polymineralic nature of the small volume represented by a given analysis point, etc. Such factors are difficult or impossible to evaluate quantitatively. Therefore, two criteria were applied in judging the acceptability of an analysis. First, the sum of the analysis was required to be within 98.5 to 101.0 wt. %, on the assumption that a good analysis may sum to slightly $<100\%$ because of undetermined minor elements. This criterion was applied to all analyses plotted in diagrams and to most tabulated analyses. Some exceptions appear in tables where better sums were not obtained for a particular type of analysis (usually on very fine-grained material). In these cases the sum is always presented in the table.

A second criterion for reliability was applied to silicate and some oxide analyses. The analyses were recalculated by computer to atomic percents of the various elements (including oxygen) and cation abundances relative to oxygen were calculated according to the ideal stoichiometry of the mineral. For example, in a stoichiometric pyroxene there should be two tetrahedral cations (Si plus some Al) and two octahedral cations (Mg, Fe, Ti, Cr, Mn, Al, etc.) for every six oxygens. Similarly, in a stoichiometric feldspar there should be five cations (Na, K, Ca, Al, Si, etc.) for every eight oxygens. The results of such calculations are presented with tabulated analyses where applied. They are considered to provide some measure of the reliability of the analysis (since compensating errors can still result in a good sum of elemental percentages) and of the mineralogical "purity" of the analysis (an analysis could be nearly perfect but be of a mixture of two or more phases).

Table VC-I. Detectors and analyzing crystals used in microprobe analysis.

| Elements, spectral line | Detector | Analyzing crystal |
|---|---|---|
| Na, Mg, Al, Si $K_a$ | Gas-flow proportional (90% argon, 10% methane) | KAP |
| S, K, Ca, Ti $K_a$ | | PET |
| Zr $L_a$ | | |
| Cr, Mn, Fe, Co, Ni $K_a$ | Sealed proportional (xenon) | LiF |

PRECEDING PAGE BLANK NOT FILMED.

## VD. Grain Mounting for Optical and X-Ray Measurements

In planning our procedures, our goal was to mount tiny grains on the tips of thin fibers in order to determine their optical properties in immersion media on a spindle stage, then to x-ray them, and finally to arrange them in a microprobe mount while on the same fiber. These manipulations require a light but strong fiber and tenacious glue, both of which must be transparent to x-rays and insoluble in immersion oils and rinsing media. After weeks of experimentation with fibers and binders, our assistant, Miss Wendy A. Frank, found the answer in thin glass fibers, 10μ in diameter, and Hysol Epoxi-patch. Clasped in a micromanipulator under a binocular microscope, the glass rod is tipped with a minute amount of the epoxy, which remains fluid long enough for picking up one edge or tip of a small particle. The glass rod is then transferred to a small, numbered hole drilled in a plastic bar cemented in a numbered plastic box. Each box has holes for 10 rods and when all are filled, the box is left overnight in an oven at a temperature of 60 to 70°C to cure the epoxy. These procedures have proved remarkably satisfactory so long as very careful handling at all times is the order of the day.

PRECEDING PAGE BLANK NOT FILMED.

## VE. Refractive Index and Optic Axial Angle Measurements

Refractive indices were determined by the immersion method using "sodium" monochromatic light (produced by an interference filter, $\lambda = 5890$ Å). Final matches were obtained by mixing oils, which were immediately afterward calibrated with a Leitz Abbé refractometer. Temperature gradients between microscope and refractometer were negligible. Maximum and minimum indices of anisotropic crystals were observed by rotating fiber-mounted specimens on a single-axis spindle stage, mounted horizontally on the microscope stage. After a match was obtained, the oil was drawn out of the covered specimen well with a capillary tube and transferred directly to the refractometer. Because many of the lunar crystals are distorted and clouded, their refractive indices are difficult to ascertain. In general, the precision of our measurements on crystals is ±0.002. On glasses, our precision approaches ±0.001.

The optic axial angle (2V) of biaxial crystals was measured conoscopically, whenever possible, on a five-axis universal stage by use of a Leitz conoscopic u-stage apparatus. In some instances, the measurement was made orthoscopically. Whenever possible, hemispheres of refractive index close to that of the central glass plate ($n = 1.554$) were used with appropriate refraction corrections for the mean index of the mineral. Precision of the measurement depends on the size of the angle: for conoscopic measurements of $2V < 40°$ the precision is ±0.5°, for $40° < 2V < 60°$ it is ±1°, for $60° < 2V$ it is ±3°. The orthoscopic precision is approximately twice the conoscopic precision.

PRECEDING PAGE BLANK NOT FILMED.

## VF. Density Determinations

Each particle was placed in Clerici solution (aqueous solution of thallium malonate and thallium formate), the specific gravity of which was adjusted until the particle hung suspended in the liquid. The specific gravity of the Clerici solution was then determined by weighing the liquid in a 2 ml or 10 ml pycnometer that had been previously calibrated with distilled water. The precision of the measurement is better than $\pm 0.003$ gm/cm$^3$.

PRECEDING PAGE BLANK NOT FILMED.

## VG. X-Ray Diffraction Procedures

For study of the fine-grained lunar soils, we acquired an Advanced Metals Research, Inc., x-ray microfocus generator that puts out a small, very high intensity beam (Figure VG-1). A focal spot of 40 × 60μ was measured at a distance of 8 cm from the window. The x-ray head has two windows and interchangeable anodes of Cu and Fe. We used only Ni-filtered Cu radiation for the lunar particles.

With this generator we use two Enraf-Nonius Universal camera bases and three interchangeable film cassettes: one standard 114.6-mm diameter Debye-Scherrer type cassette, one 57.3-mm Debye-Scherrer type, and one 57.3-mm diameter rotation camera. The camera bases are equipped with two kinds of sample holders: one precision goniometer head, and one two-axis rotator designed by us and made in the Harvard College Observatory Model Shop (Figure VG-2).

Single crystals mounted on this rotator produce excellent powder patterns. Those on the goniometer rotate about only one axis and therefore produce spotty patterns. The goniometer mount was used mainly for powder rods and grains that appeared finely polycrystalline, or shocked. Most soil particles mounted on the goniometer yielded somewhat grainy but clearly identifiable patterns.

Exposure times of 3 to 4 hr are sufficient for identification purposes of most mineral grains down to a size of about 30μ, and these periods can be shortened by use of a helium path. Many of the lunar grains are partly glassy, however, and require longer exposures to register the included crystalline materials.

A specially designed mini-camera for holding films 52 mm long, punched for obtaining powder patterns of the Straumanis type, has been fitted into a

spare cover for our 57.3-mm Debye-Scherrer camera. It produces measurable patterns in shorter exposure time. We have developed a computer program for obtaining d spacings, corrected for film shrinkage, from 2θ readings on both of our standard-size films. The program can also be applied to the 52-mm films; it treats them as an extreme case of film shrinkage.

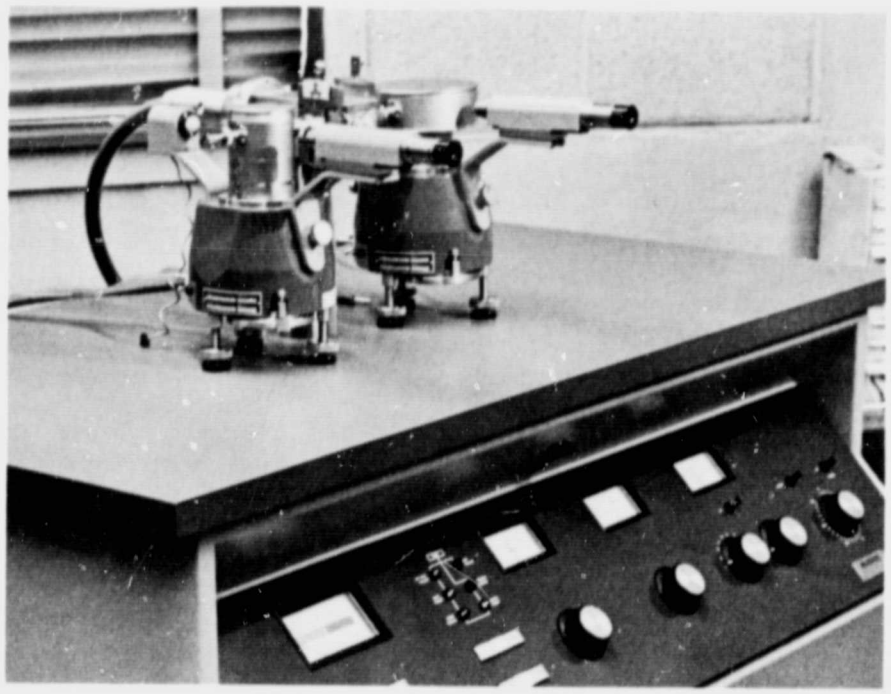


Figure VG-1. X-ray microfocus generator, Advanced Metals Research, Inc., with a camera aligned at each window. The camera bases (Enraf Nonius, Inc.) allow a choice of rotation or oscillation of the mounted crystals. Camera at right is the 114.6-mm Debye-Scherrer type cassette; that at left is the same type, 57.3-mm diameter.

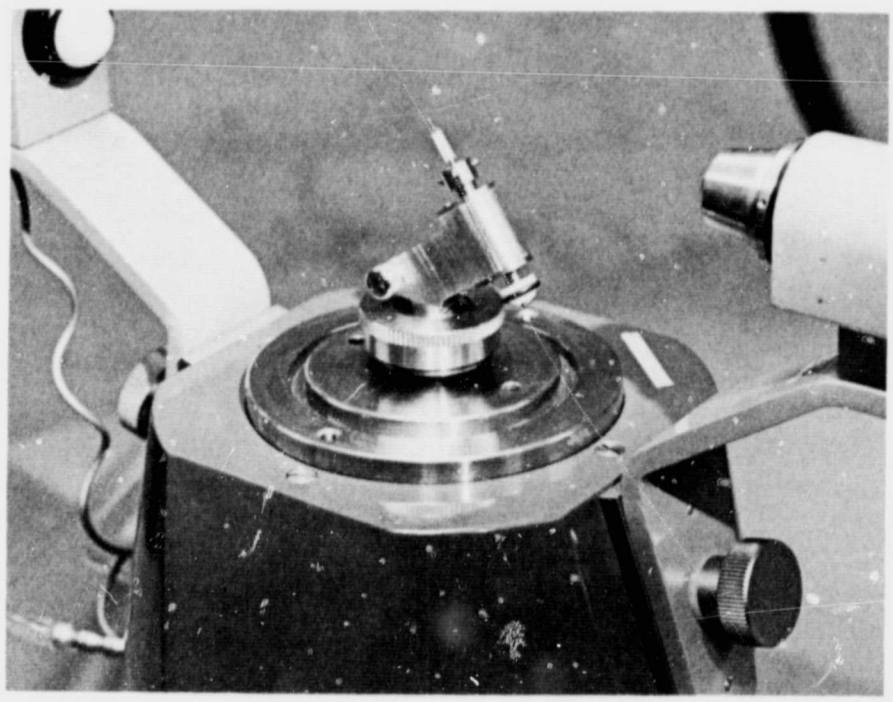


Figure VG-2. The two-axis rotating crystal mount designed by us for obtaining powder patterns from single crystals. The camera motor rotates the central vertical axis while the oblique axis is rotated by an O-ring, which rolls along the inner surface of the cylindrical metal camera base (removed for photograph).

## VI. ACKNOWLEDGMENTS

NASA grant NAS 9-8106 supported the work in this report and paid the salary of one of us (JSD). We are grateful to Fred L. Whipple for stimulating discussions of lunar theory; to Janice F. Bower for microprobe analyses; to Wendy A. Frank for handling and mounting microscopic particles; to the Lunar Science Institute for including JAW in an invaluable Symposium on the Geophysical Interpretation of the Moon (August 1969), and supplying computer facilities for heat-flow calculations; to Ann Phillips for programming the latter; and to Neil A. Armstrong, Michael Collins, and Edwin E. Aldrin, Jr., for important services rendered.

PRECEDING PAGE BLANK NOT FILMED.

## VII. REFERENCES

ADLER, I., and GOLDSTEIN, J.

1965. Absorption tables for electron probe microanalysis. NASA Tech. Note D-2984, 276 pp.

BALDWIN, R. B.

1949. The Face of the Moon. University of Chicago Press, Chicago, Illinois, 239 pp.

1968. Lunar mascons: another interpretation. Science, vol. 162, pp. 1407-1408.

BUDDINGTON, A. F.

1939. Adirondack Igneous Rocks and their Metamorphism. Geol. Soc. Amer. Mem., vol. 7, 354 pp.

BUSECK, P. R., and GOLDSTEIN, J. I.

1969. Olivine compositions and cooling rates of pallasitic meteorites. Geol. Soc. Amer. Bull., vol. 80, pp. 2141-2158.

CLARK, S. P., Jr.

1966. Handbook of Physical Constants. Geol. Soc. Amer. Mem., vol. 97, 587 pp.

CONEL, J. E., and HOLSTROM, G. B.

1968. Lunar mascons: a near-surface interpretation. Science, vol. 162, pp. 1403-1404.

DEER, W. A., HOWIE, R. A., and ZUSSMAN, J.

1962. See Ibid., 1963.

1963. Rock Forming Minerals, vol. 2: Chain Silicates. Longmans, Green & Co. Ltd., London, 379 pp.

DUKE, M. B., and SILVER, L. T.

1967. Petrology of eucrites, howardites, and mesosiderites. Geochim. Cosmochim. Acta, vol. 31, pp. 1637-1665.

DUNCUMB, P., and REED, S. J. B.

1968. The calculation of stopping power and backscatter effects in electron probe microanalysis. In Quantitative Electron Probe Microanalysis, ed. by Heinrich, K. J. F., N.B.S. Special Publication 298, pp. 133-154.

FISH, R. A., GOLES, G. G., and ANDERS, E.

1960. The record in the meteorites. III. On the development of meteorites in asteroidal bodies. Astrophys. Journ., vol. 132, pp. 243-258.

GAULT, D. E., SHOEMAKER, E. M., and MOORE, H. J.

1963. Spray ejected from the lunar surface by meteoroid impact. NASA Tech. Note D-1767, 39 pp.

GAULT, D. E., QUAIDE, W. L., OBERBECK, V. R., and MOORE, H. J.

1966. Luna 9 photographs: evidence for a fragmental surface layer. Science, vol. 153, pp. 985-988.

HEINRICH, K. J. F.

1968. Mass absorption coefficients. In The Electron Microanalyzer and its Applications, ed. by Ziebold, T. O., M.I.T. Summer Session, 1968, pp. S-22-S-34.

HERZ, N.

1969. Anorthosite belts, continental drift, and the anorthosite event. Science, vol. 164, pp. 944-947.

KOOPMAN, N. G.

1968. Fluorescence correction. In The Electron Microanalyzer and its Applications, ed. by Ziebold, T. O., M.I.T. Summer Session, 1968, pp. 70-78.

KUIPER, G. P.

1954. On the origin of the lunar surface features. Proc. U.S. Nat. Acad. Sci., vol. 40, pp. 1096-1112.

LAMAR, D. L., and McGANN, J.

1966. Shape and internal structure of the moon. Icarus, vol. 5, pp. 10-23.

LEVIN, B. J.

1962. Thermal history of the moon. In The Moon, 14th I.A.U. Symposium, Pulkovo, ed. by Kopal, Z. and Mikhailov, Z., pp. 157-167.

LSPET

1969a. Lunar Sample Information Catalogue – Apollo 11. LRL, NASA Manned Spacecraft Center, Houston, Texas.

1969b. Preliminary examination of lunar samples from Apollo 11. Science, vol. 165, pp. 1211-1227.

MacDONALD, G. J. F.

1962. On the internal constitution of the inner planets. Journ. Geophys. Res., vol. 67, pp. 2945-2974.

1964. Earth and Moon: past and future. Science, vol. 145, pp. 881-890.

MacGREGOR, I. D.

1969. The system $MgO-SiO_2-TiO_2$. Amer. Journ. Science, vol. 267A, pp. 342-363.

MENZEL, D. H.

1967. The nature of the surface of the moon, illustrated in part by 3-D slides taken from Ranger photographs. In Interpretation of Lunar Probe Data, vol. 14 of Science and Technology Series, American Astronautical Society, pp. 113-122.

MORELAND, G. C.

1968. Preparation of polished thin sections. Amer. Mineral., vol. 53, pp. 2070-2074.

MULLER, P. M., and SJOGREN, W. L.

1968. Mascons: lunar mass concentrations. Science, vol. 161, pp. 680-684.

MUNSELL COLOR COMPANY

1966. Munsell Book of Color. Munsell Color Company, Inc., Baltimore.

NESS, N. F.

1969. The electrical conductivity and internal temperature of the moon. Preprint, NASA Goddard Space Flight Center Document X-616-69-191.

O'KEEFE, J. A.

1968. Isostasy on the moon. Science, vol. 162, pp. 1405-1406.

OLSEN, E.

1969. Pyroxene gabbro (anorthosite association): similarity to Surveyor V lunar analysis. Science, vol. 166, pp. 401-402.

ÖPIK, E. J.

1969. The Moon's surface. Ann. Rev. Astron. Astrophys., vol. 7, pp. 473-526.

PATTERSON, J. H., FRANZGROTE, E. J., TURKEVICH, A. L., ANDERSON, W. A., ECONOMOU, T. E., GRIFFIN, H. E., GROTCH, S. L., and SOWINSKI, K. P.

1969. Alpha-scattering experiment on Surveyor 7: comparison with Surveyors 5 and 6. Journ. Geophys. Res., vol. 74, pp. 6120-6148.

POWELL, B. N.

1969a. Petrology and chemistry of mesosiderites. Ph.D. Thesis, Columbia University.

1969b. Petrology and chemistry of mesosiderites - I. Textures and composition of nickel-iron. Geochim. Cosmochim. Acta, vol. 33, pp. 789-810.

1969c. Silicates in mesosiderites and their genetic implications. Presented at the 32nd Annual Meeting of the Meteoritical Society, Houston, Texas.

POWELL, B. N., and WEIBLEN, P. W.

1967. On the petrology of mesosiderites. Presented at the 30th Annual Meeting of the Meteoritical Society, Moffett Field, California.

QUAIDE, W. L., and OBERBECK, V. R.

1968. Thickness determinations of the lunar surface layer from lunar impact craters. Journ. Geophys. Res., vol. 73, pp. 5247-5270.

RAMDOHR, P.

1960. Die Erzmineralien und Ihre Verwachsungen. Akademie Verlag, Berlin, 1089 pp.

RENNILSON, J. J., DRAGG, J. L., MORRIS, E. C., SHOEMAKER, E. M., and TURKEVICH, A.

1966. Surveyor I mission report, Part II, Scientific results. Jet Propulsion Lab. Tech. Rept. 32-1023, Pasadena, Calif., pp. 1-44.

STIPE, J. G.

1968. Iron meteorites as mascons. Science, vol. 162, pp. 1402-1403.

TAYLOR, S. R.

1964. Abundance of chemical elements in the continental crust: a new table. Geochim. Cosmochim. Acta, vol. 28, pp. 1273-1285.

UREY, H. C.

1952. The Planets. Yale University Press, New Haven, Connecticut, 245 pp.

UREY, H. C.

1968. Mascons and the history of the moon. Science, vol. 162, pp. 1408-1410.

UREY, H. C., ELSASSER, W. M., and ROCHESTER, M. G.

1959. Notes on the internal structure of the moon. Astrophys. Journ., vol. 129, pp. 842-848.

VINOGRADOV, A. P., SURKOV, Yu. A., CHERNOV, G. M., KIRNOZOV, F. F., and NAZARKINA, G. B.

1967. Paper presented at the 10th meeting of COSPAR, London.

WAGER, L. R., BROWN, G. M., and WADSWORTH, W. J.

1960. Types of igneous cumulates. Journ. Petrol., vol. 1, pp. 73-85.

WETHERILL, G. W.

1968. Lunar interior: constraint on basaltic composition. Science, vol. 160, pp. 1256-1257.

WOOD, J. A.

1967. The early thermal history of planets: evidence from meteorites. In Mantles of the Earth and Terrestrial Planets, ed. by Runcorn, S. K., Interscience Publishers, London, pp. 3-14.

YODER, H. S., Jr., and TILLEY, C. E.

1962. Origin of basalt magmas, and experimental study of natural and synthetic rock systems. Journ. Petrol., vol. 3, pp. 342-532.

## BIOGRAPHICAL NOTES

JOHN A. WOOD received the B.S. degree from Virginia Polytechnic Institute in 1954 and the Ph.D. degree from the Massachusetts Institute of Technology in 1958.

Dr. Wood was a research associate at the Enrico Fermi Institute for Nuclear Studies at the University of Chicago from 1963 to 1965. Since 1965, he has been a geologist at SAO and a research associate at Harvard University.

Dr. Wood's general fields of investigation are chemical analyses and mineralogical studies of meteoritic and lunar material; the study of primitive planetary material, specifically meteorites; and the problem of the origin of the planets and the solar system in general.

URSULA B. MARVIN received the B.A. degree from Tufts University, and the A.M. and Ph.D. degrees from Harvard University in geology.

Her career includes three years of teaching mineralogy and petrology at Tufts University, and six years of laboratory and field investigations of mineral deposits in the United States, Brazil, and West Africa.

Dr. Marvin joined the staff of the Smithsonian Astrophysical Observatory as a geologist in 1961 and became an associate of Harvard in 1965.

Her primary fields of investigation are mineralogical studies of lunar samples, meteorites, and the identification of cosmic dust. She is also interested in impact structures and the geological implications of satellite geodesy.

BENJAMIN N. POWELL was graduated from Amherst College in 1963, with a major in geology. He received the Ph. D. in geology from Columbia University in January 1969, and has been working at SAO since that time.

Dr. Powell is an igneous petrologist, currently specializing in the study of extraterrestrial materials, including meteorites and lunar samples.

JOHN S. DICKEY, Jr. received his Ph. D. in geology from Princeton University in 1969. He has been at SAO since January 1969.

Dr. Dickey is a petrologist, specializing in the chemistry of igneous rocks.